



ELSEVIER

Nuclear Instruments and Methods in Physics Research A 479 (2002) 117–232

**NUCLEAR  
INSTRUMENTS  
& METHODS  
IN PHYSICS  
RESEARCH**  
Section A

www.elsevier.com/locate/nima

## The Belle detector

A. Abashian<sup>a</sup>, K. Gotow<sup>a</sup>, N. Morgan<sup>a</sup>, L. Piilonen<sup>a</sup>, S. Schrenk<sup>a</sup>, K. Abe<sup>b</sup>, I. Adachi<sup>b</sup>, J.P. Alexander<sup>b,1</sup>, K. Aoki<sup>b</sup>, S. Behari<sup>b</sup>, Y. Doi<sup>b</sup>, R. Enomoto<sup>b,2</sup>, H. Fujii<sup>b</sup>, Y. Fujita<sup>b</sup>, Y. Funahashi<sup>b</sup>, J. Haba<sup>b</sup>, H. Hamasaki<sup>b</sup>, T. Haruyama<sup>b</sup>, K. Hayashi<sup>b</sup>, Y. Higashi<sup>b</sup>, N. Hitomi<sup>b</sup>, S. Igarashi<sup>b</sup>, Y. Igarashi<sup>b</sup>, T. Iijima<sup>b</sup>, Hirokazu Ikeda<sup>b</sup>, Hitomi Ikeda<sup>b</sup>, R. Itoh<sup>b</sup>, M. Iwai<sup>b</sup>, H. Iwasaki<sup>b</sup>, Y. Iwasaki<sup>b</sup>, K.K. Joo<sup>b,3</sup>, K. Kasami<sup>b</sup>, N. Katayama<sup>b</sup>, M. Kawai<sup>b</sup>, H. Kichimi<sup>b</sup>, T. Kobayashi<sup>b</sup>, S. Koike<sup>b</sup>, Y. Kondo<sup>b</sup>, M.H. Lee<sup>b,4</sup>, Y. Makida<sup>b</sup>, A. Manabe<sup>b</sup>, T. Matsuda<sup>b</sup>, T. Murakami<sup>b</sup>, S. Nagayama<sup>b</sup>, M. Nakao<sup>b</sup>, T. Nozaki<sup>b</sup>, K. Ogawa<sup>b,\*</sup>, R. Ohkubo<sup>b</sup>, Y. Ohnishi<sup>b</sup>, H. Ozaki<sup>b</sup>, H. Sagawa<sup>b</sup>, M. Saito<sup>b</sup>, Y. Sakai<sup>b</sup>, T. Sasaki<sup>b</sup>, N. Sato<sup>b</sup>, T. Sumiyoshi<sup>b</sup>, J. Suzuki<sup>b</sup>, J.I. Suzuki<sup>b</sup>, S. Suzuki<sup>b</sup>, F. Takasaki<sup>b,\*</sup>, K. Tamai<sup>b</sup>, M. Tanaka<sup>b</sup>, T. Tatomi<sup>b</sup>, T. Tsuboyama<sup>b</sup>, K. Tsukada<sup>b,5</sup>, T. Tsukamoto<sup>b</sup>, S. Uehara<sup>b</sup>, N. Ujiie<sup>b</sup>, S. Uno<sup>b</sup>, B. Yabsley<sup>b</sup>, Y. Yamada<sup>b</sup>, H. Yamaguchi<sup>b</sup>, H. Yamaoka<sup>b</sup>, Y. Yamaoka<sup>b</sup>, M. Yamauchi<sup>b</sup>, Y. Yoshimura<sup>b</sup>, H. Zhao<sup>b</sup>, R. Abe<sup>c</sup>, G. Iwai<sup>c</sup>, T. Kawasaki<sup>c</sup>, H. Miyata<sup>c</sup>, K. Shimada<sup>c</sup>, S. Takahashi<sup>c</sup>, N. Tamura<sup>c</sup>, K. Abe<sup>d</sup>, H. Hanada<sup>d</sup>, T. Nagamine<sup>d</sup>, M. Nakajima<sup>d</sup>, T. Nakajima<sup>d</sup>, S. Narita<sup>d,6</sup>, M. Sanpei<sup>d</sup>, T. Takayama<sup>d</sup>, M. Ueki<sup>d</sup>, M. Yamaga<sup>d</sup>, A. Yamaguchi<sup>d</sup>, B.S. Ahn<sup>e</sup>, J.S. Kang<sup>e</sup>, Hyunwoo Kim<sup>e</sup>, C.W. Park<sup>e</sup>, H. Park<sup>e</sup>, H.S. Ahn<sup>f</sup>, H.K. Jang<sup>f</sup>, C.H. Kim<sup>f</sup>, S.K. Kim<sup>f</sup>, S.H. Lee<sup>f</sup>, C.S. Park<sup>f</sup>, E. Won<sup>f</sup>, H. Aihara<sup>g</sup>, T. Higuchi<sup>g</sup>, H. Kawai<sup>g</sup>, T. Matsubara<sup>g</sup>, T. Nakadaira<sup>g</sup>, H. Tajima<sup>g</sup>, J. Tanaka<sup>g</sup>, T. Tomura<sup>g</sup>, M. Yokoyama<sup>g</sup>, M. Akatsu<sup>h</sup>, K. Fujimoto<sup>h</sup>, M. Hirose<sup>h</sup>, K. Inami<sup>h</sup>, A. Ishikawa<sup>h</sup>, S. Itami<sup>h</sup>, T. Kani<sup>h</sup>, T. Matsumoto<sup>h</sup>, I. Nagai<sup>h</sup>, T. Okabe<sup>h</sup>, T. Oshima<sup>h</sup>, K. Senyo<sup>h</sup>, A. Sugi<sup>h</sup>, A. Sugiyama<sup>h</sup>, S. Suitoh<sup>h</sup>, S. Suzuki<sup>h</sup>, M. Tomoto<sup>h</sup>, K. Yoshida<sup>h</sup>, R. Akhmetshin<sup>i</sup>, P. Chang<sup>i</sup>, Y. Chao<sup>i</sup>, Y.Q. Chen<sup>i</sup>, W.S. Hou<sup>i</sup>, S.C. Hsu<sup>i</sup>,

\*Corresponding author.

*E-mail address:* fumihiko.takasaki@kek.jp (F. Takasaki).

<sup>1</sup>Permanent address. Newman Laboratory, Cornell University, Ithaca, NY 14853-5001, USA.

<sup>2</sup>Present address. ICRR, Tokyo University, Tanashi, Tokyo 188-8502, Japan.

<sup>3</sup>Present address. University of Toronto, Toronto, Ont., Canada M5S 1A7.

<sup>4</sup>Present address. IPST, University of Maryland, College Park, MD 20742, USA.

\* Deceased.

<sup>5</sup>Present address. Iwate University, Morioka 020-8551, Japan.

<sup>6</sup>Permanent address. LANL, Los Alamos, NM 87545, USA.

H.C. Huang<sup>i</sup>, T.J. Huang<sup>i</sup>, M.C. Lee<sup>i</sup>, R.S. Lu<sup>i</sup>, J.C. Peng<sup>i,7</sup>, K.C. Peng<sup>i</sup>, S. Sahu<sup>i</sup>,  
H.F. Sung<sup>i</sup>, K.L. Tsai<sup>i</sup>, K. Ueno<sup>i</sup>, C.C. Wang<sup>i</sup>, M.Z. Wang<sup>i</sup>, G. Alimonti<sup>j</sup>,  
T.E. Browder<sup>j</sup>, B.C.K. Casey<sup>j</sup>, F. Fang<sup>j</sup>, H. Guler<sup>j</sup>, M. Jones<sup>j</sup>, Y. Li<sup>j</sup>, S.L. Olsen<sup>j</sup>,  
M. Peters<sup>j</sup>, J.L. Rodriguez<sup>j</sup>, M. Rosen<sup>j</sup>, S. Swain<sup>j</sup>, K. Trabelsi<sup>j</sup>, G. Varner<sup>j</sup>,  
H. Yamamoto<sup>j</sup>, Y.H. Zheng<sup>j</sup>, Q. An<sup>k</sup>, H.F. Chen<sup>k</sup>, Y.F. Wang<sup>k</sup>, Z.Z. Xu<sup>k</sup>,  
S.W. Ye<sup>k</sup>, Z.P. Zhang<sup>k</sup>, M. Asai<sup>l</sup>, Y. Asano<sup>m</sup>, S. Mori<sup>m</sup>, S. Stanič<sup>m,8</sup>, Y. Tsujita<sup>m,9</sup>,  
J. Zhang<sup>m</sup>, D. Žontar<sup>m,8</sup>, T. Aso<sup>n</sup>, V. Aulchenko<sup>o</sup>, D. Beilino<sup>o</sup>, A. Bondar<sup>o</sup>,  
L. Dneprovsky<sup>o</sup>, S. Eidelman<sup>o</sup>, A. Garmash<sup>o</sup>, A. Kuzmin<sup>o</sup>, L. Romanov<sup>o</sup>,  
N. Root<sup>o</sup>, B. Shwartz<sup>o</sup>, A. Sidorov<sup>o</sup>, V. Sidorov<sup>o</sup>, Y. Usov<sup>o</sup>, V. Zhilich<sup>o</sup>,  
A.M. Bakich<sup>p</sup>, L.S. Peak<sup>p</sup>, K.E. Varvell<sup>p</sup>, E. Banas<sup>q</sup>, A. Bozek<sup>q</sup>, P. Jalocha<sup>q</sup>,  
P. Kapusta<sup>q</sup>, Z. Natkaniec<sup>q</sup>, W. Ostrowicz<sup>q</sup>, H. Palka<sup>q</sup>, M. Rozanka<sup>q</sup>, K. Rybicki<sup>q</sup>,  
P.K. Behera<sup>r</sup>, A. Mohapatra<sup>r</sup>, M. Satapathy<sup>r</sup>, Y.H. Chang<sup>s</sup>, H.S. Chen<sup>t</sup>,  
L.Y. Dong<sup>t</sup>, J. Li<sup>t</sup>, H.M. Liu<sup>t</sup>, Z.P. Mao<sup>t</sup>, C.X. Yu<sup>t</sup>, C.C. Zhang<sup>t</sup>, S.Q. Zhang<sup>t</sup>,  
Z.G. Zhao<sup>t</sup>, Z.P. Zheng<sup>t</sup>, B.G. Cheon<sup>u</sup>, Y. Choi<sup>u</sup>, D.W. Kim<sup>u</sup>, J.W. Nam<sup>u</sup>,  
S. Chidzik<sup>v</sup>, K. Korotuschenko<sup>v</sup>, C. Leonidopoulos<sup>v</sup>, T. Liu<sup>v</sup>, D. Marlow<sup>v</sup>,  
C. Mindas<sup>v</sup>, E. Prebys<sup>v</sup>, R. Rabberman<sup>v</sup>, W. Sands<sup>v</sup>, R. Wixted<sup>v</sup>, S. Choi<sup>w</sup>,  
J. Dragic<sup>x</sup>, C.W. Everton<sup>x</sup>, A. Gordon<sup>x</sup>, N.C. Hastings<sup>x</sup>, E.M. Heenan<sup>x</sup>,  
L.C. Moffitt<sup>x</sup>, G.R. Moloney<sup>x</sup>, G.F. Moorhead<sup>x</sup>, M.E. Sevier<sup>x</sup>, G.N. Taylor<sup>x</sup>,  
S.N. Tovey<sup>x</sup>, A. Drutskoy<sup>y</sup>, R. Kagan<sup>y</sup>, P. Pakhlov<sup>y</sup>, S. Semenov<sup>y</sup>, C. Fukunaga<sup>z</sup>,  
R. Suda<sup>z</sup>, M. Fukushima<sup>aa</sup>, V.I. Goriletsky<sup>ab</sup>, B.V. Grinyov<sup>ab</sup>, V.R. Lyubinsky<sup>ab</sup>,  
A.I. Panova<sup>ab</sup>, K.V. Shakhova<sup>ab</sup>, L.I. Shpilinskaya<sup>ab</sup>, E.L. Vinograd<sup>ab</sup>,  
B.G. Zaslavsky<sup>ab</sup>, R.S. Guo<sup>ac</sup>, F. Haitani<sup>ad</sup>, Y. Hoshi<sup>ad</sup>, K. Neichi<sup>ad</sup>, K. Hara<sup>ae</sup>,  
T. Hara<sup>ae</sup>, M. Hazumi<sup>ae</sup>, T. Hojo<sup>ae</sup>, D. Jackson<sup>ae</sup>, H. Miyake<sup>ae</sup>, Y. Nagashima<sup>ae</sup>,  
J. Ryuko<sup>ae</sup>, K. Sumisawa<sup>ae</sup>, M. Takita<sup>ae</sup>, T. Yamanaka<sup>ae</sup>, H. Hayashii<sup>af</sup>,  
K. Miyabayashi<sup>af</sup>, S. Noguchi<sup>af</sup>, S. Hikita<sup>ag</sup>, H. Hirano<sup>ag</sup>, K. Hoshina<sup>ag</sup>,  
H. Mamada<sup>ag</sup>, O. Nitoh<sup>ag</sup>, N. Okazaki<sup>ag</sup>, T. Yokoyama<sup>ag</sup>, H. Ishino<sup>ah</sup>,  
S. Ichizawa<sup>ah</sup>, T. Hirai<sup>ah</sup>, H. Kakuno<sup>ah</sup>, J. Kaneko<sup>ah</sup>, T. Nakamura<sup>ah</sup>,  
Y. Ohshima<sup>ah</sup>, Y. Watanabe<sup>ah</sup>, S. Yanaka<sup>ah</sup>, Y. Inoue<sup>ai</sup>, E. Nakano<sup>ai</sup>,  
T. Takahashi<sup>ai</sup>, Y. Teramoto<sup>ai</sup>, J.H. Kang<sup>aj</sup>, H.J. Kim<sup>aj</sup>, Heejong Kim<sup>aj</sup>, Y.-  
J. Kwon<sup>aj</sup>, H. Kawai<sup>ak</sup>, E. Kurihara<sup>ak</sup>, T. Ooba<sup>ak</sup>, K. Suzuki<sup>ak</sup>, Y. Unno<sup>ak</sup>,  
N. Kawamura<sup>al</sup>, H. Yuta<sup>al</sup>, K. Kinoshita<sup>am</sup>, A. Satpathy<sup>am</sup>, S. Kobayashi<sup>an</sup>,  
T. Kuniya<sup>an</sup>, A. Murakami<sup>an</sup>, T. Tsukamoto<sup>an</sup>, S. Kumar<sup>ao</sup>, J. Singh<sup>ao</sup>, J. Lange<sup>ap</sup>,  
R. Stock<sup>ap</sup>, S. Matsumoto<sup>aq</sup>, M. Watanabe<sup>aq</sup>, H. Matsuo<sup>ar,malt</sup>, S. Nishida<sup>ar</sup>,  
T. Nomura<sup>ar</sup>, H. Sakamoto<sup>ar</sup>, N. Sasao<sup>ar</sup>, Y. Ushiroda<sup>ar</sup>, Y. Nagasaka<sup>as</sup>,

<sup>7</sup> On leave from Jožef Stefan Institute, Jamova 39, 1000 Ljubljana, Slovenia.

<sup>8</sup> Present address. JAERI, Nakameguro, Meguro-ku, Tokyo 153-0061, Japan.

<sup>9</sup> Present address. NIFS, Toki, Gifu 509-5292, Japan.

Y. Tanaka<sup>as</sup>, S. Ogawa<sup>at</sup>, H. Shibuya<sup>at</sup>, K. Hanagaki<sup>au</sup>, S. Okuno<sup>au</sup>, D.Z. Shen<sup>av</sup>,  
D.S. Yan<sup>av</sup>, Z.W. Yin<sup>av</sup>, N. Tan<sup>aw</sup>, C.H. Wang<sup>ax</sup>, T. Yamaki<sup>ay</sup>, Y. Yamashita<sup>az</sup>

<sup>a</sup> Aomori University, Aomori 030-0943, Japan

<sup>b</sup> Budker Institute of Nuclear Physics, RU-630090 Novosibirsk, Russia

<sup>c</sup> Chiba University, Yayoi, Inage-ku, Chiba 263-8522, Japan

<sup>d</sup> Chinese Academy of Science, 52 Saline Road, Beijing 100864, People's Republic of China

<sup>e</sup> Chuo University, Kasuga, Bunkyo-ku, Tokyo 112-8551, Japan

<sup>f</sup> University of Cincinnati, ML 0011 Cincinnati, OH 45221, USA

<sup>g</sup> University of Frankfurt, D-60486 Frankfurt, Germany

<sup>h</sup> Gyeongsang National University, Chinju 660-701, South Korea

<sup>i</sup> University of Hawaii, 2505 Correa Rd, Honolulu, HI 96822, USA

<sup>j</sup> Hiroshima Institute of Technology, Miyake, Saeki-ku, Hiroshima 731-5193, Japan

<sup>k</sup> IHEP Academia Sinica, P.O. Box 918, Beijing 100039, People's Republic of China

<sup>l</sup> ICRR, Tokyo University, Tanashi, Tokyo 188-8502, Japan

<sup>m</sup> Institute of Single Crystals, National Academy of Science of Ukraine, 60 Lenin Avenue, Kharkov 310001, Ukraine

<sup>n</sup> ITEP, B. Cheremushkinskaja 25, Moscow 117259, Russia

<sup>o</sup> Kanagawa University, Rokkakubashi, Kanagawa-ku, Yokohama 221-8686, Japan

<sup>p</sup> KEK, High Energy Accelerator Research Organization, Oho, Tsukuba, Ibaraki 305-0801, Japan

<sup>q</sup> Korea University, Seoul 137-701, South Korea

<sup>r</sup> H. Niewodniczanski Institute of Nuclear Physics, ul. Kawioro 26a, PL-30-055 Krakow, Poland

<sup>s</sup> Kyoto University, Kitashirakawa, Sakyo-ku, Kyoto 606-8502, Japan

<sup>t</sup> University of Melbourne, Parkville, Victoria 3079, Australia

<sup>u</sup> Nagasaki Institute of Applied Science, Aba 536, Nagasaki 851-0193, Japan

<sup>v</sup> Nagoya University, Chikusa-ku, Nagoya 464-8602, Japan

<sup>w</sup> Nara Women's University, Nishi-machi, Nara 630-8506, Japan

<sup>x</sup> National Central University, Chungli 32054, Taiwan

<sup>y</sup> National Kaohsiung Normal University, Kaohsiung, Taiwan

<sup>z</sup> National Lien-Ho Institute of Technology, Miao Li, Taiwan

<sup>aa</sup> National Taiwan University, Taipei 10764, Taiwan

<sup>ab</sup> Nihon Detal College, Hamaura-cho, Niigata 951-8151, Japan

<sup>ac</sup> Niigata University, Ikarashi, Niigata 950-2181, Japan

<sup>ad</sup> Osaka University, Toyonaka, Osaka 560-0043, Japan

<sup>ae</sup> Osaka City University, Sumiyoshi-ku, Osaka 558-8585, Japan

<sup>af</sup> Panjab University, Chandigarh 160014, India

<sup>ag</sup> Princeton University, P.O. Box 708, Princeton, NJ 08544, USA

<sup>ah</sup> Saga University, Honjo-1, Saga 840-8502, Japan

<sup>ai</sup> University of Science and Technology of China, Hefei, Anhui 230027, China

<sup>aj</sup> Seoul National University, Seoul 151-742, South Korea

<sup>ak</sup> Science University of Tokyo, Noda, Chiba 278-8510, Japan

<sup>al</sup> Sugiyama Jogakuen University, Nissin, Aichi-gun, Aichi 470-0131, Japan

<sup>am</sup> Sungkyunkwan University, Suwon 440-746, South Korea

<sup>an</sup> University of Sydney, N.S.W. 2006, Australia

<sup>ao</sup> Toho University, Miyama, Funabashi, Chiba 274-8510, Japan

<sup>ap</sup> Tohoku University, Aoba-ku, Sendai 980-8578, Japan

<sup>aq</sup> Tohoku Gakuin University, Tagajo, Miyagi 985-8537, Japan

<sup>ar</sup> University of Tokyo, Hongo, Bunkyo-ku, Tokyo 113-0033, Japan

<sup>as</sup> Tokyo Institute of Technology, Oh-Okayama, Meguro-ku, Tokyo 152-8551, Japan

<sup>at</sup> Tokyo Metropolitan University, Hachioji, Tokyo 192-0397, Japan

<sup>au</sup> Tokyo University of Agriculture & Technology, Koganei, Tokyo 184-8588, Japan

<sup>av</sup> Toyama National College of Maritime Technology, Shinminato, Toyama 933-0293, Japan

<sup>aw</sup> University of Tsukuba, Tsukuba 305-8573, Japan

<sup>ax</sup> Utkal University, Vani Vihar, Bhubaneswer 751 004, India

<sup>ay</sup> Virginia Polytechnic Institute and State University, Blacksburg, VA 24061, USA

<sup>az</sup> Yonsei University, Seoul 120-794, South Korea

---

**Abstract**

The Belle detector was designed and constructed to carry out quantitative studies of rare B-meson decay modes with very small branching fractions using an asymmetric  $e^+e^-$  collider operating at the  $\Upsilon(4S)$  resonance, the KEK-B-factory. Such studies require data samples containing  $\sim 10^7$  B-meson decays. The Belle detector is configured around a 1.5 T superconducting solenoid and iron structure surrounding the KEK-B beams at the Tsukuba interaction region. B-meson decay vertices are measured by a silicon vertex detector situated just outside of a cylindrical beryllium beam pipe. Charged particle tracking is performed by a wire drift chamber (CDC). Particle identification is provided by  $dE/dx$  measurements in CDC, aerogel threshold Cherenkov counter and time-of-flight counter placed radially outside of CDC. Electromagnetic showers are detected in an array of CsI(Tl) crystals located inside the solenoid coil. Muons and  $K_L$  mesons are identified by arrays of resistive plate counters interspersed in the iron yoke. The detector covers the  $\theta$  region extending from  $17^\circ$  to  $150^\circ$ . The part of the uncovered small-angle region is instrumented with a pair of BGO crystal arrays placed on the surfaces of the QCS cryostats in the forward and backward directions. Details of the design and development works of the detector subsystems, which include trigger, data acquisition and computer systems, are described. Results of performance of the detector subsystems are also presented. © 2002 Published by Elsevier Science B.V.

---

**Contents**

1. Introduction . . . . .	123
2. Interaction region . . . . .	124
2.1. Beam crossing angle . . . . .	124
2.2. Beam-line magnets near the interaction point . . . . .	124
2.3. Beam pipe . . . . .	126
2.4. Beam background . . . . .	126
3. Extreme forward calorimeter, EFC . . . . .	127
3.1. Design and construction . . . . .	127
3.1.1. BGO and radiation hardness . . . . .	128
3.1.2. Mechanical structure . . . . .	129
3.1.3. Light collection . . . . .	130
3.2. Electronics . . . . .	130
3.2.1. Front-end amplifier . . . . .	130
3.2.2. Rear-end receiver and digitizer . . . . .	132
3.3. Performance . . . . .	132
4. Silicon vertex detector (SVD) . . . . .	132
4.1. Double-sided silicon detector (DSSD) . . . . .	133
4.2. Mechanical structure . . . . .	134
4.2.1. Ladder . . . . .	134
4.2.2. Support structure . . . . .	135
4.3. Front-end electronics . . . . .	136
4.3.1. VA1-integrated circuit . . . . .	136
4.3.2. Hybrid . . . . .	138
4.3.3. Repeater system CORE . . . . .	138
4.4. Back-end electronics . . . . .	139
4.4.1. FADC system . . . . .	139
4.4.2. Trigger timing modules . . . . .	139

4.5.	SVD DAQ system . . . . .	140
4.6.	Monitor system . . . . .	141
4.7.	Performance . . . . .	141
5.	Central tracking chamber, CDC . . . . .	142
5.1.	Design and construction of the central tracking chamber . . . . .	142
5.1.1.	Structure and wire configuration . . . . .	143
5.1.2.	Gas . . . . .	146
5.1.3.	Electronics . . . . .	146
5.2.	Beam test by a real-size prototype drift chamber . . . . .	148
5.3.	Calibration with cosmic rays . . . . .	151
5.3.1.	CDC . . . . .	151
5.3.2.	Cathode strip detector . . . . .	152
5.4.	Performance . . . . .	153
6.	Aerogel Cherenkov counter system, ACC . . . . .	155
6.1.	Detector design . . . . .	155
6.1.1.	Production of hydrophobic silica aerogels . . . . .	156
6.1.2.	Quality of the aerogels . . . . .	156
6.1.3.	Fine-mesh photomultiplier tubes . . . . .	158
6.2.	ACC readout electronics . . . . .	159
6.2.1.	Preamplifier base assemblies . . . . .	159
6.2.2.	Charge-to-time converter modules . . . . .	160
6.2.3.	Monitoring system . . . . .	161
6.2.4.	Monte Carlo simulation . . . . .	161
6.3.	Performance of ACC . . . . .	161
6.4.	Particle identification of electrons and charged kaons, EID and KID . . . . .	162
6.4.1.	EID and fake rate . . . . .	163
6.4.2.	KID and pion fake rate . . . . .	163
7.	Time-of-flight counters (TOF) . . . . .	165
7.1.	Design and construction of TOF . . . . .	165
7.1.1.	FM-PMTs . . . . .	166
7.1.2.	Scintillators . . . . .	166
7.1.3.	Readout electronics . . . . .	167
7.2.	Beam test . . . . .	169
7.3.	Performance . . . . .	171
7.3.1.	PMT gain adjustment . . . . .	171
7.3.2.	Calibration and time resolution using $\mu$ -pair events . . . . .	172
7.3.3.	$\pi^\pm/K^\pm$ separation . . . . .	172
8.	Electromagnetic calorimetry, ECL . . . . .	174
8.1.	Design and construction of ECL . . . . .	175
8.1.1.	CsI(Tl) crystal . . . . .	176
8.1.2.	Mechanical assembly . . . . .	176
8.1.3.	Readout electronics . . . . .	177
8.1.4.	Calibration by cosmic-rays . . . . .	178
8.1.5.	Radiation hardness . . . . .	179
8.2.	Beam tests . . . . .	181
8.2.1.	$\pi^2$ beam . . . . .	182
8.2.2.	Photon beams at the ROKK-1M facility . . . . .	183
8.3.	Performance . . . . .	191

9.	$K_L$ and muon detection system, KLM . . . . .	192
9.1.	Design and construction . . . . .	192
9.1.1.	Glass-resistive plate counters . . . . .	194
9.1.2.	Barrel modules . . . . .	194
9.1.3.	End-cap modules . . . . .	196
9.1.4.	High-voltage system . . . . .	196
9.1.5.	Gas mixing and distribution . . . . .	197
9.2.	Readout electronics . . . . .	198
9.3.	Efficiency and resolution . . . . .	199
9.4.	Performance . . . . .	200
9.4.1.	$K_L$ detection . . . . .	200
9.4.2.	Muon detection . . . . .	201
10.	Detector solenoid and iron structure . . . . .	202
10.1.	Solenoid magnet . . . . .	202
10.2.	Iron yoke . . . . .	202
10.3.	Magnetic field mapping of the Belle solenoid . . . . .	202
11.	Trigger . . . . .	204
11.1.	CDC trigger system . . . . .	206
11.1.1.	$r$ - $\phi$ trigger . . . . .	206
11.1.2.	$z$ trigger . . . . .	208
11.2.	TOF trigger system . . . . .	210
11.2.1.	Timing logic . . . . .	211
11.2.2.	Delay and decision logic . . . . .	212
11.3.	ECL trigger system . . . . .	212
11.3.1.	Trigger cell . . . . .	212
11.3.2.	Total energy trigger . . . . .	213
11.3.3.	Cluster counting trigger . . . . .	214
11.4.	KLM trigger . . . . .	215
11.4.1.	KLM signal out . . . . .	215
11.4.2.	KLM trigger scheme . . . . .	216
11.4.3.	Trigger efficiency . . . . .	217
11.5.	EFC trigger system . . . . .	218
11.6.	GDL . . . . .	219
11.7.	Trigger operation for beam run . . . . .	219
12.	Data acquisition . . . . .	221
12.1.	Readout . . . . .	221
12.1.1.	FASTBUS TDC readout systems . . . . .	221
12.1.2.	SVD readout system . . . . .	222
12.1.3.	Readout sequence control . . . . .	223
12.2.	Event builder . . . . .	223
12.3.	Online computer farm . . . . .	224
12.4.	Data monitoring system . . . . .	224
12.5.	Mass storage system . . . . .	225
12.6.	Run control . . . . .	225
12.7.	Performance . . . . .	225
13.	Offline computing system . . . . .	225
13.1.	Computing power . . . . .	226
13.2.	Tape libraries and servers . . . . .	227

13.3. PC farms . . . . .	227
13.4. Offline software . . . . .	228
13.5. Level 4 offline trigger software . . . . .	228
13.6. DST production and skimming . . . . .	230
Acknowledgements . . . . .	231
References . . . . .	231

## 1. Introduction

The Belle collaboration evolved from the B-factory task force that was organized to study the physics potential of a high luminosity, asymmetric  $e^+e^-$  collider operating at the  $\Upsilon(4S)$  resonance. In particular, the task force addressed the possibilities for experiments that tested the Kobayashi–Maskawa mechanism for CP-violation [1]. It was demonstrated that such tests could be done with a data of  $\sim 10^7$  B-meson decays, corresponding to integrated luminosities at the  $\Upsilon(4S)$  of order 100/fb, accumulated with a  $4\pi$  detector with state-of-the-art capabilities [2].

The scientific goals of the Belle collaboration were discussed in a Letter of Intent [3] submitted to the March 1994 TPAC (TRISTAN Program Advisory Committee) meeting. The LoI describes the implications of these goals for the detector and provides a reference detector design based on the R&D program initiated by the task force. With the approval of the LoI the Technical Design Report was written by the Belle collaboration [4].

Fig. 1 shows the configuration of the Belle detector. The detector is configured around a 1.5 T superconducting solenoid and iron structure surrounding the KEKB beams at the Tsukuba interaction region [5]. The beam crossing angle is  $\pm 11$  mr. B-meson decay vertices are measured by a silicon vertex detector (SVD) situated just outside of a cylindrical beryllium beam pipe. Charged particle tracking is provided by a wire drift chamber (CDC). Particle identification is provided by  $dE/dx$  measurements in CDC, and aerogel Cherenkov counters (ACC) and time-of-

flight counters (TOF) situated radially outside of CDC. Electromagnetic showers are detected in an array of CsI(Tl) crystals located inside the solenoid coil. Muons and  $K_L$  mesons are identified by arrays of resistive plate counters interspersed in the iron yoke. The detector covers the  $\theta$  region extending from  $17^\circ$  to  $150^\circ$ . A part of the otherwise uncovered small-angle region is instrumented with a pair of BGO crystal arrays (EFC) placed on the surfaces of the QCS cryostats in the forward and backward directions. The expected (or achieved) performance of the detector is summarized in Table 1.

At the time of writing of TDR the detector technologies for particle identification and extreme forward calorimeters were not finalized, and R&D works were continued. All the other detector components entered the full construction stage. After extensive studies and tests of a few options for particle identification techniques the ACC system was chosen as the particle identification system. The extreme forward calorimeter system with BGO crystal arrays was also chosen as EFC over the option of a silicon–tungsten sandwich calorimeter. Confronted with various technical difficulties the design of SVD was changed to the present design following the recommendation made by the SVD review committee of June 1997.

Along with development and construction works of readout electronics for all the detector components, the trigger, data acquisition, and computing systems are also developed.

The present report summarizes the results of works by the Belle collaboration during the design,

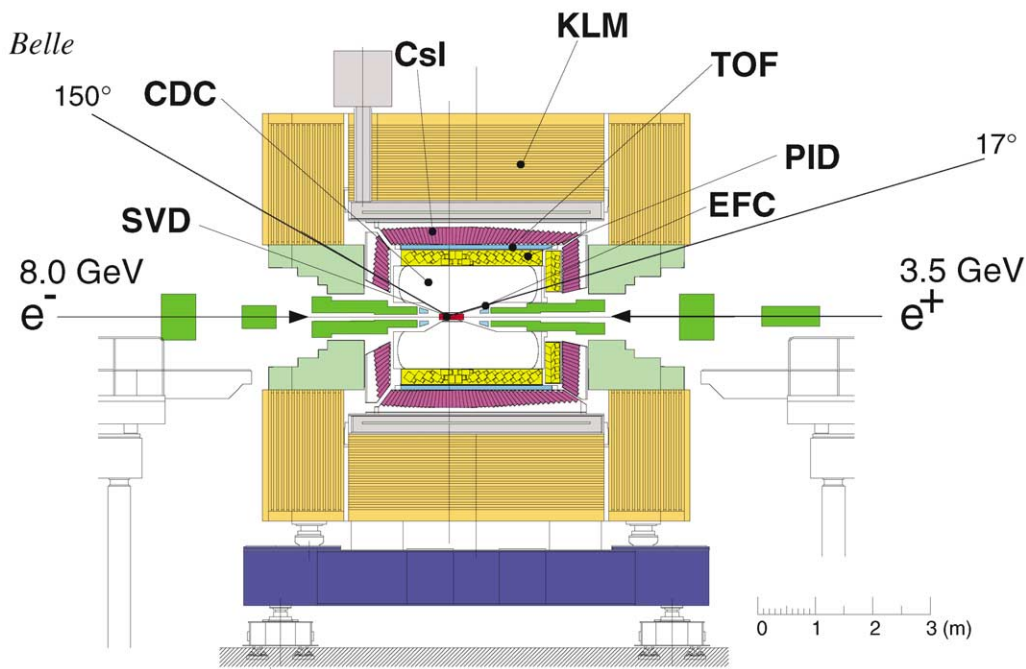


Fig. 1. Side view of the Belle detector.

construction, testing, and commissioning stages of the Belle detector.

## 2. Interaction region

### 2.1. Beam crossing angle

The layout of the interaction region is shown in Fig. 2 [4]. The beam crossing angle of  $\pm 11$  mrad allows us to fill all RF buckets with the beam and still avoid parasitic collisions, thus permitting higher luminosity. Another important merit of the large crossing-angle scheme is that it eliminates the need for the separation-bend magnets, significantly reducing beam-related backgrounds in the detector. The risk associated with this choice of a non-zero crossing angle is the possibility of luminosity loss caused by the excitation of synchro-beta resonances [5].

The low-energy beam line ( $e^+$ ) is aligned with the axis of the detector solenoid since the lower-momentum beam particles would suffer more bending in the solenoid field if they were off-axis.

This results in a 22 mrad angle between the high-energy beam line ( $e^-$ ) and the solenoid axis.

### 2.2. Beam-line magnets near the interaction point

The final-focus quadrupole magnets (QCS) are located inside the field volume of the detector solenoid and are common to both beams. In order to facilitate the high gradient and tunability, these magnets are superconducting at the expense of a larger size. In order to minimize backgrounds from QCS-generated synchrotron radiation, their axes are aligned with the incoming  $e^+$  and  $e^-$  beams. This requires the radius of the backward-angle region cryostat to be larger than that of the one in the forward-angle region. The inner aperture is determined by the requirements of injection and the need to avoid direct synchrotron radiation incident on the beam pipe inside the cryostats. The  $z$ -positions are determined by the detector acceptance ( $17^\circ \leq \theta \leq 150^\circ$ ).

To minimize solenoid-field-induced coupling between the  $x$  and  $y$  beam motions, superconducting compensation solenoid magnets are located

Table 1  
Performance parameters expected (or achieved) for the Belle detector

Detector	Type	Configuration	Readout	Performance
Beam pipe	Beryllium double wall	Cylindrical, $r = 20$ mm $0.5/2.5/0.5$ (mm) = Be/He/Be		He gas cooled
EFC	BGO	Photodiode readout segmentation: 32 in $\phi$ ; 5 in $\theta$	$160 \times 2$	RMS energy resolution: 7.3 % at 8 GeV 5.8% at 3.5 GeV
SVD	Double-sided Si strip	Chip size: $57.5 \times 33.5$ mm <sup>2</sup> Strip pitch: 25 (p)/50 (n) $\mu$ m 3 layers: 8/10/14 ladders	$\phi$ : 40.96k $z$ : 40.96k	$\sigma_{A_z} \sim 80$ $\mu$ m
CDC	Small cell drift chamber	Anode: 50 layers Cathode: 3 layers $r = 8.3$ – $86.3$ cm $-77 \leq z \leq 160$ cm	A: 8.4k C: 1.8k	$\sigma_{r\phi} = 130$ $\mu$ m $\sigma_z = 200$ – $1400$ $\mu$ m $\sigma_{p_t}/p_t = 0.3\% \sqrt{p_t^2 + 1}$ $\sigma_{dE/dx} = 6\%$
ACC	Silica aerogel	960 barrel/228 end-cap FM-PMT readout		$N_{p.e.} \geq 6$ K/ $\pi$ separation: $1.2 < p < 3.5$ GeV/ $c$
TOF	Scintillator	128 $\phi$ segmentation $r = 120$ cm, 3-m long	$128 \times 2$	$\sigma_t = 100$ ps K/ $\pi$ separation: up to 1.2 GeV/ $c$
TSC		64 $\phi$ segmentation	64	
ECL	CsI (towered structure)	Barrel: $r = 125$ – $162$ cm End-cap: $z = -102$ cm and $+196$ cm	6624 1152 (F) 960 (B)	$\sigma_E/E = 1.3\%/\sqrt{E}$ $\sigma_{pos} = 0.5$ cm/ $\sqrt{E}$ ( $E$ in GeV)
KLM	Resistive plate counters	14 layers (5 cm Fe + 4 cm gap) 2 RPCs in each gap	$\theta$ : 16k $\phi$ : 16k	$\Delta\phi = \Delta\theta = 30$ mr for $K_L$ $\sim 1\%$ hadron fake
Magnet	Supercon.	Inner radius = 170 cm		$B = 1.5$ T

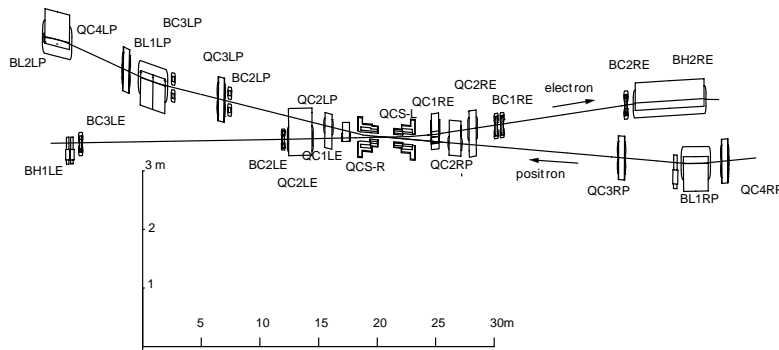


Fig. 2. Layout of the interaction region for the beam crossing angle of  $\pm 11$  mr.

near the interaction point (IP), occupying the same cryostat as the QCS magnets. Since the  $\int B_z dz$  between IP and QCS is required to be nearly zero, these magnets run as high as 4.8 T. The cryostats for QCS and the compensation magnets are supported from a movable stage that provides a common support base for all the accelerator magnets located in the experimental hall.

The QC1 magnets are located outside the QCS cryostats and help provide the vertical focus for the high-energy beam only. Although these are normal conductor magnets with an iron return yoke, a special design is necessary because of the small beam separation in this region. The one in the forward region is a half-quadrupole with the iron septum. In order to reduce the synchrotron radiation background from the incoming beam, the backward region QC1 is a special full-quadrupole [5]. The locations are chosen so as to avoid the leakage field of the detector solenoid.

### 2.3. Beam pipe

The precise determination of decay vertices is an essential feature of the Belle experiment. Multiple coulomb scattering in the beam-pipe wall and the first layer of the silicon detector are the limiting factors on the  $z$ -vertex position resolution, making the minimization of the beam-pipe thickness a necessity. Moreover, since the vertex resolution improves inversely with the distance to the first detection layer, the vertex detector has to be placed as close to the interaction point as possible and, thus, to the beam pipe wall. This is complicated by the fact that the beam pipe at the interaction region is subjected to beam-induced heating at levels as high as a few hundred watts. This requires an active cooling system for the beam pipe and a mechanism for shielding the vertex detector from this heat.

Fig. 3 shows the cross-section of the beryllium beam pipe at the interaction point. The central part ( $-4.6 \text{ cm} \leq z \leq 10.1 \text{ cm}$ ) of the beam pipe is a double-wall beryllium cylinder with an inner diameter of 40 mm. A 2.5 mm gap between the inner and outer walls of the cylinder provides a helium gas channel for cooling. The machine vacuum is supported by the 0.5 mm thick inner

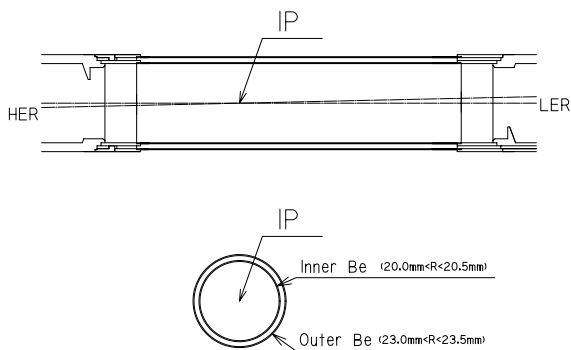


Fig. 3. The cross-section of the beryllium beam pipe at the interaction point.

wall. The outer wall is also 0.5 mm thick. The beryllium central section is brazed to aluminum pipes that extend outside of the collision region as shown in Fig. 4. The conical shape of the aluminum beam pipe allows the synchrotron X-rays generated in the QCS and QC1 magnets to pass through the detector region without hitting the beam pipe wall. The helium-gas cooling is adopted instead of water in order to minimize the material in the beam pipe.

Assuming a uniformly distributed 100 W heat load on the inner wall, the maximum temperature increase for the inner (outer) beryllium wall is calculated to be 25(5) $^{\circ}\text{C}$  for a 2 g/s He flow velocity at a 1.5 atm pressure and a 0.0007 atm pressure drop. The calculation assumes that the aluminum tubes in contact with the ends of the beryllium section are maintained at a fixed temperature by an independent cooling system. The total material thickness of the central beryllium section is 0.3% of a radiation length. Outside the outer beryllium cylinder, a 20  $\mu\text{m}$  thick gold sheet is attached in order to reduce the low-energy X-ray background ( $< 5 \text{ keV}$ ) from the high-energy ring. Its thickness corresponds to 0.6% of a radiation length.

### 2.4. Beam background

With the elimination of the separation-bend magnets near IP, the synchrotron radiation backgrounds are not so severe as they were for TRISTAN, where the critical energy was higher.

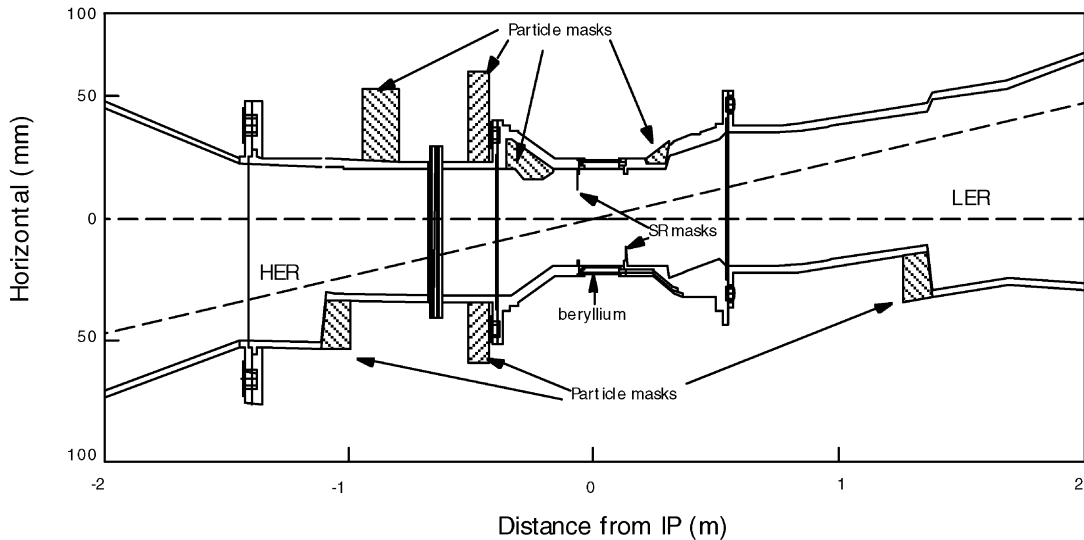


Fig. 4. The arrangement of the beam pipe and horizontal masks.

The apertures of the beam pipe and masks (SR-Mask) near IP were designed so that synchrotron radiation from QCS and QC1 go through without hitting them. In these synchrotron radiation calculations, we protect against beam tails out to  $10\sigma_x$  and  $30\sigma_y$ . The beam–beam simulations indicate no long tails in the interaction region. Mask-A shields the beryllium beam pipe from back-scattered photons. Although some photons from QC2 and QC3 can hit SR-Mask, they have a critical energy less than 2 keV and are easily absorbed in the material of the mask. The masks are gold plated for this purpose. Photons from upstream magnets far from IP are intercepted by movable masks installed just upstream of QC3.

Particle backgrounds were expected to be more critical at KEKB. A DECAY TURTLE calculation indicates that the rate of spent particles from both beams directly hitting the beam pipe between the two cryostats is 130 kHz for  $10^{-9}$  Torr vacuum. Particle-masks were installed outside the beam pipe to reduce the particle background. Movable masks installed in the arcs and the non-IR straight sections cut off the beam tails far from IR. These masks could reduce radiation levels at the detector during injection.

### 3. Extreme forward calorimeter, EFC

In order to improve the experimental sensitivity to some physics processes such as  $B \rightarrow \tau\nu$ , the extreme forward calorimeter, EFC, is needed to further extend the polar angle coverage by ECL,  $17^\circ < \theta < 150^\circ$  [4]. EFC covers the angular range from  $6.4^\circ$  to  $11.5^\circ$  in the forward direction and  $163.3^\circ$  to  $171.2^\circ$  in the backward direction. The EFC detector is attached to the front faces of the cryostats of the compensation solenoid magnets of the KEKB accelerator, surrounding the beam pipe [6,7]. EFC is also required to function as a beam mask to reduce backgrounds for CDC. In addition, EFC is used for a beam monitor for the KEKB control and a luminosity monitor for the Belle experiment. It can also be used as a tagging device for two-photon physics.

#### 3.1. Design and construction

Since EFC is placed in the very high radiation-level area around the beam pipe near the interaction point, it is required to be radiation-hard. Therefore, two options for EFC were considered: (1) a silicon and tungsten sandwich calorimeter

and (2) a radiation-hard BGO (Bismuth Germanate,  $\text{Bi}_4\text{Ge}_3\text{O}_{12}$ ) crystal calorimeter. Both candidates are equally radiation-hard and effective as a beam mask. After studying the two options carefully, we chose the BGO option because it costs less in terms of money and manpower and gives better energy resolution [8].

### 3.1.1. BGO and radiation hardness

BGO has very desirable characteristics for electromagnetic calorimeters:

- radiation hardness at megarad level,
- excellent  $e/\gamma$  energy resolution of  $(0.3\text{--}1)\%/\sqrt{E(\text{GeV})}$ ,
- high density of  $7.1 \text{ gm/cm}^3$ ,
- short radiation length of  $1.12 \text{ cm}$ ,
- large refractive index of  $2.15$ ,
- suitable scintillating properties with the fast decay time of about  $300 \text{ ns}$  and peak scintillation at about  $480 \text{ nm}$ , and
- non-hygroscopic nature.

Pure BGO crystals with silicon photodiodes were proven to be capable of detecting minimum-ionizing particles (MIPs) with a large  $S/N$  ratio [9]. In the same experiment the nuclear counter effect (NCE) was also clearly observed. NCE is the extra amount of charge produced in the photodiode by a charged particle directly hitting it, on the top of the charge produced by the scintillation light. The signal from MIPs is well separated from electronics noise and NCE signal.

The radiation hardness of undoped BGO crystals from two manufacturers, the Institute of Single Crystals, Kharkov, Ukraine and the Institute of Inorganic Chemistry, Novosibirsk, Russia, was measured [10]. BGO crystals from Novosibirsk are found to be quite radiation hard at least up to  $10.5 \text{ Mrad}$  equivalent dose with a maximum of  $15\%$  damaging effect, while Kharkov crystals degrade by more than  $40\%$  in terms of light output and transparency. It was concluded that BGO crystals from Novosibirsk can be used for the Belle detector.

Radiation damage tests were carried out using a  $^{60}\text{Co}$  source ( $\sim 1000 \text{ C}$ ) at National Tsing University, Taiwan [11]. A total of 10 pieces of undoped trapezoid BGO crystals with an approx-

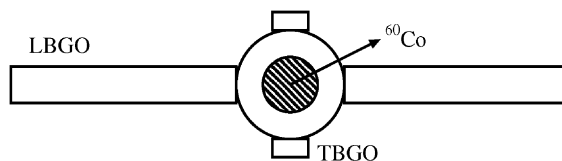


Fig. 5. Top view of the experimental setup in the radiation source room. BGO crystals were  $3 \text{ cm}$  away from the center of a  $^{60}\text{Co}$  source of  $\sim 1000 \text{ C}$ .

imate dimension of  $12 \times 2 \times 1 \text{ cm}^3$  from Novosibirsk were used in the tests. Fig. 5 shows the experimental setup. Trapezoid BGO crystals were irradiated longitudinally (LBGO) or transversely (TBGO). Light outputs were measured using a  $90 \mu\text{C}^{137}\text{Cs}$  source after irradiation and the ratio of signals from an irradiated crystal and the non-irradiated reference crystal was obtained, Fig. 6 shows some of the results.

Stable characteristics of the BGO crystals were observed under very high dose conditions. The light output decreases by  $\sim 30\%$  after receiving  $\sim 10 \text{ Mrad}$  dose. The crystals may have suffered some permanent damage but can recover to  $90\%$  of their original light output in a period of a day [12]. Furthermore, after a low dose irradiation of  $115 \text{ krad}$  the light output recovers to  $100\%$  of the original value within hours, as shown in Fig. 7. After receiving the BGO crystals used in the final assembly, the scintillation light yields of all the crystals were checked by a radioactive source. The percentage spread of the distribution is only  $6\%$  [13]. The radiation hardness check was done by using sample crystals, two per ingot, and some randomly selected crystals of the final assembly. Their performance characteristics are quite different from those of crystals produced in a small quantity. The light yield drops about  $25\text{--}50\%$  after receiving  $1 \text{ krad}$  dose and remains stable afterwards, checked up to  $10 \text{ Mrad}$ . The irradiation rate to receive  $1 \text{ krad}$  dose does not make much difference since the recovery is slow, in days or weeks. This characteristics is good for a stable operation in the Belle environment.

Radiation damage tests on optical reflector [14] and epoxy-based optical glue [15] which are used in the BGO detector assembly were performed. The reflectance of optical white fluorocarbon

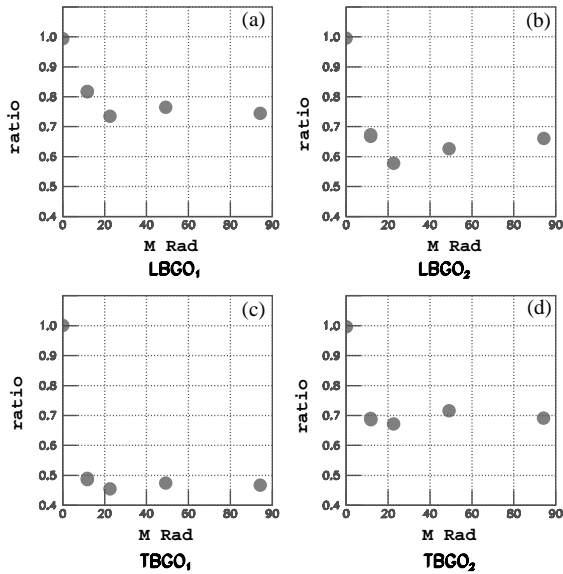


Fig. 6. Results of the first week irradiation. The horizontal scale is in equivalent doses and the vertical scale is the light yield normalized to the original value without irradiation: (a) and (b) correspond to the crystals irradiated longitudinally, and (c) and (d) to those irradiated transversely.

reflector, Goretex [16], was monitored to see any effect of radiation damage. No radiation damage was observed for the maximum equivalent dose of 8.6 Mrad. The epoxy-based optical glue was found later to be inadequate to bond the photodiode surface on a BGO crystal. An RTV type of glue, KE45T, was proved to be good. Its radiation hardness was checked acceptable up to 10 Mrad maximum equivalent dose.

Photodiodes are good for a radiation dose of about 50 krad and the least radiation-hard element. They are, however, protected behind the BGO crystals, the container, and the accelerator magnets. In case they are radiation damaged, they can be replaced relatively easily.

### 3.1.2. Mechanical structure

The finer lateral segmentation can provide the better position resolution. The segmentation, however, is limited by front-end electronics. The detector is segmented into 32 in  $\phi$  and 5 in  $\theta$  for both the forward and backward cones. A three-

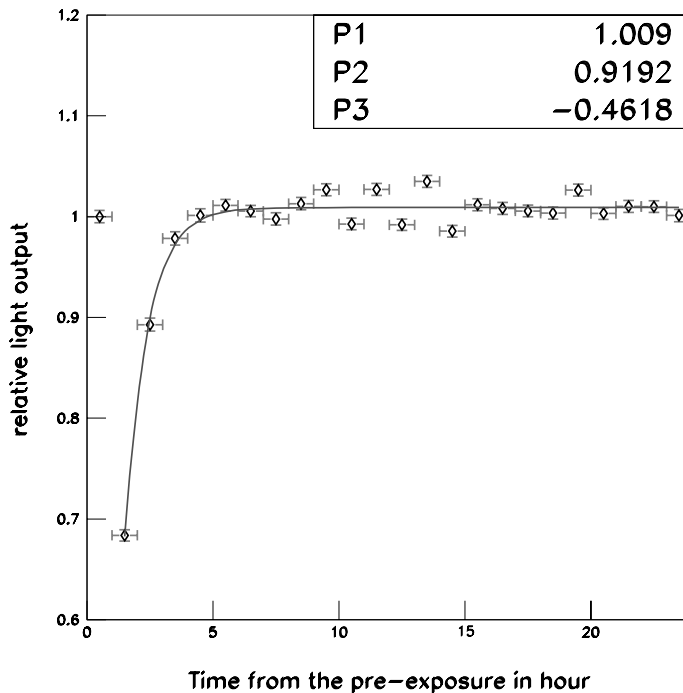


Fig. 7. BGO test crystal 1 received a dose of 115 krad in 1 h at its front surface. The time dependence of the relative output is shown before and after the irradiation.

dimensional view of the crystal arrangement is shown in Fig. 8.

The schematic side view of the forward EFC is shown in Fig. 9. The distance between the front surface of the detector and the interaction point is 60 and 43.5 cm in the forward and backward EFCs, respectively. The inner bore radius of the detector is 6.5 cm.

The BGO crystals are housed in a bucket-shape container made of 1 mm thick stainless steel, the inner bore of which is the beam pipe. The container is attached to the front surface of the

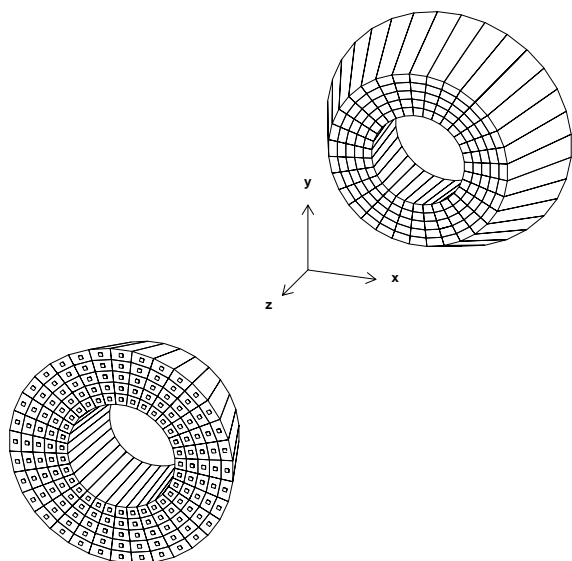


Fig. 8. An isometric view of the BGO crystals of the forward and backward EFC detectors.

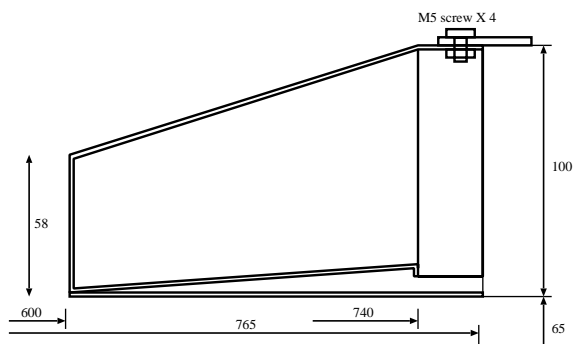


Fig. 9. Side view of the mounting of forward EFC.

compensation solenoids. Since the space allocated for EFC is limited, the radiation lengths of the forward and backward crystals are 12 and 11, respectively. Front-end circuits for photodiodes and preamps as well as miscellaneous instruments are installed in the space between the magnet surface and the backend of the BGO crystals which is 2.7 and 2.0 cm for the forward and backward EFC detectors, respectively.

### 3.1.3. Light collection

EFC points approximately to the interaction point to make a tower geometry. The crystals are shaped in trapezoid and their dimensions of the front and rear surfaces are significantly different. As a result, scintillation lights generated along the crystal axes are not collected uniformly. A Monte Carlo simulation by GEANT indicates that a good uniformity of light collection is important to get a good energy resolution. Therefore, all crystals were matt-treated to achieve a uniform light collection. The largest surface of the forward crystals and the second largest surface of the backward crystals were made dim. All other surfaces were polished. The nonuniformity of light collection for various types of crystals was reduced to about 10% level [7]. After the matt treatment, all the crystals were wrapped by a 100  $\mu\text{m}$  Teflon sheet and a 20  $\mu\text{m}$  aluminized Mylar sheet.

## 3.2. Electronics

The readout chain of EFC is shown in Fig. 10. The major parts are:

- front-end amplifier,
- rear-end receiver and digitizer, and
- trigger system (see Section 11.5).

### 3.2.1. Front-end amplifier

The circuit diagram for the preamplifier and shaper for a photodiode is shown in Fig. 11. The photodiode used is Hamamatsu S5106. Its active area is  $5 \times 5 \text{ mm}^2$ . Scintillation lights generated in each BGO crystal are collected by two photodiodes except for the crystals in the two inner-most layers, where only one photodiode collects lights in each crystal.

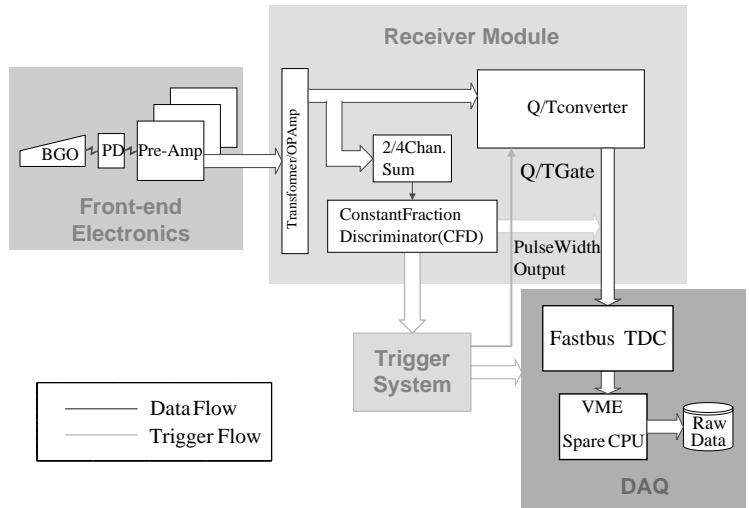


Fig. 10. Block diagram of EFC readout electronics.

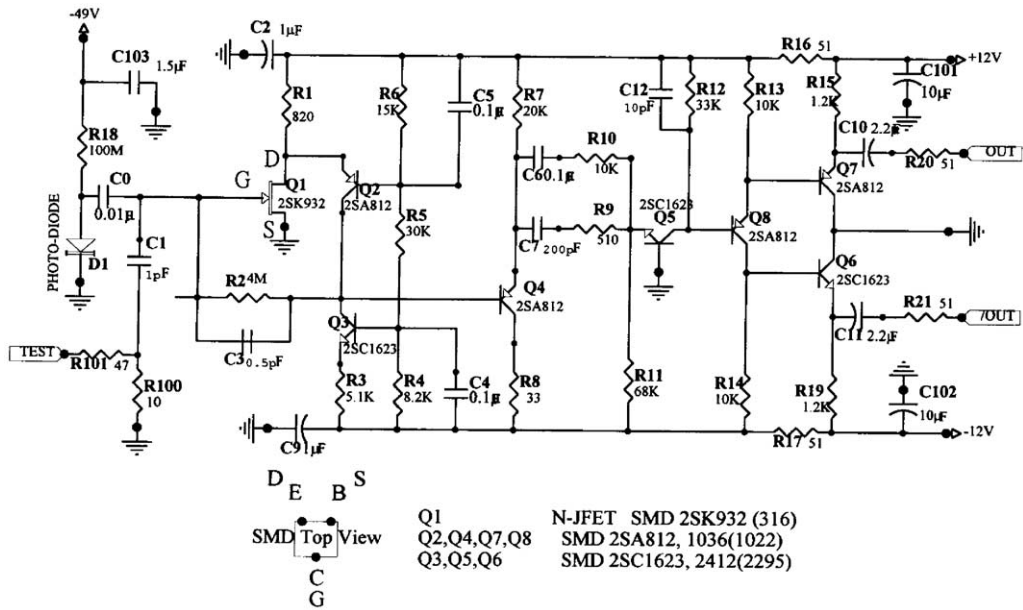


Fig. 11. Schematic diagram of the preamplifier-shaper circuit.

The printed circuit boards (PCB) for the front-end electronics are stacked together and mounted right behind the rear face of the BGO crystals. The boards include a board for housing photodiodes and distributing their biases, a board to house LEDs and to drive them at each crystal, and a

mother board to mount 10 preamplifiers. The rise time of the signal of the preamplifier and shaper is about 300 ns. The gain is 6 and 12 V/pC for the forward and the backward EFC, respectively.

Signals are sent differentially through a cable of 16 individually shielded twisted pairs of 16 m in

length to the receivers located outside of the Belle detector. The cable also supplies powers for preamplifiers and biases for photodiodes, and sends pulses for pulsing a preamplifier and LED. Each crystal can be pulsed by a light pulse through fiber cables.

### 3.2.2. Rear-end receiver and digitizer

The receiver receives analog signals through a transformer which cancels a common-mode noise in the twisted-pair cable. After the gain adjustment, the signal is split into two. One is sent to a charge integrator and the other to a sum amplifier which makes an analog sum of preamplifier signals from a trigger cell. The cell is a group of two or four BGO crystals.

The summed signal is sent to a constant-fraction discriminator (CFD) for generating gates for the charge integrator and the trigger. The integrator integrates the analog signal within the gate and produces an ECL signal whose width is proportional to the charge integrated. It is implemented by LeCroy MQT300A chip. The ECL signal is sent through a 30-m long twisted-pair cable to the electronics hut.

The ECL signal goes through a fanout located in the hut, making another copy. One signal is sent to a time-to-digital converter (TDC) for local EFC DAQ. The other is sent to TDC for Belle global DAQ. TDC used is a multi-hit Fastbus TDC of LeCroy 1887S and is operated in a common-stop mode.

### 3.3. Performance

The energy sum spectra for Bhabha events show a correlation between the forward and backward EFC detectors. A clear peak at 8 GeV with an RMS resolution of 7.3% is seen for the forward EFC, while a clear peak at 3.5 GeV with an RMS resolution of 5.8% is seen in the backward EFC. These results are compatible with the beam test results [17] and are slightly worse than those obtained by a GEANT Monte Carlo simulation. The discrepancies are due to dead channels and crystal-to-crystal non-uniformity. An expected counting rate for Bhabha events is a few kHz at an ultimate luminosity of  $10^{34}/\text{cm}^2/\text{s}$ .

EFC has provided a fast online feedback about the luminosity and background rates to the KEKB operations group. Fig. 12 shows an operational history of a typical beam fill at KEKB. The coincidence and accidental rates of the forward and the backward EFC are shown as a function of time in seconds together with  $e^+$  (LER) and  $e^-$  (HER) beam currents. During the injection period from 0 to 1800 s accidental Bhabha rates are quite high, but after the injection the accidental rate is very low. Singles rates of EFC can provide very useful information for diagnosing of background sources.

## 4. Silicon vertex detector (SVD)

A primary goal of the Belle experiment is to observe time-dependent CP asymmetries in the decays of B mesons. Doing so requires the measurement of the difference in z-vertex positions for B meson pairs with a precision of  $\sim 100 \mu\text{m}$ . In addition, the vertex detector is useful for identifying and measuring the decay vertices of D and  $\tau$  particles. It also contributes to the tracking.

Since most particles of interest in Belle have momenta of 1 GeV/c or less, the vertex resolution is dominated by the multiple-Coulomb scattering. This imposes strict constraints on the design of the detector. In particular, the innermost layer of the vertex detector must be placed as close to the interaction point as possible; the support structure must be low in mass but rigid; and the readout electronics must be placed outside of the tracking volume.

The design must also withstand large beam backgrounds. With the anticipated high-luminosity operation of KEKB, the radiation dose to the detector due to beam background is expected to be 30 krad/yr at the full design current. Radiation doses of this level both degrade the noise performance of the electronics (the readout fails outright at  $\sim 200$  krad) and induce leakage currents in the silicon detectors. In addition, the beam backgrounds induce large single-hit count rates. The electronic shaping time — currently set to 1000 ns — is determined by a tradeoff between the desire to minimize count-rate and leakage current

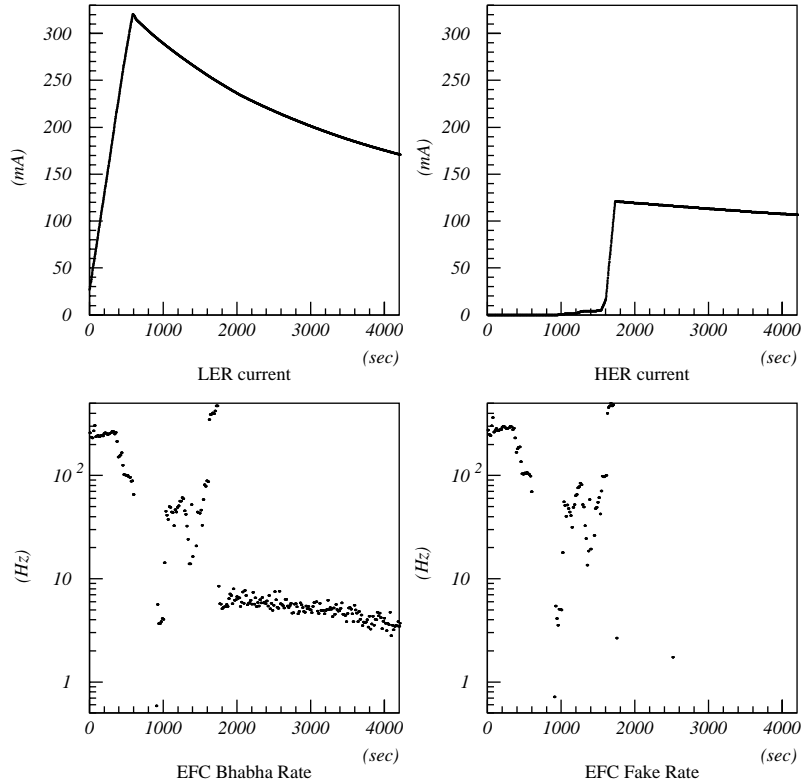


Fig. 12. An operational history of a typical beam fill of KEKB. The top figures show  $e^+$  and  $e^-$  beam current, and the bottom figures the coincidence rate of the forward and backward detectors (left) and their accidental rates (right) of EFC.

effects, which argue for short shaping times, and input-FET noise of front-end integrated circuits, which is minimized with longer shaping times.

Fig. 13 shows side and end views of SVD. It consists of three layers in a barrel-only design and covers a solid angle  $23^\circ < \theta < 139^\circ$  where  $\theta$  is the angle from the beam axis. This corresponds to 86% of the full solid angle. The radii of the three layers are 30, 45.5 and 60.5 mm. Each layer is constructed from independent ladders. Each ladder comprises double-sided silicon strip detectors (DSSDs) reinforced by boron-nitride support ribs. The design uses only a single type of DSSD, which reduces the cost of detector production, minimizes the amount of detector development work, and streamlines testing and bookkeeping during production. The benefit also extends to hybrid production and ladder assembly, where only a single type of hybrid is necessary and the design of the ladder assembly fixtures is greatly simplified.

The readout chain for DSSDs is based on the VA1 integrated circuit [18]. The VA1 has excellent noise performance ( $200e^- + 8e^-/\text{pF}$ ) and reasonably good radiation tolerance of 200 krad. The back-end electronics is a system of flash analog-to-digital converters (FADCs), digital signal processors (DSPs), and field programmable gate arrays (FPGAs), mounted on standard 6U VME boards. DSPs perform on-line common-mode noise subtraction, data sparsification and data formatting.

#### 4.1. Double-sided silicon detector (DSSD)

We use S6936 DSSDs fabricated by Hamamatsu Photonics (HPK). These detectors were originally developed for the DELPHI micro-vertex detector [19]. Each DSSD consists of 1280 sense strips and 640 readout pads on opposite sides. The sense strips are biased via 25 M $\Omega$  polysilicon bias resistors. The  $z$ -strip pitch is 42  $\mu\text{m}$  and the

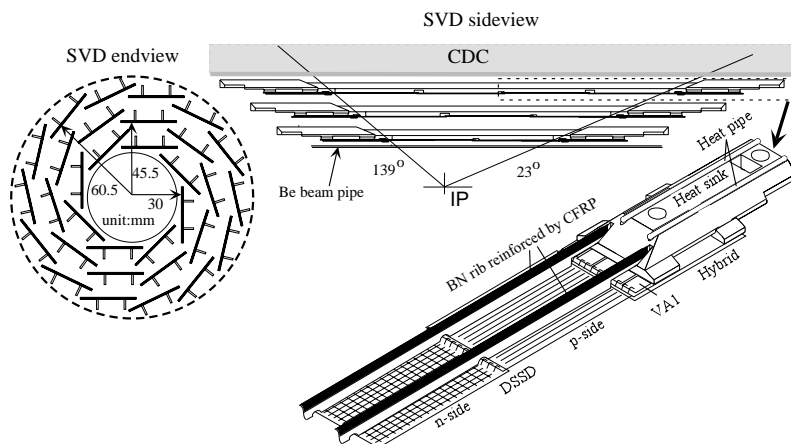


Fig. 13. Detector configuration of SVD.

$\phi$ -strip pitch is 25  $\mu\text{m}$ . The size of the active region is  $53.5 \times 32.0 \text{ mm}^2$  on the  $z$ -side and  $54.5 \times 32.0 \text{ mm}^2$  on the  $\phi$ -side. The overall DSSD size is  $57.5 \times 33.5 \text{ mm}^2$ . In total 102 DSSDs are used.

For the  $z$ -coordinate ( $z$  is the approximate beam direction) measurement, a double-metal structure running parallel to  $z$  is employed to route the signals from orthogonal  $z$ -sense strips to the ends of the detector. Adjacent strips are connected to a single readout trace on the second metal layer which gives an effective strip pitch of 84  $\mu\text{m}$ . The ohmic side is chosen to be on the  $z$ -side and a p-stop structure is employed to isolate the sense strips. A relatively large thermal noise ( $600e^-$ ) is observed due to the common-p-stop design.

On the  $\phi$  side, only every other sense-strip is connected to a readout channel. Charge collected by the floating strips in between is read from adjacent strips by means of capacitive charge division.

#### 4.2. Mechanical structure

SVD consists of 8, 10 and 14 ladders in the inner, middle and outer layers, respectively. The total number of full ladders is 32. The ladders are arranged to include some overlap regions in the  $r$ - $\phi$  plane to help the internal alignment among the sensors. The fraction of the overlap region is 9.7%, 3.8%, and 8.7% for the inner, middle, and outer layers, respectively. The ladders are supported by a

structure consisting of end-rings, support cylinders, and an outer cover, as shown in Fig. 14.

##### 4.2.1. Ladder

Each ladder is made of two half-ladders that are electrically independent, but mechanically joined by support ribs. The support ribs are made of boron nitride (BN) sandwiched by carbon-fiber reinforced plastic (CFRP). This arrangement is necessary to avoid directly gluing CFRP to DSSD since CFRP is much stiffer but conductive, and induces noise to the detector. The dimensions of the BN and CFRP are 6.25–6.65 mm high  $\times$  0.5 mm wide and 3.7 mm high  $\times$  0.15 mm wide, respectively, giving a stiffness of  $EI = 3.5$ – $4.0 \text{ Nm}^2$ . The average thickness of the rib is approximately 0.15% of the radiation length. To reduce the number of fixture types needed for ladder assembly, the ladder design is modular, with each module made as symmetrically as possible. As a result, only two basic module types are needed: a single detector module and a double detector module. Each module consists of a detector unit and a hybrid unit, as shown in Fig. 13.

A detector unit consists of either a single detector or two detectors with an overlap joint. In order to minimize the noise of the double-detector modules, different sides of the two detectors are connected — meaning that p-strips on one detector are wire-bonded to n-strips on the

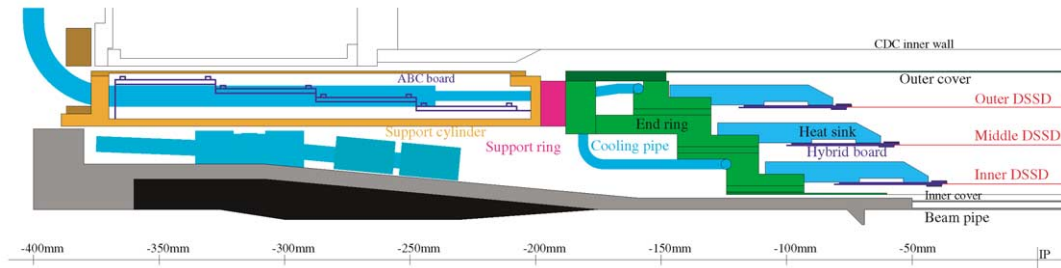


Fig. 14. Overview of the SVD supporting system.

other detector. This is possible because the detectors incorporate integrated coupling capacitors and the readout system can process pulses of either polarity.

A hybrid unit is produced by gluing two hybrids back-to-back to read both sides of DSSD. Since the preamplifier chips are a heat source, careful attention is paid to the thermal path way through the hybrid, across glue joints, and into the heat sink. Boron-nitride-loaded epoxy is used to join the two hybrids due to good heat conductivity of  $\sim 0.8 \text{ W/m K}$ .

The heat sink is made of aluminum nitride, whose high thermal conductivity (150–200 W/m K) and low coefficient of thermal expansion (CTE) (2–3 ppm/K) make it an attractive option for both heat conduction and mechanical support. The thermal conductivity is further enhanced by embedding two heat pipes<sup>10</sup> in the heat sink. Measurements indicate that the total temperature drop across the heat sink will be  $1.8^\circ\text{C}$  at normal preamplifier power levels. The attachment of the hybrid to the heat sink is also by means of the boron-nitride-loaded epoxy.

#### 4.2.2. Support structure

The ladders are mounted on the forward and backward end-rings, which provide mechanical support and cooling. The positions of the ladders are fixed by cylindrical pins, which penetrate

cylindrical holes in the heat sinks and the end-rings. The end-rings are made of aluminum, which was chosen for its low mass, machinability, and thermal conductivity. Cooling tubes, in which  $15^\circ\text{C}$  water is circulating, are embedded in the end-ring.

When the SVD electronics are turned on, thermal effects cause the ladder and end-ring to expand by estimated amounts 3 and  $40 \mu\text{m}$ , respectively. To accommodate this expansion, a sliding mechanism is introduced to allow the ladder to move with respect to the end-ring in the longitudinal ( $z$ ) direction. At the backward side, the pins and holes have the same diameter of 5 mm. On the other hand at the forward side, the diameters of pin and hole in the end-ring are 3 mm, but the diameter of the hole in the heat sink is 5 mm. A spring-loaded attachment pushes the 3-mm pin to one side of the 5-mm hole in the heat sink. This mechanism ensures that the forward end of the ladder is able to slide in the longitudinal direction but is not able to move in the transverse direction. The principle of this design is that the ladder end will slide before the ladder bows, thus preserving the essential planar nature of the ladder module. The precision of the machining and the assembly is about  $50 \mu\text{m}$  and the position of DSSDs were measured with a precision of  $\pm 10 \mu\text{m}$ .

The end-rings are supported by the forward and backward support cylinders, which are made of 2.5-mm-thick CFRP. These support cylinders are connected by the outer cover, which is made of 0.5-mm-thick CFRP. The outer cover and the support cylinders form a single overall support envelope of considerable stiffness,  $EI =$

<sup>10</sup>The HP-NB series of heat pipes produced by Thermacore Inc. 780 Eden Road, Lancaster, PA 17601, USA are used. The heat pipes transfer heat by evaporation and condensation of water. Internal pressure of the heat pipe is saturation pressure of water so that the water will vaporize with any thermal input.

$1 \times 10^4 \text{ Nm}^2$ . Based on ANSYS simulation, the gravitational sag at the center of the structure is expected to be about  $10 \mu\text{m}$ . This structure is supported at three points on the forward (one point) and backward (two points) end-plates of CDC. The backward end of the backward support cylinder is also fixed to CDC by means of a thin diaphragm, which rigidly constrains the  $r$  and  $\phi$  location of SVD, but allows easy motion in the  $z$  direction. This longitudinal degree of freedom accommodates thermal expansion and contraction of SVD and CDC as well as changes in the length of CDC brought about by changes in atmospheric pressure.

The beam pipe inside SVD is also supported by the CDC end-plates through diaphragms that are independent of SVD. The beam pipe support is designed such that the heat load and any vibrations originating from the pipe and its cooling system do not affect the performance of the SVD system. The end-rings, the end-ring flanges, and the outer cover can all be divided into two (clamshell) halves in  $r$ - $\phi$ . This makes it possible to assemble the SVD ladders in a tight space around the beam pipe.

#### 4.3. Front-end electronics

Signals from each side of DSSDs are read out by electronics comprising VA1 front-end integrated circuits [18] mounted on ceramic hybrids. Each hybrid holds five 128-channel VA1 chips. Two hybrid cards are connected to an interface card (designated ABC) by  $0.025''$  pitch multiconductor cables terminated in nanostrip connectors [20]. ABCs are connected to a repeater (CORE) system through 2-m-long flat cables. Analog current signals from VA1 are converted to voltage signals and buffered in the repeater system before being transmitted to FADCs in the Belle electronics hut over 30-m-long shielded differential coaxial cables.

A second signal data path, which is bidirectional, transmits the level-0 trigger signal (the “hold” pulse) and various digital clocking pulses that drive the readout to VA1. This path is also used to carry slow control and monitor data between the hybrids and an online computer.

Fig. 15 shows a schematic drawing of the SVD readout system.

##### 4.3.1. VA1-integrated circuit

The VA1 chip [18] is a 128-channel CMOS-integrated circuit fabricated in the Austrian Micro Systems (AMS)  $1.2\text{-}\mu\text{m}$  CMOS process. VA1 was specially designed for the readout of silicon vertex detectors and other small signal devices. It has excellent noise characteristics ( $\text{ENC} = 200e^- + 8e^-/\text{pF}$  at  $1 \mu\text{s}$  shaping time), and consumes only  $1.2 \text{ mW/channel}$ .

A block diagram of the VA1 chip is shown in Fig. 16. Signals from the strips are amplified by charge-sensitive preamplifiers, followed by CR–RC shaping circuits. The outputs of the shapers are fed to track and hold circuits, which consist of capacitors and CMOS switches. Under normal conditions, the switches are closed and the voltages on the capacitors simply follow the shaper outputs.

When an external trigger causes the HOLD state to be asserted, the analog information from all channels is captured on storage capacitors and then sequentially read using on-chip scanning analog multiplexers. The multiplexers from the five chips on a single hybrid are daisy chained and routed to fast analog-to-digital converters (FADCs), located in the electronics hut about 30 m away from the detector. Operation of the multiplexer is controlled by a shift register having one bit per channel. This simple “track-and-hold” architecture is generally well suited to the Belle DAQ system.

Although input-FET noise considerations of VA1 argue for a somewhat longer shaping time, the shaping time for VA1s is adjusted to  $1 \mu\text{s}$  to minimize the occupancy due to the beam background. Since this time is shorter than the nominal Belle level-1 trigger latency ( $2.2 \mu\text{s}$ ), a pretrigger signal from the TOF system is used to assert the VA1 HOLD line until the level-1 signal is formed. If a level-1 signal does not occur within  $1.2 \mu\text{s}$ , the HOLD line is deasserted and the system is immediately ready for another event. If the level-1 does fire, a normal readout sequence ensues.

VA1 also provides for testing the inputs of individual channels. This is done by using a

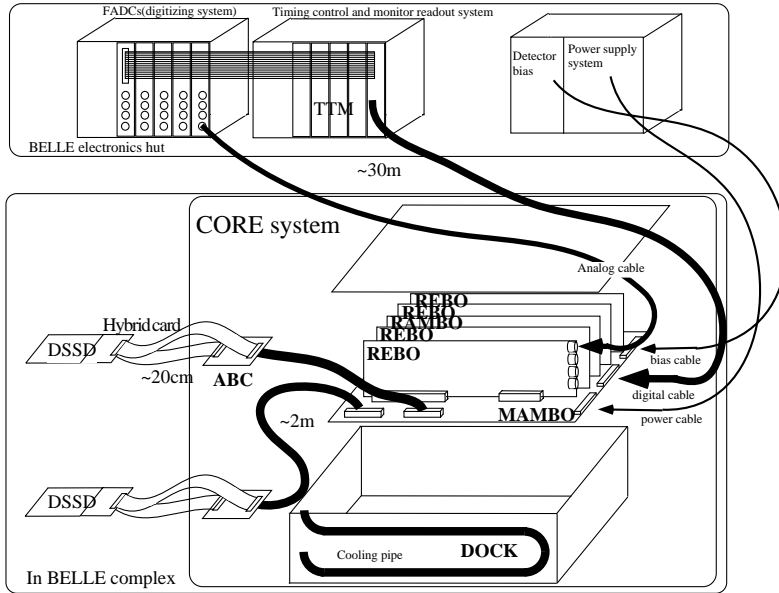


Fig. 15. Schematic drawing of the SVD readout system.

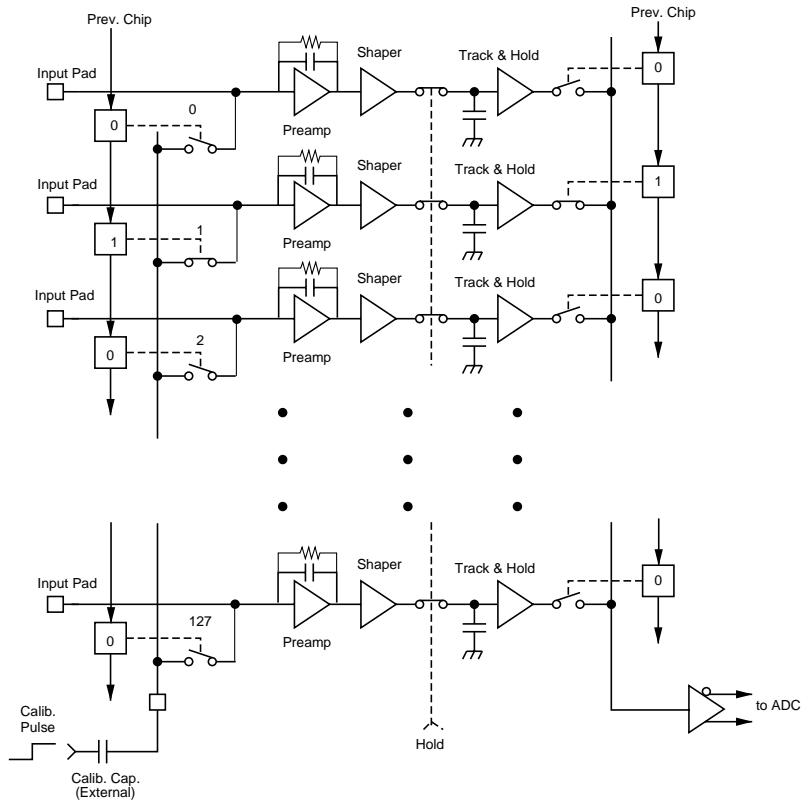


Fig. 16. Block diagram of the VA1 chip.

shift-register-controlled switching network on the input side of the chip to sequentially couple an externally provided test pulse into each channel. When in the test mode, the input and output shift registers track on another, allowing one to observe the shaper output for each channel directly by holding the hold switches in the track (closed) position. Accurate calibration can be achieved by using a precision external calibration capacitor.

Radiation hardness tests of VAI indicate that it is radiation tolerant to levels of order 200 krad. Prior to complete chip failure, a fractional increase in noise of 1.6%/krad was observed. After 150 krad irradiation the noise level for the p–n flip sensors ( $C_{\text{strip}} = 29$  pF) seems to be marginal.

The detector capacitance, measured noise (ENC, electron noise charge), and signal-to-noise ratio ( $S/N$ ) for a normally incident minimum ionizing particle are summarized in Table 2.

The dependence of expected  $S/N$  on radiation dose is given in Table 3.

Table 2

Detector capacitance (C), expected noise (ENC) and signal-to-noise ratio ( $S/N$ ) at 0 krad

Half-ladder	Side	C (pF)	ENC (e <sup>-</sup> )	$S/N$
S6936 × 1	p	7	400	47
	n	22	1000	19
S6936 × 2	p–n	29	1100	17

Table 3

Expected signal-to-noise ratio after irradiation. The radiation dose values shown are for the inner layer. The radiation doses in the middle and outer layers are assumed to scale as  $r^{-1}$

Half-ladder	Side	0 krad	50 krad	100 krad	150 krad
Inner (1 DSSD)	p	47	31	23	18
	n	19	16	13	11
Middle fwd (1 DSSD)	p	47	35	28	23
	n	19	17	15	13
Middle bwd (2 DSSDs)	p–n	18	16	14	12
	p–n	18	17	15	14
Outer (2 DSSDs)	p–n	18	17	15	14

#### 4.3.2. Hybrid

The hybrids comprise VAI IC's and a small number ( $\sim 25$ ) of passive surface-mount (SM) components mounted on thermally conductive aluminum-nitride ceramic substrates. The inputs of VAIs are wire-bonded to the strips of DSSDs. The passive components are used for bypassing, calibration, bias adjustment, and clock termination. Connections to the external system were made via “nano-strip” connectors, which were selected to accommodate space restrictions (they require only 1.3 mm of vertical clearance). The vendor of these connectors [20] also provides matching ribbon-cable versions that are used to carry the connections to the ABC cards.

#### 4.3.3. Repeater system CORE

A control and readout (CORE) system [21] is required to provide the following functions:

- *Analog control of the VAI front-end chips.* The CORE system provides bias voltages and currents. The ability to adjust the bias parameters remotely is particularly important in view of the possibility that the optimal values may change with time as the chips are irradiated.
- *Digital control of the VAI front-end chips.* Various pulses and digital levels are used to control the data-acquisition sequence of the VAI chips. The CORE serves to condition, buffer, and distribute these signals to VAIs.
- *Analog buffering and amplification.* Since the cable length between the detector and the electronics hut is about 30 m, CORE incorporates differential gain/buffer stages to provide immunity to electromagnetic interference. To meet the readout speed requirements of Belle DAQ, CORE is capable of supporting MUX scan rates up to 5 MHz. This allows a single FADC channel to scan all channels of a 640-channel hybrid in 128  $\mu$ s.
- *Monitoring of analog levels.* CORE monitors a large number ( $68 \times 4 \times 8$ ) of analog levels to verify the bias parameters of VAI and buffers, and the hybrid temperatures.

As shown in Fig. 15, each CORE system module consists of a backplane motherboard (MAMBO), four boards for readout signal buffering and front-end control (REBOs), a board for monitoring (RAMBO), and eight interface cards (ABCs). There are a total of eight cooled aluminum and copper housings (DOCKs) which hold the CORE system boards; four each in the forward and backward regions of the detector. The temperature at the surface of DOCK is maintained at  $\sim 23^\circ\text{C}$ .

ABCs, which are physically situated about 20 cm from the front-end hybrids, provide a passive electrical interface between the repeater system and the hybrids. In addition, they serve as passive one-to-two fanouts for the digital control signals running from the repeater to the hybrids, thereby reducing the number of cables required. ABCs also facilitate ready disconnection for maintenance.

MAMBO is an interface board for ABC, REBO, RAMBO and cables to the Belle electronics hut. MAMBO transmits digital signals to and from TTMs using the low-voltage differential signaling (LVDS) standard. LVDS reduces EMI to the analog part of CORE as well as to other parts of the detector. Mounted on MAMBO are ADCs to monitor temperature, the bias currents and voltages, the amplitude of a calibration test pulse, and the logic levels for the digital signals.

REBO consists of an analog block and a digital block. The analog block comprises digital-to-analog converters (DACs), voltage-to-current converters, current-to-voltage converters and amplifiers. The digital block controls DACs in the analog block, and buffers the digital signals to the front-end electronics.

#### 4.4. Back-end electronics

The Belle DAQ system employs a simple track-and-hold architecture, in which the front-end electronics is temporarily inhibited upon receipt of a level-1 trigger. The time required for the analog multiplexer scan of VA1 outputs determines the readout deadtime. Since the scan rate is 5 MHz and each FADC channel must read 640 VA1 front-end channels, the minimum deadtime is 128  $\mu\text{s}$ , which is less than the 200  $\mu\text{s}$  global

maximum for Belle. Once all scans are complete and the digital data are buffered in FIFOs, the modules release the busy signal and the system is ready to accept and process another level-1 trigger [22].

This data buffering scheme allows the DSP modules to implement pedestal subtraction and zero suppression, and low-level data formatting asynchronously, so that no additional deadtime is introduced.

##### 4.4.1. FADC system

Fig. 17 shows the block diagram of the FADC module, which is called “Halny”.<sup>11</sup> Each “Halny” module incorporates four channels of FADC, FIFO buffering, and Motorola DSP56302 digital signal processor. The DSPs carry out the pedestal subtraction and zero suppression calculations on a channel-by-channel basis and implement low-level data formatting. The DSPs also calculate pedestals and hit thresholds using a dynamic algorithm that automatically adjusts for pedestal shifts and changes in noise level.

##### 4.4.2. Trigger timing modules

Trigger timing modules (TTMs) are used to control the timing of the front-end readout electronics and to control the Halny FADC modules. TTMs are in turn driven by the central data-acquisition (CDAQ) system. In addition to distributing timing signals TTMs are used to transmit slow control and monitoring information to and from the front-end electronics. These signals pass through the CORE system, which provides buffering, fanout and level translation.

The TTM system consists of nine modules: one master and eight slaves. The two types of modules use the same hardware but achieve different functionality through differently configured field-programmable gate-array logic. The master TTM receives timing control signals from a timing distributor module (TDM), supplied from CDAQ, and retransmits these signals to the slave TTMs.

<sup>11</sup> “Halny” is the warm and violent wind blowing in the Tatra mountains. This name was given to paraphrase the name of the less capable SIROCCO module [23]. (Sirocco is a mild alpine wind.)

Each slave TTM handles the interaction with one repeater DOCK via a point-to-point LVDS link. TTMs are also used to send signals to each FADC in FADC crates. RS 485 (differential TTL) is used

for the communication between TTMs and FADCs.

#### 4.5. SVD DAQ system

The SVD DAQ system consists of a data manager, a run manager and an interlock. The data manager transfers data from the FADC output FIFOs to the central event builder and the run manager controls the DAQ hardware. The interlock monitors running conditions and sends signals to the run manager when an abnormal state is detected. Fig. 18 shows a block diagram of the data acquisition and the monitoring system for SVD. The SVD back-end electronics system comprises a TTM system in a VME crate and four FADC VME systems. An FADC system consists of eight FADC modules and a SPARC VME module. The VME modules (TDM, TTMs and HALNYs) are controlled by a VME master module (i.e. a SPARC VME module) in each VME crate.

The four FADC subsystems collect and transmit data to the event builder in parallel. SPARC VME boards resident in each of the four FADC crates carry out this task. The SPARC VME boards poll the status of each HALNY board in its crate and waits for a response indicating that a digitized

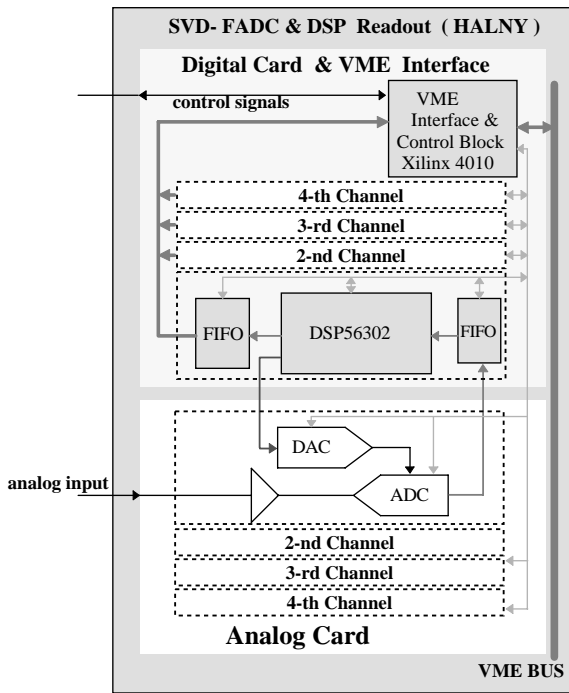


Fig. 17. Block diagram of a Halny FADC module.

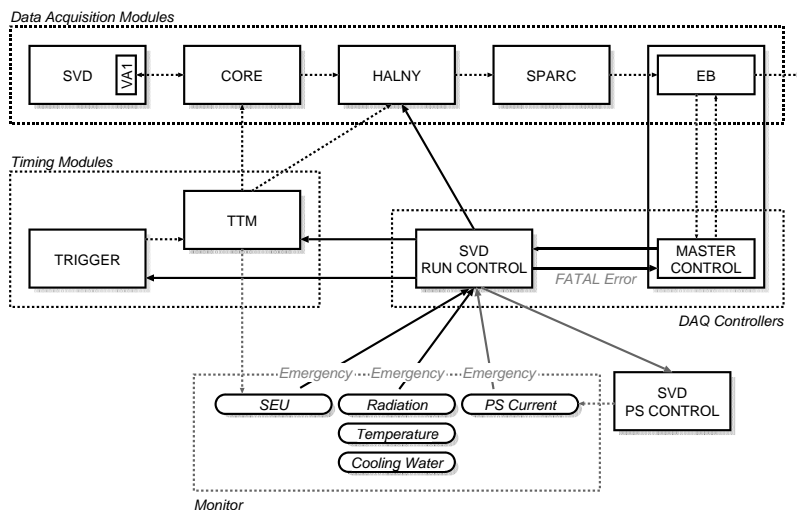


Fig. 18. Block diagram of the SVD DAQ system.

event is ready to be read. HALNY data is transferred from the output FIFOs on a word-by-word basis.

The SVD run manager controls DAQ VME modules (TDM, TTMs and HALNYs). It initiates or terminates trigger sequences, downloads firmware to the TTMs and Halnys, and issues resets at the beginning of each run and when requested by CDAQ. It also controls the run mode of the VA1 and CORE front-end electronics, via TTMs. Finally, it initiates recovery procedures upon request from the interlock.

The SVD interlock system monitors running conditions of SVD. The data integrity is checked by the consistency of the event size and begin/end event markers. The condition of VA1s is monitored by checking the digital outputs from the hybrids and by tracking their power-supply currents. Temperatures of the hybrids, heat sinks and end-rings, and water circulation are monitored to make sure that the cooling system is in working order. The beam abort signal from the radiation monitor described below is also fed into the interlock. When the system senses a fault condition on one of its inputs, it shuts down the power supplies for the front-end electronics and sends an abort signal to the run manager.

#### 4.6. Monitor system

The SVD monitor system consists of temperature monitors using resistive temperature detectors (RTDs), instantaneous radiation monitors based on PIN diodes, total-dose measurements using a RADFET technique (electronic readout) and an alanine dosimeter. These sensors are read using a commercial data logger system [24].

A total of 48 RTDs [25] are attached to the SVD cooling system and the interaction-region (IR) beam pipe. The monitor data has been used as the interlock signal for the cooling systems for SVD and the IR beam pipe. The operation of the cooling system has been highly reliable: no temperature fault condition has been asserted during the past year of operation.

The eight sets of unbiased PIN photo diodes (HPK S3590-08) [26] used as real-time radiation monitors are read out by an operational amplifier

OPA129 (Burr-Brown). Output signals are recorded by the data logger. The signals are also sent to a discriminator module. When more than two channels indicate an instantaneous radiation dose exceeding 1 rad/s, the multiplicity logic sends a beam abort request to the KEKB accelerator. The frequency of beam aborts varies with accelerator conditions, but in stable operation is approximately one per day.

A RADFET is a MOSFET [27] optimized for radiation measurement. When it is irradiated, the threshold voltage of the FET is shifted due to the accumulation of charge in the gate oxide. Since this mechanism is essentially the same as the mechanism of radiation damage in the VA1 chips, it provides a good measure of radiation damage in those chips.

The alanine dosimeters are passive device based on electron spin resonance (ESR) measurement of radiation-induced free radicals in an amino acid alanine ( $\text{CH}_3\text{-CH-NH}_2\text{-COOH}$ ). They provide a measure of long-term integrated dose and accessible for reading only in conjunction with major detector accesses.

#### 4.7. Performance

High SVD strip yields and good  $S/N$  ratios are needed to ensure the efficient matching between tracks detected by CDC and clusters detected by SVD. Distributions of normalized cluster energies for minimum ionizing particles (MIPs) from hadronic events are shown in Fig. 19, where the cluster energy is normalized to the same track path length in DSSD (300  $\mu\text{m}$ ). The measured most-probable peak height is approximately  $19,000e^-$ . The noise level and the  $S/N$  ratio for each DSSD side (p, n and p-n) are summarized in Table 2. Strip yields, which are defined to be the fraction of channels with  $S/N$  ratios larger than 10:1, are measured to be 98.8% on layer 1, 96.3% on layer 2, and 93.5% on layer 3 [28].

The track-matching efficiency is defined as the probability that a CDC track within the SVD acceptance has associated SVD hits in at least two layers, and in at least one layer with both the  $r-\phi$  and  $r-z$  information. Tracks from  $K_S$  decays were excluded since these tracks did not necessarily go

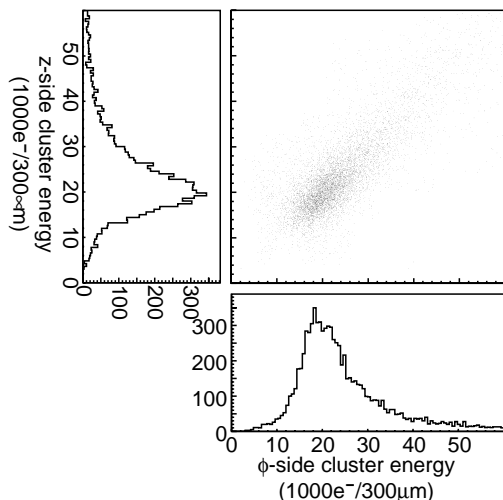


Fig. 19. Cluster energy distribution in which the cluster energy is normalized by the track path length in DSSD.

through SVD. Fig. 20 shows the SVD–CDC track matching efficiency for hadronic events as a function of time. The average matching efficiency is better than 98.7%, although we observe slight degradation after 1 yr operation as a result of the gain loss of VA1 from radiation damage [28].

The momentum and angular dependence of the impact parameter resolution are shown in Fig. 21 and well represented by the following formula:  $\sigma_{xy} = 19 \oplus 50/(p\beta \sin^{3/2} \theta) \mu\text{m}$  and  $\sigma_z = 36 \oplus 42/(p\beta \sin^{5/2} \theta) \mu\text{m}$ .

We performed the same study for the MC sample and obtained an IP resolution of  $\sigma_{xy} = 15 \oplus 49/(p\beta \sin^{3/2} \theta) \mu\text{m}$  and  $\sigma_z = 28 \oplus 41/(p\beta \sin^{5/2} \theta) \mu\text{m}$ . This indicates that the IP resolution term dominated by the scattering is well simulated by the MC data. The flat components are larger in the real data than in the MC simulation, which indicates the amount of remaining misalignment errors. Detailed description of Belle SVD performance studies can be found elsewhere [29].

## 5. Central tracking chamber, CDC

The efficient reconstruction of charged particle tracks and precise determination of their momenta is an essential ingredient to virtually all of the

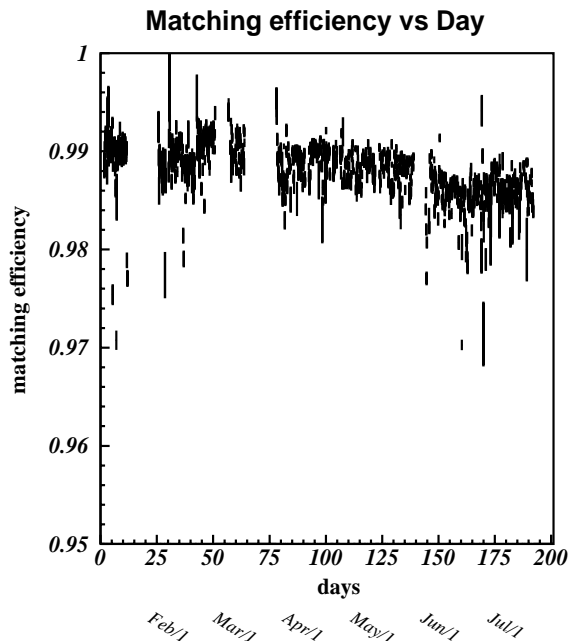


Fig. 20. SVD–CDC track matching efficiency as a function of the date of data taking.

measurements planned for the Belle experiment. Specifically, the physics goals of the experiment require a momentum resolution of  $\sigma_{p_t}/p_t \sim 0.5\% \sqrt{1+p_t^2}$  ( $p_t$  in GeV/c) for all charged particles with  $p_t \geq 100$  MeV/c in the polar angle region of  $17^\circ \leq \theta \leq 150^\circ$ . In addition, the charged particle tracking system is expected to provide important information for the trigger system and particle identification information in the form of precise  $dE/dx$  measurements for charged particles [4].

### 5.1. Design and construction of the central tracking chamber

The Belle central drift chamber, CDC, was designed and constructed to meet the requirements for the central tracking system [30,31]. Since the majority of the decay particles of a B meson have momenta lower than 1 GeV/c, the minimization of multiple scattering is important for improving the momentum resolution. Therefore, the use of a

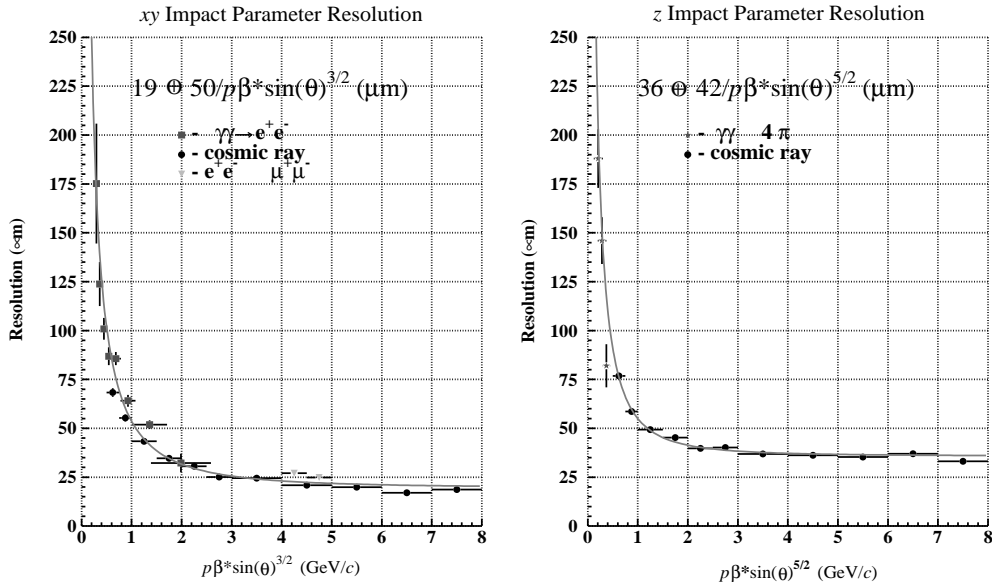


Fig. 21. Impact parameter resolution.

low-Z gas is desirable, while a good  $dE/dx$  resolution must be retained.

5.1.1. Structure and wire configuration

The structure of CDC is shown in Fig. 22. It is asymmetric in the  $z$  direction in order to provide an angular coverage of  $17^\circ \leq \theta \leq 150^\circ$ . The longest wires are 2400 mm long. The inner radius is extended down to 103.5 mm without any walls in order to obtain good tracking efficiency for low- $p_t$  tracks by minimizing the material thickness. The outer radius is 874 mm. The forward and backward small- $r$  regions have conical shapes in order to clear the accelerator components while maximizing the acceptance.

The chamber has 50 cylindrical layers, each containing between three and six either axial or small-angle-stereo layers, and three cathode strip layers. Table 4 gives the detailed parameters of the wire configuration. CDC has a total of 8400 drift cells. We chose three layers each for the two innermost stereo superlayers and four layers each for the three outer stereo superlayers in order to provide a highly efficient fast  $z$ -trigger combined

with the cathode strips. We determined the stereo angles in each stereo superlayer by maximizing the  $z$ -measurement capability while keeping the gain variations along the wire below 10%.

The individual drift cells are nearly square and, except for the inner three layers, have a maximum drift distance between 8 and 10 mm and a radial thickness that ranges from 15.5 to 17 mm. The drift cells in the inner layers are smaller than the others and their signals are read out by cathode strips on the cylinder walls. These cell dimensions were optimized based on the results of beam test measurements [32]. Fig. 23 shows the cell arrangement in which the neighboring radial layers in a superlayer are staggered in  $\phi$  by a half cell to resolve left-right ambiguities. The sense wires are gold-plated tungsten wires of 30  $\mu\text{m}$  in diameter to maximize the drift electric field. The field wires of unplated aluminum of 126  $\mu\text{m}$  in diameter are arranged to produce high electric fields up to the edge of the cell and also to simplify the drift time-to-distance relation. The aluminum field wires are used to reduce the material of the chamber. The electric field strength at the surface of the

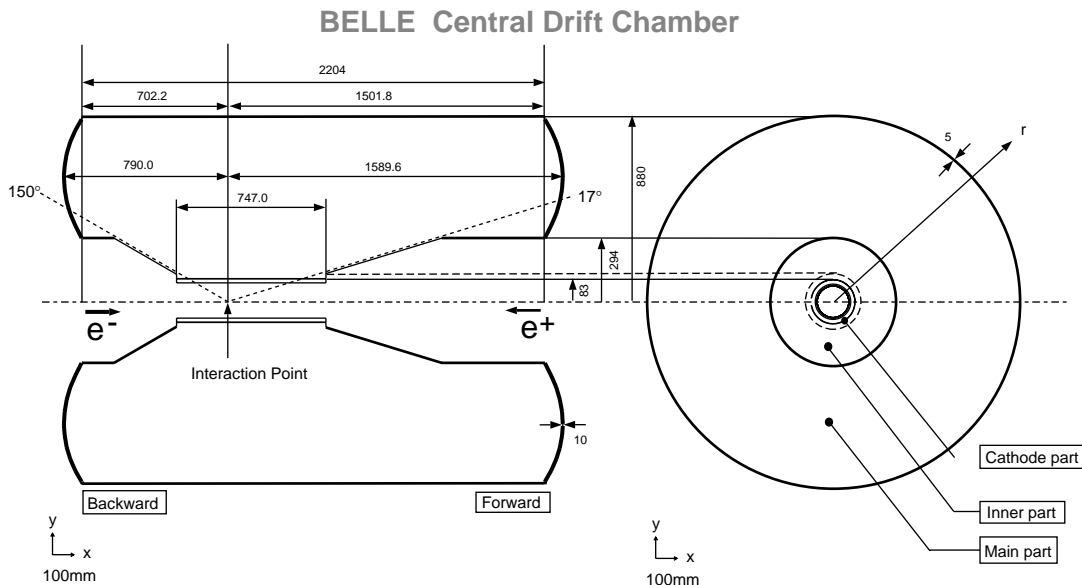


Fig. 22. Overview of the CDC structure. The lengths in the figure are in units of mm.

Table 4  
Configurations of the CDC sense wires and cathode strips

Superlayer type and no.	No. of layers	Signal channels per layer	Radius (mm)	Stereo angle (mrad) and strip pitch (mm)
Cathode	1	$64(z) \times 8(\phi)$	83.0	(8.2)
Axial 1	2	64	88.0–98.0	0.
Cathode	1	$80(z) \times 8(\phi)$	103.0	(8.2)
Cathode	1	$80(z) \times 8(\phi)$	103.5	(8.2)
Axial 1	4	64	108.5–159.5	0.
Stereo 2	3	80	178.5–209.5	71.46–73.75
Axial 3	6	96	224.5–304.0	0.
Stereo 4	3	128	322.5–353.5	–42.28–45.80
Axial 5	5	144	368.5–431.5	0.
Stereo 6	4	160	450.5–497.5	45.11–49.36
Axial 7	5	192	512.5–575.5	0.
Stereo 8	4	208	594.5–641.5	–52.68–57.01
Axial 9	5	240	656.5–719.5	0.
Stereo 10	4	256	738.5–785.5	62.10–67.09
Axial 11	5	288	800.5–863.0	0.

aluminum field wires is always less than 20 kV/cm, a necessary condition for avoiding radiation damage [33].

Three  $z$ -coordinate measurements at the innermost radii are provided by cathode strips as shown in Fig. 24 [34]. They were glued on the inner cylinder surface of the chamber and on both sides

of a 400  $\mu\text{m}$  thick CFRP cylinder located between the second and third anode layers. In order to maintain the mechanical strength and accuracy, aluminum guard rings were attached on the both ends with electrically conducting glue. The deviation from a perfect cylindrical shape is less than 100  $\mu\text{m}$  in radius. The cathode strips are divided

into eight segments in the  $\phi$  direction and have an 8.2 mm pitch in the  $z$  direction. The strip width is 7.4 mm. The total number of cathode channels is

1792. The deterioration of the momentum resolution due to multiple scattering in the cathode materials is minimized.

**BELLE Central Drift Chamber**

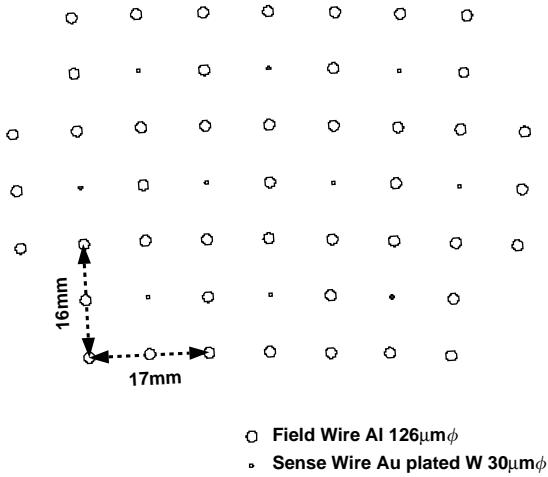


Fig. 23. Cell structure of CDC.

The total wire tension of 3.5 tons is supported by the aluminum end-plates and the CFRP cylinder structures that extend between the end-plates. Each end-plate consists of three parts; the cathode, inner and main parts as indicated in Fig. 22. The cathode part of a 16 mm thick flat plate corresponds to the three innermost anode layers and three cathode layers. The conically shaped inner part covers 11 anode layers in the radial range from 103.5 to 294 mm. The end-plate thickness in the  $z$  direction is 11–18 mm for the backward side and 25–31 mm for the forward side. The end-plate of the main part is 10 mm in thickness and has a curved profile to minimize distortions caused by the wire tension. The three end-plate parts are connected to each other by stainless-steel bolts and gas sealed with silicone glue. The 754.5 mm radial space between the 3rd and 50th anode layers contains only gases and wires.

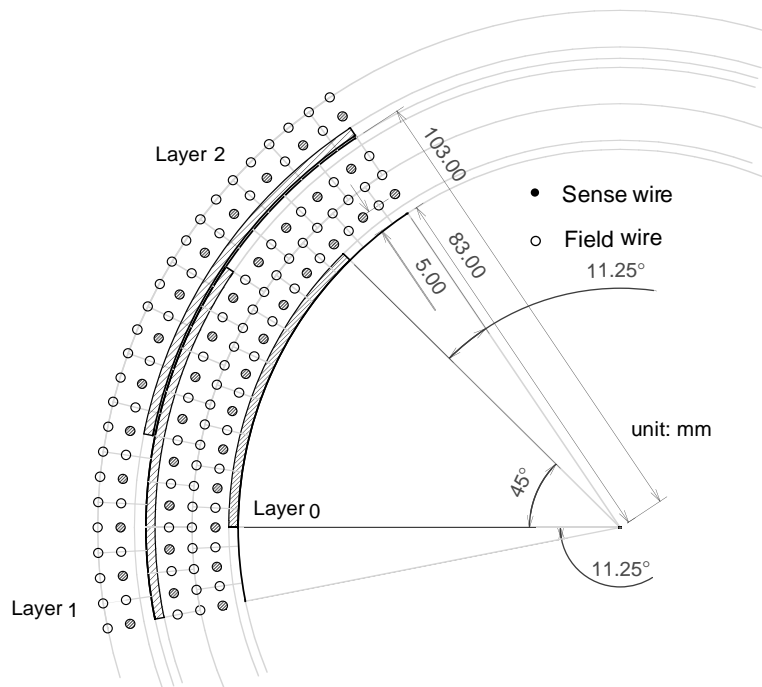


Fig. 24. Cell structure and the cathode sector configuration.

The feed-through holes were drilled by a custom designed drilling machine at the KEK machine shop. The hole position accuracy is better than 30  $\mu\text{m}$ .

### 5.1.2. Gas

The use of a low- $Z$  gas is important for minimizing multiple Coulomb scattering contributions to the momentum resolution. Since low- $Z$  gases have a smaller photo-electric cross-section than argon-based gases, they have the additional advantage of reduced background from synchrotron radiation. We have selected a 50% helium–50% ethane gas mixture. This mixture has a long radiation length (640 m), and a drift velocity that saturates at 4  $\text{cm}/\mu\text{s}$  at a relatively low electric field [32,35]. This is important for operating square-cell drift chambers because of large field non-uniformities inherent to their geometry. The use of a saturated gas makes calibrations simpler and helps to ensure reliable and stable performance. Even though the gas mixture has a low  $Z$ , a

good  $dE/dx$  resolution is provided by the large ethane component [36].

Several test chambers were constructed and beam tests were carried out. Figs. 25(a) and (b) show measured gas gain and drift velocity data for a 50% helium–50% ethane gas mixture [32].

### 5.1.3. Electronics

A schematic diagram of the readout electronics of CDC is shown in Fig. 26 [37]. Signals are amplified by Radeka-type pre-amplifiers [38], and sent to Shaper/Discriminator/QTC modules in the electronics hut via  $\sim 30$  m long twisted pair cables. This module receives, shapes, and discriminates signals and performs a charge( $Q$ )-to-time( $T$ ) conversion (QTC). The module internally generates a logic-level output, where the leading edge  $T_{\text{LE}}$  corresponds to the drift time ( $t_d$ ) and the width  $T_W$  is proportional to the input pulse height ( $T_W = a \times Q + b$ ). This technique is a rather simple extension of the ordinary TDC/ADC readout scheme, but allows us to use only TDCs to measure both the timing and charge of the signals.

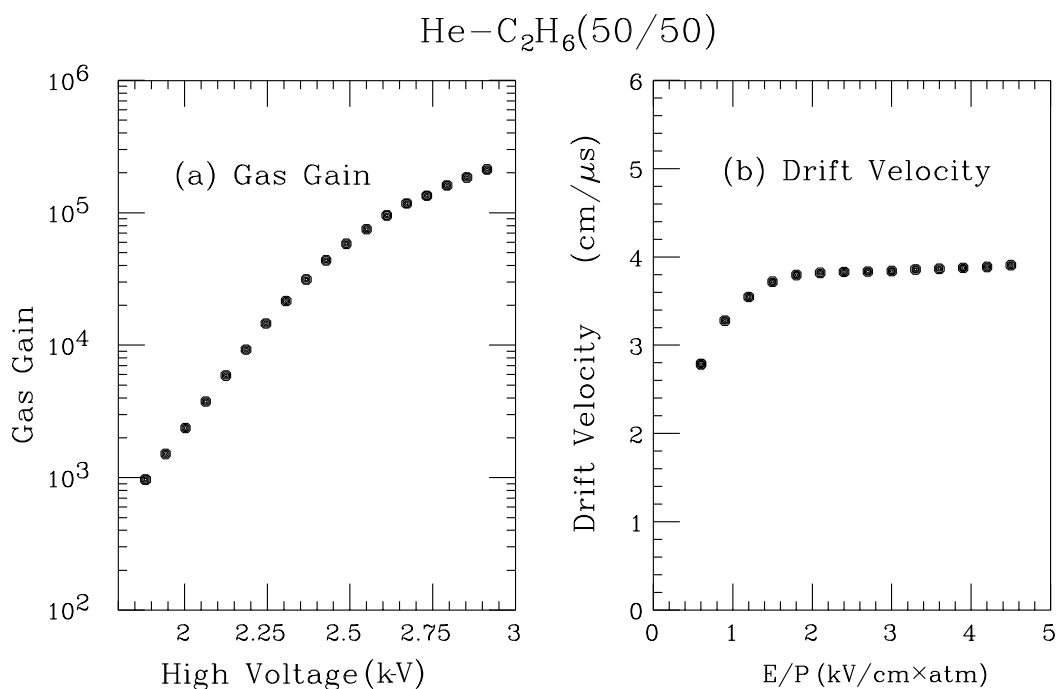


Fig. 25. (a) The measured gas gain and (b) drift velocity for a 50% He and 50% C<sub>2</sub>H<sub>6</sub> gas mixture.

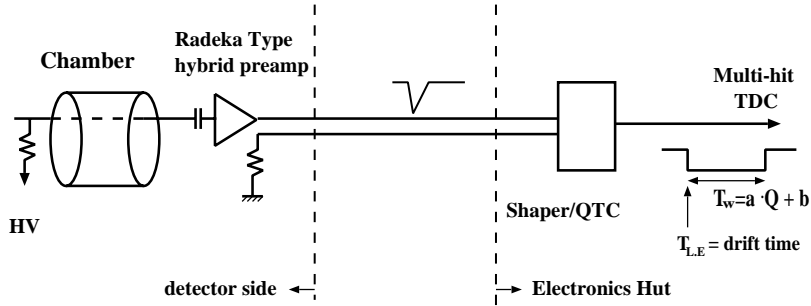


Fig. 26. CDC readout electronics scheme.  $T_{LE}$  and  $T_w$  are the leading edge and width of the pulse, respectively.

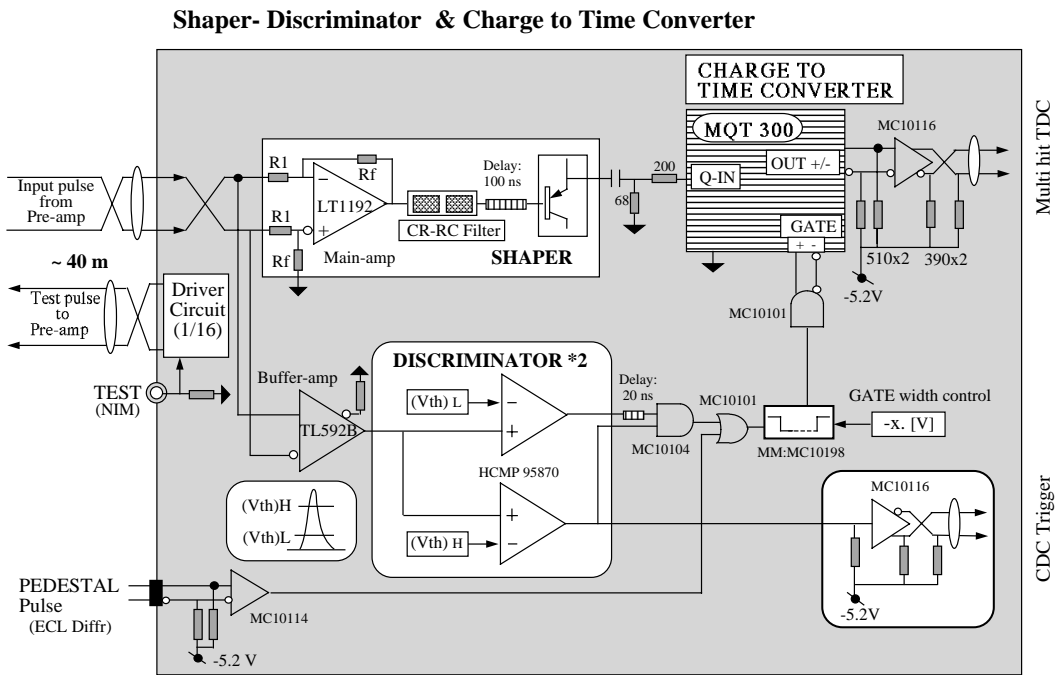


Fig. 27. Schematic circuit of the Shaper/QTC board.

Since multi-hit TDCs work in the common stop mode, one does not need a long delay that analog signals usually require in an ADC readout with a gate produced by a trigger signal.

A prototype Shaper/QTC board with 32 channels (VME9U) was fabricated and tested using a test beam. Fig. 27 shows the schematic circuit of a single channel. The signals from a pre-amplifier are split into two paths of circuit; one is an “analog circuit” and the other is a “digital circuit”. The digital circuit provides self-gated signals to the

QTC chip, and trigger output signals. It consists of an amplifier, comparators, and a gate signal generation circuit. In order to have good timing resolution without increasing the hit rates for the gate and trigger signals due to noise signals, we use a “double-threshold method”. The signal from a low-threshold comparator is delayed by 20 ns before forming a coincidence with a signal from a high-threshold comparator so that the timing of the coincidence signal is determined by the low-threshold comparator. Threshold voltages are

supplied externally from precisely regulated adjustable voltage power supplies. We used a fast video-amplifier chip TL592B (Texas Instruments, USA) for the amplifier and a MAX9687 (Maxim, USA) for the comparator. An MC10198 (Motorola, USA) mono-stable multi-vibrator chip was used to produce an ECL-level gate pulse. The gate width was adjusted by the value of the resistors soldered on the board. The width was chosen to be  $\sim 850$  ns in the beam test. We observed that the jitter of the gate width was 0.5 ns (RMS) and the width was stable within  $\pm 1$  ns during the beam test.

The analog circuit provides input signals to the QTC chip. It consists of an amplifier, a shaping circuit, and a delay. The shaping circuit has two stages of pole-zero cancellation with time constants of 120/30 and 56/20 ns. A passive LC delay line of 100 ns is used to delay the analog signal to arrive after the leading edge of the gate. We used an LT1192 (Linear Technology, USA) chip for an amplifier of the analog circuit because it provides a wider linear region and better bandwidth than a TL592B.

We set the gains to be 10 and 30 for the amplifiers in the analog and digital circuits, respectively. These are adjusted by the resistor values soldered on the board. Since a QTC chip is operated in a self-gate mode, the charge data are automatically pedestal suppressed in contrast to the ordinary ADC readout. In order to take pedestal data, the board takes “pedestal pulses” from the front panel connector which forces a trigger of the gate circuits of all the channels without input signals.

For  $Q$ -to- $T$  conversion, we used chips recently developed by LeCroy, MQT300 [39]. The MQT300 chip performs  $Q$ -to- $T$  conversion in three ranges. The conversion gain for the low range is 0.01 pC/ns, with a factor of 8 and 64 larger conversion gains for the middle and high ranges. The full range in the specification is  $\sim 4$   $\mu$ s above the pedestals, but the chip provided a good linearity within 1% deviation up to  $\sim 7$   $\mu$ s above the pedestals. Each range can be enabled or disabled by the jumper pins on the Shaper/QTC board. In the beam test, we enabled and recorded all three ranges for a detailed check of the Shaper/

QTC board performance. The MQT300 chip produces the output pulses as an exclusive OR of the output pulses of the enabled ranges. When the three ranges are enabled, two pulses are produced. Since the dynamic range provided by a single range of MQT300 chips is large enough for the CDC readout application, we plan to use them only with a single range (middle range) in the actual Belle experiment.

A beam test was carried out at the  $\pi 2$  beam line of the KEK 12-GeV PS. Data were taken both with the QTC/multi-hit TDC and the conventional TDC/ADC readout scheme in order to compare the performance of two readout schemes directly with the same conditions. In the QTC/multi-hit TDC scheme case, the output signals from the Shaper/QTC board are recorded by LeCroy 3377 CAMAC TDC modules. In the TDC/ADC scheme case the previous beam test arrangement was used [36]. Spatial resolutions as a function of the drift distance were measured with various beam conditions. No significant difference is seen between the two readout schemes and they are consistent with the previous result.  $dE/dx$  distributions were also measured with the two readout schemes. Again no significant difference is seen. These results confirm that the new readout scheme worked successfully and is applicable to the CDC readout.

## 5.2. Beam test by a real-size prototype drift chamber

A real-size prototype of Belle CDC was constructed and used in a beam test to study the gas-gain saturation effect in  $dE/dx$  measurements. The chamber is 235 cm long, and the inner and outer radii are 25 cm to 90 cm, respectively. It has 41 layers of sense wires, 9 layers fewer than the final design [36]. A beam test was carried out at the  $\pi 2$  beam line. The chamber was placed in a null magnetic field. The drift time was measured by a LeCroy FASTBUS TDC 1876 and the total charge was integrated by a LeCroy FASTBUS 1885F.

The measured spatial resolution was 120–150  $\mu$ m depending on the layer and incident angles in the direction perpendicular to the wires.

For the  $dE/dx$  measurement we took the truncated mean in order to minimize the contribution of the Landau tail in the  $dE/dx$  distribution. In the analysis of this section 80% truncated means are used to measure  $dE/dx$ . The  $dE/dx$  resolution

was obtained to be 5.2% for 3.5 GeV/c pions at an incident angle of  $45^\circ$ . Fig. 28 shows measured  $dE/dx$  distributions as a function of  $\beta\gamma$ . The solid curve is a fit to the data at an angle of  $45^\circ$ , based on the most-probable energy loss formula [36].

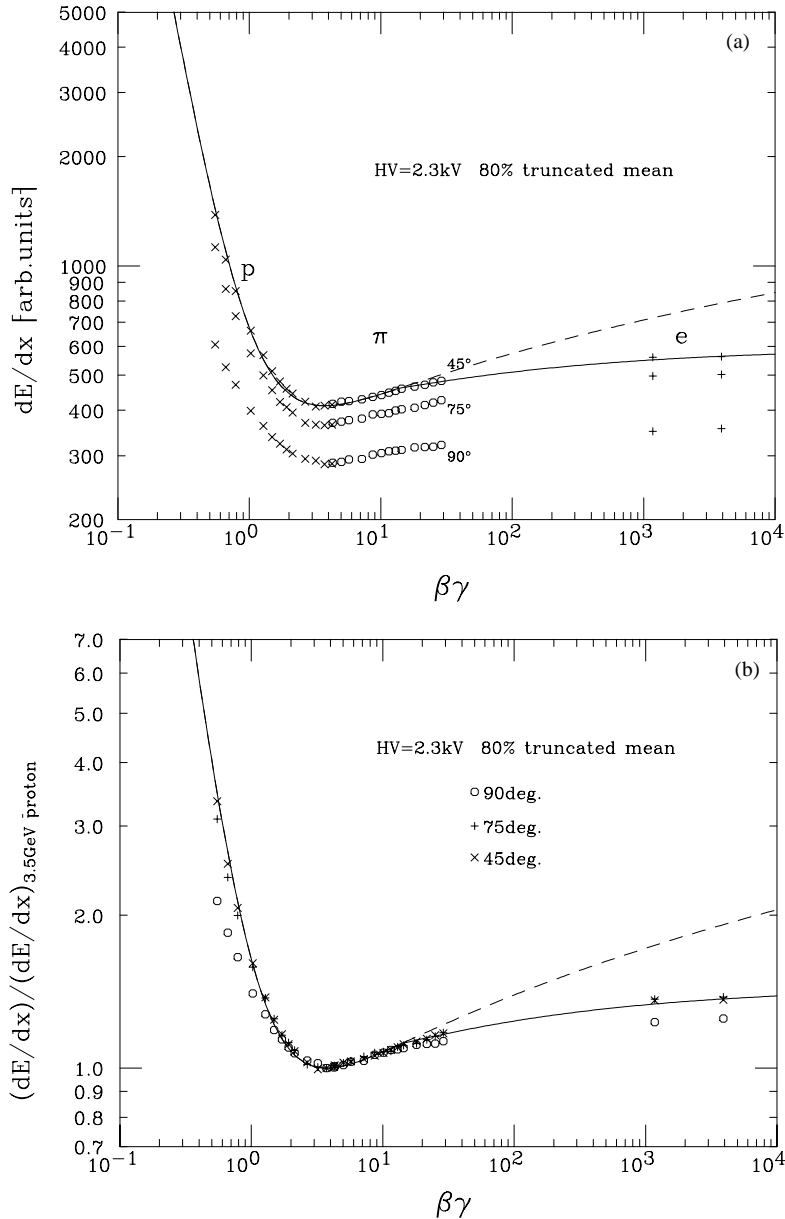


Fig. 28. (a) Measured  $dE/dx$  vs.  $\beta\gamma$  and (b) the same as (a), but normalized with the  $dE/dx$  measured by 3.5 GeV/c protons ( $\beta\gamma = 3.73$ ). The solid curve is a fit to the data at an incident angle of  $45^\circ$ , and the dashed curve is that with  $\delta = 0$ .

The density correction term  $\delta$  was parameterized to fit the electron data. The dashed curve corresponds to the case of  $\delta = 0$ .

The incident angle dependence of  $dE/dx$  was measured. The normalized  $dE/dx$  distributions to  $dE/dx$  values calculated from the fit obtained for the incident angle of  $45^\circ$  decrease with increasing

incident angles. This indicates a clear space charge effect. The gas-gain saturation effect is mainly determined by the projected ion pair density produced by the incident particles. Fig. 29 shows distributions of  $(dE/dx)_{\text{meas.}}/(dE/dx)_{\text{expect}}$  vs.  $(dE/dx)_{\text{meas.}}/\cos\theta$  for various beam conditions. The  $x$ -axis corresponds to the projected ion pair

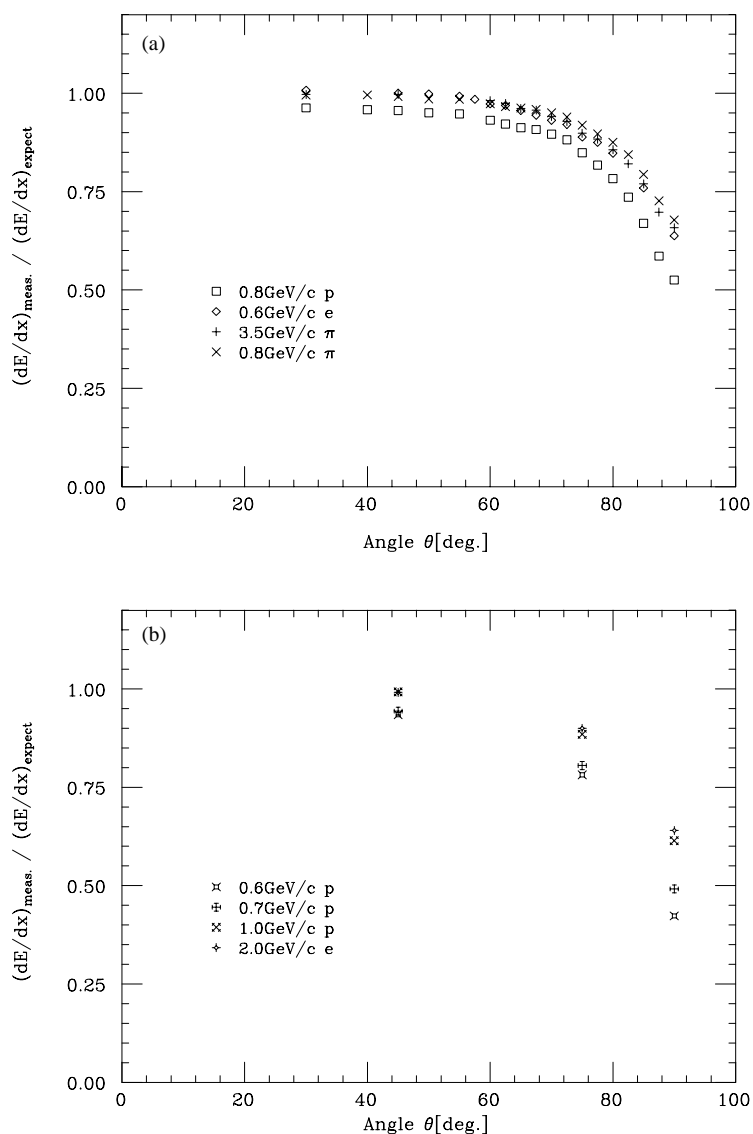


Fig. 29. (a)  $(dE/dx)_{\text{meas.}}/(dE/dx)_{\text{expect}}$  vs.  $(dE/dx)_{\text{meas.}}/\cos\theta$  (avalanche density on the sense wire) for 0.8 GeV/c protons, 0.8 GeV/c pions, 0.6 GeV/c electrons and 3.5 GeV/c pions, and (b)  $(dE/dx)_{\text{meas.}}/(dE/dx)_{\text{expect}}$  vs.  $(dE/dx)_{\text{meas.}}/\cos\theta$  for 0.6, 0.7 and 1.0 GeV/c protons and 2.0 GeV/c electrons. The solid curves are the fit results. The  $90^\circ$  data are treated separately.

density and the magnitude of the  $y$ -axis is essentially independent of incident particles.

It is important to correct data for the space charge effect to maintain the particle identification performance expected from the obtained resolution and  $\beta\gamma$  dependence of  $dE/dx$ .

### 5.3. Calibration with cosmic rays

#### 5.3.1. CDC

Cosmic-ray data were taken with the solenoid operating at its nominal 1.5 T field. A positive high voltage was applied to the sense wires, and the field wires were connected to the end-plates and kept at ground. The sense wire high voltages, typically 2.35 kV, were adjusted layer-by-layer to keep the same gas gain (several  $\times 10^4$ ) for different cell sizes. The chamber was operated at a constant pressure slightly above one atmosphere.

The standard trigger and data acquisition system developed for operation in the Belle experiment was used in the cosmic-ray run. Back-to-back cosmic-ray events were triggered by the Belle TOF counter system [40]. The event timing was determined with a 0.7 ns resolution using TOF information. The acceptance for cosmic-ray tracks was determined by TOF which has a smaller polar angle acceptance than CDC.

We accumulated a sample of  $5 \times 10^7$  cosmic-ray tracks. After requiring tracks to go through the interaction region ( $-2.0 \text{ cm} \leq dz \leq 3.0 \text{ cm}$  and  $|dr| \leq 2 \text{ cm}$ ), 56,743 events remain, where  $dr$  is the closest distance in the  $r$ - $\phi$  plane and  $dz$  is the closest distance in the  $z$  coordinate.

Extensive works on the optimization of the drift-time vs. distance function were carried out by minimizing residual distributions for the function iteratively. Separate functions were used for each layer and each incident angle of the track with respect to the radial direction. A correction for the signal propagation time along the wire was applied after the first 3-D track reconstruction. Corrections were also made for the effects of wire sag and distortions of the end-plates caused by the wire tension by using the measured data. The relative alignment of the cathode and inner end-plates with respect to the main end-plates was determined using cosmic-ray data. The rotations and transla-

tions thus acquired were found to be less than  $200 \mu\text{m}$ , consistent with the estimated construction accuracy.

Fig. 30 shows the  $z$  dependence of  $B_z$ , the axial component of the magnetic field, measured before the installation of CDC. The non-uniformity of the magnetic field is as large as 4% along the central axis. The Kalman filtering method [41] was used to correct the effects due to the non-uniformity of the measured magnetic field. Fig. 31 shows the spatial resolution as a function

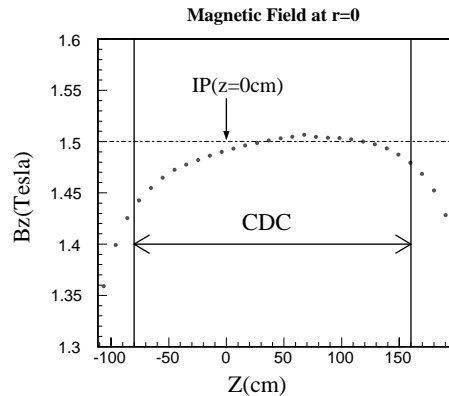


Fig. 30. Measured axial component of the magnetic field produced by the Belle solenoid. The nominal value of the magnetic field inside CDC is 1.5 T. The difference between the minimum and maximum values along the central axis is about 4%.

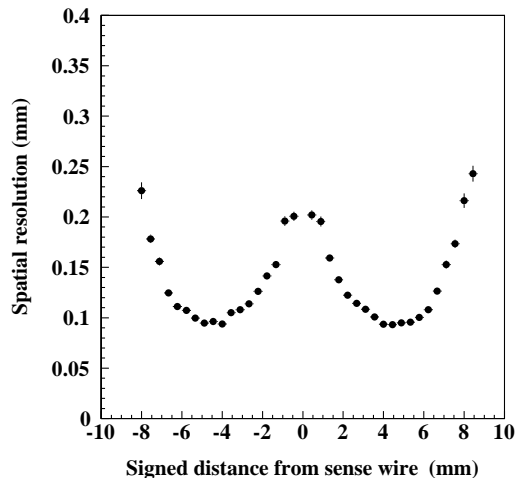


Fig. 31. Spatial resolution as a function of the drift distance.

of the drift distance. Near the sense wire and near the cell boundary the spatial resolution is significantly poorer. The spatial resolution for tracks passing near the middle of the drift space is approximately 100  $\mu\text{m}$ .

The  $p_t$  resolution as a function of  $p_t$  is shown in Fig. 32. The solid curve indicates the result fitted to the data points, i.e.  $(0.201 \pm 0.003)p_t \oplus (0.290 \pm 0.006)/\beta$  in % ( $p_t$  in GeV/c). The dashed curve shows the ideal expectation for  $\beta = 1$  particles, i.e.  $(0.188p_t \oplus 0.195)$  in %. No apparent systematic effects due to the particle charge were observed.

### 5.3.2. Cathode strip detector

The performance test was carried out using cosmic-rays before the CDC was installed into the Belle detector. Data were taken with a simple trigger system with scintillation counters located in the inner cylinder to select cosmic-rays that passed through the beam pipe area inside CDC. Without any special optimization, the anode wire data provide an extrapolation resolution of 160  $\mu\text{m}$  in the  $r$ - $\phi$  plane and 3.6 mm in the  $z$  direction to the CDC cathode part. Anode-wire tracks were used to estimate the detection efficiency of the cathode readout.

The charge distribution on the cathode strips depends on the anode-cathode gap and the spread

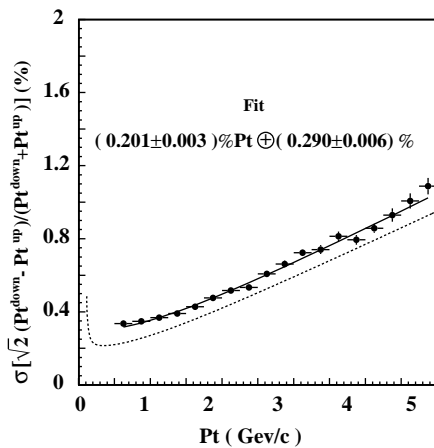


Fig. 32.  $p_t$  dependence of  $p_t$  resolution for cosmic-rays. The solid curve shows the fitted result  $(0.201\% p_t \oplus 0.290\%/\beta)$  and the dotted curve  $(0.118\% p_t \oplus 0.195\%)$  shows the ideal expectation for  $\beta = 1$  particles.

of the avalanche at the anode. When an incoming particle is inclined with respect to the normal incidence, the electron avalanche is spread along the anode wire, making the induced charge distribution broader. This effect was made minimal owing to the gate expansion and the limitation of the charge integration time to 150 ns.

Consecutive cathode hits are recognized as a “cluster”. At least three strips are required to form a cluster. If two local charge maxima are separated more than three strips, they are regarded as separate clusters. The matching of a track to a cathode-hit cluster is done by requiring that the extrapolated  $\phi$  is within the  $\phi_{\min}$  and  $\phi_{\max}$  region covered by the cathode strip hits and that the extrapolated  $z$  is within the  $z$  region covered by the strip hits. Fig. 33 shows the cathode efficiency as a function of incident angle for  $V_{\text{th}} = 50$  mV and an anode high voltage at 2.3 kV. The cathode strip efficiency is defined as the ratio of the number of matched tracks to the number of sampled tracks. As the Belle tracking trigger requires at least two hits in the three cathode layers for each track, the trigger efficiency by the cathode strips is better than 99%, even for the worst case of the incident angle of  $90^\circ$  where the cathode charge is smallest due to gas gain saturation.

The spatial resolution of the cathode readout was obtained with the self-tracking method in the  $z$

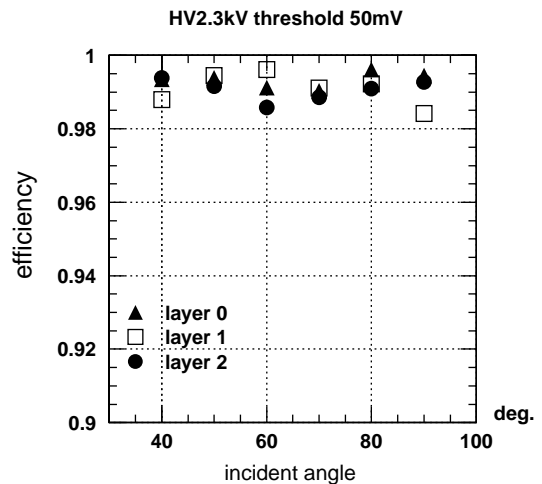


Fig. 33. Angular dependence of the cathode detection efficiency.

direction using cathode data alone. Fig. 34 shows measured results of the intrinsic cathode resolution as a function of incident angle. The data for the three layers are consistent. The data measured in a beam test using a prototype detector is also shown [4].

To evaluate the improvement in the three-dimensional tracking provided by the cathode data, each cosmic-ray track that passed through the entire CDC was treated as two separate tracks (*up* and *down*) going outwards from the beam pipe area. The tracking performance was evaluated by

checking the mismatch of these two track segments,  $\Delta z = z_{\text{up}} - z_{\text{down}}$ , at the closest approach to the beam axis. Figs. 35(a) and (b) show  $\Delta z$  distributions, respectively (a) without and (b) with including the cathode cluster information in three-dimensional tracking with the axial and stereo anode wire information. The  $\Delta z$  resolution was improved from about 3 to 0.64 mm with the cathode data. We note that  $\Delta z$  obtained in the present analysis is equivalent to  $\sqrt{2}$  times of the track extrapolation resolution of CDC to the interaction point.

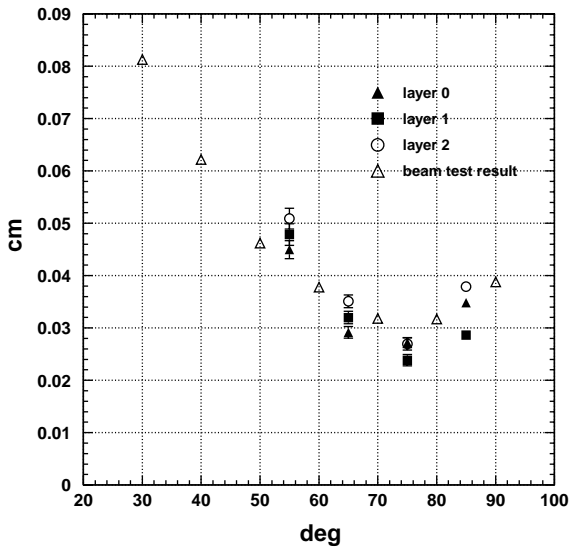


Fig. 34. Angular dependence of the cathode resolution.

#### 5.4. Performance

The Belle experiment has been taking data at the  $\Upsilon(4S)$  resonance energy since June 1999. In order to operate CDC in the high-beam-background environment, we readjusted high voltages and electronics parameters such as the bias voltage of the preamplifiers. These changes reduce cross-talk noise hits caused by the very large signals due to background particles spiraling around sense wires. These changes also reduced the preamplifier gains and slowed their response times. The calibration constants were recalculated using the beam data. In addition, corrections for the additional magnetic field non-uniformity caused by the accelerator magnet components near the interaction region were introduced into the Kalman filter using a magnetic field map data measured with these magnets in place. We again obtained 130  $\mu\text{m}$

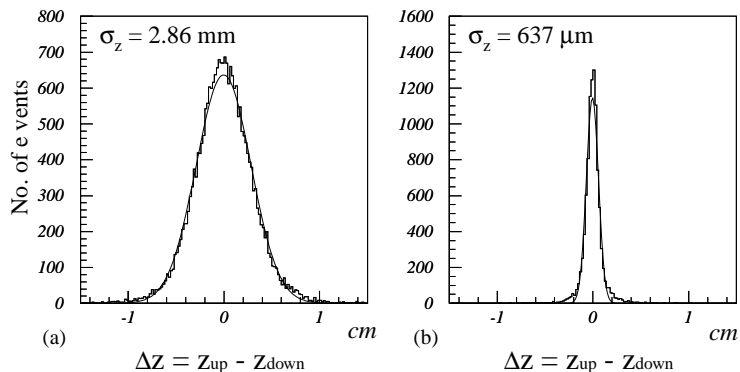


Fig. 35. The effect of the cathode readout information on  $\Delta z = z_{\text{up}} - z_{\text{down}}$  for cosmic-ray tracks: (a) without and (b) with the use of the cathode information in tracking, respectively.

overall spatial resolution, although the residual distribution has considerable non-Gaussian tails.

We analyzed  $e^+e^- \rightarrow \mu^+\mu^-$  events, detected as two charged tracks by CDC and identified as muons by the outer detectors, to extract the  $p_t$  resolution of CDC. We can calculate the  $p_t$  resolution using the fact that each muon track has the same momentum in the cm system. The  $p_t$  resolution measured is  $1.64 \pm 0.04\%$  in the  $p_t$  range from 4 to 5.2 GeV/c, which is imposed by kinematics and the acceptance of the TOF system used for triggering. This result is somewhat worse than the resolution of 1.38% expected from Monte Carlo simulations.

The  $\phi$  dependence of the  $\Delta p_t$  resolution has been checked with  $e^+e^- \rightarrow \mu^+\mu^-$  events. No significant  $\phi$ -dependent systematic effects were observed.

The  $K_S^0$  mass was reconstructed from  $K_S^0 \rightarrow \pi^+\pi^-$  decays in hadronic events in order to check the  $p_t$  resolution at low momenta. Most of the decay pions have momenta below 1 GeV/c as shown in Fig. 36. Fig. 37 shows a  $\pi^+\pi^-$  invariant mass distribution. The FWHM of the distribution is  $7.7 \text{ MeV}/c^2$ , which is slightly worse than the idealized Monte Carlo prediction of  $6.9 \text{ MeV}/c^2$ .

The truncated-mean method was employed to estimate the most probable energy loss. The largest

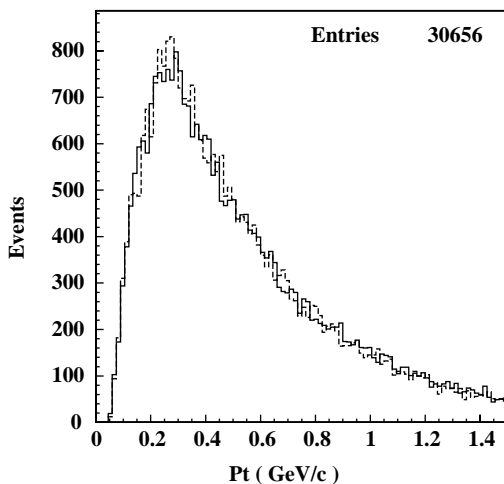


Fig. 36. Transverse momentum distributions for pions from  $K_S^0$  decays. The solid and dashed histograms correspond to  $\pi^-$  and  $\pi^+$  tracks, respectively.

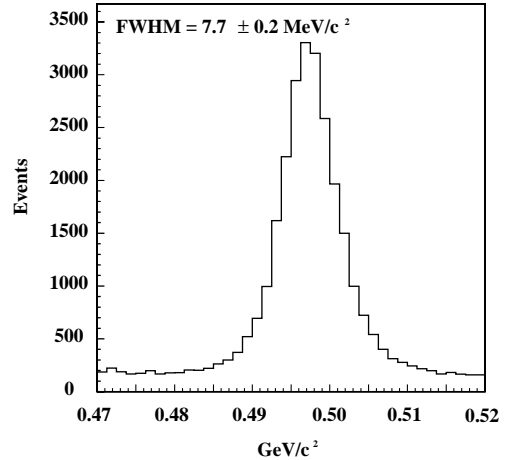


Fig. 37. Inclusive  $K_S^0 \rightarrow \pi^+\pi^-$  mass distribution for multi-hadronic events.

20% of measured  $dE/dx$  values for each track were discarded and the remaining data were averaged in order to minimize occasional large fluctuations in the Landau tail of the  $dE/dx$  distribution. As described in section of the beam test [36], the  $\langle dE/dx \rangle$  thus obtained is expected to give a resolution of 5%. A scatter plot of measured  $\langle dE/dx \rangle$  and particle momentum is shown in Fig. 38, together with the expected mean energy losses for different particle species. Populations of pions, kaons, protons, and electrons can be clearly seen. The normalized  $\langle dE/dx \rangle$  distribution for minimum ionizing pions from  $K_S^0$  decays is shown in Fig. 39. The  $\langle dE/dx \rangle$  resolution was measured to be 7.8% in the momentum range from 0.4 to 0.6 GeV/c, while the resolution for Bhabha and  $\mu$ -pair events was about 6%. These results are somewhat worse than the Monte Carlo results.

At present the resolutions obtained from the beam data seem to be slightly worse than those expected from the cosmic-ray data and Monte Carlo simulations. Although the present performance level of CDC provides the momentum resolution sufficient for the goals of the Belle experiment, efforts to further improve CDC performance are being made.

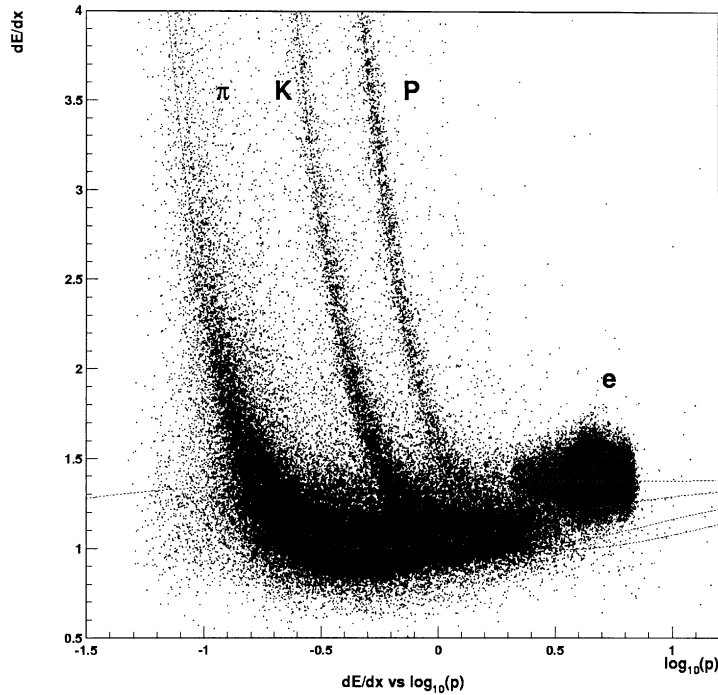


Fig. 38. Truncated mean of  $dE/dx$  vs. momentum observed in collision data.

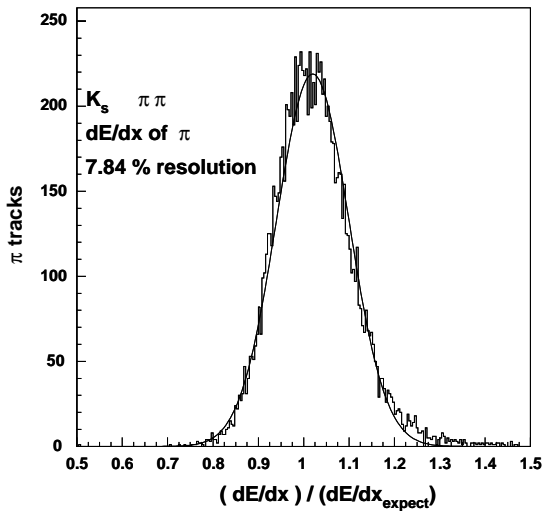


Fig. 39. Distribution of  $\langle dE/dx \rangle / \langle dE/dx \rangle_{\text{exp}}$  for pions from  $K_S^0$  decays.

## 6. Aerogel Cherenkov counter system, ACC

Particle identification, specifically the ability to distinguish  $\pi^\pm$  from  $K^\pm$ , plays a key role in the

elucidation of CP violation in the B system. An array of silica aerogel threshold Cherenkov counters has been selected as part of the Belle particle identification system to extend the momentum coverage beyond the reach of  $dE/dx$  measurements by CDC and time-of-flight measurements by TOF [4,6].

### 6.1. Detector design

The configuration of the silica aerogel Cherenkov counter system, ACC, in the central part of the Belle detector is shown in Fig. 40 [42,43]. ACC consists of 960 counter modules segmented into 60 cells in the  $\phi$  direction for the barrel part and 228 modules arranged in 5 concentric layers for the forward end-cap part of the detector. All the counters are arranged in a semi-tower geometry, pointing to the interaction point. In order to obtain good pion/kaon separation for the whole kinematical range, the refractive indices of aerogels are selected to be between 1.01 and 1.03, depending on their polar angle region. A typical

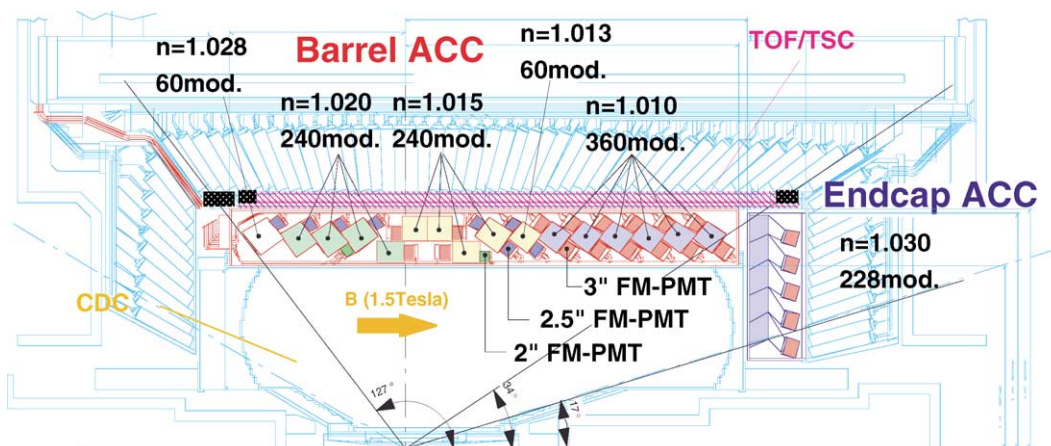


Fig. 40. The arrangement of ACC at the central part of the Belle detector.

single ACC module is shown in Figs. 41(a) and (b) for the barrel and the end-cap ACC, respectively. Five aerogel tiles are stacked in a thin (0.2 mm thick) aluminum box of approximate dimensions  $12 \times 12 \times 12 \text{ cm}^3$ . In order to detect Cherenkov lights effectively, one or two fine mesh-type photomultiplier tubes (FM-PMTs), which are operated in a magnetic field of 1.5 T [44], are attached directly to the aerogels at the sides of the box. We use PMTs of three different diameters: 3 in. (R6683), 2.5 in. (R6682), and 2 in. (R6681) of Hamamatsu Photonics, depending on refractive indices, in order to get uniform response for light velocity particles.

#### 6.1.1. Production of hydrophobic silica aerogels

Since aerogels having the required low refractive indices were not commercially available, we decided to produce aerogels by our own efforts. We adopted a new production method for the preparation of aerogels, in which methylalkoxide oligomer is used as a precursor [45]. This oligomer is hydrolyzed and polymerized in a basic catalyst ( $\text{NH}_4\text{OH}$ ) in a solution of methyl or ethyl alcohol. The average size of aerogels is  $120 \times 120 \times 24 \text{ mm}^3$  and they are formed in aluminum molds coated with a thin PTFE film. The gelation time ranges from a few minutes to 10 min depending on densities.

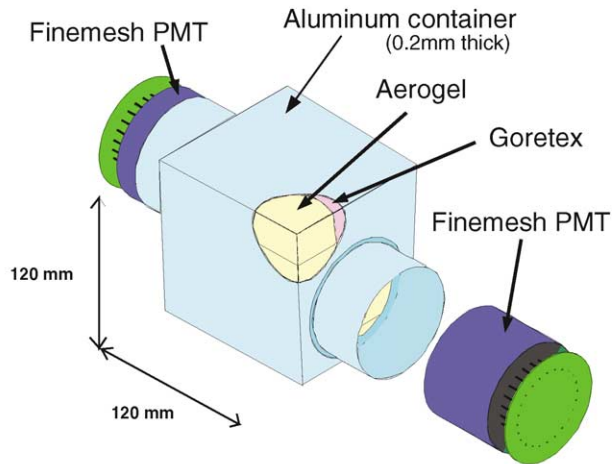
Silica aerogels have been used in several experiments, but their transparencies became worse within a few years of use, which was our great worry to adopt an aerogel Cherenkov counter as a particle identification device. This phenomenon may be attributed to the hydrophilic property of silica aerogels. In order to prevent such effects, we have made our silica aerogels highly hydrophobic by changing the surface hydroxyl groups into trimethylsilyl groups [46]. This modification is applied before the drying process. As a result of this treatment, our silica aerogels remain transparent even 4 yr after they were produced.

After three weeks of aging including the surface modification, the aerogels were dried by a supercritical drying method of  $\text{CO}_2$ . This drying process took 48 h. The volume of extractor is 140  $\ell$  and we could produce about 38  $\ell$  of silica aerogel in one batch. After seven months of operation (two batches/week), we produced about 2  $\text{m}^3$  of silica aerogel. Details of the production method can be found in Refs. [45,47].

#### 6.1.2. Quality of the aerogels

All the aerogel tiles thus produced have been checked for optical transparency, transmittance of unscattered light, refractive index, dimension, etc. Fig. 42 shows typical transmittance curves obtained by a photo-spectrometer for aerogels of

## a) Barrel ACC Module



## b) Endcap ACC Module

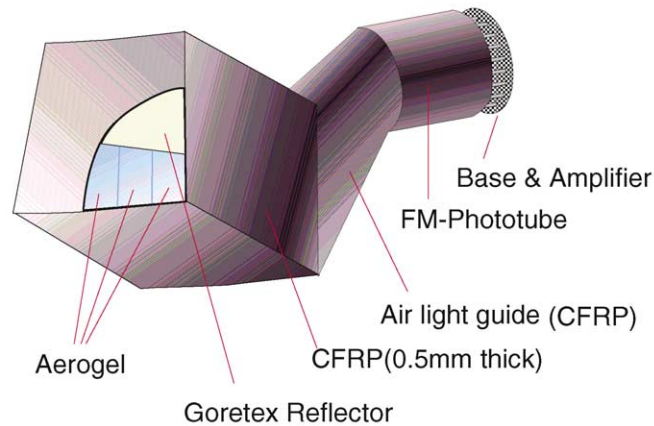


Fig. 41. Schematic drawing of a typical ACC counter module: (a) barrel and (b) end-cap ACC.

four different refractive indices. The  $n = 1.028$  aerogels have better transmittance than the others. Their average transmission length ( $A$ ) at 400 nm is 46 mm, while the others are around 25 mm. Here  $A$  is defined by the function:  $T = T_0 \exp(-d/A)$ , where  $T_0$  and  $T$  are the incident and transmitted light intensities, respectively, and  $d$  is the thickness of an aerogel tile. These aerogels were produced from the alcogel which was prepared by using methyl alcohol as a solution.

The refractive indices are well controlled as  $\Delta n/(n - 1) \sim 3\%$  for all the produced aerogel tiles, which is essentially the same as the measurement error of the refractive index determined by measuring a deflection angle of laser light (He-Ne: 543.5 nm) at a corner of each aerogel tile.

We carried out a test to ensure the radiation hardness of aerogels by placing aerogel samples ( $n = 1.012, 1.018$  and  $1.028$ ) in high-intensity  $\gamma$ -rays from a  $^{60}\text{Co}$  source [48]. Transparencies and

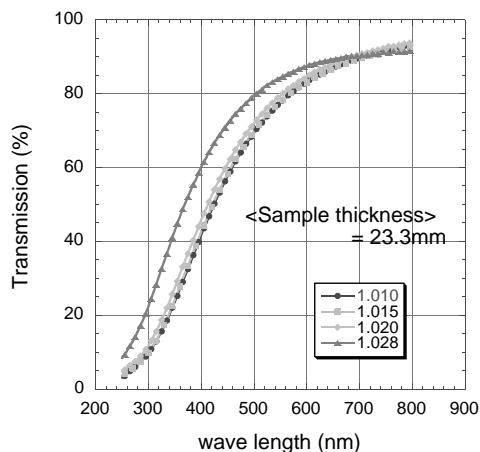


Fig. 42. Light transmittance spectra for silica aerogels (thickness = 23.3 mm) of  $n = 1.01$ , 1.015, 1.02 and 1.028. The silica aerogels of  $n = 1.028$  prepared by using methanol as the preparation solvent shows the best transmittance data.

refractive indices of aerogels were measured up to 9.8 Mrad, which corresponds to more than 10 yrs of running at KEKB. Neither deterioration on the transparency nor change in the refractive indices were observed within the errors of measurements after the irradiation. Measurement accuracies were 0.8% for the transparency and  $<0.0006$  for the refractive index. Deterioration in transparency and changes of refractive index after 9.8 Mrad  $\gamma$ -ray irradiation were observed to be less than 1.3% and 0.001 at 90% confidence level, respectively.

### 6.1.3. Fine-mesh photomultiplier tubes

Since ACC is placed in a high magnetic field of 1.5 T in the Belle detector, we decided to use fine-mesh photomultiplier tubes (FM-PMTs) for the detection of Cherenkov lights, taking advantage of its large effective area and high gain [44]. Other candidate photo-sensors such as microchannel-plate photomultiplier tubes (MCP-PMT) and hybrid photodiodes (HPD) were still at R&D stages or extremely expensive when this decision was made. The FM-PMTs were produced by Hamamatsu Photonics [49].

A sectional view of an FM-PMT is shown in Fig. 43. Each FM-PMT has a borosilicate glass window, a bialkali photo-cathode, 19 fine-mesh dynodes, and an anode. Three types of FM-PMTs

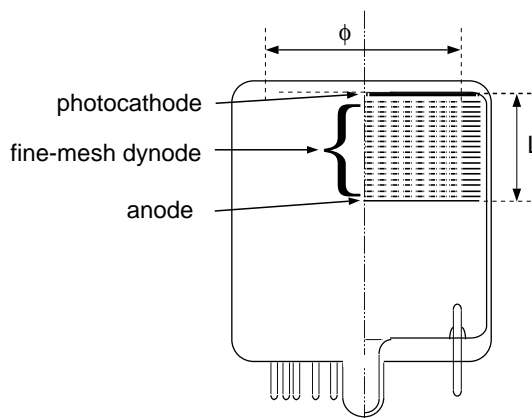


Fig. 43. Sectional view of FM-PMT.

of 2, 2.5, and 3 in. in diameter are used in ACC. The effective diameters ( $\phi$ ) of these FM-PMTs are 39, 51, and 64 mm. The cathode-to-anode distance ( $L$ ) is about 20 mm. The average quantum efficiency of the photo-cathode is 25% at 400 nm wavelength. The optical opening of the mesh is about 50%.

The FM-PMTs with 19 dynode stages of fine mesh have high gain ( $\sim 10^8$ ) with moderate HV values ( $<2500$  V). The gain of FM-PMT decreases as a function of field strength as shown in Fig. 44. The gain reduction is  $\sim 10^{-3}$  for FM-PMTs placed parallel to the direction of magnetic field and slightly recovers when they are tilted. The FM-PMTs used for ACC were produced with dynodes with a finer mesh spacing than conventional products at that time, to give approximately 10 times higher gain as shown in Fig. 44.

Effects of a magnetic field on the pulse-height resolution have been evaluated by tracing the change of a quantity  $N_{\text{eff}}$ , which is defined as  $N_{\text{eff}} = (\mu/\sigma)^2$ , by using the mean ( $\mu$ ) and sigma ( $\sigma$ ) of the recorded ADC spectrum. The quantity  $N_{\text{eff}}$  represents the effective photostatistics for the spectrum, which is a convolution of a single-photoelectron (pe) response of the device and the Poisson statistics with  $N_{\text{pe}}$ , the average number of photoelectrons emitted from the photo-cathode. For FM-PMTs, the ratio  $N_{\text{pe}}/N_{\text{eff}}$  is about 2 at  $B = 0$ . The relatively large excess noise factor is due to the fact that a single-photoelectron

spectrum does not have any characteristic peak [50]. Reduction of  $N_{\text{eff}}$  in a magnetic field has been measured for 2, 2.5 and 3 in. FM-PMTs, with  $N_{\text{eff}}$  at  $B = 0$  ( $N_{\text{eff}}^0$ ) of about 20. Table 5 shows the ratio  $N_{\text{eff}}/N_{\text{eff}}^0$  at  $B = 1.5$  T for two ranges of

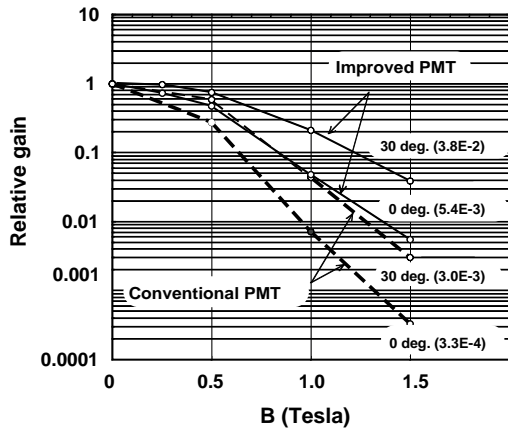


Fig. 44. Relative gains of conventional and improved FM-PMTs in magnetic fields. The tubes were placed parallel ( $0^\circ$ ) or tilted by  $30^\circ$  with respect to the field direction.

Table 5  
Measured ratio  $N_{\text{eff}}/N_{\text{eff}}^0$  at  $B = 1.5$  T. The number of tested samples for each condition is shown in parentheses

PMT diam. (in.)	2000–2200 V		2600–2800 V	
	$\theta = 0^\circ$	$\theta = 30^\circ$	$\theta = 0^\circ$	$\theta = 30^\circ$
2	0.74 (7)	0.64 (10)	0.75 (10)	0.73 (10)
2.5	0.80 (5)	0.73 (5)	0.85 (8)	0.85 (8)
3	0.79 (2)	0.77 (4)	0.87 (6)	0.99 (7)

applied HVs. As the field  $B$  increases, the resolution deteriorates and the quantity  $N_{\text{eff}}$  decreases. The decrease in  $N_{\text{eff}}$  is larger when the field is at a large angle such as  $30^\circ$  than the case of  $\theta = 0^\circ$ , and the decrease in  $N_{\text{eff}}$  at a large angle is more significant for smaller FM-PMTs. However, it is noticed that, in a magnetic field, the resolution improves, namely the quantity  $N_{\text{eff}}$  increases, by applying higher voltage, while no significant change is found in absence of the field.

### 6.2. ACC readout electronics

Signals from the FMPMTs are processed using the signal chain shown in Fig. 45. The system comprises three main elements: (i) low-noise preamplifiers mounted directly on the FMPMT bases, (ii) specially designed charge-to-time converter boards, and (iii) LeCroy Model 1877 pipeline TDCs. The time-to-converter approach makes efficient use of the data acquisition system by combining both pulse height and timing information into a single channel. Moreover, the pipelined nature of the TDC eliminates the need for the bulky delay cables found in traditional gated-integrator data acquisition schemes.

#### 6.2.1. Preamplifier base assemblies

The preamplifier base assemblies consist of resistive dividers formed using surface mount resistors attached to a printed circuit boards soldered directly to the wire leads of the PMTs. The total string resistance was chosen to be fairly high ( $\sim 25 \text{ M}\Omega$ ) so as to keep the power

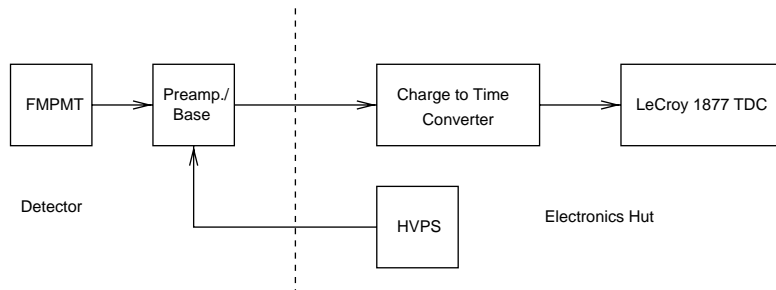


Fig. 45. System-level block diagram of the ACC readout electronics.



is followed by a filter circuit which eliminates high-frequency noise.

The output of the filter amp is routed through a lumped delay line ( $t_d = 50$  ns) to the input of the LeCroy MQT301 charge-to-time integrated circuit. The MQT301 monolithic is the heart of the circuit and performs the actual charge-to-time conversion.

The output signal from the filter amp is routed to a second amplifier and then on to a discriminator circuit based on the Analog Devices AD96687 ECL comparator. This output from this discriminator is ultimately used to gate the internal integrator in the MQT301 chip. The additional gain stage in front of the AD96687 ensures that the circuit will be sensitive to the smallest signals of interest. (Signals too small to fire the discriminator are obviously ignored, even if they result in a measurable charge at the MQT301 input.) A pair of ECL flip-flops, a second AD96687 channel, and a collection of ECL AND gates are used to implement logic circuitry that sets the MQT gate width and guards against fault conditions caused by input pileup.

Each of the 26 channels on a QTC board has three independent adjustments: (i) a VGA gain setting, (ii) a discriminator threshold setting, and (iii) an MQT301 gate-width adjustment. These settings are controlled using MAXIM MAX529 octal serial DACs. The serial DACs are set remotely from a computer using a simple serial interface.

### 6.2.3. Monitoring system

A monitoring system for ACC has been designed and constructed [51]. It consists of blue LEDs, a diffuser box, and optical distributors. The monitoring system is required to supply roughly the same light intensity as that of Cherenkov lights generated by light velocity particles in each ACC module, i.e. approximately 18 photoelectrons. The monitoring light intensity should be stable ( $\sim 95\%$ ) in terms of aging and temperature variation to measure possible drifts of PMT gains and light yields of aerogels in a long period and those due to temperature changes.

The employed LED light source has been observed to have the long-term stability of

$98.0 \pm 0.4\%$ . The measured temperature coefficient of the LED is  $(-0.003 \pm 0.035)\%/^{\circ}\text{C}$  over a temperature range of  $5\text{--}70^{\circ}\text{C}$ . The uniformity of light intensity of the monitoring system has been measured to be  $94.20 \pm 0.09\%$ . The overall performance on uniformity and intensity of the light output has been found to satisfy all the requirements for the ACC monitoring system.

### 6.2.4. Monte Carlo simulation

In order to understand the performance of ACC, a Monte Carlo program [52] has been developed to simulate the behavior of Cherenkov photons in the aerogel as realistically as possible. The program consists of two parts: photon transportation inside aerogel tiles and one-dimensional amplification in an FM-PMT. All the conceivable effects are taken into account as functions of wavelength. The only unknown factor is the absorption in the aerogel, which is treated as a free parameter and later determined by comparing simulation results with the test beam data.

A Cherenkov photon is transported inside the aerogel radiator according to the photon-transport algorithm developed in the present simulation. The program simulates the output photoelectron yields as accurately as 5% with only a single parameter. The experimental data of a pulse-height spectrum for single-photoelectron events is well reproduced [50]. The agreement between the simulation and data for the excess noise factor with and without magnetic fields is satisfactory. The incident position dependence of the light yields is also well reproduced by this simulation.

This simulator is implemented in a Belle standard detector simulator based on the GEANT 3. Good performance of pion/kaon separation by ACC has been demonstrated successfully.

## 6.3. Performance of ACC

The performance of prototype ACC modules has been tested using the  $\pi 2$  beam line at KEK PS. Typical pulse-height distributions for 3.5 GeV/c pions and protons measured by an aerogel counter, with  $n = 1.015$  and read by two 2.5 in. FM-PMTs, are shown in Figs. 47(a) and (b), with and without a magnetic field of 1.5 T, respectively.

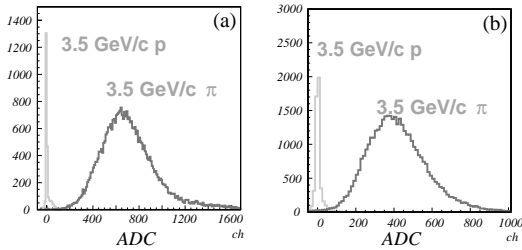


Fig. 47. Pulse-height spectra for 3.5 GeV/c pions (above threshold) and protons (below threshold) obtained by a single module of ACC in (a) non-magnetic field and (b) a magnetic field of 1.5 T. Silica aerogels with  $n = 1.015$  were stacked to form the module.

The number of photoelectrons ( $N_{pe}$ ) for 3.5 GeV/c negative pions is measured to be 20.3. In the case of Fig. 47(b), we used a preamplifier and applied a higher HV to get almost the same gain as that without a magnetic field. Pions and protons are clearly separated by more than  $3\sigma$ . It was found that cracks in the aerogel do not make a difference in the light yield.

After ACC was installed into the Belle detector in December 1998, the initial calibration of the detector was carried out using cosmic-rays. The Belle detector has been rolled into the interaction point and commissioned with  $e^+e^-$  beams since May 1999.

Fig. 48 shows the measured pulse-height distribution for the barrel ACC for  $e^\pm$  tracks in Bhabha events and also  $K^\pm$  candidates in hadronic events, which are selected by TOF and  $dE/dx$  measurements [53]. The figure demonstrates a clear separation between high-energy electrons and below-threshold particles. It also indicates good agreement between the data and Monte Carlo simulations [52].

A careful calibration for the pulse height of each FM-PMT signal has been performed with  $\mu$ -pair events. Figs. 49(a) and (b) show the average number of photoelectrons  $\langle N_{pe} \rangle$  for each counter row in the barrel ACC and each layer of the end-cap ACC, respectively. In the barrel ACC each row has on average 60 boxes and the row number is given from left to right in Fig. 40. The layer number of the end-cap ACC is given from the inner to the outer side. The light yield for the  $\mu$

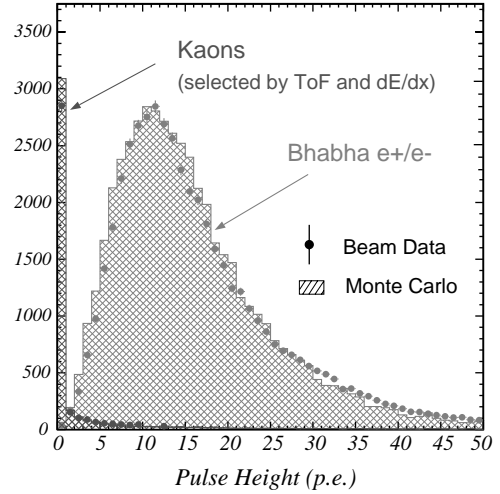


Fig. 48. Pulse-height spectra in units of photoelectrons observed by barrel ACC for electrons and kaons. Kaon candidates were obtained by  $dE/dx$  and TOF measurements. The Monte Carlo expectations are superimposed.

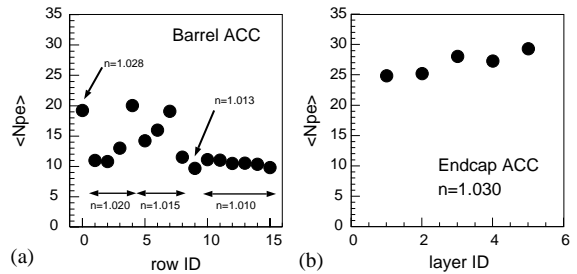


Fig. 49. Average number of photoelectrons  $\langle N_{pe} \rangle$  for (a) each counter row in barrel ACC and (b) each layer in end-cap ACC.

tracks depends on the refractive index of aerogel radiators, size and number of FM-PMTs attached on the counter module, and geometry of the counter module box. The light yield ranges from 10 to 20 for the barrel ACC and from 25 to 30 for the end-cap ACC, high enough to provide useful  $\pi/K$  separation.

#### 6.4. Particle identification of electrons and charged kaons, EID and KID

In the analyses of physics data of Belle, EID and KID are performed by using data samples measured with CDC, ACC, TOF, and ECL.

### 6.4.1. EID and fake rate

Electrons are identified by using the following discriminants:

- the ratio of energy deposited in ECL and charged track momentum measured by CDC,
- transverse shower shape at ECL,
- the matching between a cluster at ECL and charged track position extrapolated to ECL,
- $dE/dx$  measured by CDC,
- light yield in ACC, and
- time-of-flight measured by TOF.

We made probability density functions (PDF) for the discriminants beforehand. Based on each PDF, likelihood probabilities are calculated with track-by-track basis, and unified into a final likelihood output. This likelihood calculation is carried out taking into account the momentum and angular dependence. Fig. 50 shows the output from the above procedure. Closer to unity the particle is more likely to be an electron. The solid

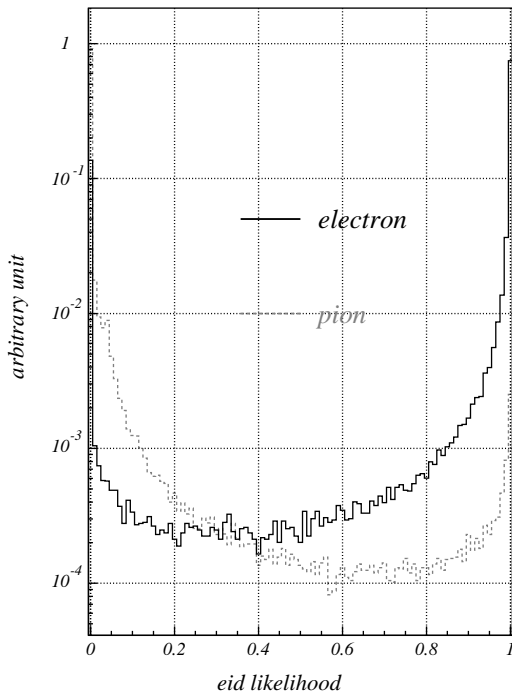


Fig. 50. The distribution of final unified discriminant to identify electrons. The solid histogram is for electrons in  $e^+e^- \rightarrow e^+e^-e^+e^-$  events and the dashed one for charged pions.

(dashed) histogram shows for  $e^\pm$  in  $e^+e^- \rightarrow e^+e^-e^+e^-$  data ( $\pi^\pm$  in  $K_S \rightarrow \pi^+\pi^-$  decays in data). The clear separation can be seen.

The efficiency and fake rate are displayed in Fig. 51 using electrons in real  $e^+e^- \rightarrow e^+e^-e^+e^-$  events for the efficiency measurement, and  $K_S \rightarrow \pi^+\pi^-$  decays in real data for the fake rate evaluation. For momentum greater than 1 GeV/c, the electron identification efficiency is maintained to be above 90% while the fake rate to be around 0.2–0.3%.

### 6.4.2. KID and pion fake rate

The K/ $\pi$  identification is carried out by combining information from three nearly independent measurements:

- $dE/dx$  measurement by the CDC,
- TOF measurement, and
- measurement of the number of photoelectrons ( $N_{pe}$ ) in the ACC.

As in the case of EID, the likelihood function for each measurement was calculated and the product of the three likelihood functions yields the

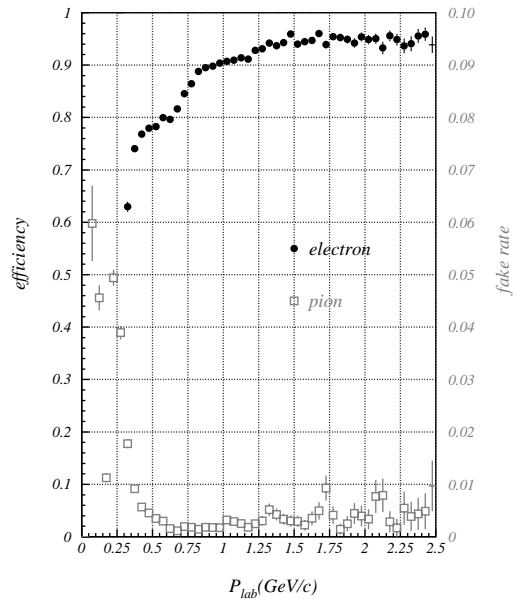


Fig. 51. Electron identification efficiency (circles) and fake rate for charged pions (squares). Note the different scales for the efficiency and fake rate.

overall likelihood probability for being a kaon or a pion,  $P_K$  or  $P_\pi$ .

A particle is then identified as a kaon or a pion by cutting on the likelihood ratio (PID):

$$\text{PID}(K) = \frac{P_K}{P_K + P_\pi} \quad (1)$$

$$\text{PID}(\pi) = 1 - \text{PID}(K). \quad (2)$$

The validity of the  $K/\pi$  identification has been demonstrated using the charm decay,  $D^{*+} \rightarrow D^0 \pi^+$ , followed by  $D^0 \rightarrow K^- \pi^+$ . The characteristic slow  $\pi^+$  from the  $D^{*+}$  decay allows these decays to be selected with a good  $S/N$  ratio (better than 30), without relying on particle identification. Therefore, the detector performance can be directly probed with the daughter  $K$  and  $\pi$  mesons from the  $D$  decay, which can be tagged by their relative charge with respect to the slow pion. Fig. 52 shows two-dimensional plots of the likelihood ratio  $\text{PID}(K)$  and measured momenta for the kaon and pion tracks. The figure demonstrates the clear separation of kaons and pions up to around  $4 \text{ GeV}/c$ . The measured  $K$  efficiency and  $\pi$  fake rate in the barrel region are plotted as

functions of the track momentum from  $0.5$  to  $4.0 \text{ GeV}/c$  in Fig. 53. The likelihood ratio cut,  $\text{PID}(K) \geq 0.6$ , is applied in this figure. For most of

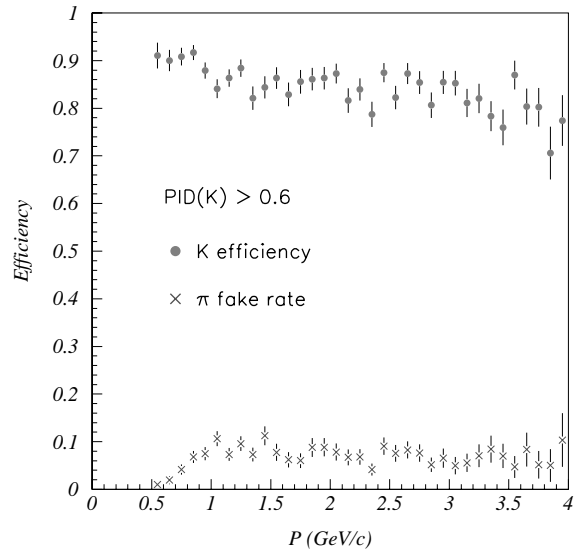


Fig. 53.  $K$  efficiency and  $\pi$  fake rate, measured with  $D^{*+} \rightarrow D^0(K\pi) + \pi^+$  decays, for the barrel region. The likelihood ratio cut  $\text{PID}(K) \geq 0.6$  is applied.

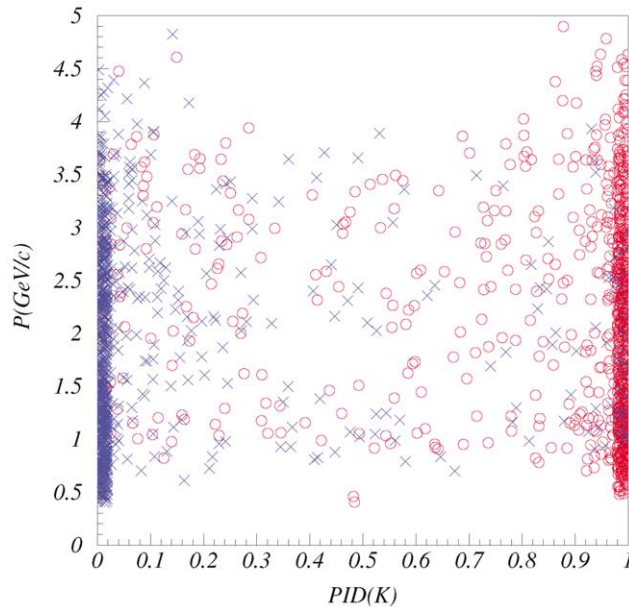


Fig. 52. Likelihood ratio  $\text{PID}(K)$ , versus momenta for daughter tracks from  $D^0 \rightarrow K^- \pi^+$  decays, tagged by the charge of the slow  $\pi^+$ 's. The open circles correspond to kaons and the cross-points to pions.

the region, the measured K efficiency exceeds 80%, while the  $\pi$  fake rate is kept below 10%.

### 7. Time-of-flight counters (TOF)

A time-of-flight (TOF) detector system using plastic scintillation counters is very powerful for particle identification in  $e^+e^-$  collider detectors. For a 1.2 m flight path, the TOF system with 100 ps time resolution is effective for particle momenta below about 1.2 GeV/c, which encompasses 90% of the particles produced in  $\Upsilon(4S)$  decays. It can provide clean and efficient b-flavor tagging.

In addition to particle identification, the TOF counters provide fast timing signals for the trigger system to generate gate signals for ADCs and stop signals for TDCs. To avoid pile-up in the trigger queue, the rate of the TOF trigger signals must be kept below 70 kHz. The gate and stop timing for the CsI calorimeter and CDC sets a time jitter requirement of less than  $\pm 10$  ns. Simulation studies indicate that to keep the fast trigger rate below 70 kHz in any beam background conditions, the TOF counters should be augmented by thin trigger scintillation counters (TSC) [4,6].

#### 7.1. Design and construction of TOF

To achieve the design goal of 100 ps, the following design strategies have been adopted:

- use of fast scintillator with an attenuation length longer than 2 m,

- elimination of light guides to minimize the time dispersion of scintillation photons propagating in the counter, and
- use of photo-tubes with large-area photocathodes to maximize photon collection.

These considerations led us to a configuration with fine-mesh-dynode photomultiplier tubes (FM-PMT) [54] mounted directly on the TOF and TSC scintillation counters and placed in a magnetic field of 1.5 T.

The TOF system consists of 128 TOF counters and 64 TSC counters. Two trapezoidally shaped TOF counters and one TSC counter, with a 1.5-cm intervening radial gap, form one module. In total 64 TOF/TSC modules located at a radius of 1.2 m from the interaction point cover a polar angle range from  $34^\circ$  to  $120^\circ$ . The minimum transverse momentum to reach the TOF counters is about 0.28 GeV/c. Module dimensions are given in Fig. 54. These modules are individually mounted on the inner wall of the barrel ECL container. The 1.5 cm gap between the TOF counters and TSC counters was introduced to isolate TOF from photon conversion backgrounds by taking the coincidence between the TOF and TSC counters. Electrons and positrons created in the TSC layer are impeded from reaching the TOF counters due to this gap in a 1.5 T field [55]. Table 6 provides parameters for the TOF and TSC counters. The width of the TOF counter is approximately 6 cm.

A Monte Carlo study with a full detector simulation including the effects of the material of

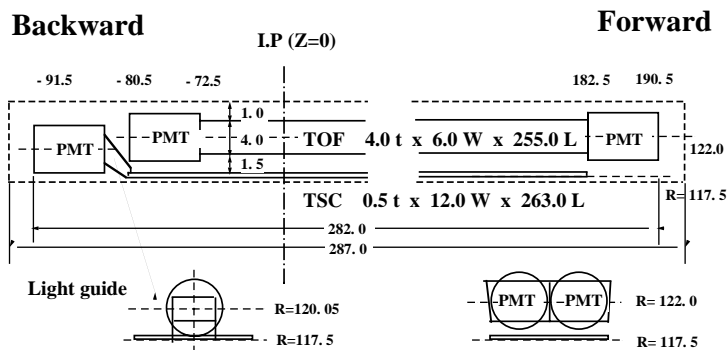


Fig. 54. Dimensions of a TOF/TSC module.

Table 6

Parameters of the TOF and TSC counters. Scintillator materials are Bicron BC408 for TOF and Bicron BC412 for TSC

Counter	Thickness (cm)	$z$ coverage (cm)	$r$ (cm)	$\phi$ segm.	No. of PMTs
TOF	4.0	-72.5 to +182.5	122.0	128	2
TSC	0.5	-80.5 to +182.5	117.5	64	1

the barrel ACC and back-splash from the barrel ECL indicates that the clean hit probability is about 90% for particles from  $\bar{B}\bar{B}$  events in the 128-segmented barrel TOF solid angle.

### 7.1.1. FM-PMTs

Hamamatsu (HPK) type R6680 fine-mesh photomultipliers, with a 2-in. diameter and 24 stages of 2000 mesh/inch dynodes, have been selected for the TOF counter. The 24 dynode stages provide a gain of  $3 \times 10^6$  at a high voltage below 2800 V in a magnetic field of 1.5 T. The bi-alkali photo-cathode with an effective diameter of 39 mm covers 50% of the end area of each TOF counter. The transit time spread is 320 ps (RMS), the rise and fall times are 3.5 and 4.5 ns, respectively, and the pulse width is about 6 ns at FWHM. Figs. 55(a) and (b) show gains and time resolutions of eight typical FM-PMTs as a function of magnetic field strength. The measurements were performed with the field parallel to the tube axis, using an N2-dye laser of 420 nm wavelength. Although the gain was reduced by a factor of about 200 at 1.5 T, the time resolution was not significantly affected. Degradation of the time resolution of about 10% to 15% was observed when the magnetic field was raised from 0 to 1.5 T. All FM-PMTs were tested for their gains and time resolutions before the final module assembly.

FM-PMTs were attached to the TOF counter ends with an air gap of  $\sim 0.1$  mm. In the case of the TSC counters the tubes were glued to the light guides at the backward ends. The air gap for the TOF counter selectively passes earlier arrival photons and reduces a gain saturation effect of FM-PMT due to large pulses at a very high rate. As the time resolution is determined by the rising edge of the time profile of

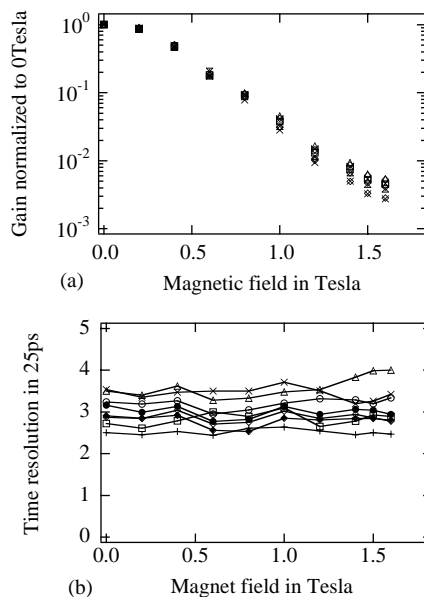


Fig. 55. 1.5 T field test of FM-PMTs. (a) Gains and (b) time resolutions as a function of magnetic field.

arrival photons at PMT, the air gap hardly affects the time resolution.

### 7.1.2. Scintillators

The TOF and TSC scintillators (BC408, Bicron) were wrapped with one layer of 45  $\mu$ m thick polyvinyl film (Tedlar) for light tightness and surface protection. This thin wrapping minimizes the dead space between adjacent TOF counters. Careful measurements of the physical dimensions of all counters were made to ensure the dimensions of each counter consistent with the TOF assembly tolerance.

The attenuation length and light yield of all of the TOF scintillators were measured using a cosmic-ray test stand. A lucite Cherenkov counter was used to suppress low-momentum cosmic-rays.

Fig. 56(a) shows the result of attenuation length measurements for some of TOF scintillators. The attenuation length was evaluated by using a ratio of signal charges and a time difference between two PMTs of a TOF counter. The measured light propagation velocity was 14.4 cm/ns. The average attenuation length was 3.9 m, which satisfies the specification for the minimum attenuation length of 2.5 m. Fig. 56(b) shows the result of measurements of light yields seen by each PMT for cosmic-rays at the center of a counter.

and then to a multihit TDC for charge measurement. The other generates signals corresponding to two different threshold levels: a high level (HL) and a low level (LL). Two LeCroy MVL107s are used for discriminators, with threshold levels set between 0.3–0.5 mips for HL and 0.05–0.1 mips for LL. The LL output provides the TOF timing and the HL output provides a trigger signal. HL is used to make a self gate for LeCroy MQT300A Q-to-T conversion and also to gate the LL output. A common trigger is prepared for pedestal calibration of MQT300A. The signal T is further processed in a time stretcher for readout by TDC 1877S. The MQT output Q is a timing signal corresponding to the charge, which is directly recorded with TDC 1877S.

7.1.3. Readout electronics

A block diagram of a single channel of the TOF front-end electronics is shown in Fig. 57. Each PMT signal is split into two. One is sent to Q-to-T

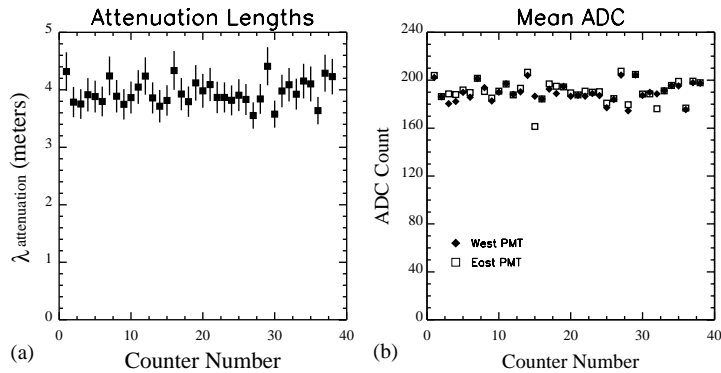


Fig. 56. (a) Attenuation lengths and (b) light yields of 38 TOF scintillators.

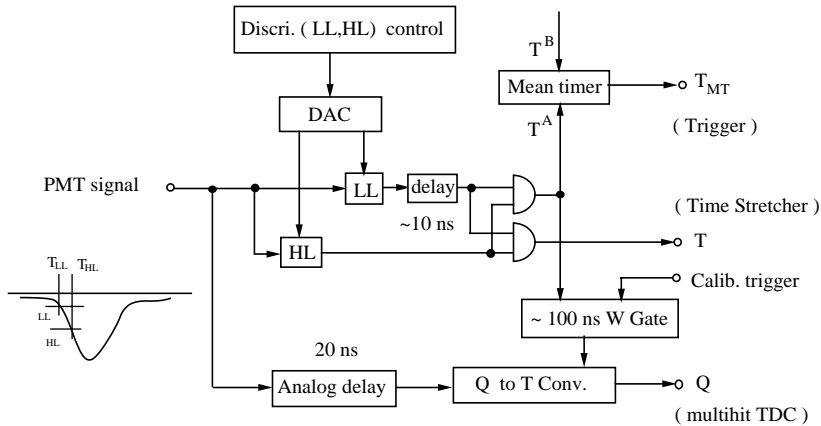


Fig. 57. Block diagram of a single channel of TOF front-end electronics.

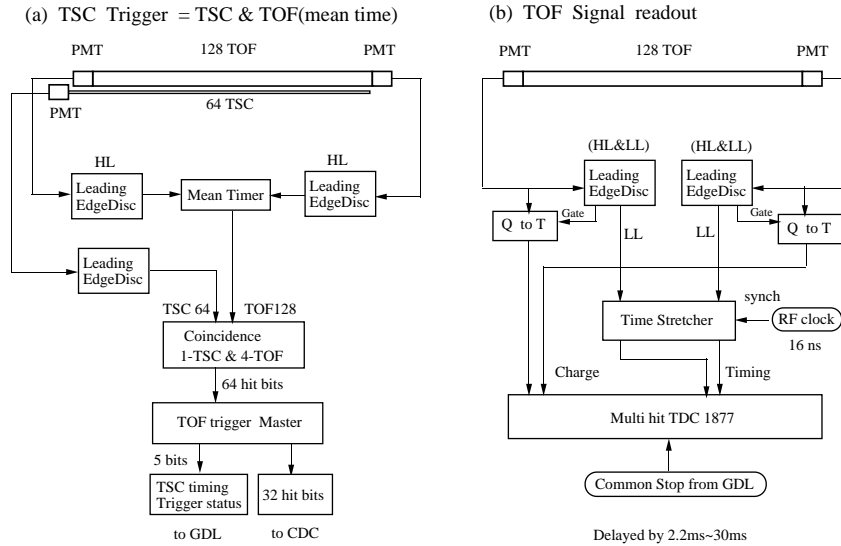


Fig. 58. Block diagrams of the TOF electronics for (a) trigger and (b) readout.

Figs. 58(a) and (b) show block diagrams of the TOF front-end electronics for (a) event trigger and (b) readout of charge and timing of TOF signals. The gated LL signals from two ends of a counter are mean-timed and coincided with the TSC signals to create a fast trigger signal. The nominal coincidence arrangement between one TSC counter and four TOF counters is used to ensure triggers for low-momentum tracks. Fig. 59 shows the TSC trigger rates calculated by a Monte Carlo simulation in various coincidence arrangements with TOF counters as a function of discrimination level in units of mips for Bhabha and spent electrons [56]. The time jitter of the signal is smaller than 3.5 ns in each event, and provides a precise event timing to the Belle trigger system to make TDC-stop to CDC and ADC-gate to CsI readout. The time jitter is reduced to 0.5 ns by applying a correction of the hit position in TOF counters.

The time-stretcher (TS) circuit [57] expands the time difference between the TOF pulse and the reference clock by a factor 20, which enables us to measure the time with a 25 ps precision with the Belle standard 0.5 ns multihit TDC readout scheme. The timing of each TOF signal is

measured relative to an edge of the reference clock. The time interval  $T$  between the TOF signal and the second reference clock edge is measured as shown in Fig. 60. The output contains an expanded time, where the time interval between the second (trailing) and third (rising) edges represents the time of  $T$  expanded by a factor of  $f$  ( $= 20$ ). In this scheme the time interval to be measured is always in the range between 16 and 32 ns.

The TS reference clock is provided by an RF clock that is precisely synchronized with the beam collisions. The reference clock with a period of approximately 16 ns can be generated from the RF signal of  $508.8875 \pm 10^{-6}$  MHz, with a time jitter of 20 ps. As the RF clock is used for the whole KEKB timing control, the reference clock is necessarily synchronized with the beam collision timing. A collision bunch number from 0 to 8 is determined in an offline analysis. Due to the small expansion factor of 20 and use of a 16 ns clock, this system provides a virtually deadtime-less TDC (1  $\mu$ s). The final TOF information is obtained by applying a time walk correction to the time information.

The main parameters for the TOF readout system are summarized in Table 7.

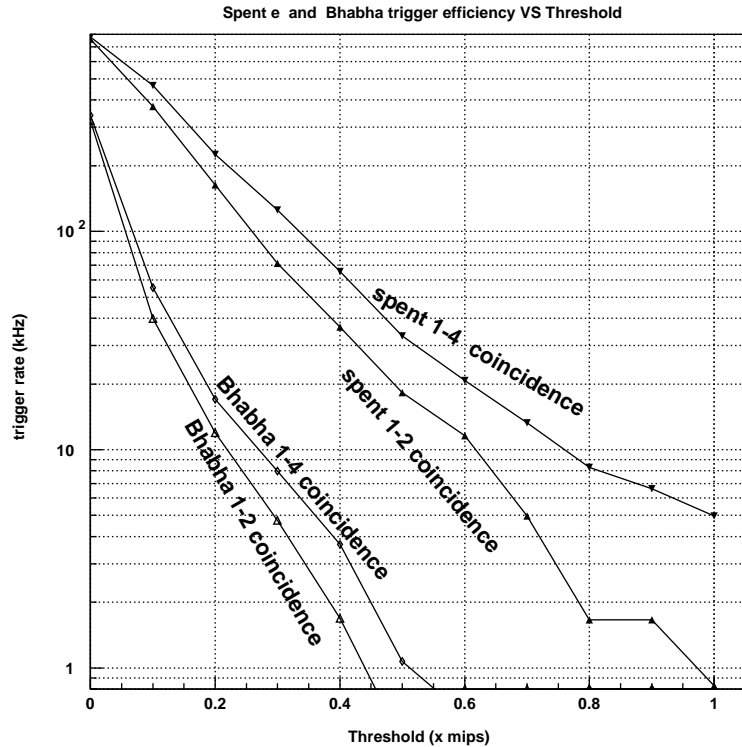


Fig. 59. Event trigger rates due to background photons from Bhabha and spent electrons.

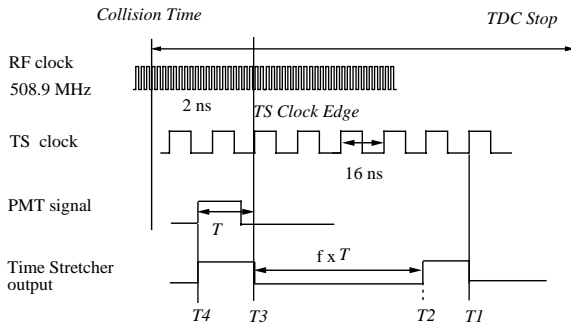


Fig. 60. Time stretcher scheme for TOF.

7.2. Beam test

A TOF module built in accordance with the final design was assembled and tested using the  $\pi 2$  test beam line of KEK-PS. The test counter was set on a movable stage that enabled the position and incident angle of the beam on the counter to vary simultaneously so that the geometry of the Belle TOF detector was reproduced.

Fig. 61 shows the TOF time resolution as a function of beam position. A time-walk correction was applied at each position and the start-counter time-jitter of 35 ps was subtracted in quadrature. An intrinsic time resolution of approximately 80 ps was obtained over the whole counter. In the Belle experiment we expect some additional contributions to the time resolution:

- a 10% degradation of the intrinsic resolution caused by the 1.5 T magnetic field as was observed in a beam test of a same-size TOF counter with a similar fine-mesh PMT,
- a 20 ps contribution due to the 4 mm beam bunch length and jitter in the RF signal used as the reference time, and
- a 20 ps contribution from time stretcher read-out electronics.

Including these errors in quadrature gives an expected overall time resolution that meets the Belle design goal of 100 ps.

Table 7  
Parameters for TOF/TSC electronics

Input signal	BC408 (Scint.) R6680 (PMT)	$\tau_{\text{rise}} \sim 4$ ns (PMT $\sim 2.5$ ns) FWHM $\sim 10$ ns $V_{\text{peak}} \leq 5$ V (1.2–1.5 V/mip) Signal rate $\leq 17$ kHz at $\geq 0.2$ mip
Q-to-T	MQT300	Self gate (width $\leq 100$ ns) Dynamic range: 0–500 pC (11 bits) Nonlinearity $\sim 0.1\%$ Dead time = 5 $\mu$ s max.
Discriminator	MDC100A (MVL407S)	Level: 0–2 V HL for self-gate/trigger LL for timing
Mean timer	Delay line	Input signal width = 30 ns Delay = 32 ns Time jitter $\leq 5$ ns
Time stretcher		Clock period = 16 ns (8 RF) Expansion factor = 20 Time jitter $\leq 20$ ps Dead time $\leq 1$ $\mu$ s
Reference time	RF clock	Total uncertainty $\sim 30$ ps

Fig. 62 shows time-of-flight distributions for  $\pi^+$  and protons at 2.5 GeV/c which indicate  $5\sigma$  separation of  $\pi^+/p$  at 2.5 GeV/c for the beam at a forward region. This implies approximately  $3\sigma$   $\pi/K$  separation at 1.25 GeV/c. A tail at later times is attributed to a gain saturation of the PMT at high signal rates. A rate of minimum ionizing particles on a whole TOF counter was observed to be about 14 kHz during the test with a positive beam. At this rate and with a PMT high voltage of 1500 V, the average anode current was about 10  $\mu$ A of a total base current of 60  $\mu$ A. In order to minimize the saturation, the ratio of anode to base currents should be kept below 10%. With the present IR and beam pipe design and assuming a PMT gain of  $3 \times 10^6$ , a Monte Carlo simulation predicts an anode current of 2.4  $\mu$ A. This indicates that the beam test conditions described above were much severe than those expected in the Belle environment. In order to guarantee a further safety margin under high beam background conditions, the nominal base current was increased to 300  $\mu$ A in the final design.

Fig. 63 shows the effective light yield seen by a TSC PMT as a function of beam position. A

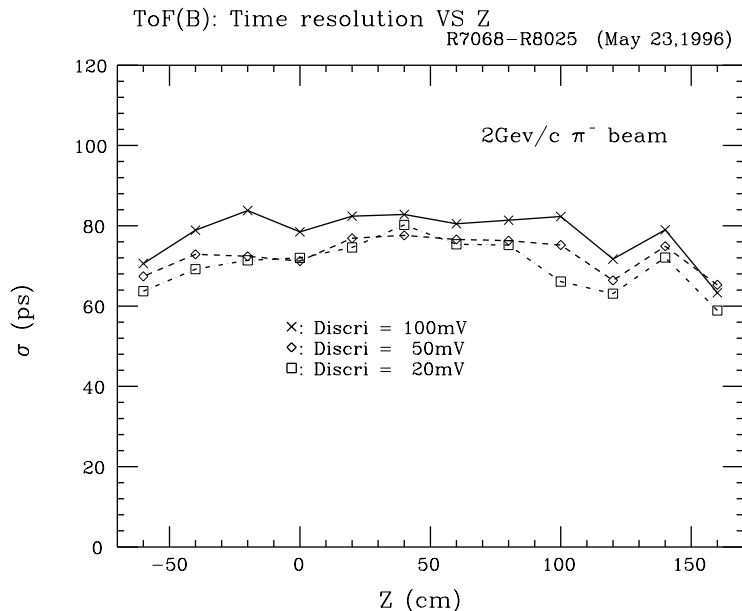


Fig. 61. Time resolution of a Belle TOF module as a function of hit position.

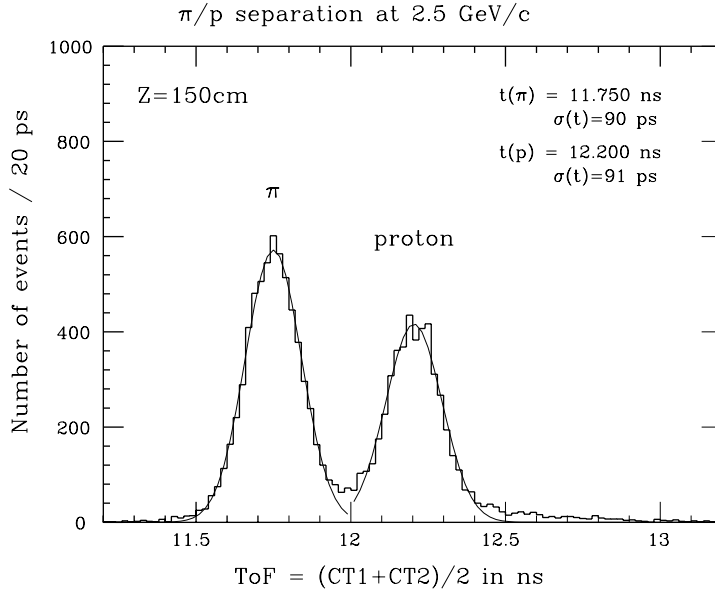


Fig. 62.  $\pi/p$  separation at 2.5 GeV/c.

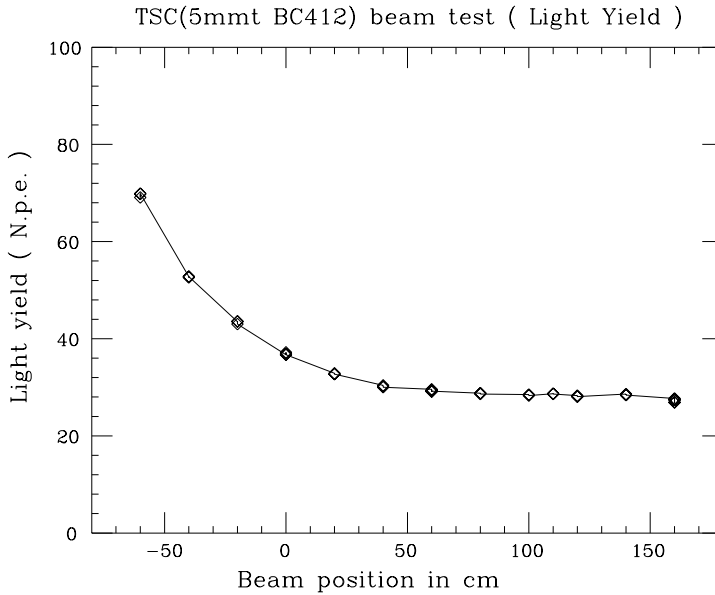


Fig. 63. Light yield of a TSC counter as a function of hit position.

minimum ionizing track produces more than 25 photoelectrons over the whole counter. This ensures a high efficiency of 98% for TOF trigger even at a nominal discrimination level of 0.5 mips.

### 7.3. Performance

#### 7.3.1. PMT gain adjustment

The gain of each PMT was adjusted using pulses provided by a laser calibration system, which

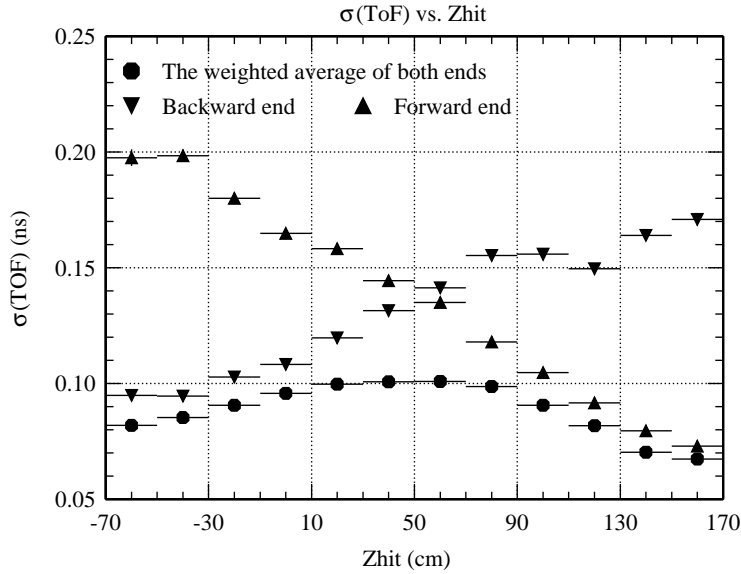


Fig. 64. Time resolution for  $\mu$ -pair events.

consists of an  $N_2$ -dye laser source (420 nm) and three optical fiber bundles for the TOF forward and backward PMTs and the TSC PMTs. The variation of the PMT gains was 18% (RMS).

### 7.3.2. Calibration and time resolution using $\mu$ -pair events

Muons from  $150 \times 10^3$   $\mu$ -pair events corresponding to an accumulated luminosity of  $250 \text{ pb}^{-1}$  were used for calibration [58]. Electrons in Bhabha events are frequently accompanied by back splash from ECL behind the TOF counters and thus cannot be used to simulate hadrons reliably.

The following empirical formula was used for the time walk correction to get a precise observed time

$$T_{\text{obs}}^{\text{twc}} = T_{\text{raw}} - \left( \frac{z}{V_{\text{eff}}} + \frac{S}{\sqrt{Q}} + F(z) \right) \quad (3)$$

where  $T_{\text{raw}}$  is the PMT signal time,  $z$  is the particle hit position on a TOF counter,  $V_{\text{eff}}$  is the effective velocity of light in the scintillator,  $Q$  is the charge of the signal,  $S$  is the coefficient of time walk, and

$$F(z) = \sum_{n=0}^{n=5} A_n z^n. \quad (4)$$

The coefficients,  $1/V_{\text{eff}}$ ,  $S$  and  $A_n$  for  $n = 0-5$ , were determined by minimizing residuals defined as  $\delta t = T_{\text{obs}}^{\text{twc}} - T_{\text{pred}}$  for all available TOF hits. Here,  $T_{\text{pred}}$  is the time-of-flight predicted using the track length calculated from the fit to hits in CDC. The optimization can be done for all PMTs together or for each PMT separately.

Fig. 64 shows time resolutions for forward and backward PMTs and for the weighted average time as a function of  $z$ . The resolution for the weighted average time is about 100 ps with a small  $z$  dependence. This satisfies the design goal, and we expect further improvement. The distribution of fitted residuals  $\delta t$  shows an oscillatory behavior of amplitude of  $\pm 25$  ps as a function of  $z$  after calibration. This indicates that the fifth-order polynomial  $F(z)$  does not match the data well, and a better choice of the formula may give us further improvement.

### 7.3.3. $\pi^\pm/K^\pm$ separation

After the calibration constants (TWC), optimized on  $\mu$ -pair events, were applied to hadronic events, sizeable deviations from zero for the  $\delta t$  residuals were observed. In particular the deviations were found to be momentum-dependent and different for each of the hadron species.

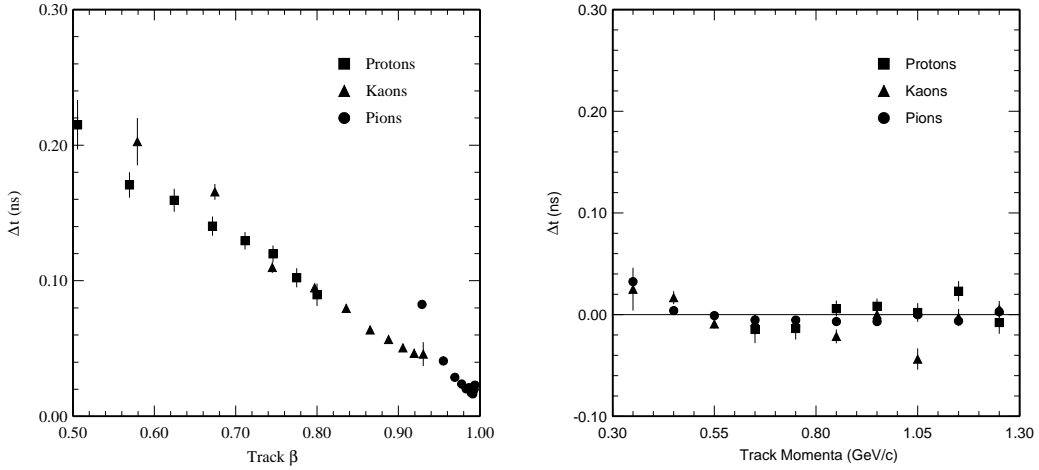


Fig. 65. Systematics of TOF  $\delta t$  residuals. The figure on the left shows the  $\beta$  dependence of the  $\delta t$  residual after application of the  $\mu$ -pair optimized calibration constants but before the  $\beta$  correction for each hadron species. The figure on the right shows the distribution of the residuals as a function of momentum after application of all calibration constants.

Deviations were observed as large as two sigma away from zero for low-momentum tracks identified as kaons and protons by other detector subsystems. Further investigation revealed that the observed momentum and hadronic species dependence could in fact be reasonably modeled by a single linear function in terms of the track's velocity, see the left-hand side of Fig. 65. A velocity or  $\beta$  parameterization was then applied in the TOF reconstruction algorithm to correct for this effect. The  $\beta$  parameterization was determined from an analysis of a large sample of hadronic events. In the right-hand side of Fig. 65, we show the momentum distribution of the  $\delta t$  residual after the application of the  $\beta$  correction. The large  $\delta t$  systematics observed earlier were largely removed over the relevant momentum range and for each of the hadron types. Further study is planned to establish the origin of the velocity dependence in the  $\delta t$  distribution. Fig. 66 shows the TOF resolution averaged over all counters and  $z$  as a function of momentum for each hadron species.

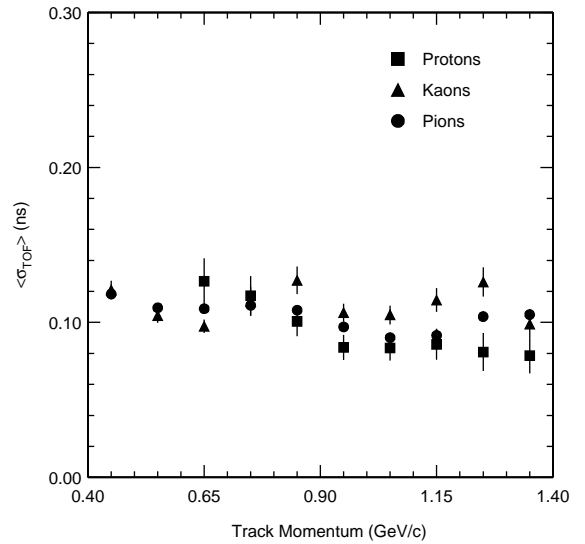


Fig. 66. The TOF resolution, averaged over all counters and  $z$ , as a function of momentum for each hadron species.

Fig. 67 shows the mass distribution for each track in hadron events, calculated using the equation

$$\text{mass}^2 = \left(\frac{1}{\beta^2} - 1\right)P^2 = \left(\left(\frac{cT_{\text{obs}}^{\text{twc}}}{L_{\text{path}}}\right)^2 - 1\right)P^2 \quad (5)$$

where  $P$  and  $L_{\text{path}}$  are the momentum and path length of the particle determined from the CDC track fit assuming the muon mass, respectively. Clear peaks corresponding to  $\pi^\pm$ ,  $K^\pm$  and protons are seen. The data points are in good agreement with a Monte Carlo prediction (histogram) obtained by assuming  $\sigma_{\text{TOF}} = 100$  ps.

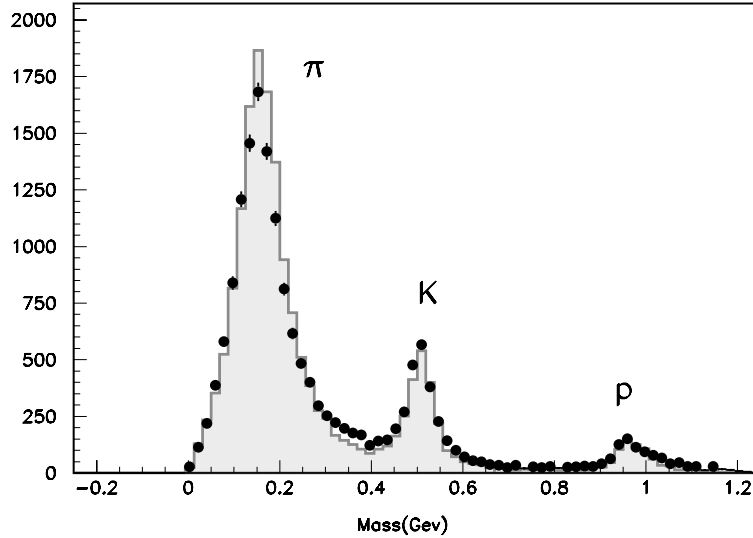


Fig. 67. Mass distribution from TOF measurements for particle momenta below 1.2 GeV/c.

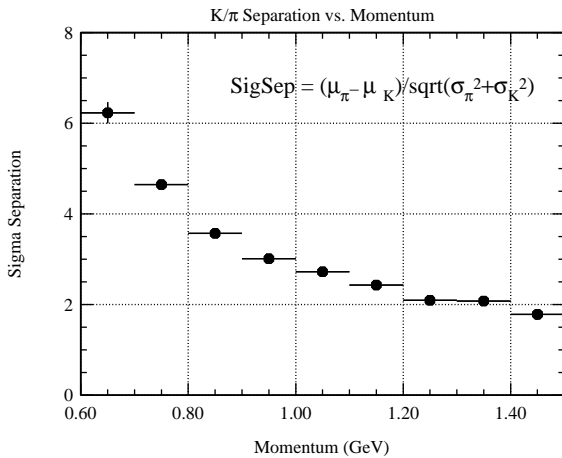


Fig. 68.  $\pi^\pm/K^\pm$  separation by TOF.

The identification power of  $\pi^\pm/K^\pm$  separation is shown in Fig. 68 as a function of momentum. The identification power is defined as

$$\sigma_{\pi^\pm/K^\pm} = \frac{T_{\text{obs}}^{\text{twc}}(K) - T_{\text{obs}}^{\text{twc}}(\pi)}{\sqrt{\sigma_K^2 + \sigma_\pi^2}}, \quad (6)$$

where  $\sigma_K$  and  $\sigma_\pi$  are the time resolution for K and  $\pi$ , respectively, at each momentum. This demonstrates clear  $2\sigma$  separation for particle momenta up to 1.25 GeV/c.

## 8. Electromagnetic calorimetry, ECL

The main purpose of the electromagnetic calorimeter is the detection of photons from B-meson decays with high efficiency and good resolutions in energy and position. Since most of these photons are end products of cascade decays, they have relatively low energies and, thus, good performance below 500 MeV is especially important. Important two-body decay modes such as  $B \rightarrow K^* \gamma$  and  $B^0 \rightarrow \pi^0 \pi^0$  produce photons energies up to 4 GeV and good high resolution is needed to reduce backgrounds for these modes. Electron identification in Belle relies primarily on a comparison of the charged particle momentum and the energy deposits in the electromagnetic calorimeter. Good electromagnetic energy resolution results in better hadron rejection. High momentum  $\pi^0$  detection requires the separation of two nearby photons and a precise determination of their opening angle. This requires a fine-grained segmentation in the calorimeter.

In order to satisfy the above requirements, we have decided to use a highly segmented array of CsI(Tl) crystals with silicon photodiode readout installed in a magnetic field of 1.5 T inside a superconducting solenoid magnet [4]. CsI(Tl) crystals have various nice features such as a large photon

## BELLE CsI ELECTROMAGNETIC CALORIMETER

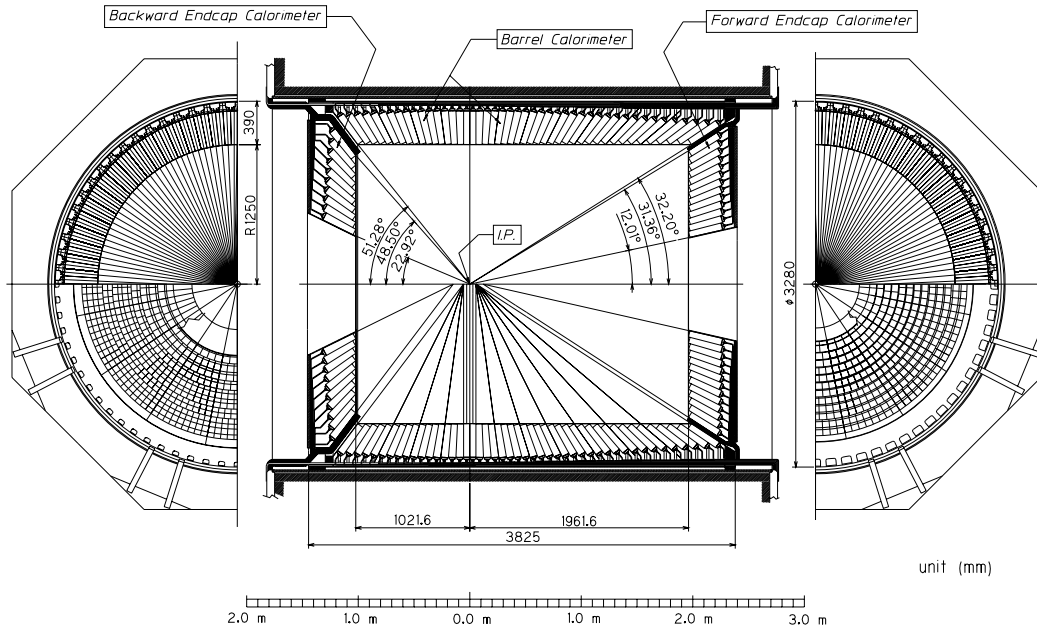


Fig. 69. Overall configuration of ECL.

yield, weak hygroscopicity, mechanical stability and moderate price.

### 8.1. Design and construction of ECL

The overall configuration of the Belle calorimeter system, ECL, is shown in Fig. 69. ECL consists of the barrel section of 3.0 m in length with the inner radius of 1.25 m and the annular end-caps at  $z = +2.0$  and  $-1.0$  m from the interaction point. The geometrical parameters of each section are given in Table 8.

Each crystal has a tower-like shape and is arranged so that it points almost to the interaction point. There is a small tilt angle of  $\sim 1.3^\circ$  in the  $\theta$  and  $\phi$  directions in the barrel section to avoid photons escaping through the gap of the crystals. End-cap crystals are tilted by  $\sim 1.5^\circ$  and  $\sim 4^\circ$  in the  $\theta$  direction in the forward and backward sections, respectively. The calorimeter covers the polar angle region of  $17.0^\circ < \theta < 150.0^\circ$ , corresponding to a total solid-angle coverage of 91% of  $4\pi$ . Small gaps between the barrel and end-cap crystals provide a pathway for cables and room for

Table 8  
Geometrical parameters of ECL

Item	$\theta$ coverage	$\theta$ seg.	$\phi$ seg.	No. of crystals
Forward end-cap	12.4–31.4°	13	48–144	1152
Barrel	32.2–128.7°	46	144	6624
Backward end-cap	130.7–155.1°	10	64–144	960

supporting members of the inner detectors. The loss of solid angle associated with these gaps is approximately 3% of the total acceptance. The entire system contains 8736 CsI(Tl) counters and weighs 43 tons.

The size of each CsI(Tl) crystal is determined by the condition that approximately 80% of the total energy deposited by a photon injected at the center of the crystal is contained in that crystal. Crystals with smaller cross-sections would have somewhat improved position resolution and two-photon separation but at the cost of an increased number of channels and poorer energy resolution. The latter is caused by the increase of gaps and inactive

materials between crystals. The transverse dimensions of the crystals vary depending upon their polar angle positions; typical dimension of a crystal being 55 mm  $\times$  55 mm (front face) and 65 mm  $\times$  65 mm (rear face) for the barrel part. Dimensions of the end-cap crystals have a large variation. The dimensions of the front and rear surfaces vary from 44.5 to 70.8 mm and from 54 to 82 mm, respectively. The number of crystals having different dimensions is 39, 29, and 30 for the forward end-cap, barrel, and backward end-cap sections, respectively. The 30 cm length ( $16.2X_0$ ) is chosen to avoid deterioration of the energy resolution at high energies due to the fluctuations of shower leakages out the rear of the counter. A beam test result indicates that the energy resolution for 25 cm CsI(Tl) counters is  $\sim 2.5\%$  for electron energies above 1 GeV [59].

The energy resolution of this system at low energies is dominated by electronic noises and the fluctuations of lateral shower leakages. In order to accommodate increases in the lateral shower size for low-energy photons, more counters must be used in the summation for the energy calculation. This puts a premium on low electronic noise for each channel. We aim at around 200 keV incoherent thermal noise and less than 100 keV coherent pickup noise in the whole electronics chain.

The linearity and energy resolution of the calorimeter will deteriorate if there is significant nonuniformity in light collection efficiency in a crystal. This effect as well as the influences of calibration and inactive materials in front of the calorimeter have been quantified by means of a Monte Carlo simulation, the results of which are presented later.

#### 8.1.1. CsI(Tl) crystal

The technical specifications for production of CsI(Tl) crystals are required to meet a number of stringent optical and mechanical requirements such as the average light output, light uniformity, dimensions, and radiation hardness. The Budker Institute of Nuclear Physics (BINP) in Novosibirsk, Russia with the collaboration of Single Crystal Institute and Factory in Kharkov, Ukraine, Crismatec Co. in France, and the Shanghai

Institute of Ceramics (SIC) in China have produced CsI(Tl) crystals to meet the Belle ECL specifications.

Optical properties of each crystal were tested by irradiation with a collimated  $^{137}\text{Cs}$  source at nine points along the crystal and measuring photoelectric peaks for 662 keV  $\gamma$ -rays. Output signals from a standard bialkali photomultiplier tube (Hamamatsu R1847S) were shaped by an amplifier with a 1  $\mu\text{s}$  shaping time and digitized by a peak-sensing ADC. The nonuniformity of the light collection is defined by the ratio of the difference between the largest and smallest photo-peak values among the nine measurements to the average photo-peak value. The nonuniformity is required to be less than 9% for all crystals and less than 7% for 90% of total crystals.

Measurements of the crystal dimensions were done with an automated device with eight linear gauges. The system has a 20  $\mu\text{m}$  precision for unwrapped crystals. The lateral dimensions are required to be  $+0$  and  $-200$   $\mu\text{m}$  from the specified dimensions and the length to be  $\pm 1$  mm from the specified length.

#### 8.1.2. Mechanical assembly

Each crystal is wrapped in a diffuse reflector sheet for the best collection of scintillation light at the end of the crystal. After testing several candidates, we have chosen a single layer of 200  $\mu\text{m}$  thick Goretex teflon as the wrapping material because it gives a good light output, is easy to handle, and is expected to be stable against aging. The mechanical assembly of a single CsI(Tl) counter is shown in Fig. 70. All sides of the crystal, except for the end face for light readout, are covered by a single layer of 200  $\mu\text{m}$  thick porous teflon. It is then covered by a laminated sheet of 25  $\mu\text{m}$  thick aluminum and 25  $\mu\text{m}$  thick mylar for light and electrical shielding. An aluminum-shielded preamplifier box is attached on the aluminum base plate with screws.

Two photodiodes, each having an active area of 10 mm  $\times$  20 mm, are glued at the center of crystal end surface via acrylite plate of 1 mm in thickness. The acrylite plate is used because direct glue joints between the photodiode and the CsI were found to fail after temperature cycling, probably due to the

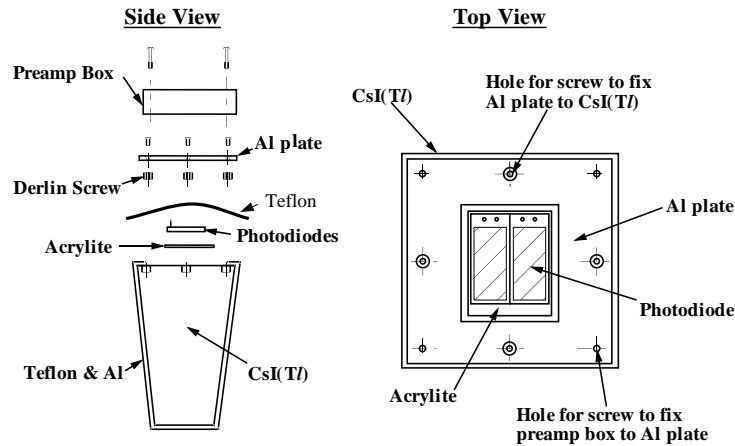


Fig. 70. Mechanical assembly of the ECL counter.

different thermal expansion coefficients of silicon and CsI. ECCOBAND 24 glue from Grace Japan Co. is used.

The barrel crystals were installed in a honeycomb-like structure formed by 0.5-mm-thick aluminum septum walls stretched between the inner and outer cylinders. The outer cylinder, the two end-rings, and the reinforcing bars are made of stainless steel and form a rigid structure that supports the weight of the crystals. The inner cylinder is made of 1.6-mm-thick aluminum to minimize the inactive material in front of the calorimeter. Except for the barrel end, eight crystals, four rows in  $\theta$  and two columns in  $\phi$ , were inserted in each cell and fixed to the reinforcing bars through a fixing jig at the back. In each cell at the barrel end, 10 crystals, five rows in  $\theta$  and two columns in  $\phi$ , were inserted. The whole barrel structure was installed in a thick stainless-steel cylinder supported from the magnet. Finite element calculations indicate that the whole barrel structure would sag  $\sim 200 \mu\text{m}$  in the final assembly that is considered to be safe for the contained crystals. The overall support structure is made gas tight and flushed with dry air to provide a low-humidity (5%) environment for the CsI(Tl) crystals. The preamplifier heat, a total of 3 kW, is removed by a liquid cooling system. An operating temperature of lower than  $30^\circ\text{C}$  with  $\pm 1^\circ\text{C}$  stability is required for the stable operation of the electronics.

The end-cap support structure is similar to that of the barrel. Here the crystal weight is transmitted via a front plate, thin septa, a side wall, inner/outer walls to thick back-reinforced bars that are supported from blocks mounted on a support cylinder. The end-cap calorimeter can be slid out using an additional end-cap mover with rails when access to the inner detectors is necessary.

### 8.1.3. Readout electronics

A block diagram of readout electronics is shown in Fig. 71. Each CsI(Tl) counter is read out by an independent pair of silicon PIN photodiodes (Hamamatsu S2744-08) and charge-sensitive preamplifiers [60] attached at the end of the crystal. The preamplifier output is transmitted on about 10-m long,  $50 \Omega$  twisted pair cables to a shaping circuit where the two signals from the same crystal are summed. The summed signal is then split into two streams: one for the main data acquisition for energy measurements and the other for the trigger electronics. The main signals for energy measurements are shaped with a  $\tau = 1 \mu\text{s}$  time constant and fed into a charge-to-time ( $Q$ -to- $T$ ) converter, LeCroy MQT300A, installed on the same card. The output of  $Q$ -to- $T$  converter is transmitted via twisted pair to a TDC module, LeCroy 1877S multi-hit TDC module, in the electronics hut for digitization. The trigger signal is shaped with a shorter time constant and  $\sim 16$  lines are combined to form an analog sum for the level-1 trigger.

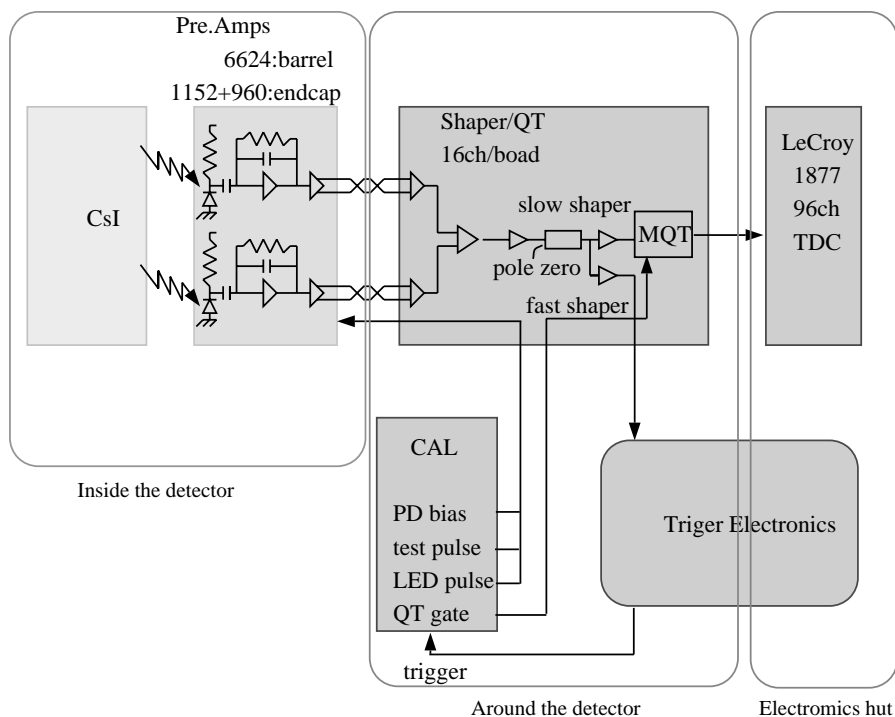


Fig. 71. Block diagram of the ECL readout electronics.

The specifications for the large-size silicon PIN photodiode are listed in Table 9. An improved version (S2744-08) of Hamamatsu photodiodes with higher quantum efficiency satisfies the above specifications. Each photodiode was burned in before shipment at 80°C for 50 h with 70 V bias voltage applied.

We performed a photodiode endurance test by keeping 160 units of S2744-03 photodiodes with a 60 V reverse bias at a temperature of 60°C for 4000 h. The typical dark current at 60°C is 300 nA. The dark current of each photodiode was measured at room temperature several times during the test and the average values of these measurements are about 3.2 nA. The dark current of 160 pieces was very stable and no photodiode showed a large increase.

A unit of two-channel preamplifiers consists of two hybrid chips and a mother board installed in an aluminum shielding case [60]. An extensive performance test was carried out for 100 pieces of

preamplifiers produced. The test result was quite satisfactory.

The readout electronics was calibrated with 60 keV  $\gamma$ -rays from a  $^{241}\text{Am}$  source. The photon absorbed with the PIN diode depletion layer produces 16,600 electron–hole pairs. That allowed to calibrate the electronics in units of photoelectrons.

#### 8.1.4. Calibration by cosmic-rays

All of the CsI(Tl) counters were calibrated using cosmic-rays before assembled in the support structure. The counters were put into a light-shielded box and placed in a measuring system called a “cosmic-ray calibration stand”, comprising 8 layers of drift chambers for tracking and two layers of scintillation counters for triggering and timing. Since these can trace cosmic-ray tracks with a position resolution of better than 1 mm, the position and path lengths of cosmic-rays in a crystal can be calculated precisely. The signals

Table 9

## Photodiode specifications

Sensitive area	10 × 20 mm <sup>2</sup>	
Wafer thickness	300 μm	
Applied high voltage	≤70 V	
Capacitance	Average ≤85 pF, max ≤105 pF	
Sensitivity (λ = 560 nm)	Average ≥320 mA/W, min ≥310 mA/W	
Temperature dependence	≤0.01%	
Dark current	Average ≤4 nA, max ≤15 nA	
Temperature dependence	Average ≤10%/°C	
Radiation hardness	At 6 Gy	At 68 Gy
Change of dark current	≤8%	≤40%
Change of capacitance	≤0.4%	≤1%
Change of sensitivity	≤0.3%	≤0.3%

from the preamplifiers of two photodiodes after being summed were then shaped and amplified with a shaper having the time constant of 1 μs, and digitized by LeCroy MQT300A and 3377 TDC. A typical distribution of pulse heights per path length which corresponds to a minimum ionization loss of about 5.67 MeV/cm has the energy resolution of about 25%. The systematic measurement error was estimated to be less than 1%.

#### 8.1.5. Radiation hardness

At the KEK B factory, a large number of soft  $\gamma$ -rays having an energy of up to a few MeV are generated by spent beam electrons and positrons hitting the beam pipes and radiation shielding masks. The dose of the beam-induced background in the barrel region has been estimated to be up to 5 rad/yr in the first 2 cm of depth under steady operation at an integrated luminosity of  $10^{41}$  cm<sup>-2</sup>/yr. With a large safety margin, the requirement for radiation hardness is set such that the light-output decreases to less than 3%, 10%, and 20% at radiation dose of 10, 100, and 1000 rad, respectively. According to the previous measurements, it was not self-evident whether our CsI(Tl) crystals would satisfy this requirement.

In order to test the radiation hardness, several full-size crystals made by each producer were irradiated up to 1000 rad by the <sup>60</sup>Co source of 51 TBq at the irradiation facility of Tokyo

Institute of Technology [61]. The irradiation rates were about 3, 3, and 25 rad/min for 10, 100, and 1000 rad irradiation, respectively. The attenuation length of 1.17 and 1.33 MeV  $\gamma$ -rays from the <sup>60</sup>Co source is about 5.4 cm in a CsI crystal.

Irradiation was done in two ways: (a) uniform irradiation in which crystals were irradiated from the sides of the crystal over the whole region and (b) front face irradiation in which the sides of the crystals were shielded and the irradiation was made from the front surface simulating the actual case. The radiation damage is restricted in the front region, and approximately 90% of the total dose is absorbed in the first 10 cm region out of the total length of 30 cm. The light output of irradiated crystals was measured in two methods: one with a photomultiplier tube (PM) (Hamamatsu R1847-S) and a <sup>137</sup>Cs source, and the other with two photodiodes (PDs) (Hamamatsu S2744-08, the sensitive area of 10 mm × 20 mm) and cosmic-ray muons. The latter arrangement is the same as in the actual Belle ECL.

Two kinds of recoveries of damage after irradiation were observed: (1) a decrease in the phosphorescence intensity and (2) a partial restoration of the light output. The intensity of the stray phosphorescence was too strong to measure the photoelectric peak of 662 keV  $\gamma$ -rays immediately after irradiation. After a period of a few hours to one day the intensity decreased and

weakened to the level at which measurements were possible. In general, the loss of light-output of a CsI(Tl) crystal after radiation damage partially recovered. Fig. 72 shows a typical history of light output measured using a PMT. The light output recovered partially during a period of about 1, 2, and 4 weeks after irradiation of 10, 100, and 1000 rad, respectively. Unless specifically mentioned, we use the saturated value of the light output at each dose.

The light output measured with a PMT and PDs as a function of dose for front-face irradiation is shown in Fig. 73. The results with a PMT and with PDs agree at a level of a few %. The figure shows that all of the crystals tested, except for the prototype made by Shanghai Institute of Ceramics (SIC), satisfy the requirement of radiation hardness up to 1000 rad. The radiation hardness of SIC crystals was improved to fulfill the requirement by doping with a material with the property to cancel the suspicious impurity. Fig. 74 shows the results of light output for new SIC crystals and the original prototype SIC crystals measured using the PMT readout after front-face irradiation.

The position dependence of the light output measured with PMT and PDs readouts for uniform and front-face irradiation indicates that the change in the light output depends little on the position along a crystal, even for front-face irradiation. This result itself is a good evidence that the mechanism of scintillation emission in

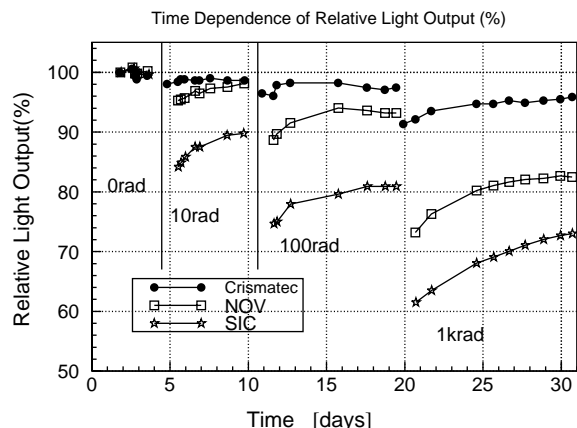


Fig. 72. Time dependence of the light output for uniform irradiation (PMT readout).

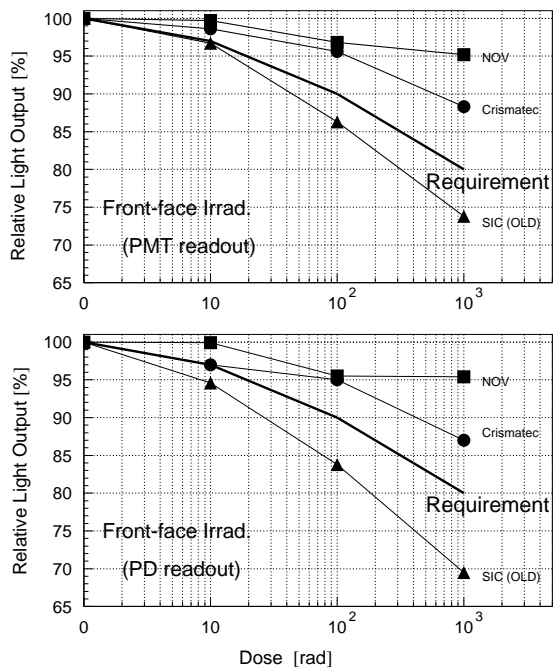


Fig. 73. Light output as a function of radiation dose for front-face irradiation. The upper and lower figures are the data with the PMT readout and the PD readout, respectively. The light output values are normalized to those before irradiation. The thick line represents the requirement for the radiation hardness of ECL. All crystals, except for SIC-prototypes, satisfy the requirement.

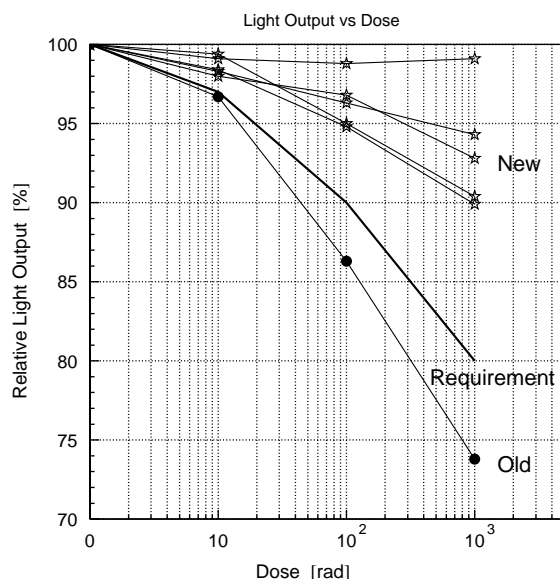


Fig. 74. Light output of new SIC crystals vs. radiation dose (front-face irradiation).

CsI(Tl) crystals is little affected by irradiation. We conclude that only the overall gain factors need to be corrected for the effect of radiation damage in the running conditions.

The results of studies of the radiation-damage mechanism indicate that the main cause of radiation damage is due to the degradation in the attenuation length caused by the formation of color centers, rather than a deterioration of the mechanism of scintillation light emission. The coloration of CsI(Tl) to red or brown was observed after irradiation. The degree of coloration was correlated with the change in the light output. The prototype crystals by Shanghai Institute of Ceramics (SIC) were colored at 100 rad irradiation while those by Novosibirsk (NOV) and Crismatec were at 1000 rad or beyond. In the case of the front-face irradiation, coloration was observed in the front region and the front part of SIC prototype crystals became red after 100 rad irradiation.

In order to investigate the cause of radiation damage we measured the spectra of the transmittance, excitation, and emission at 0, 10, 100, and 1000 rad irradiation with spectrophotometers. Sliced pieces of 5.5 cm × 5.5 cm × 2.7 cm in size

were used for these studies. The transmittance was measured across a thickness of 5.5 cm with the reproducibility of  $\pm 1\%$ . The measurements of the excitation and emission were made on the surface of each crystal with somewhat poorer reproducibilities of  $\pm 5\%$ . The results for the SIC prototype and NOV are shown in Fig. 75. Clear absorption bands at around 430 and 520 nm on the transmittance curves can be seen for the SIC prototype, indicating a formation of color centers. On the other hand, the deterioration in the transmittance was small for NOV. A Monte Carlo ray-tracing simulation also supported the idea that the main result of radiation damage is the formation of color centers.

## 8.2. Beam tests

Beam tests of the Belle ECL detectors were carried out using electron/pion beams at the  $\pi 2$  beam line of KEK 12-GeV PS in June and July 1994, and photon beams produced at the ROOK-1M facility of the Budker Institute of Nuclear Physics (BINP), Russia, in three separate periods, November 1995–January 1996, July 1996, and September–October 1997 [62–64].

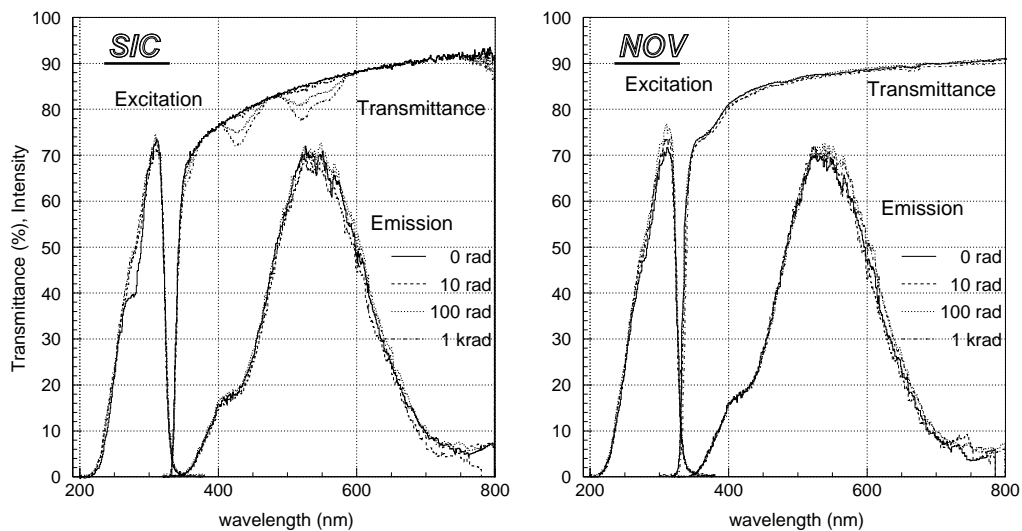


Fig. 75. Spectra of the transmittance across a thickness of 5.5 cm and of excitation and emission at a surface of each crystal after 0, 10, 100 and 1000 rad irradiation for SIC prototype and NOV. The transmittance data were corrected for the reflection loss at the surfaces. Clear absorption bands are observed on the transmittance curve for the SIC prototype. The spectra of excitation and emission were corrected for wavelength dependence of the quantum efficiencies of PMT.

### 8.2.1. $\pi^2$ beam

The performance test of a prototype of the Belle ECL detectors was carried out using the  $\pi^2$  beam line at KEK in an energy range from 0.25 to 3.5 GeV [59]. An array of  $6 \times 5$  CsI(Tl) counters with the same mechanical assembly and readout electronics as those of Belle ECL were used to measure the energy and position resolution for electrons and the  $e/\pi$  separation for two sets of matrix configurations: one corresponded to the center and the other to the edge of the barrel calorimeter. Fig. 76 shows the schematic top view of the two matrix configurations. The whole matrix was placed on a movable table controlled by an online computer.

The energy resolution was measured by using electrons which impinged  $\pm 2$  cm from the center of the matrix by summing the energy deposit weighted by the calibration constant of each

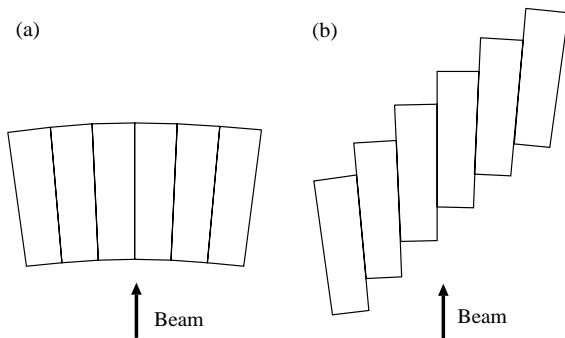


Fig. 76. Top view of two matrix configurations: (a) normal array and (b) staggered array.

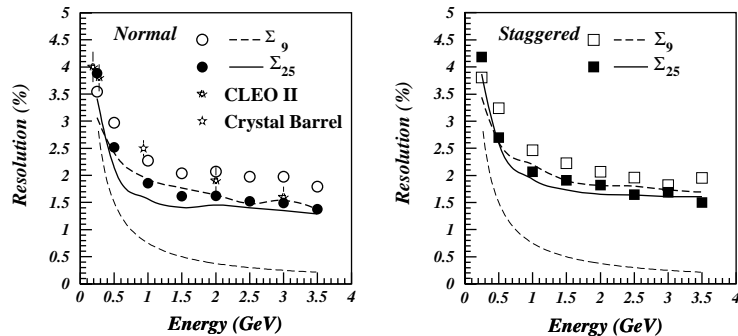


Fig. 77. Energy resolution as a function of beam energy. Results from a GEANT simulation are shown by the dashed curve (9 blocks) and the solid curve (25 blocks). Also plotted are the results of CLEO II (9 blocks) and Crystal Barrel. The dotted curve shows the contribution from electronics noise for 25 blocks.

crystal. The summation was carried out for a  $3 \times 3$  matrix (9 crystals) and a  $5 \times 5$  matrix (25 crystals). The total energy deposit was then scaled event by event by the momentum measured by the spectrometer in order to compensate for the spread of beam momentum. The energy resolution measured for the two matrix arrangements (normal and staggered) is shown in Fig. 77 as a function of beam momentum together with the measurements of CLEO II [65] and Crystal Barrel [66]. A Monte Carlo simulation using GEANT 3.15 reproduced the general behavior of the energy resolution but tended to predict a slightly better overall resolution. This may be explained by the nonuniformity of the light collection in the crystal, which was not included in the simulation.

The impact point of an electron on the matrix was calculated from the position of each crystal summed with the weight of its energy deposit. Position resolutions were determined from the correlation between the impact position and the position obtained by the drift chamber system to be 3.6 mm for 2.0 GeV/ $c$  electrons and 5.8 mm for 0.5 GeV/ $c$  electrons.

The difference of the energy deposit in the calorimeter can be used to distinguish electrons from charged pions. Fig. 78 shows the energy deposit summed over 25 crystals for 1 GeV/ $c$  electrons and pions injected near to the center of the matrix. We see a difference in the spectra for  $\pi^+$  and  $\pi^-$  due to the difference in cross-sections. We define the probability for a pion to be misidentified as an electron by  $N_{\text{mis}}/N_{\text{tot}}$ , where

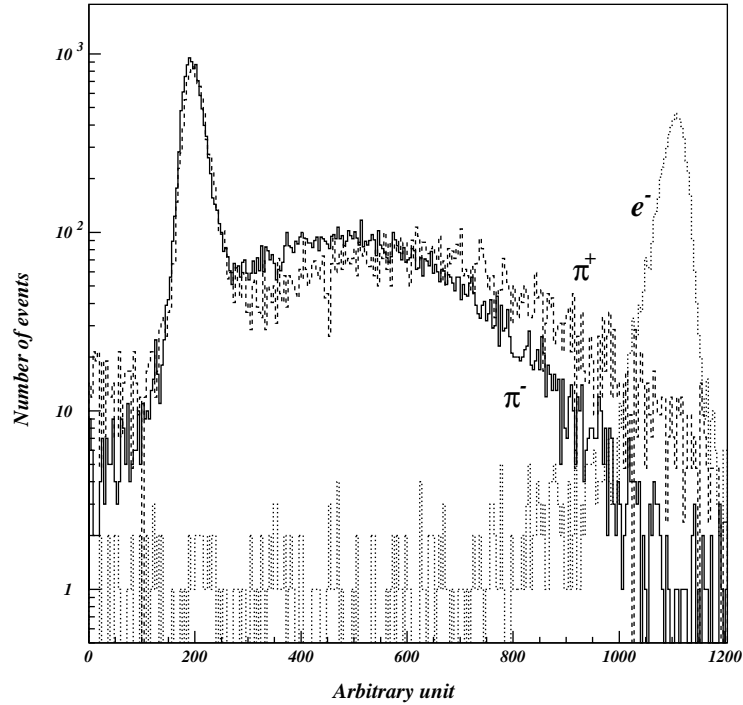


Fig. 78. Distribution of the energy deposit by electrons (red histogram), by positive pions (green histogram) and by negative pions (blue histogram) at 1 GeV/c.

$N_{\text{mis}}$  is the number of pion events with an energy deposit in the electron energy region and  $N_{\text{tot}}$  is the total number of pion events. The electron region is defined as  $\pm 3\sigma_e$  around the peak of the electron energy deposit, where  $\sigma_e$  is the energy resolution of the electrons. The results of an  $e/\pi$  separation for positive and negative pions are shown in Fig. 79 for energies of 0.5–3 GeV and for the normal and staggered arrays. The misidentification probability is found to be less than 1% above 2 GeV/c.

### 8.2.2. Photon beams at the ROKK-1M facility

Extensive tests of a prototype of the Belle ECL calorimeter were carried out using photon beams produced at the ROKK-1M facility of BINP in the photon energy range from 20 MeV to 5.4 GeV. Fig. 80 shows the layout of the ROKK-1M facility. The beam of backward scattered photons was used in the photon energy range below 850 MeV. The photon energy was determined by measuring the scattered electron energy by the tagging system, the energy resolution of which was

$\sigma_E/E \sim 10^{-3}$ . The second harmonic of a (Nd:YAG) pulse laser corresponds to the photon energy of 2.34 eV. The Compton photon (CP) energy spectrum is roughly uniform with a sharp edge at the maximum CP energy,  $E_C = 4\gamma^2\omega_0/(1 + 4\gamma\omega_0/m_e)$ , where  $\omega_0$  is the energy of the laser photon and  $m_e$  is the electron mass. The photon energy resolution was kept less than 1% for a wide range of photon energies by optimizing the electron beam energies. The main background process for Compton photons is the beam electron bremsstrahlung at the residual gas nuclei. As will be described later, bremsstrahlung photons were used to obtain the energy resolution for high-energy photons.

The experimental setup is shown in Fig. 81. The prototype consists of a  $6 \times 6$  matrix of the CsI(Tl) counters with the same characteristics as those of the Belle ECL counters. The support frame of the counters allowed to move the prototype within  $\pm 10$  cm in the vertical and horizontal directions as well as to adjust the angle of the prototype to the

photon beam within  $\pm 0.2$  rad. The layout of the readout system used in the tests is shown in Fig. 82. The trigger signal was produced by coincidence of the laser pulse, a signal from the

tagging system, and the beam crossing phase in the absence of the signal from the veto counter.

The energy deposition in a crystal is calculated as  $E_i = \alpha_i A_i$ , where  $E_i$  is the energy deposition in the  $i$ th crystal,  $A_i$  is the corresponding ADC channel, and  $\alpha_i$  is the calibration coefficient. One of the simple ways of calibration is to use cosmic-rays, as described in the section of the calibration by cosmic-rays. The average energy deposition in the crystal is proportional to the track length within the crystal volume which depends both on the particle angle and coordinate along the crystal. For a minimum ionizing particle the average energy deposition per unit length in CsI is 5.67 MeV/cm that provides about 30–40 MeV energy deposition in each counter.

The tracks of cosmic muons were reconstructed by the hodoscopes of the muon streamer tubes. The hodoscope position resolution of 15 mm is sufficient to measure the track length inside the crystal with an accuracy better than 1.5% when a particle crosses two opposite side surfaces. The calibration by cosmic-rays was performed regularly between beam-test runs. Fig. 83 shows the longitudinal nonuniformity of light collection of a typical counter. The mean nonuniformity in the longitudinal direction for all the crystals used in the tests was about 7%.

As the electronics noise is the crucial point for the calorimeter resolution at low energies, this characteristic was carefully studied. The noise

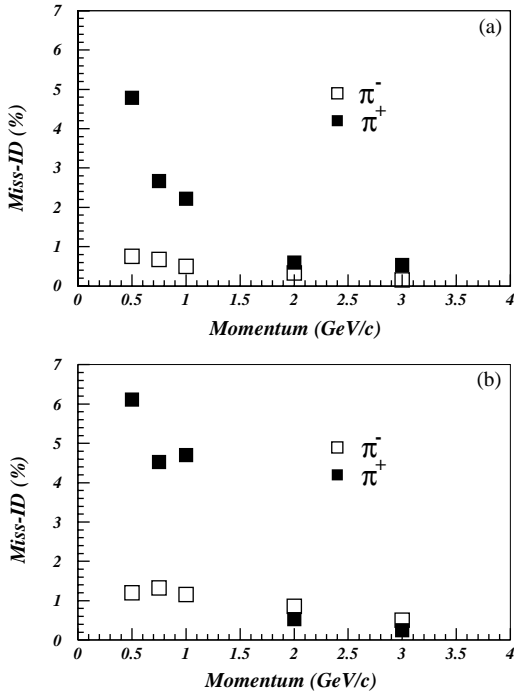


Fig. 79. Probability to misidentify a pion as an electron (a) for the normal array and (b) for the staggered array.

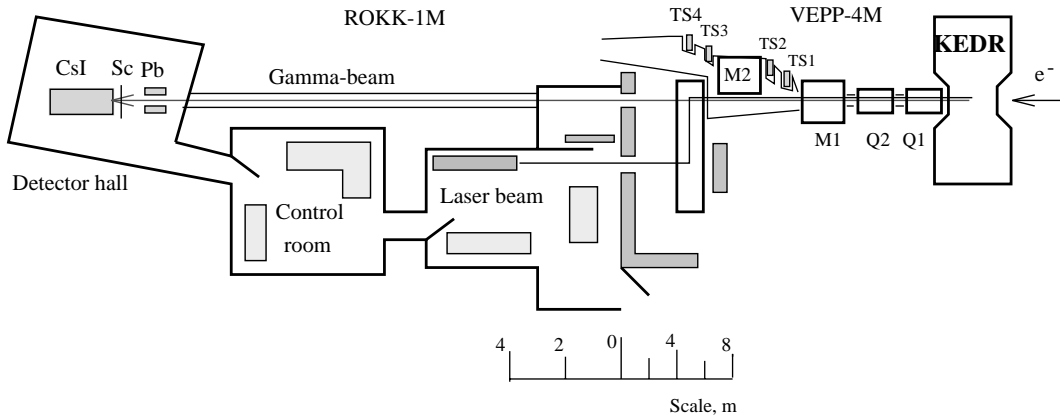


Fig. 80. Layout of the VEPP-4M experimental region with the KEDR tagging system.  $Q_1$  and  $Q_2$  are quadrupoles, and  $M_1$  and  $M_2$  are bending magnets.

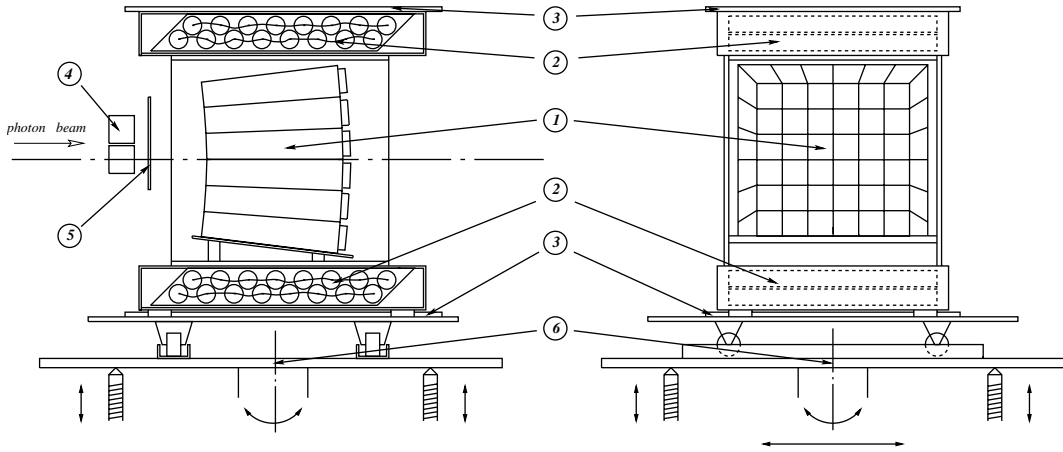


Fig. 81. Experimental layout: (1) CsI(Tl) crystals; (2) drift-tube hodoscopes; (3) plastic scintillation counters for cosmic trigger; (4) a lead collimator; (5) a veto counter; (6) and a movable platform for the position adjustment.

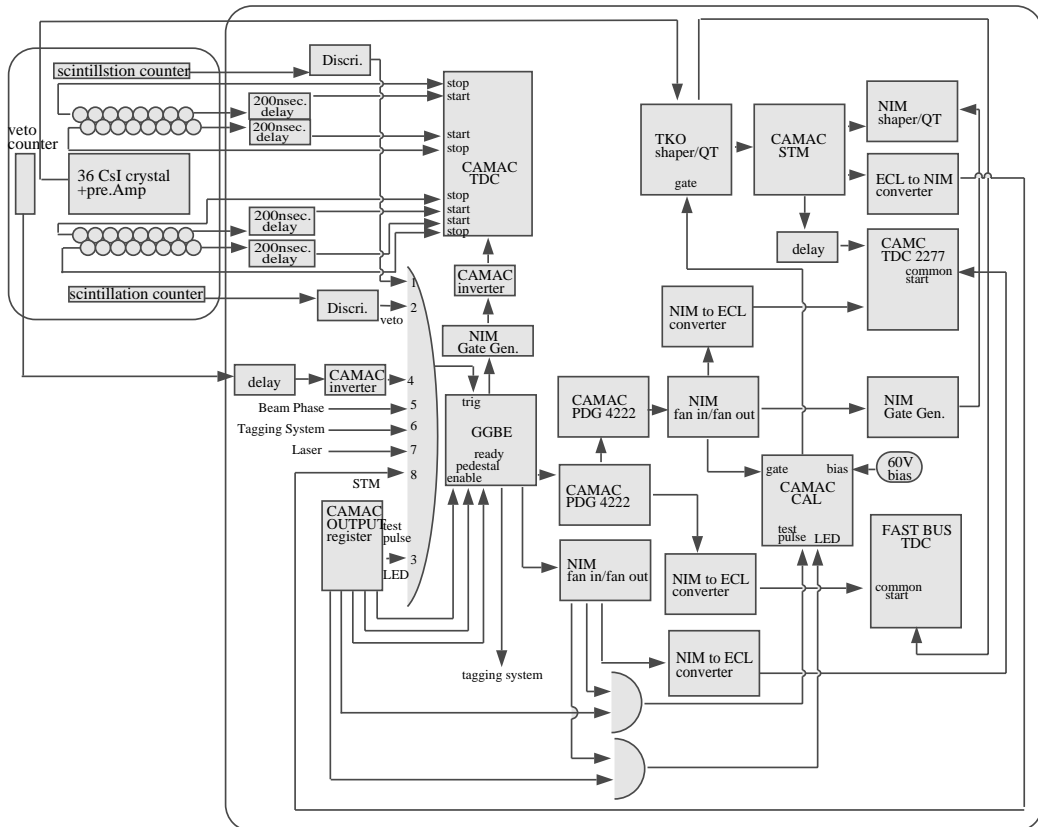


Fig. 82. Schematic diagram of the beam test experiment.

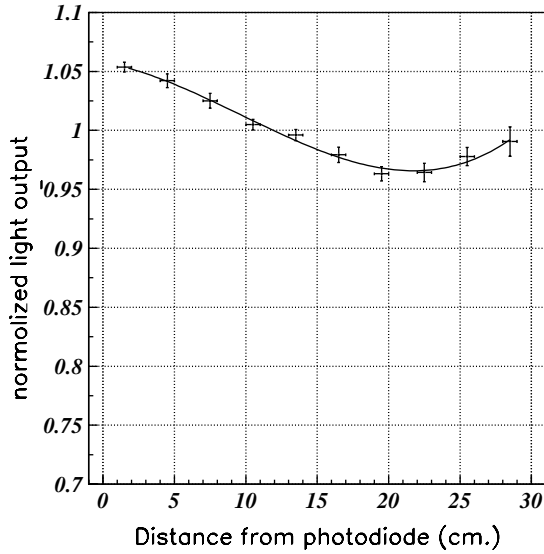


Fig. 83. Longitudinal nonuniformity of light collection of the crystal.

value was estimated by a pedestal distribution width both for a single channel and for the sum of a few channels. By fitting the pedestal distributions, the noise contributions from a single channel ( $\sigma_{i,0}$ ) and the sum of  $n$  channels ( $\sigma_n$ ) were determined. The coherent and incoherent noise components are separated using the following equations:

$$\sigma_{i,0}^2 = \sigma_{i,inc}^2 + \sigma_{i,coh}^2 \quad (7)$$

$$\sigma_n^2 = \sum_{i=1}^n \sigma_{i,inc}^2 + \left( \sum_{i=1}^n \sigma_{i,coh}^i \right)^2 \quad (8)$$

$$\langle \sigma_{i,coh}^2 \rangle = \frac{\sigma_n^2 - \sum_{i=1}^n \sigma_{i,0}^2}{n^2 - n} \quad (9)$$

$$\langle \sigma_{i,inc}^2 \rangle = \frac{\left( \sum_{i=1}^n \sigma_{i,coh} \right)^2 - \sigma_n^2}{n^2 - n} \quad (10)$$

where  $\sigma_{i,inc}$  and  $\sigma_{i,coh}$  stand for the incoherent and coherent noise components of the  $i$ th channel, respectively.

The total incoherent and coherent noise components were determined to be 189–250 and 17–50 keV, respectively. It was found that the dominant part of the coherent noise came from the ADC itself. The latest measurement of the

coherent noise of 17 keV gives a substantially improved noise level. These results are very satisfactory.

For reconstruction of the photon energy the energy deposition in the  $3 \times 3$  ( $E_9$ ) and the  $5 \times 5$  ( $E_{25}$ ) matrix around the crystal with the maximum energy was used. Using the energy measured by the tagging system  $E_{TS}$  as a photon energy  $E_\gamma$ , the energy resolution dependence on the photon energy was studied for each beam energy from the low limit determined by the tagging system acceptance up to the Compton edge. Distributions of the ratio  $E_9/E_\gamma$  or  $E_{25}/E_\gamma$  have an asymmetric shape which was fitted by the normal logarithmic function written as

$$f(\varepsilon) = N \exp \left\{ -\frac{1}{2\sigma_0^2} \ln^2 \left( 1 - \frac{\varepsilon - \varepsilon_p}{\sigma_E} \eta \right) - \frac{\sigma_0^2}{2} \right\} \quad (11)$$

where  $\varepsilon$  is the deposited energy,  $\varepsilon_p$  is the energy corresponding to the peak position,  $\eta$  is a parameter describing the asymmetry of the distribution, and  $N$  is the normalization factor. The energy resolution  $\sigma_E$  is defined by the full-width at half-maximum of the distribution as

$$\sigma_E = \frac{\text{FWHM}}{\xi} \quad (12)$$

$$\xi = 2\sqrt{\ln 4} \approx 2.36 \quad (13)$$

and  $\sigma_0$  is expressed via  $\eta$

$$\sigma_0 = \frac{2}{\xi} \sinh^{-1} \left( \frac{\eta \xi}{2} \right). \quad (14)$$

The energy resolution of the CsI was obtained by the relation

$$\sigma_{E_{CsI}} = \sqrt{\sigma_E^2 - \sigma_{E_\gamma}^2}. \quad (15)$$

Since the tagging system resolution  $\sigma_{E_\gamma}/E_\gamma$  is better than 1% for  $E_\gamma > 100$  MeV, the effect of the subtraction is small.

Another possibility to measure the CsI energy resolution is the analysis of the edge of the Compton photon spectrum detected by the CsI matrix. This method does not use information from the tagging system and provides an independent check of the results. The CsI energy distribution is fitted by the convolution of the function of Eq. (11) and Compton distribution approximated

by

$$f(E) = N \left\{ \left( E - \frac{1}{2}E_C \right)^2 + \frac{1}{4}E_C^2 \right\} \quad (16)$$

where  $E_C$  is the Compton spectrum edge. Examples of the fit are shown in Fig. 84.

In the latest measurement [64] the bremsstrahlung edge was also used to determine the energy resolution at higher energies. The same procedure

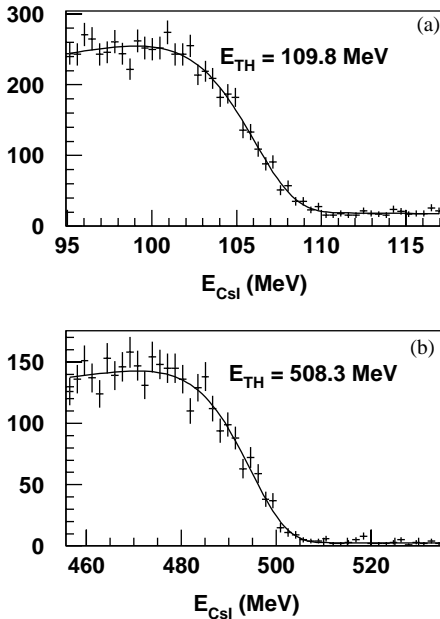


Fig. 84. Typical Compton-edge distributions at (a) 109.8 MeV and (b) 508.3 MeV. The solid curves are the fitted results.

was used as for the Compton edge analysis. A typical distribution is shown in Fig. 85.

The energy resolution was obtained for the  $3 \times 3$  and  $5 \times 5$  CsI matrices in two ways: the total energy sum was used in the first method and the energy sum from the counters above a certain threshold energy in each matrix was used in the second method. Fig. 86 shows the results of the analysis. Figs. 86(c) and (d) correspond to the energy resolution for the threshold energy of 0.5 MeV. The energy resolution without threshold for the  $5 \times 5$  matrix is substantially better at higher energies, above 100 MeV, than that for the  $3 \times 3$  matrix because of better energy containment, while it is appreciably poorer at lower energies, below 30 MeV, due to large contribution of summed electronics noise. This situation in the low-energy region has been improved by applying an optimum threshold energy. Fig. 87 shows the energy resolution as a function of threshold energy at various photon energies. At photon energies below 100 MeV, the threshold energy above 2 MeV degrades the energy resolution. On the other hand, the energy resolution is very insensitive to the threshold energy at photon energies above 300 MeV. In the photon energy range of interest the threshold energy of 0.5 MeV seems to be optimum. The resolutions obtained by the three methods are consistent over the energy range from 20 MeV to 5.4 GeV.

The energy resolution obtained with the threshold energy of 0.5 MeV (Figs. 84(c) and (d)) can be fitted by the quadratic sum ( $\oplus$ ) of three terms as

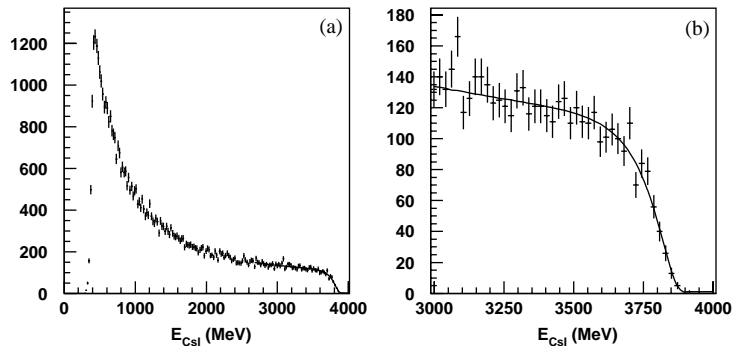


Fig. 85. (a) Typical bremsstrahlung energy distribution for a 4036 MeV electron beam and (b) an expanded view of the edge region with the fitted curve.

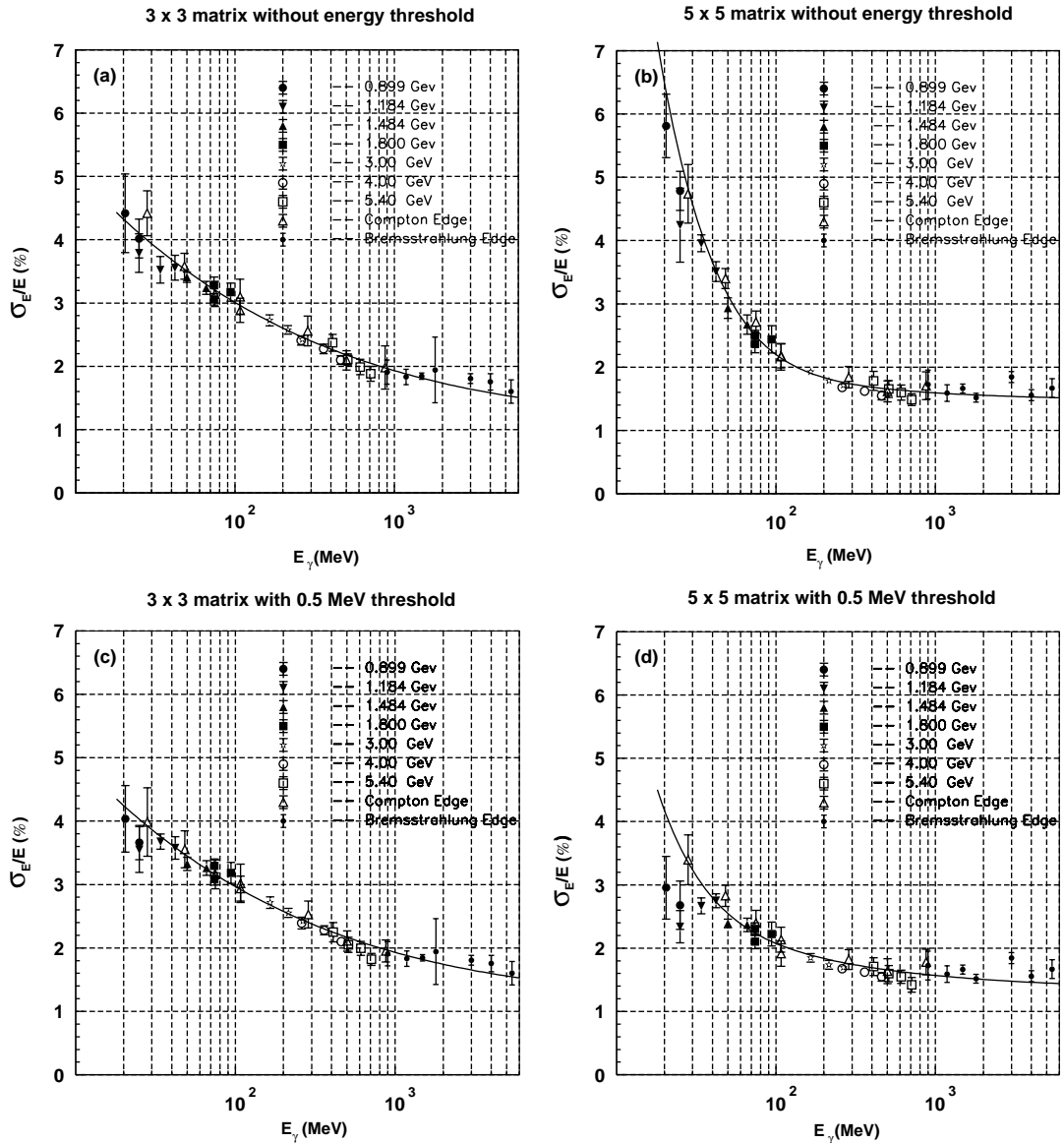


Fig. 86. Energy resolution as a function of incident photon energy for the (a)  $3 \times 3$  and (b)  $5 \times 5$  matrices with the total energy sum, and for the (c)  $3 \times 3$  and (d)  $5 \times 5$  matrices with a 0.5 MeV threshold. The error bars are the RMS values of four measurements taken with the crystals (3,3), (3,4), (4,3) and (4,4) into the photon beam.

follows:

$$\frac{\sigma_E}{E} = \frac{0.0066(\%)}{E} \oplus \frac{1.53(\%)}{E^{1/4}} \oplus 1.18\% \quad (17)$$

for the  $3 \times 3$  matrix sum, and

$$\frac{\sigma_E}{E} = \frac{0.066(\%)}{E} \oplus \frac{0.81(\%)}{E^{1/4}} \oplus 1.34\% \quad (18)$$

for the  $5 \times 5$  matrix sum,  $E$  in GeV. Since details of the fitted results are not completely identical, we quote the latest results.

The linearity of the energy response was studied in the energy range from 20 MeV to 5.4 GeV by fitting the edge of the Compton and bresstrahlung spectra. The correlation between  $E_{CS1}$  obtained by

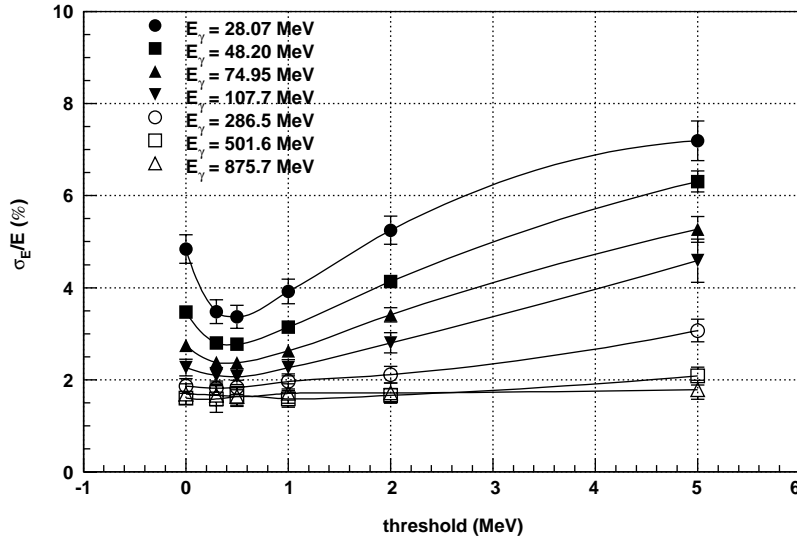


Fig. 87. Energy threshold dependence of the energy resolution at various photon energies.

fitting the data and the theoretical edge value ( $E_{TH}$ ) calculated from the electron beam energy is plotted in Fig. 88(a). The value of  $E_{CSI}$  was obtained from the energy sum of the  $5 \times 5$  matrix with a threshold energy of 0.5 MeV. The linearity defined as  $(E_{CSI} - E_{TH})/E_{TH}$  is plotted in Fig. 88(b). For all energy ranges,  $E_{CSI}$  is smaller than  $E_{TH}$  because of shower leakage from the central  $5 \times 5$  counters. At higher energies the leakage from the rear end of the crystal becomes dominant. The major part of the error bars comes from the RMS deviation of the four measurements, for which the photon beam was injected at different crystals. The total uncertainty including the electronics nonlinearity was estimated to be approximately  $\pm 1\%$ . We conclude that the energy deposit in the  $5 \times 5$  matrix with a 0.5 MeV threshold reproduced the absolute photon beam energy within  $-3 \pm 2\%$  in a broad energy range from 20 MeV to 5.4 GeV. A GEANT simulation could reproduce the experimental data well within  $\pm 1\%$ , except for a small systematic shift of  $-2\%$  below 100 MeV.

A narrow photon beam of rectangular shape ( $4 \text{ mm} \times 4 \text{ mm}$ ) was used to study the position dependence of energy deposition and energy

resolution. Figs. 89 and 90 show the measured position dependence of the energy deposit and energy resolution as a function of lateral horizontal position. The Compton photon beam in the energy range of  $E_{tag} = 470 \pm 50 \text{ MeV}$  was used. Small decreases in energy and degradations in energy resolution were measured at the air gap and the aluminum fin (0.5 mm thick). The GEANT Monte Carlo simulation reproduced the behavior of the data quite well.

The position resolution was measured by moving the prototype in the transverse direction along the horizontal plane. First the shower center of gravity ( $X_{cg}$ ) was calculated using the relation

$$X_{cg} = \frac{\sum_{i=1}^{36} X_i E_i}{\sum_{i=1}^{36} E_i}, \quad (19)$$

where  $X_i$  is the  $x$ (or  $y$ )-coordinate of the center of the  $i$ th counter and  $E_i$  is its energy deposit. A scatter plot of the average  $\langle X_{cg} \rangle$  vs. the photon impact coordinate ( $X_{beam}$ ) is shown in Fig. 91(a). The position  $X_{beam}$  is smeared uniformly within the aperture of the collimator. The center of gravity gives the correct position at the center of the crystal and at the gap between two crystals, but

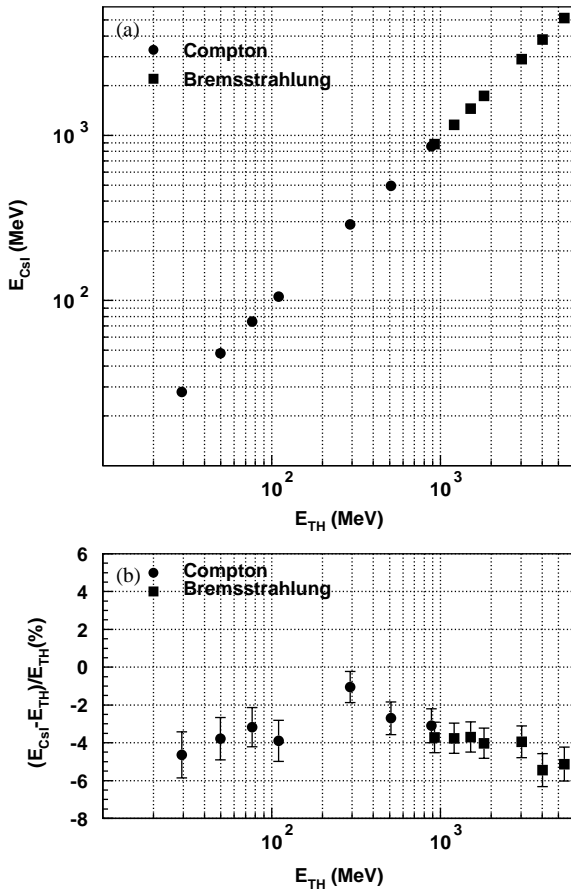


Fig. 88. (a) The incident photon energy vs. the measured energy in CsI from data, and (b) the energy linearity obtained from the data.

shows systematic shifts at the other positions. In order to correct the systematic effect an empirical function was used to get the correlation between  $X_{beam}$  and  $X_{cg}$  and to calculate the corrected position  $X_{cor}$ . Fig. 91(b) shows a scatter plot of  $X_{beam}$  vs.  $X_{cor}$ . The systematic shift seen in Fig. 91(a) is almost removed. The residual distribution  $(X_{cor} - X_{beam})$  corresponds to the average resolution of the corrected beam-impact position.

Fig. 92 shows the position dependence of the spatial resolution for 470 MeV photons. The solid and open circles correspond to the experimental data and Monte Carlo results, respectively. The energy dependence of the average position resolu-

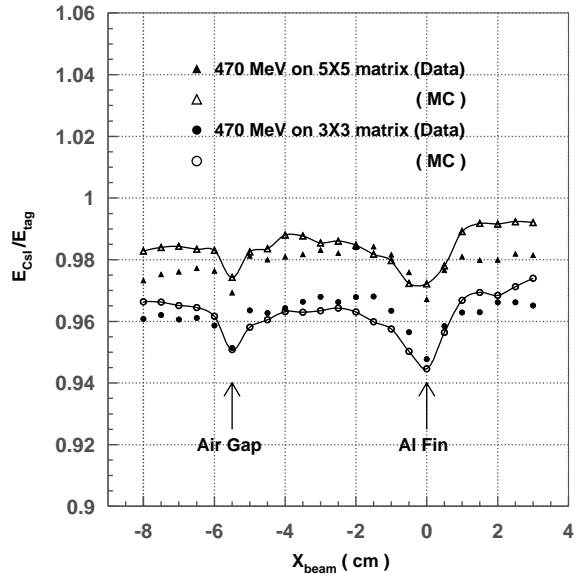


Fig. 89. Position dependence of the energy deposit. The solid triangles and circles are the results obtained by a GEANT Monte Carlo simulation.

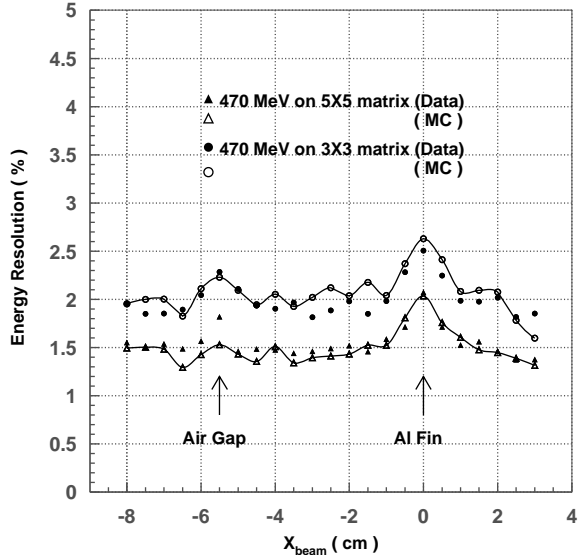


Fig. 90. Position dependence of the energy resolution. The open triangles and circles are the results obtained by a GEANT Monte Carlo simulation.

tion is shown in Fig. 93 as a function of photon energy. The points above 1 GeV are Monte Carlo data. The solid curve is fitted by the relation

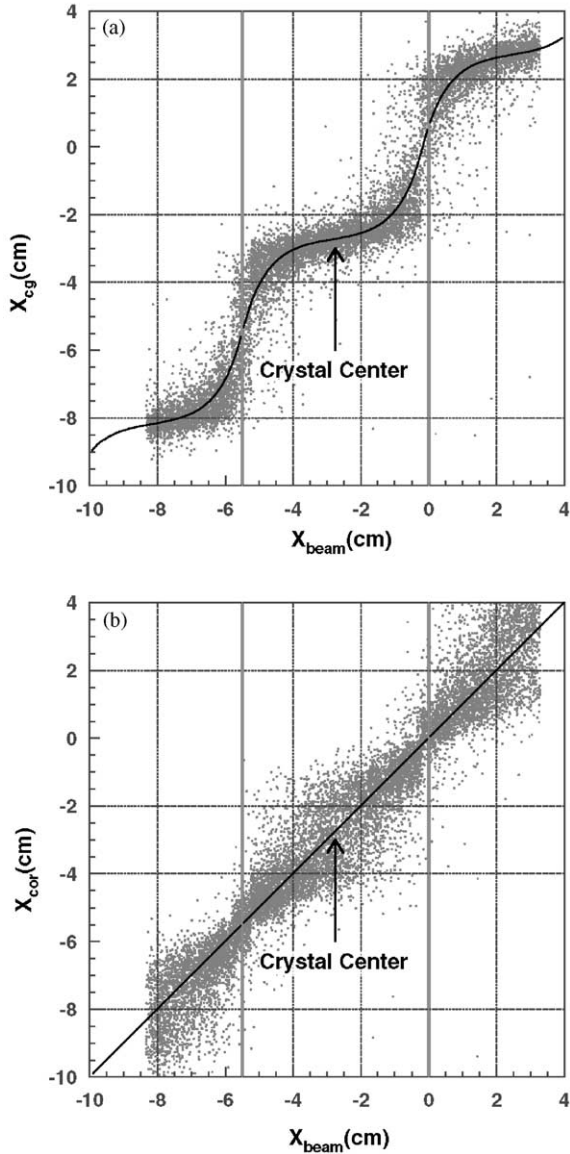


Fig. 91. Scatter plots of  $X_{\text{beam}}$  and  $X_{\text{cg}}$  (a) before and (b) after a correction. The gap between the crystals is shown by the thick vertical lines. The solid curve in (a) is the fit to an empirical formula.

$$\sigma_X(\text{mm}) = 0.27 + \frac{3.4}{\sqrt{E}} + \frac{1.8}{\sqrt[4]{E}} \quad (20)$$

where  $E$  is measured in units of GeV.

The present results of the energy and spatial resolutions measured by the photon beams for the

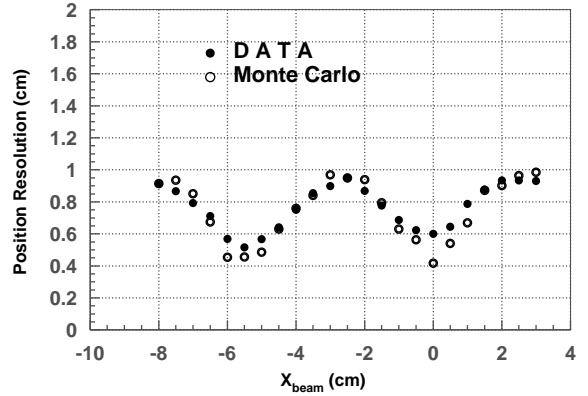


Fig. 92. Position dependence of the spatial resolution for 470 MeV photons.

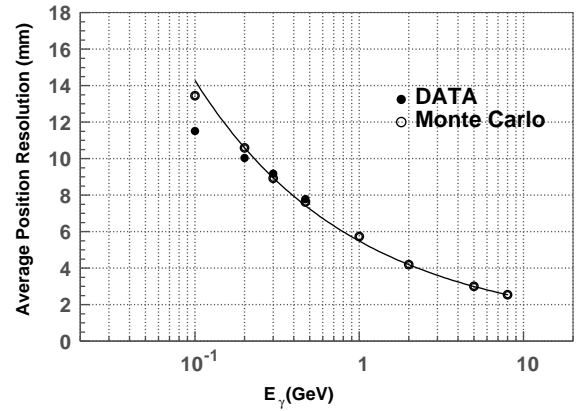


Fig. 93. Energy dependence of the average position resolution. The solid curve is a fit to Eq. (20).

Belle ECL prototype counters are in reasonable agreement with those measured using the electron beam at KEK in the energy range above 1 GeV [59].

### 8.3. Performance

Before the final installation, the light output of each crystal was calibrated by using cosmic-rays. The crystal by crystal variation of about 10% was measured. The channel-by-channel gain variation of electronics was found to be about 5%. After the installation into the Belle detector in the fall of 1998, the consistency and stability of the calibra-

tion constants have been monitored with cosmic-rays which penetrated through more than three neighboring counters. The stability of the crystal gains has been observed to be better than 1% during a period over 3 months [67].

The absolute energy calibration has been carried out by using Bhabha and  $e^+e^- \rightarrow \gamma\gamma$  events. With a Bhabha sample, the calibration constant of  $j$ th counter  $g_j$  can be obtained by minimizing  $\chi^2$  defined as

$$\chi^2 = \sum_k^{\text{events}} \left( \frac{E_k(\theta)f(\theta) - \sum_j g_j E_j}{\sigma} \right)^2 \quad (21)$$

where  $E_k$  is the expected energy of the Bhabha electrons. This value is known as a function of  $\theta$  in the asymmetric collider. The function  $f(\theta)$  is the correction factor due to the shower leakage and the front material effect, which was determined by a Monte Carlo simulation. This function was introduced in the  $\chi^2$  minimization in order to maintain the consistency between real and Monte Carlo events. The minimization was carried out by taking  $\sim 8000 \times 8000$  sparse matrix inversion into account. Approximately 50 events per counter were used for this calibration.

After the KEKB collider was commissioned in June 1999, a large number of Bhabha and  $\gamma\gamma$  events have been accumulated to perform the absolute counter-by-counter calibration. The energy resolution was achieved to be 1.7% for the barrel ECL, and 1.74% and 2.85% for the forward and backward ECL, respectively, as shown in Fig. 94.

Two-photon invariant mass distributions in hadronic events are shown in Figs. 95(a) and (b). The clear peaks of  $\pi^0$  and  $\eta$  are seen at each nominal mass and the energy resolution has been achieved to be 4.9 MeV for  $\pi^0$  and less than 10 MeV for  $\eta$ .

During the operation period of KEKB, ECL received radiation doses associated with the beam background. Thus, the light output of each CsI counter has decreased. The instantaneous dose rate is proportional to the total current through the PIN photodiode and the accumulated dose can be calculated by integrating the dose rate over the period of time. An increase of 2.5 nA/crystal for

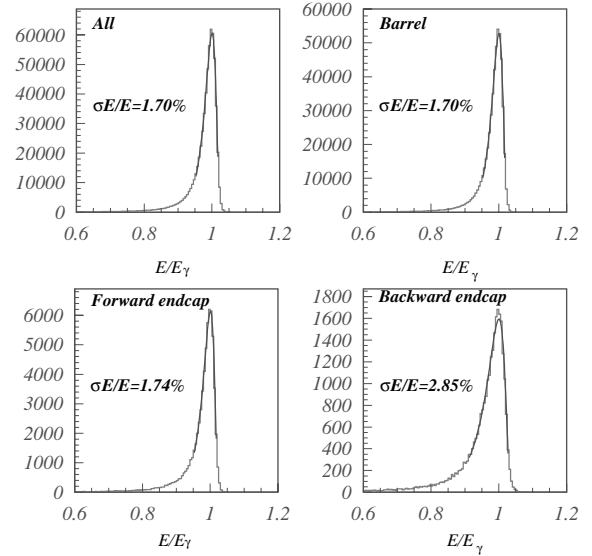


Fig. 94. Energy resolutions measured from Bhabha event samples: overall, barrel, forward end-cap and backward end-cap.

1 yr ( $\sim 10^7$  s) corresponds to 100 rad. During the period of June and July 1999, ECL was irradiated with the dose of 4 and 13 rad/crystal for the barrel and innermost backward end-cap ECL, respectively, as shown in Figs. 96(a) and (b). Fig. 97 shows the degradation rate of light output as a function of  $\theta$ . The light output decreased about 1% in the barrel region and about 2% in the end-cap regions.

## 9. $K_L$ and muon detection system, KLM

The KLM detection system was designed to identify  $K_L$ 's and muons with high efficiency over a broad momentum range greater than 600 MeV/c. The barrel-shaped region around the interaction point covers an angular range from  $45^\circ$  to  $125^\circ$  in the polar angle and the end-caps in the forward and backward directions extend this range to  $20^\circ$  and  $155^\circ$  [4,68].

### 9.1. Design and construction

Fig. 1 shows the side view of the Belle detector with the indicated location of the KLM detection

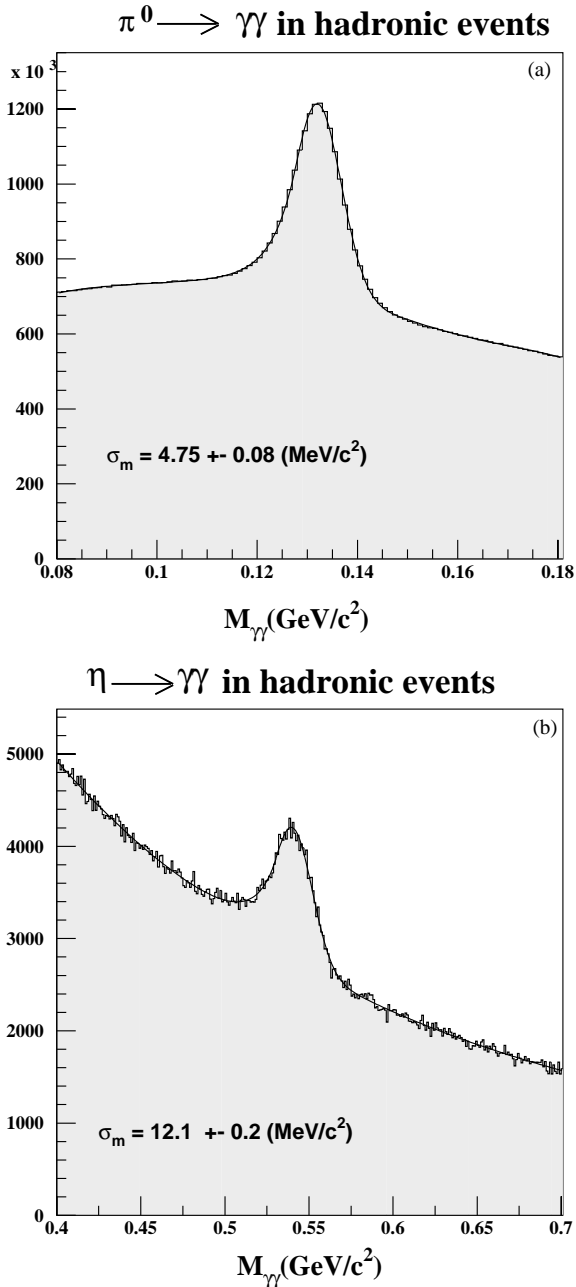


Fig. 95. Two photon invariant mass distribution for hadronic events (a) in  $\pi^0 \rightarrow \gamma\gamma$  and (b) in  $\eta \rightarrow \gamma\gamma$  where each photon energy was required to be greater than 30 MeV in the barrel region.

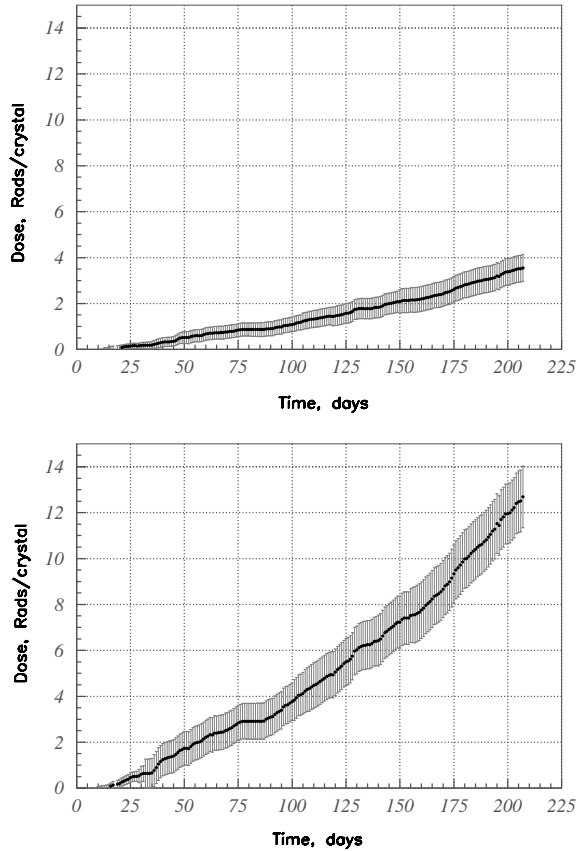


Fig. 96. Radiation dose at barrel ECL (upper) and end-cap ECL (lower) as a function of time.

system. KLM consists of alternating layers of charged particle detectors and 4.7 cm-thick iron plates. There are 15 detector layers and 14 iron layers in the octagonal barrel region and 14 detector layers in each of the forward and backward end-caps. The iron plates provide a total of 3.9 interaction lengths of material for a particle traveling normal to the detector planes. In addition, the electromagnetic calorimeter, ECL, provides another 0.8 interaction length of material to convert  $K_L$ 's.  $K_L$  that interacts in the iron or ECL produces a shower of ionizing particles. The location of this shower determines the direction of  $K_L$ , but fluctuations in the size of the shower do not allow a useful measurement of the  $K_L$  energy. The multiple layers of charged particle detectors and iron allow the discrimination between muons and charged hadrons ( $\pi^\pm$  or  $K^\pm$ ) based upon their

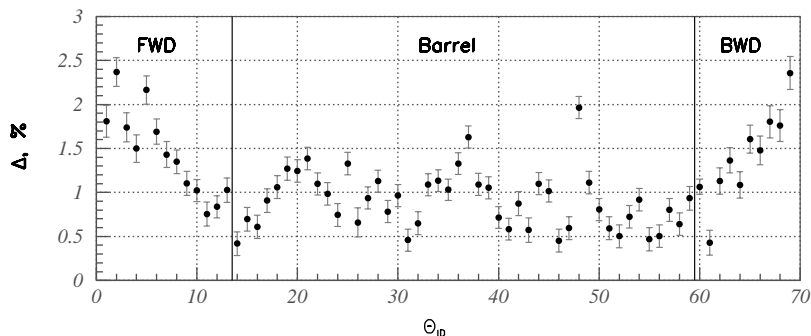


Fig. 97. Degradation of the light output of the ECL counters as a function of  $\theta$ -id.

range and transverse scattering. Muons travel much farther with smaller deflections on average than strongly interacting hadrons.

#### 9.1.1. Glass-resistive plate counters

The detection of charged particles is provided by glass-electrode-resistive plate counters (RPCs) [69–73]. Glass RPCs have a long history dating back to the early 1970s [74], but this is the first experiment in which large area glass detectors operated at atmospheric pressure have been used. Resistive plate counters have two parallel plate electrodes with high bulk resistivity ( $\geq 10^{10} \Omega \text{ cm}$ ) separated by a gas-filled gap. In the streamer mode, an ionizing particle traversing the gap initiates a streamer in the gas that results in a local discharge of the plates. This discharge is limited by the high resistivity of the plates and the quenching characteristics of the gas. The discharge induces a signal on external pickup strips, which can be used to record the location and the time of the ionization.

#### 9.1.2. Barrel modules

There are minor differences between the barrel and the end-cap modules. The barrel-resistive plate counters which were constructed in the United States consist of two parallel sheets of 2.4-mm-thick commercially available float glass, the content of which is 73% silicon dioxide, 14% sodium oxide, 9% calcium oxide, and 4% trace elements. The bulk resistivity of the glass is  $10^{12}$ – $10^{13} \Omega \text{ cm}$  at room temperature. The plates are separated by 1.9 mm thick extruded noryl spacers epoxied to

both plates using 3M 2216 epoxy. Fig. 98 shows a barrel RPC with the spacers placed every 10 cm so that they channel the gas flow through the RPC to provide uniform gas composition throughout the active volume. A T-shaped noryl spacer was epoxied around the perimeter forming a gas tight unit. The spacers have the cross-sections shown in Fig. 99. They were designed with concave regions for the epoxy joints and were extruded to an accuracy of  $\pm 0.05 \text{ mm}$ . Tilting table tops were used to lift the RCPs into the vertical orientation to avoid flexing the epoxy joints. After assembly, the RCPs were always moved in the vertical orientation or supported by a rigid flat surface. The barrel RPCs are rectangular in shape and vary in size  $2.2 \times 1.5$ – $2.2 \times 2.7 \text{ m}^2$ .

To distribute the high voltage on the glass, the outer surface was coated with Koh-i-noor 3080F india ink. The ink was mixed 30% black and 70% white by weight to achieve a surface resistivity of  $10^6$ – $10^7 \Omega/\text{square}$ . This resistivity is chosen so that this surface does not shield the discharge signal from the external pickup pads but is small compared to the resistivity of the glass to provide a uniform potential across the entire surface.

Fig. 100 shows the cross-section of a superlayer, in which two RPCs are sandwiched between the orthogonal  $\theta$  and  $\phi$  pickup-strips with the ground planes for signal reference and proper impedance. This unit structure of two RPCs and two readout-planes is enclosed in an aluminum box and is less than 3.7 cm thick. Each RPC is electrically insulated with a double layer of 0.125 mm thick mylar. Signals from both RPCs are picked up by

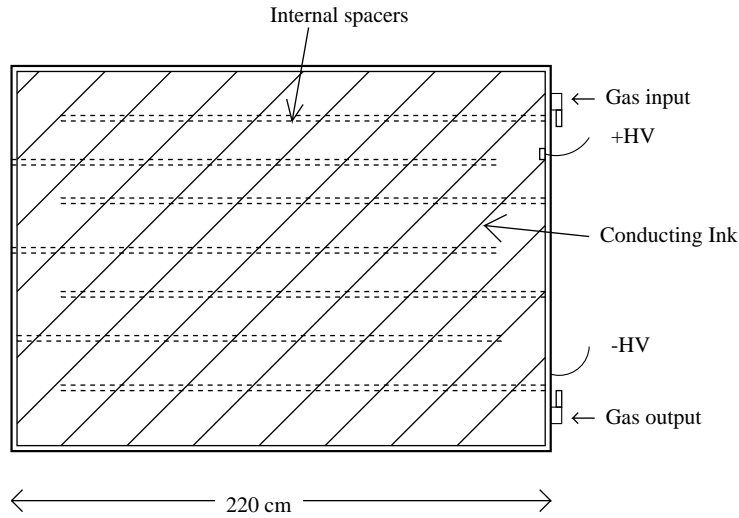


Fig. 98. Schematic diagram of the internal spacer arrangement for barrel RPC.

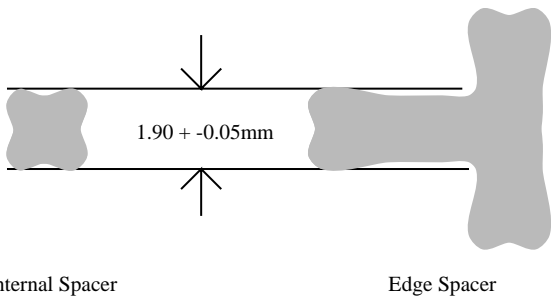


Fig. 99. Cross-section of the internal spacer and edge in KLM.

copper strips above and below the pair of RPCs, providing a three-dimensional space point for particle tracking. Multiple scattering of particles as they travel through the iron is typically a few centimeters. This sets the scale for the desired spatial resolution of KLM. The pickup strips in the barrel vary in width from layer to layer but are approximately 50 mm wide with lengths from 1.5 to 2.7 m. The geometry of the pickup strips was chosen so that the pickup strip behaves as a transmission line with a characteristic impedance of  $\sim 50 \Omega$  to minimize signal reflections at the junction with the twisted-pair readout cable. The barrel modules have a  $100 \Omega$  resistor connecting the pickup strip to ground at the cable end of the pickup strip to create an effective impedance of  $50 \Omega$  at that point. This reduces the size of the

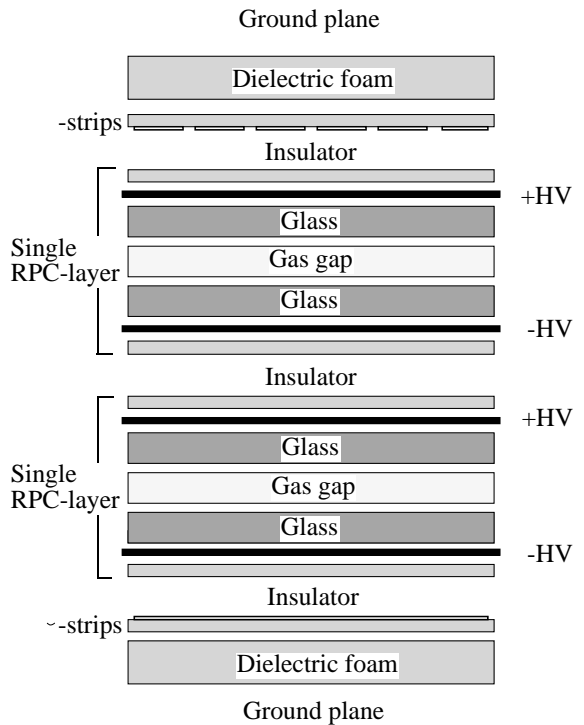


Fig. 100. Cross-section of a KLM superlayer.

signal which reaches the readout boards for the barrel modules by a factor of two.

The double-gap design provides redundancy and results in high superlayer efficiency of

$\geq 98\%$ , despite the relatively low single-layer RPC efficiency of 90–95%. In particular, the effects of dead regions near the spacers are minimized by offsetting their locations for the two RPCs that comprise a superlayer. To provide overall operational redundancy, care is taken to supply gas and HV independently for each RPC layer so that the superlayer can continue to operate even if a problem develops with one RPC.

Each barrel module has two rectangular RPCs with 48  $z$  pickup strips perpendicular to the beam direction. The smaller 7 superlayers closest to the interaction point have 36  $\phi$  strips and the outer 8 superlayers have 48  $\phi$  strips orthogonal to the  $z$  strips. The backward region of the upper octant has modules that are 63 cm shorter than the modules in the other octants in order to accommodate plumbing for the cooling of the superconducting solenoid. This chimney region can be seen in Fig. 1. This amounts to less than 2% of the solid angle of the barrel coverage and has a minimal effect on the acceptance since it is in the backward hemisphere.

The glass RPCs are relatively robust except for overpressure situations which can push the two sheets of glass apart, breaking the glass-spacer epoxy joint. To avoid this hazard, the gas volume was not sealed during shipping. Relief bubblebers protect the RPCs during operation. The RPCs

were checked for gas leaks prior to installation. The sensitivity of our measurement was about  $0.05 \text{ cm}^3/\text{min}$  and this was the leak rate limit we set for all installed RPCs.

### 9.1.3. End-cap modules

The glass used in the end-cap RPCs is 2.0 mm thick and has a chemical content of  $\text{SiO}_2$  70–74%,  $\text{CaO}$  6–12%,  $\text{Na}_2\text{O}$  12–16%,  $\text{Al}_2\text{O}_3$  0–2%, and  $\text{MgO}$  0–4%. The epoxy used to attach the spacers and to seal the gas volume was 3M DP460. The high voltage distribution on the glass was accomplished by applying a conducting carbon tape SHINTRON STR-9140 with a surface resistivity of  $10^7$ – $10^8 \Omega/\text{square}$  to the outer surface of the glass.

Each superlayer module contains 10  $\pi$ -shaped RPCs as shown in Fig. 101. The  $\theta$  strips are 36 mm wide and vary in length from 2 to 5 m. The  $\phi$  strips are 1.83 m long and vary in width from 19 to 47 mm. Fig. 102 shows an end-cap superlayer module cutaway view with the 96  $\phi$  and 460 pickup-strips in each module.

### 9.1.4. High-voltage system

During data taking, the modules are operated typically with a total gap voltage of 8 kV. We chose to separately apply positive voltage to the anodes and negative voltage to the cathodes. This

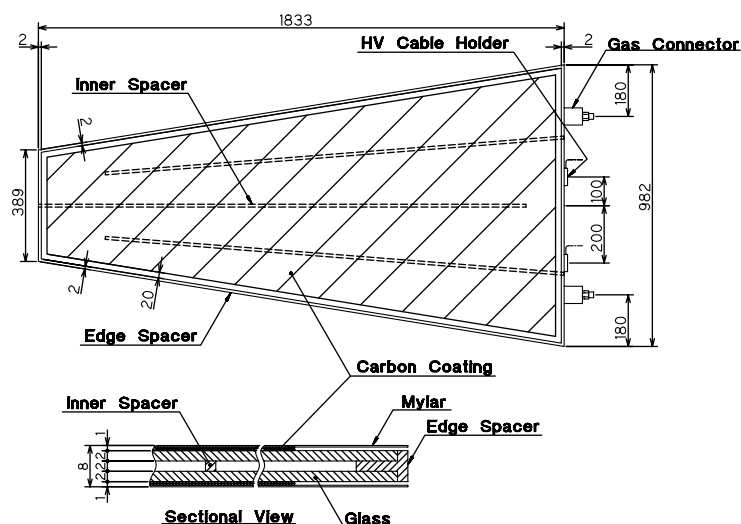


Fig. 101. Schematic diagram of the internal spacer arrangement of the end-cap RPC.

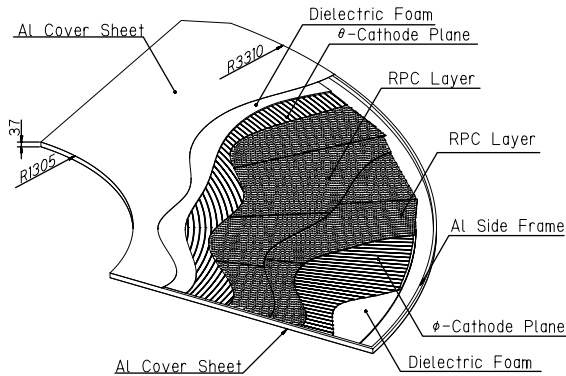


Fig. 102. Cut-away view of an end-cap superlayer module of KLM.

approach minimizes external discharges through and around insulators. Moreover, it helps reduce the overall HV system cost.

The LeCroy VISyN high-voltage system is used which consists of Model 1458 mainframes and plug-in modules, Model 1468P for the anodes and Model 1469N for the cathodes. The cathodes are set at  $-3.5$  kV, and the anodes are set at  $+4.7$  kV for the barrel RPCs and  $+4.5$  kV for the end-cap RPCs. To reduce the system cost, the anode planes are ganged together and controlled by one positive high-voltage channel. In the barrel, eight anode planes are ganged together, while in the end-caps, five anode planes are ganged together. The total current drawn by the RPCs during operation is approximately  $5$  mA or  $\sim 1\mu\text{A}/\text{m}^2$  of the RPC area. For properly operating chambers, most of this current flows through the noryl spacers.

#### 9.1.5. Gas mixing and distribution

We have investigated gas mixtures in search of an environmentally friendly and non-combustible mixture that provides high detection efficiency and stable RPC operation [76]. We compared 16 different mixtures with butane concentrations of 4%, 8%, 12%, and 25% and argon concentrations of 20%, 25%, 30%, and 35% with the balance of the gas being HFC-134a. The RPC performance in terms of efficiency, dark current, singles rate, and timing resolution was compared at an operating point  $200$  V/mm above the knee of the efficiency plateau curve. The butane reduces the presence of after-pulses by absorbing photons from the initial

Table 10

Physical parameters of the gases used in KLM

Gas	Symbol	Mol. weight	Density (g/l)
Argon	Ar	39.95	1.784 (0°C, 1atm)
Butane–silver	$\text{C}_4\text{H}_{10}$	58.12	2.6 (0°C, 1atm)
HFC-134a	$\text{CH}_2\text{FCF}_3$	102.0	4.5

discharge. The non-flammable limit for the butane is about 12% at the mixing ratio of 1:1 for the argon and HFC-134a. We found very little difference between flammable and non-flammable mixtures and have chosen a non-combustible mixture of 62% HFC-134a, 30% argon, and 8% butane–silver. Table 10 lists some basic physical parameters of these gases. Butane–silver is a mixture of approximately 70% n-butane and 30% iso-butane. The cost of butane–silver is one-tenth of the cost of 99.5% pure iso-butane.

Two separate banks of bottles are arranged for each type of gas. When one side becomes empty, the supply line automatically switches to the other. Tank quantities are measured by weight for butane and HFC-134a and by pressure for argon. A diagram of the mixing system is shown in Fig. 103. The three gases are sent to MKS model 1179A mass flow controllers for mixing in the appropriate ratios. Four gas mixing systems are used separately for the inner RPCs in the barrel superlayers, the barrel outer RPCs, the end-cap inner RPCs, and the end-cap outer RPCs. The flow rates from the mass flow controllers are monitored via a network connection and the high voltage is automatically lowered if a deviation from the desired flow rate is detected. During normal operation, we flow a total of  $4.5$  l/min, which corresponds to approximately one volume change per day.

The gas distribution system is designed to provide an independent gas supply to each RPC in a superlayer. Therefore, if one supply line fails for any reason, the other RPC in the same superlayer will still be operational. To ensure uniform distribution of the flow without the need for tedious adjustments, a “flow resistor” was inserted in series upstream of each RPC. These devices are 10-cm-long stainless-steel tubes with an inner diameter of  $254\mu\text{m}$ . The flow impedance of

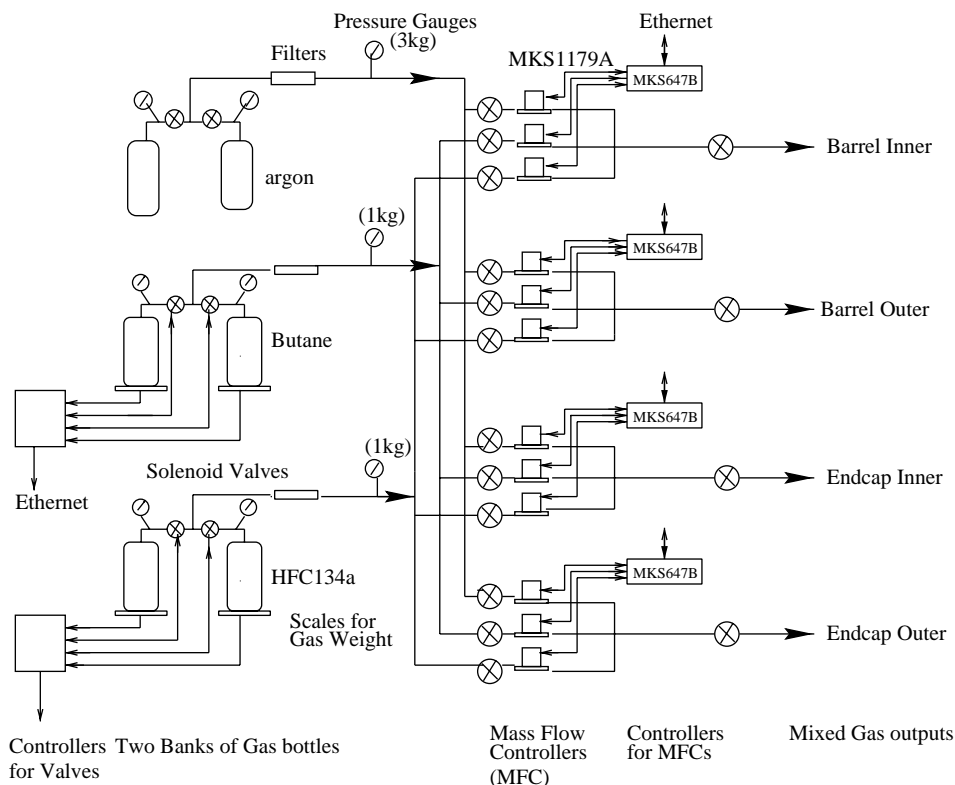


Fig. 103. KLM gas mixing system.

the tubes is about 10 times larger than that of an RPC layer. Thus, the flow rate is determined by the flow resistor (uniform to about 15%) and almost independent of variations in the flow resistance of individual RPCs.

The exhaust system has an active control of the exhaust pressure and relief bubblers at various points in the system to prevent any overpressure situations. Tests indicated that epoxy joints between the glass plates and the internal spacers begin to detach when a barrel RPC is pressurized above 50 mmAq. For safety reasons, the exhaust gas is dumped outside the experimental hall through a 20 m vertical exhaust line. Due to the large density of the mixed gas a suction pump system is used.

## 9.2. Readout electronics

Readout of 38k pickup strips is accomplished with the use of custom-made VME-based discrimi-

minator/time-multiplexing boards developed by Princeton University and Osaka City University groups. The system consists of the signal discrimination and multiplexing boards, crate controller boards (one per crate) for crate-wide control and data processing, string controller boards for downloading and controlling multiple readout crates, and FASTBUS time-to-digital converters.

The discriminator boards are 6U-size VME boards with 96 input channels per board. A comparator (MAX908CPD) is used to generate a logic signal if the voltage on the input channel exceeds the threshold voltage. This threshold can be selected via a programmable digital-to-analog converter to be any value from  $-250$  mV to  $+250$  mV. A time multiplexer scheme combines hit information from 12 RPC channels into a single high-speed serial data stream that is passed to a LeCroy 1877 pipelined TDC. The multiplexing is accomplished with a Xilinx XC4005E FPGA. A schematic diagram of the readout

electronics is shown in Fig. 104. In addition, the logical OR of the hits for each 12-channel group is generated and is available for use as a fast trigger signal.

Each VME crate has a crate-controller board which transmits control data from the string controller to the discriminator boards via the dedicated VME backplane. A 10 MHz clock signal from the crate-controller board is distributed throughout the crate for the discriminator boards in time sequencing the RPC hits. The string controller is a multi-function VME-compatible board using a Xilinx 4013 programmable gate array to allow downloading and control of a string of up to 8 RPC readout crates. Once the discriminator board is programmed, the time sequenced hit information travels directly from each 96 channel board to 8 TDC channels residing in a FASTBUS crate. In this manner, 38k RPC channels are reduced to 3200 FASTBUS TDC channels, resulting in significant cost savings. It is also possible to read RPC strip-hit data directly through the string controllers, as was done during system commissioning when the production TDC system was not yet available.

9.3. Efficiency and resolution

The relatively high resistance of the glass [75],  $\sim 5 \times 10^{12} \Omega \text{ cm}$ , limits the rate capability of these counters to  $\sim 0.2 \text{ Hz/cm}^2$ . However, in the present

application in which the particle flux is little more than the cosmic-ray flux, the detectors function with high efficiency. Signals typically have a 100 mV peak into a 50  $\Omega$  termination and have a full-width at half-maximum of less than 50 ns. A typical RPC has a singles rate of less than 0.03 Hz/cm<sup>2</sup> with few spurious discharges or after-pulses. We operate the barrel (end-cap) modules at 4.3 (4.2) kV/mm with a signal threshold of 40 (70) mV. The choice of different operating points is due to the differences in the characteristics of the pickup strips for the barrel and end-cap modules.

Fig. 105 shows efficiency vs. voltage curves for individual RPC layers alone and in combination in a typical superlayer in the end-cap. These data were obtained using cosmic-rays. The efficiency was obtained by tracing a particle using other superlayers. The predicted location of the track was searched within  $\pm 1$  strip. Although the area near the internal spacers is inactive, care was taken to ensure that the internal spacers do not overlap. Under the normal operating condition, the superlayer acts as a logical “OR” for hits in either RPC layer and has an average efficiency typically over 98%.

Cosmic-rays were used to map the efficiency and to determine the relative positions of all the superlayer modules. In addition, the response of the modules to penetrating muons was measured and the results were used as input to the simulation

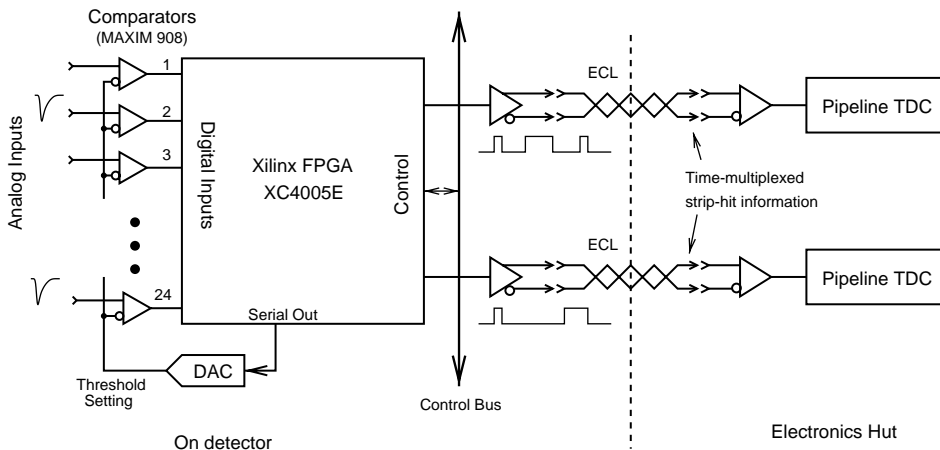


Fig. 104. Schematic diagram of the KLM readout electronics.

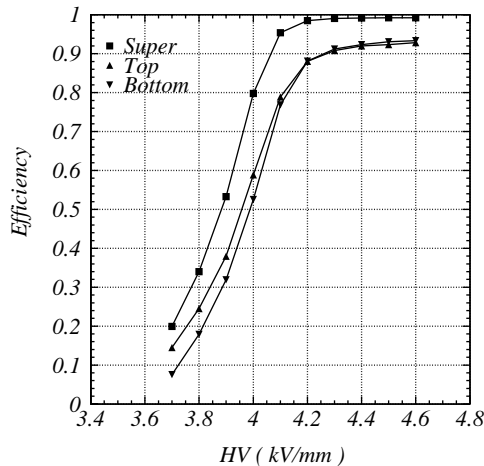


Fig. 105. Efficiency plateau curves for RPCs alone and in combination in a typical superlayer of KLM.

programs. For example, for a given set of operating voltage and discriminator threshold, a penetrating muon generates the average hits of 1.4 strips and 1.9 strips per layer in the barrel and end-cap modules, respectively.

The spatial resolution of the modules is shown in Fig. 106. This residual distribution is the difference between the measured and predicted hit locations using a track that has been fitted using hits in the adjacent layers. The multiplicity referred to is the number of strips in the superlayer that have signals over threshold. When two or more adjacent strips have signals over threshold, the hit location used for particle tracking is calculated by averaging the strips together. For hits with 1, 2, 3, and 4 strips, the standard deviations are 1.1, 1.1, 1.7, and 2.9 cm, respectively. The multiplicity weighted standard deviation for this residual distribution is 1.2 cm and gives angular resolution from the interaction point of better than 10 mrad. TDCs provide time information for the hits that can be used to eliminate hits which are out of time with respect to the  $e^+e^-$  collision. The time resolution of KLM is a few ns.

#### 9.4. Performance

The system has been operating over 1 yr. When we first installed the modules, we used  $\frac{1}{4}$  in.

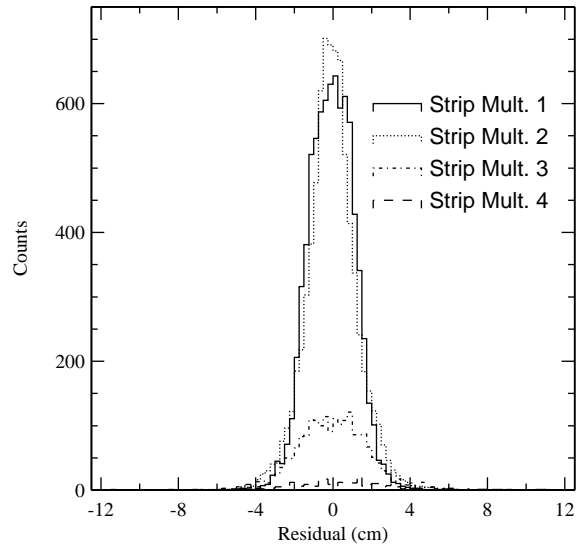


Fig. 106. Spatial resolution of a superlayer of KLM.

diameter flexible polyolefin tubing from the gas distribution manifolds to the RPCs. After several weeks of operation, we noticed an increase in the dark current drawn by some of the RPCs and the corresponding decrease in efficiency. This was found to be due to water vapor in the air migrating through the tubing and entering the RPC active volume. Some of these tubes were as long as 12 m and we measured concentrations of  $H_2O$  as high as 2000 ppm in some RPC exhaust lines. Approximately 50% of the barrel modules were affected. The efficiency of some barrel RPCs dropped below 50% before corrective measures were taken. We replaced the plastic tubing with copper tubing to prevent additional water vapor entering the RPCs. The contaminated RPCs eventually dried out and have recovered most of their lost efficiency. Other than the initial water vapor problem, which has been solved, the RPCs have been operated reliably and with an average efficiency of better than 97%.

##### 9.4.1. $K_L$ detection

In order to identify  $K_L$ , a cluster must be observed in KLM. Then, tracks of charged particles measured in CDC are extrapolated into KLM. Clusters within  $15^\circ$  of an extrapolated charged particle track are excluded from  $K_L$  cluster candidates. For an isolated cluster, the

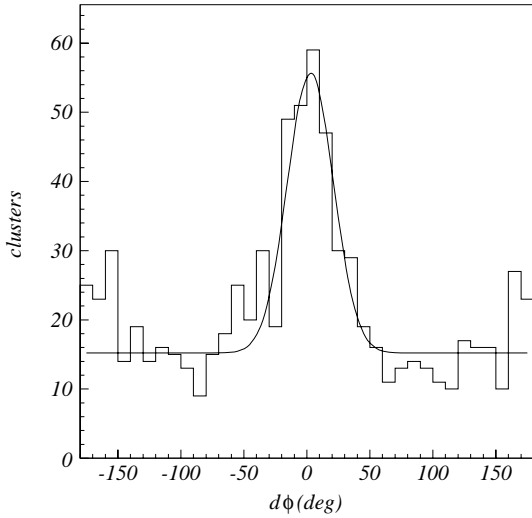


Fig. 107. Difference between the neutral cluster and the direction of missing momentum in KLM.

center of gravity of the hits is calculated and used to determine the direction of the cluster from the interaction point. Fig. 107 shows a histogram of the difference between the direction of the  $K_L$  cluster candidate and the missing momentum direction. The data was obtained during the summer 1999 commissioning run of the KEK B-factory. The missing momentum vector is calculated using all the other measured particles in the event. The histogram shows a clear peak where the direction of the neutral cluster measured in KLM is consistent with the missing momentum in the event. A large deviation of the missing momentum direction from the neutral cluster direction is mainly due to undetected neutrinos and particles escaping the detector acceptance. Fig. 108 shows the number of neutral clusters per event and a Monte Carlo simulation of the predicted number of  $K_L$  clusters per event. The average number of  $K_L$  clusters per event is 0.5. The agreement with the prediction gives us the confidence that the detector and our reconstruction software are performing correctly.

#### 9.4.2. Muon detection

Cosmic-rays were used to measure the detection efficiency and resolution of the superlayers. The momenta of cosmic muons were measured by

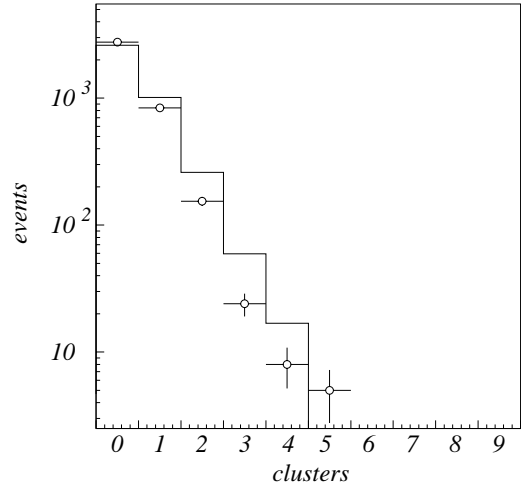


Fig. 108. Number of neutral clusters per event in KLM.

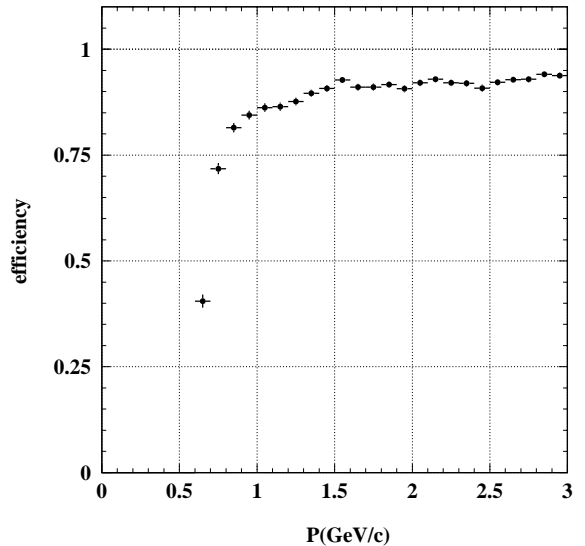


Fig. 109. Muon detection efficiency vs. momentum in KLM.

CDC with the solenoid field of 1.5 T. Below 500 MeV/c, the muon does not reach KLM. A comparison of the measured range of a particle with the predicted range for a muon allows us to assign a likelihood of being a muon. In Fig. 109 the muon detection efficiency vs. momentum is shown for a likelihood cut of 0.66. Some fraction of charged pions and kaons will be misidentified as muons. A sample of  $K_S \rightarrow \pi^+\pi^-$  events in the  $e^+e^-$

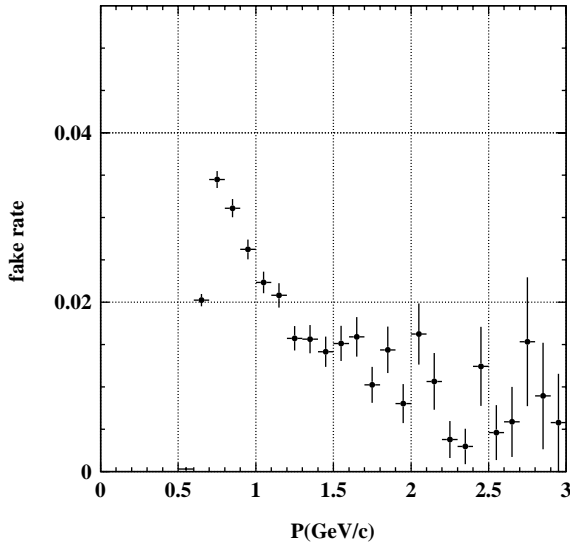


Fig. 110. Fake rate vs. momentum in KLM.

collision data was used to determine this fake rate. The fraction of pions which are misidentified as muons is shown in Fig. 110, again with a muon likelihood cut of 0.66. The solid points with error bars are the measured data and the histogram is the result of a Monte Carlo simulation. Above 1.5 GeV/c we have a muon identification efficiency of better than 90% with a fake rate of less than 5%.

## 10. Detector solenoid and iron structure

### 10.1. Solenoid magnet

A superconducting solenoid provides a magnetic field of 1.5 T in a cylindrical volume of 3.4 m in diameter and 4.4 m in length [77,4,6]. The coil is surrounded by a multilayer structure consisting of iron plates and calorimeters, which is integrated into a magnetic return circuit. The main coil parameters are summarized in Table 11. The overall structure of the cryostat and the schematic drawing of the coil cross-section are shown in Fig. 111.

Table 11

Main parameters of the solenoid coil

Items	Parameters
Cryostat	
Radius: outer/inner	2.00 m/1.70 m
Central field	1.5 T
Total weight	23t
Effective cold mass	~6t
Length	4.41 m
Coil	
Effective radius	1.8 m
Length	3.92 m
Conductor dimensions	3 × 33 mm <sup>2</sup>
Superconductor	NbTi/Cu
Stabilizer	99.99% aluminum
Nominal current	4400 A
Inductance	3.6 H
Stored energy	35 MJ
Typical charging time	0.5 h
Liquid helium cryogenics	Forced flow two phase
Cool down time	≤ 6 day
Quench recovery time	≤ 1 day

### 10.2. Iron yoke

The iron structure of the Belle detector serves as the return path of magnetic flux and an absorber material for KLM [4,6]. It also provides the overall support for all of the detector components. It consists of a fixed barrel part and movable end-cap parts, both on the base stand. The barrel part, shown in Fig. 112, consists of eight KLM blocks and 200-mm thick flux-return plates surrounding the outermost layers of the KLM blocks. Neighboring KLM blocks are joined using fitting blocks. Each end-cap part can be retracted for an access to the inner detectors.

The weight of the iron yoke is 608 and 524 (= 262 × 2) ton for the barrel yoke and end-cap yokes, respectively.

### 10.3. Magnetic field mapping of the Belle solenoid

The magnetic field mapping was carried out with the accelerator magnets located inside the Belle solenoid excited to their nominal field values [78]. The two superconducting magnet complexes, QCS-R and QCS-L, are inserted in the holes along the axis of the end yokes. Each magnet complex

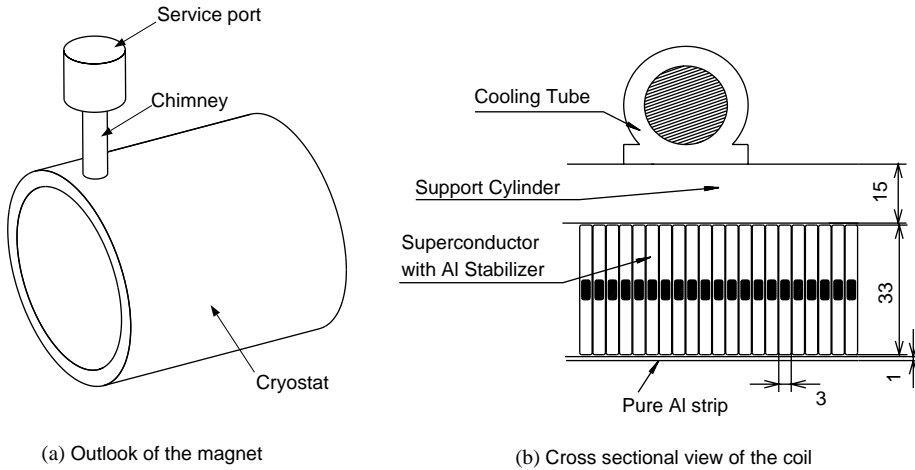


Fig. 111. An outlook of the solenoid and the cross-sectional view of the coil.

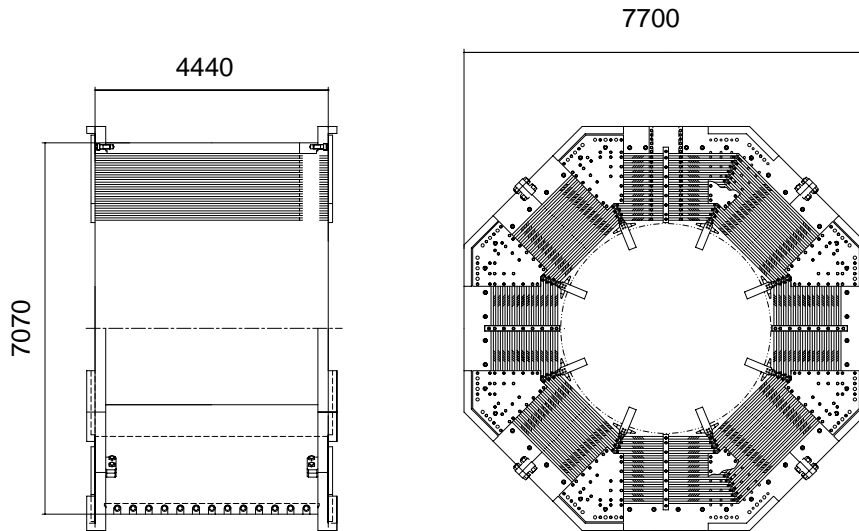


Fig. 112. Barrel part of the iron yoke.

consists of a solenoidal coil for compensation of the Belle solenoidal field, a quadrupole for focusing of the beams onto the interaction point, and several correction coils all located in a single cryostat [79].

Fig. 113 shows the side and end views of the field mapping arrangement and a conceptual illustration of the field mapping device is shown in Fig. 114. The volume to be mapped was reasonably isolated from the outside because of

the limited gap between the pole tips and the QCS cryostat. Since the accessibility was limited, the field mapping device must be fully contained inside the Belle solenoid. Conventional magnetic motors could not be used to drive the device. We used an ultrasonic motor as a driver [80].

A commercial field probe with three orthogonally oriented Hall sensors was used to measure the  $r, z$  and  $\phi$  field components [81]. An NMR probe installed on one of the connecting rods provided

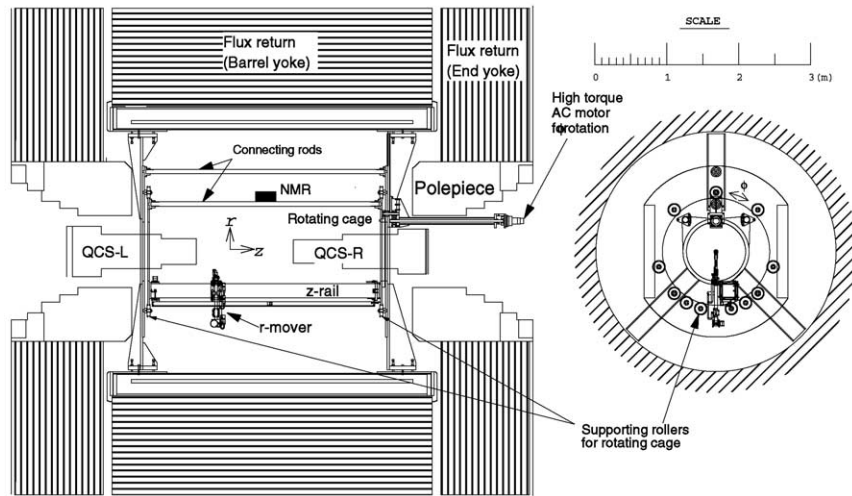


Fig. 113. Side and end views of the field mapping device. Some of the rods connecting both end-plates are not shown.

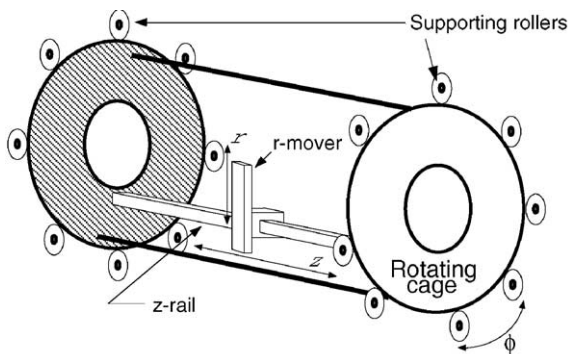


Fig. 114. Conceptual illustration of the field mapping device.

an absolute calibration of field strength with a precision better than 1 G [82]. It was also used to monitor the stability of the magnet during the measurement.

A field map of 100,000 points was made for a period of a month. Fig. 115 shows a contour plot of fields measured inside the tracking volume for the nominal magnet settings. The field strength is shown in Fig. 116 as a function of  $z$  for various radii. The tracking performance was evaluated with the reconstructed mass peak of  $J/\psi$  particles from  $B$  meson decays. The fitted value of the peak mass was  $3.089 \text{ GeV}/c^2$  compared with the estab-

lished value of  $3.0969 \text{ GeV}/c^2$ . Thus, the uncertainty in the absolute calibration of the present measurement is estimated to be approximately 0.25%.

## 11. Trigger

The total cross-sections and trigger rates at the goal luminosity of  $10^{34}/\text{cm}^2/\text{s}$  for various physical processes of interest are listed in Table 12. We need to accumulate samples of Bhabha and  $\gamma\gamma$  events to measure the luminosity and to calibrate the detector responses, but, since their rates are very large, these trigger rates must be prescaled by a factor  $\sim 100$ . Because of their distinct signatures, this should not be difficult. Although the cross-section for physics events of interest is reasonably small, they can be triggered by appropriately restrictive conditions.

Because of the high beam current, high beam backgrounds are expected. Based on simulation studies, we expect  $\sim 100 \text{ Hz}$  from beam-related backgrounds which are dominated by spent electrons and positrons. Since the rates are very sensitive to actual accelerator conditions, it is difficult to make a reliable estimate. Therefore, the trigger system is required to be robust against

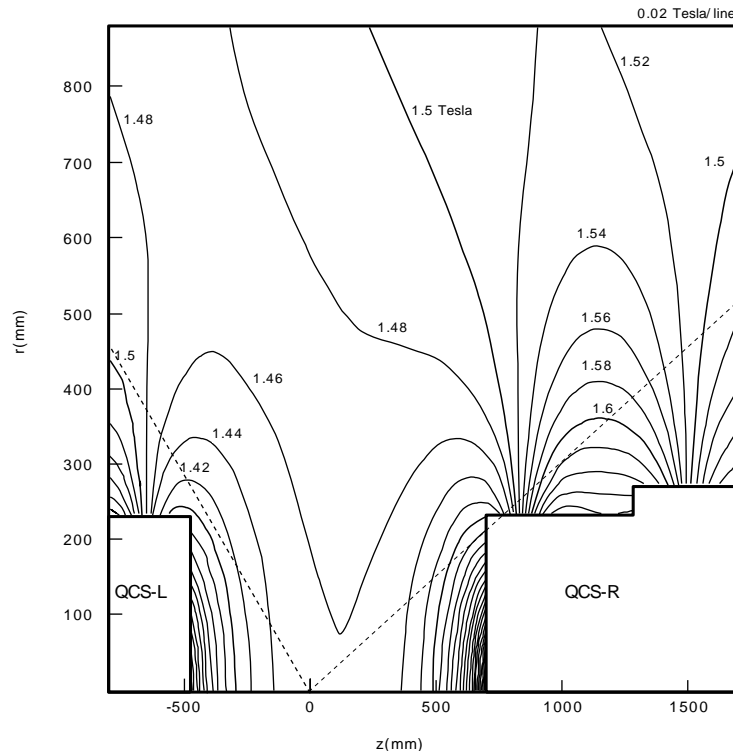


Fig. 115. Contour plot of magnetic fields measured in the Belle coordinate system with the origin at the interaction point.

unexpectedly high beam background rates. The trigger conditions should be flexible so that background rates are kept within the tolerance of the data acquisition system (max. 500 Hz), while the efficiency for physics events of interest is kept high. It is important to have redundant triggers to keep the efficiency high even for varying conditions. The Belle trigger system has been designed and developed to satisfy these requirements.

The Belle trigger system consists of the Level-1 hardware trigger and the Level-3 software trigger. The latter has been designed to be implemented in the online computer farm. Fig. 117 shows the schematic view of the Belle Level-1 trigger system [83]. It consists of the sub-detector trigger systems and the central trigger system called the Global Decision Logic (GDL). The sub-detector trigger systems are based on two categories: track triggers and energy triggers. CDC and TOF are used to yield trigger signals for charged particles. CDC provides  $r-\phi$  and  $r-z$  track trigger signals. The

ECL trigger system provides triggers based on total energy deposit and cluster counting of crystal hits. These two categories allow sufficient redundancy. The KLM trigger gives additional information on muons and the EFC triggers are used for tagging two photon events as well as Bhabha events. The sub-detectors process event signals in parallel and provide trigger information to GDL, where all information is combined to characterize an event type. Information from SVD has not been implemented in the present trigger arrangement.

Considering the ultimate beam crossing rate of 509 MHz ( $\sim 2$  ns interval) with the full bucket operation of KEKB [5], a “fast trigger and gate” scheme is adopted for the Belle trigger and data acquisition system. The trigger system provides the trigger signal with the fixed time of 2.2  $\mu$ s after the event occurrence. The trigger signal is used for the gate signal of the ECL readout and the stop signal of TDC for CDC, providing  $T_0$ . Therefore, it is important to have good timing accuracy. The

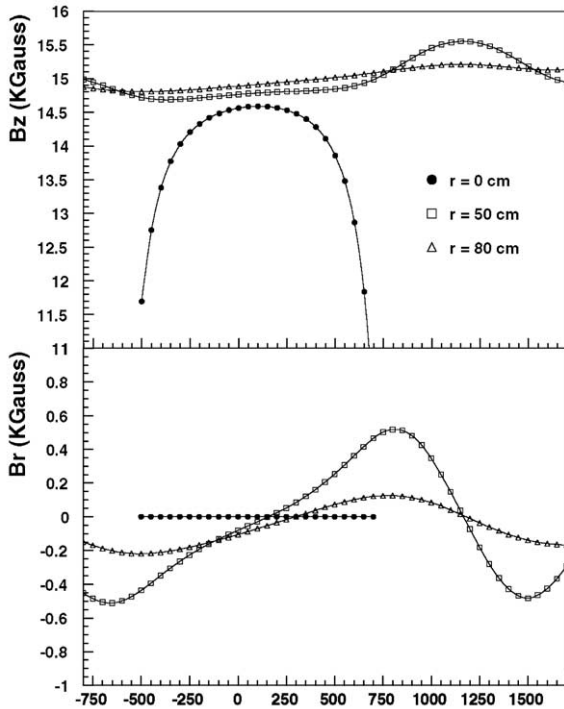


Fig. 116. Field strength as a function of  $z$  for  $r = 0, 50,$  and  $80$  cm.

Table 12

Total cross-section and trigger rates with  $L = 10^{34}/\text{cm}^2/\text{s}$  from various physics processes at  $\Upsilon(4S)$

Physics process	Cross section (nb)	Rate (Hz)
$\Upsilon(4S) \rightarrow B\bar{B}$	1.2	12
Hadron production from continuum	2.8	28
$\mu^+\mu^- + \tau^+\tau^-$	1.6	16
Bhabha ( $\theta_{\text{lab}} \geq 17^\circ$ )	44	4.4 <sup>a</sup>
$\gamma\gamma$ ( $\theta_{\text{lab}} \geq 17^\circ$ )	2.4	0.24 <sup>a</sup>
$2\gamma$ processes ( $\theta_{\text{lab}} \geq 17^\circ$ , $p_t \geq 0.1$ GeV/c)	$\sim 15$	$\sim 35$ <sup>b</sup>
Total	$\sim 67$	$\sim 96$

<sup>a</sup> Indicates the values pre-scaled by a factor 1/100.

<sup>b</sup> Indicates the restricted condition of  $p_t \geq 0.3$  GeV/c.

timing of the trigger is primarily determined by the TOF trigger which has the time jitter less than 10 ns. ECL trigger signals are also used as timing signals for events in which the TOF trigger is not available. In order to maintain the 2.2  $\mu\text{s}$  latency,

each sub-detector trigger signal is required to be available at the GDL input by the maximum latency of 1.85  $\mu\text{s}$ . Timing adjustments are done at the input of GDL. As a result, GDL is left with the fixed 350 ns processing time to form the final trigger signal. In the case of the SVD readout the TOF trigger also provides the fast Level-0 trigger signal with a latency of  $\sim 0.85$   $\mu\text{s}$ . The Belle trigger system, including most of the sub-detector trigger systems, is operated in a pipelined manner with clocks synchronized to the KEKB accelerator RF signal. The base system clock is 16 MHz which is obtained by subdividing 509 MHz RF by 32. The higher-frequency clocks, 32 and 64 MHz, are also available for systems requiring fast processing.

The Belle trigger system extensively utilizes programmable logic chips, Xilinx Field Programmable Gate Array (FPGA) and Complex Programmable Logic Device (CPLD) chips [84], which provide the large flexibility of the trigger logic and reduce the number of types of hardware modules.

### 11.1. CDC trigger system

The CDC trigger is one of the key elements of the Belle trigger system. It is required to be fully efficient for tracks originating from the interaction point and relatively insensitive to background tracks from other sources. CDC provides two types of triggers: the  $r$ - $\phi$  trigger based on signals from axial superlayers and the  $z$ -trigger which is formed from the direct  $z$  information provided by the cathode strips and  $z$  coordinates inferred from the axial and stereo superlayers.

#### 11.1.1. $r$ - $\phi$ trigger

The CDC  $r$ - $\phi$  trigger is the main component of the charged track triggers. It has to identify tracks originating from the interaction point, discriminate against various background track sources, and make a fast determination of the track  $p_t$ , the track direction, and the number of tracks. The  $r$ - $\phi$  trigger is formed using discriminated axial-wire hit signals. Anode wires in each superlayer are grouped into track segment finder (TSF) cells and the hit pattern in each cell is examined by a memory look-up (MLU) table to test the presence of a candidate track segment. MLUs are latched

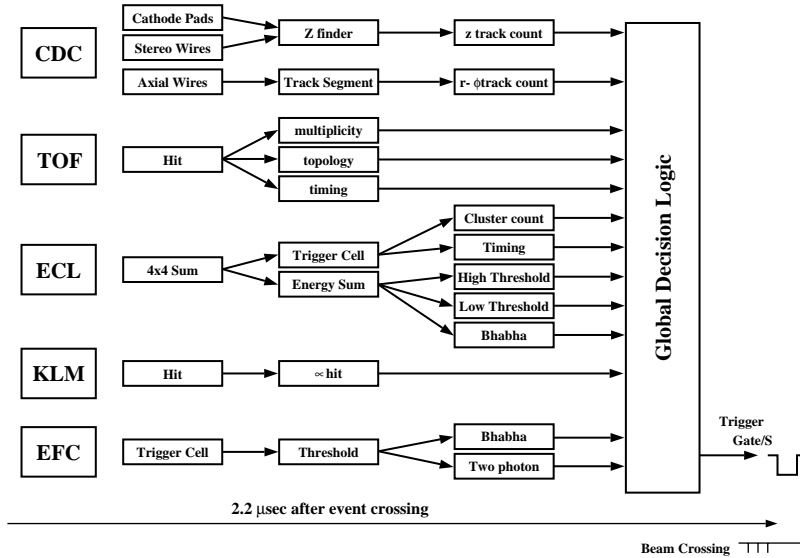


Fig. 117. The Level-1 trigger system for the Belle detector.

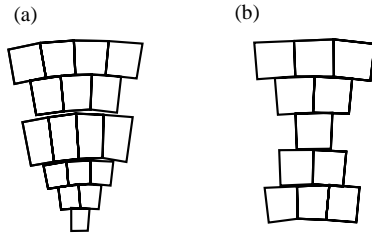


Fig. 118. CDC track segment finder (TSF) cells for (a) innermost superlayer and (b) outer superlayers.

periodically by a sample clock of 16 MHz. Fig. 118 shows the TSF cells for the CDC superlayers. The numbers of wires in a TSF cell are 17 for the innermost superlayer and 11 for outer superlayers, as shown in Figs. 118(a) and (b), respectively. In the order of the increasing superlayer radius, the numbers of TSF cells are 64, 96, 144, 192, 240, and 288. The TSF cells in the innermost superlayer are very important for rejecting tracks that originate away from the interaction point and the MLU pattern for these layers must be determined with special care.

The TSF-cell outputs are logically ORed in a superlayer to form track finder (TF) wedges. Fig. 119 shows one of 64 TF wedges. The number of TSF cells to be ORed depends on the  $p_t$

threshold chosen. The hit patterns of the TF wedges are fed into the next MLU stage. The second-stage MLU provides several output bits for different track categories according to patterns:

- short track (track in the three innermost trigger layers,  $p_t \geq 200 \text{ MeV}/c$ ) or
- full track (track which goes through all CDC trigger layers,  $p_t \geq 300 \text{ MeV}/c$ ).

The output signals from the 64 TF wedges are fed into the next stage to determine an event topology:

- counting of the number of short and full tracks,
- determination of the maximum opening angle between tracks, and
- recognition of back-to-back track topologies.

The conditions are under software control and have considerable flexibility. The topology signals are sent to GDL.

Figs. 120 and 121 show the efficiency of short and full tracks as a function of  $p_t$  and  $\theta$  obtained from beam data samples, respectively. The efficiency drops at  $p_t = 0.2$  and  $0.3 \text{ GeV}/c$  for the short and full tracks, respectively, as designed. The

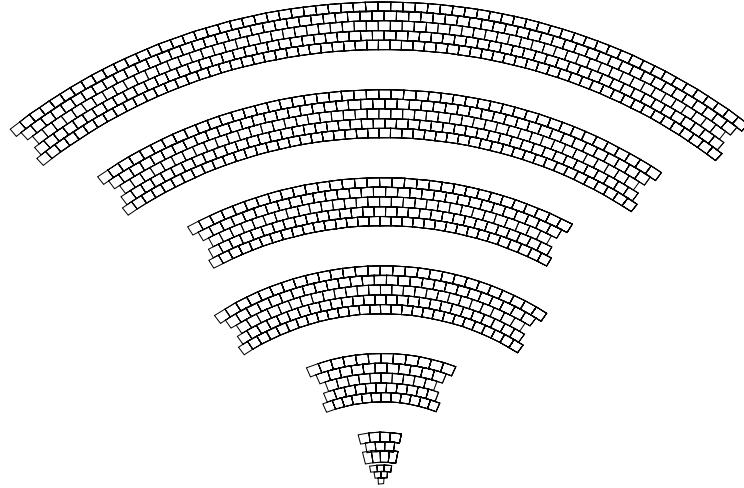
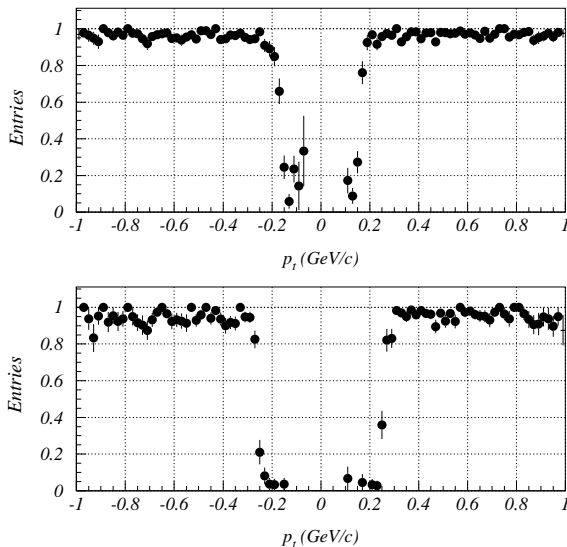


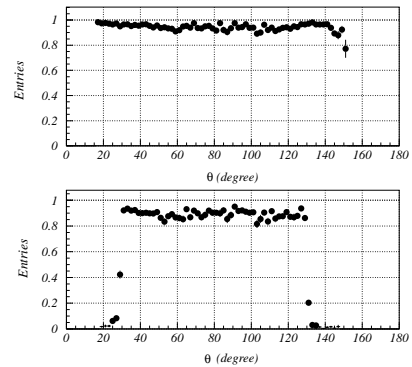
Fig. 119. CDC track finder (TF) wedge.

Fig. 120. CDC  $r$ - $\phi$  trigger efficiency as a function of  $p_t$  for the short (top) and full (bottom) tracks. For the full tracks, only tracks in  $40^\circ < \theta < 140^\circ$  are used.

short track is efficient for the full angular acceptance ( $17^\circ < \theta < 150^\circ$ ), while the full track covers the barrel region only ( $30^\circ < \theta < 130^\circ$ ).

### 11.1.2. $z$ trigger

A fast  $z$  trigger is important for discriminating charged tracks produced at the interaction point from background tracks from interactions of spent

Fig. 121. CDC  $r$ - $\phi$  trigger efficiency as a function of  $\theta$  for the short (top) and full (bottom) tracks. Only tracks above the designed  $p_t$  threshold are used.

electrons with the material around the beam pipe, beam gas events, and cosmic-rays. The  $z$  trigger was designed by utilizing the  $z$ -position information from the three cathode layers and the axial/stereo layers of CDC [85]. The cathode hit information provides direct information on the  $z$ -coordinate close to the interaction point. The accuracy of the cathode  $z$ -position is determined by the cathode-strip width of 8 mm and the cathode-strip-cluster size which is typically from 1 to 3 strips for a normally incident track. Since these cathode layers are located at the innermost CDC region, the additional  $z$  information provided by the stereo wires is necessary for good

trigger performance. Fig. 122 shows the trigger tower map. One axial/stereo  $z$ -trigger layer consists of consecutive two axial and two stereo layers. Each pair of neighboring axial and stereo wires yields a calculated  $z$ -position. The coincidence of two axial or stereo layers is formed to reduce accidental trigger signals due to uncorrelated noise hits. The accuracy of calculated  $z$ -coordinates is around 50 cm for a single pair of axial stereo cell hits.

The  $z$ -position is calculated in 8 azimuthal  $\phi$  segments individually. In order to avoid the inefficiency for tracks around the  $\phi$  segment boundary, the calculated  $z$  signals of adjacent  $\phi$  segments are ORed. The tracks in the  $r$ - $z$  plane ( $z$ -

tracks) are reconstructed by seven sets of  $z$ -positions as shown in Fig. 122. A pattern yielded by tracks is represented by a “trigger tower map”. When the  $z$ -positions in the inner and outer layers line up with the same tower bit, which presents the same polar angle from the  $z$ -axis ( $\theta$ ), it is regarded as being a track from the interaction point. In order to reduce the effects of inefficiencies of CDC wire and cathode hits, we require at least two hit layers among the three cathode layers and at least one hit layer in each of the middle and outer layers with the logic shown in Fig. 122.

The schematic diagram of the  $z$ -trigger logic is shown in Fig. 123. There are five processes for the wire logic and four for the cathode logic. The

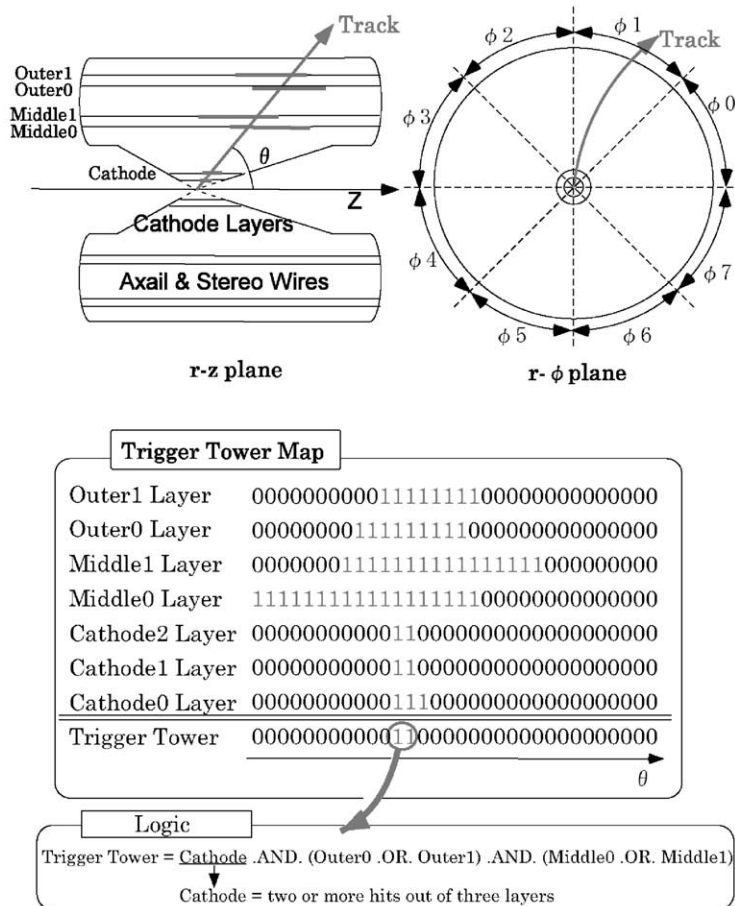


Fig. 122. Trigger tower map. The  $z$ -positions of each layer are calculated in 8 azimuthal segments individually. When a track passes through CDC, as shown in the upper figure, it yields the trigger tower map shown in the lower figure. If the  $z$ -positions of the middle and outer layers of the cathode line up with the same  $\theta$  value, it is regarded as being a track from the interaction point.

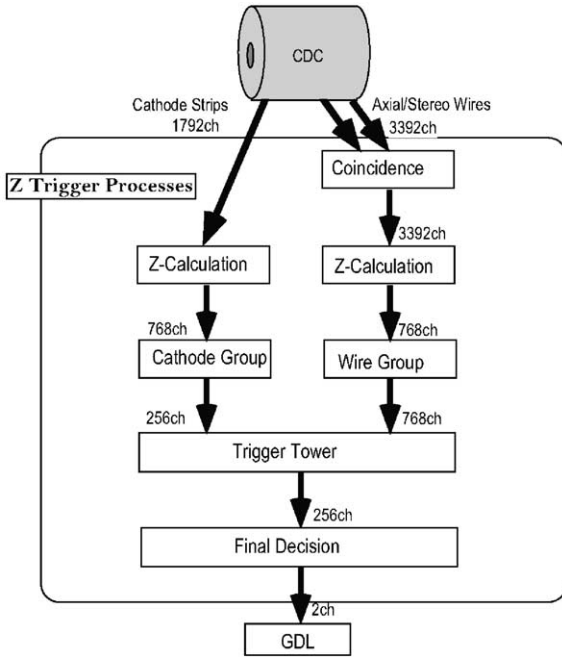


Fig. 123. Schematic diagram of the  $z$ -trigger algorithm.

number of  $z$ -tracks formed by the trigger tower process is counted in the final decision process. Finally, a two-bit signal corresponding to the number of  $z$  tracks originating from the interaction point is transmitted to GDL.

The  $z$ -trigger system is constructed with three types of modules. The detail of hardware implementation is described in Ref. [85]. The main trigger module is a 9U-VME containing 7 Xilinx FPGA chips (XC4005HPG223) with 384 I/O's. All  $z$ -trigger logics are implemented in the FPGA chips using 53 of these modules. The  $z$ -trigger processes are run in a pipeline mode synchronized with a 16 MHz clock in order to avoid any deadtime losses. The trigger signals from the  $z$ -calculation and trigger-tower logic are read by TDC to monitor the  $z$ -trigger logic. The  $z$ -trigger logic run in a pipelined mode with 11 steps synchronized with a 16 MHz clock requires 687.5 ns. Including the drift time in CDC and propagation delay in the cables, the maximum latency of the  $z$ -trigger system was found to be about 1.45  $\mu$ s.

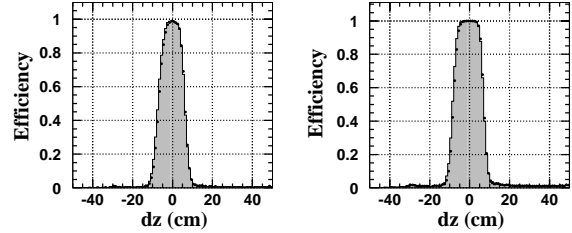


Fig. 124. Trigger efficiency as a function of  $dz$  for a single track (left) and an event (right) with the “at least one  $z$ -track” condition. The dots are the efficiency for cosmic data of the  $z$ -trigger logic, and the histogram is the efficiency for the reconstructed logic using CDC hit data as the input.

Fig. 124 shows the trigger efficiency as a function of the distance from the IP ( $dz$ ) for single tracks with  $p_t > 500$  MeV/ $c$  (left figure) and for events with the “at least one  $z$ -track” condition (right figure) for cosmic-rays. The tracks originating from  $|dz| > 10$  cm are effectively rejected. The efficiency is greater than 98% for single tracks with  $p_t > 300$  MeV/ $c$ .

In order to keep the efficiency high, we require at least one  $z$ -track in the actual trigger condition. Because of quite high hit rates at the innermost layers of the CDC due to the beam background, the rejection power of the  $z$ -trigger is reduced. Fig. 125 shows the  $z$ -distribution of the track for two-track events with and without the  $z$ -trigger requirement, in which we require at least one  $z$ -track. The  $z$ -trigger reduces about one-third of background events without losing beam interaction events.

### 11.2. TOF trigger system

The TOF trigger system provides an event timing signal and information on the hit multiplicity and topology to GDL. The multiplicity and topology information can be used to perform internal event selection and reduce the rate of timing signals to acceptable levels before it is delivered to GDL. A prompt Level-0 (L0) trigger signal is also delivered to SVD based on independent event selection criteria.

The timing signal of an event is required to be sufficiently precise to make a gate for the ECL readout and to provide  $T_0$  to the CDC readout,

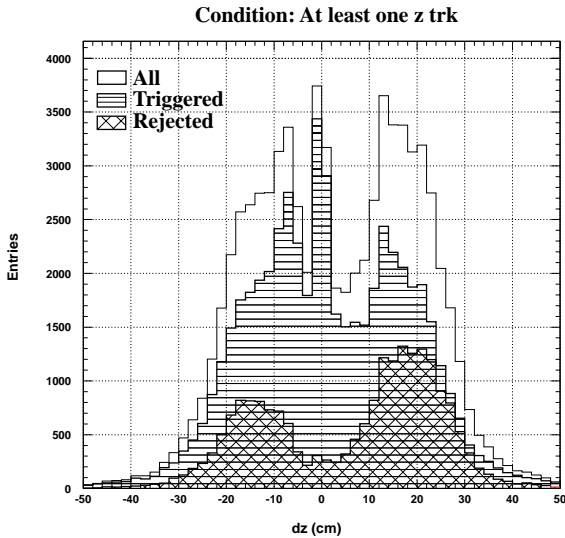


Fig. 125.  $z$ -distribution of two-track events with (single-hatched histogram) and without (blank histogram)  $z$ -trigger requirements. The cross-hatched histogram shows the  $z$ -distribution of rejected events.

namely to have a time jitter less than 10 ns. Owing to the very fast time response of TOF signals, a time jitter of about 5 ns is feasible. Although the timing of each PMT signal varies in a time range of 4–33 ns depending on the hit position, the mean time stays within a small time range of 4.8–7.2 ns for the Belle TOF configuration. The time jitter caused by variations in pulse height (time walk effect) is expected to be less than 1 ns at the nominal discrimination level. Thus, the TOF mean time can provide a precise event timing signal with a jitter of about 5 ns. This signal must be delivered at rates below 70 kHz to ensure only one timing signal to appear in the GDL event window.

The SVD readout electronics calls for a shaping time faster than  $\sim 2 \mu\text{s}$  required by GDL to make an event decision. The TOF readout and trigger electronics can provide a prompt trigger signal with approximately a 0.85  $\mu\text{s}$  delay. This includes  $\sim 500 \text{ ns}$  to make internal event multiplicity and topology calculations used to reduce the level zero rate to acceptable levels. The trigger rate must be below 40 kHz to ensure a reasonable deadtime in the SVD readout electronics.

### 11.2.1. Timing logic

The TOF trigger timing logic consists of four stages shown in Fig. 126. The nominal timing discriminator is gated with a high level discriminator set at approximately  $\frac{1}{3}$  MIP (minimum ionizing particle). This is repeated for both the forward and backward PMTs. Signals from the forward and backward PMTs are then required to be within 32 ns coincidence window by the mean timer circuit. This removes random noise hits in scintillators or PMTs.

Next, the mean time signal is required to be in coincidence with a hit in the corresponding TSC counter. To allow for track curvature, the coincidence is taken between one TSC and four TOF counters, which removes background hits caused by photons converted in the TOF scintillators. The combination of one TSC and four TOF scintillators constitutes one trigger segment.

The above logic is repeated 64 times to form a 64-bit hit pattern. Finally, the TOF trigger timing signal is formed by taking OR of all 64 segments.

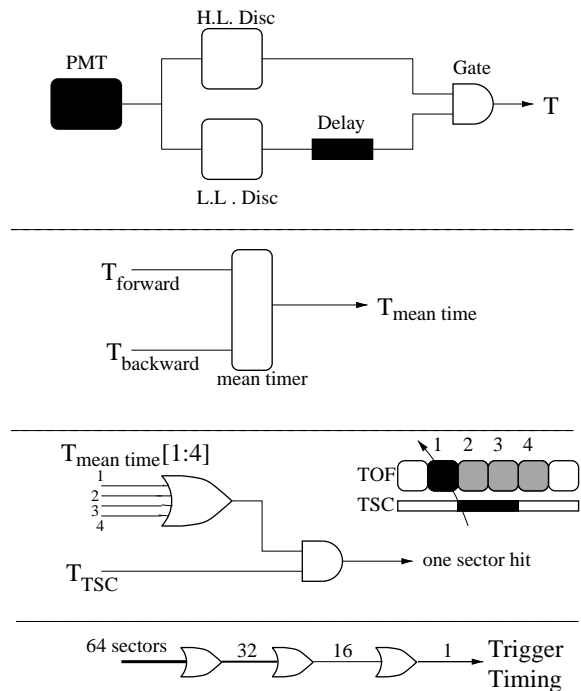


Fig. 126. TOF trigger timing logic.

Thus the first arriving segment hit determines the event timing.

### 11.2.2. Delay and decision logic

Fig. 127 shows the TOF trigger decision logic. The TOF detector multiplicity and event topology are calculated in 32 MHz pipelines consisting of Xilinx FPGA chips. The use of FPGAs allows us to change the pipeline logic depending on the running conditions. The multiplicity pipeline calculates the multiplicity of hits for GDL and the multiplicity clusters for SVD where a cluster is formed by adjacent hits. A multiplicity threshold is set independently for GDL and SVD. The topology pipeline is currently designed to trigger events with a back-to-back topology. It can also independently determine the event opening angle. Various pipeline algorithms take typically less than 15 cycles which introduce a 500 ns delay.

The timing signal must be delayed while the event multiplicity and topology are calculated in the pipelines. Furthermore, the delay time should be programmable to allow for different pipeline delays. The timing signal is thus delayed using a FIFO which is also controlled by the 32 MHz RF clock. The delay is set to an integral number of clock cycles when FIFO is initialized. To maintain the  $\sim 5$  ns timing resolution, the timing signal is converted to a 7-bit signal at the FIFO input, each bit separated by 5 ns. The relative delay between the incoming timing signal and the RF clock edge is encoded into 7 bits. A similar decoding is

applied at the FIFO output which restores the initial phase to within  $\pm 2.5$  ns.

The timing signal is then combined with the information from the pipelines and sent to GDL and SVD. Currently, to keep the timing signal rate below 70 kHz the timing signal is only given for events in which the multiplicity of hits is greater than or equal to two. This criteria also gives an acceptable rate for SVD.

### 11.3. ECL trigger system

The calorimeter is expected to generate fast trigger signals in order to provide a fully efficient trigger for both neutral and charged particles. Two kinds of trigger schemes are taken into account, namely a total energy trigger and a cluster counting trigger. These triggers are complementary each other since the former is sensitive to events with high electromagnetic energy deposits while the latter to multi-hadronic events that contain low-energy clusters and minimum ionizing particles. Fig. 128 shows the schematic diagram of the calorimeter signal flow and the electronics arrangement to perform the two trigger schemes.

#### 11.3.1. Trigger cell

Fast shaped signals with a shaping time of 200 ns from each counter are generated in Shaper/QT (SHQT) and merged into a trigger cell (TC) composed of adjacent  $4 \times 4$  crystals that are the minimum unit for the ECL trigger system. A gain adjustment of 3 bits on each TC is performed to compensate for different light output of each crystal. Each TC is manipulated on a special trigger circuit board called sum-trigger module (STM) and a TC signal above a certain threshold energy from 50 to 100 MeV depending on trigger conditions is recognized as a hit cluster. The RMS variation of threshold values among TCs is  $\sim 3\%$  and has been stable during real data taking runs. Furthermore, a constant fraction discriminator is adopted in order to minimize the time-jitter of the trigger signal and to minimize its time spread. In the actual experimental situation, the noise level of TC units was measured to be about 8 MeV and the RMS timing resolution less than 20 ns. The latter value should be compared with a long decay

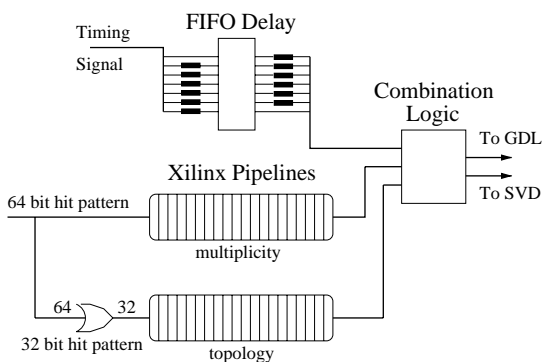


Fig. 127. TOF trigger delay and decision logic.



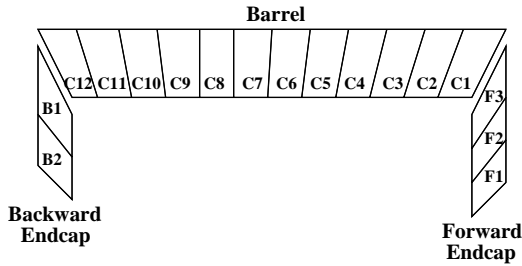


Fig. 129. Calorimeter division for the selection of Bhabha events in the  $\theta$ -direction. Here each unit represents one  $\phi$ -ring summation.

Table 13  
Various energy cuts to trigger Bhabha events<sup>a</sup>

Type	Logic	Threshold (GeV)
1	F1 + F2 + B1 + B2	9.0
2	F2 + F3 + B1 + B2 + C11	9.0
3 <sup>b</sup>	F2	6.5
4	F3 + C10 + C11	9.0
5	C1 + C9 + C10	9.0
6	C1 + C2 + C9	9.0
7	C2 + C8 + C9	9.0
8	C3 + C7 + C8	9.0
9	C4 + C6 + C7	9.0
10	C5 + C6	9.0
11 <sup>c</sup>	C10	3.5

<sup>a</sup>F, C and B represent the forward end-cap, barrel and backward end-cap calorimeters, respectively.

<sup>b</sup>Indicates backward gap.

<sup>c</sup>Forward gap.

$\phi$ -ring summation. The neighboring combinations are slightly overlapped with the next  $\phi$ -ring in order to save Bhabha events passing through the boundary region. These logics provide the trigger efficiency greater than 99% in real data taking runs.

Fig. 130(a) shows the singles rate of the total energy trigger for cosmic-rays as a function of threshold energy. Electronics noise and cosmic-ray contributions are clearly separated around 200 MeV, and the RMS noise level is about 50 MeV. For the physics trigger of total deposit energy, the threshold of about 1 GeV has been used stably.

### 11.3.3. Cluster counting trigger

Simple cluster counting often results in more hits than the real number of particles due to a wide spread of a cluster, and the trigger decision must be made reasonably fast.

An extensive GEANT-based Monte Carlo simulation study was performed in order to avoid such troubles, and a new algorithm which counts only the number of isolated clusters (ICN) was developed. The algorithm is shown in Fig. 131. This logic is implemented for each TC (denoted “0”). With this logic, only TC at the upper most and right most corner of a connected cluster produces a final hit signal. Other TCs do not give any final signal because they are vetoed by adjacent TC hits. The logic implemented on a Xilinx FPGA chip provides a clear separation between Bhabha and other hadronic physics events, and works exceptionally well.

This simple clustering logic is applied to over 132 TC input signals and the number of isolated clusters is then tallied. In addition, we delay the 132 input and 16 output signals to record in a set of FIFO pattern register on the board (CCM). The recorded cluster and ICN bits from the pattern register are read out through the VME-bus to allow a continuous monitoring of the operation of CCM. FPGA counts the number of clusters asynchronously and the timing latency of CCM turned out to be about 50 ns. Five CCM modules are needed to cover all the TCs and each CCM output is merged at the ECL trigger master (ETM) that provides the final number of ICNs. It consists of 3 bits and 1 carry-bit and is used in the physics trigger.

On the other hand, a simulation study indicates that the physics trigger design might not be adequate due to a relatively large contribution from cosmic-rays to the trigger. Thus, we have designed a very simple cosmic veto logic, in which ICNs are divided into four quadrants and arranged to make sure that particles are produced from the  $e^+e^-$  interaction point. With this condition, the contribution from cosmic-rays could be lowered to about 10 Hz as shown in Fig. 130(b).  $ICN > 3$  has been used to trigger physics events in real data taking runs.

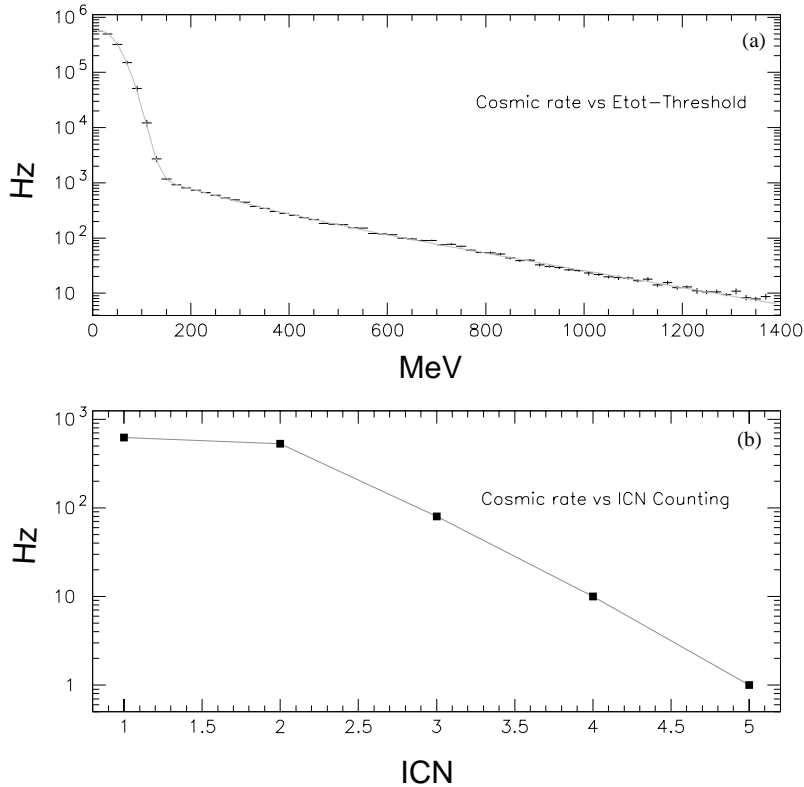


Fig. 130. (a) Singles rates of the total energy sum ( $E_{tot}$ ) as a function of threshold energy. Electronics noises and cosmic-rays are clearly separated around  $E_{th} = 200$  MeV. (b) Singles rates as a function of the number of isolated clusters (ICN).

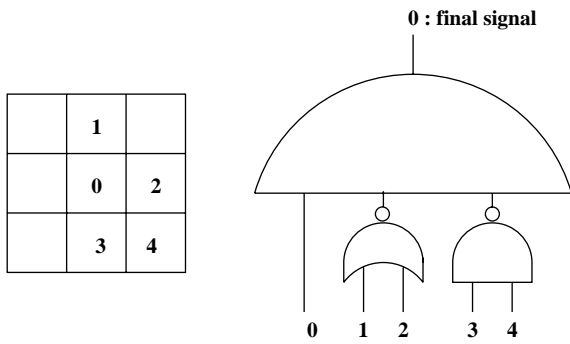


Fig. 131. A logic diagram for the isolated cluster number counting. Among nine TC cells, only three center cells and two right cells are considered in isolated cluster counting logic.

#### 11.4. KLM trigger

The role of the KLM trigger system is to save events which include muon tracks as many as possible. Thus, the high efficiency of KLM muon

trigger is more important than the cleanliness of trigger signals in the system design.

##### 11.4.1. KLM signal out

The KLM subsystem consists of barrel KLM and end-cap KLM. Barrel KLM is divided into forward and backward parts and each part consists of 8 sectors. End-cap KLM also consists of forward and backward parts and each part has 4 sectors. Each sector has 15 superlayers for barrel KLM and 14 superlayers for end-cap KLM. Each superlayer consists of 2 RPC layers. The output of superlayers has 48 copper strips (barrel  $\phi$ ,  $z$ , and end-cap  $\theta$  readout) or 96 copper strips (end-cap  $\phi$  readout). Raw output signals are sent to readout boards, located at the Belle detector, to discriminate noise signals and then the number of channels is reduced by using a time-multiplex circuit implemented on Xilinx FPGAs mounted on the readout boards. The time-multiplex circuit

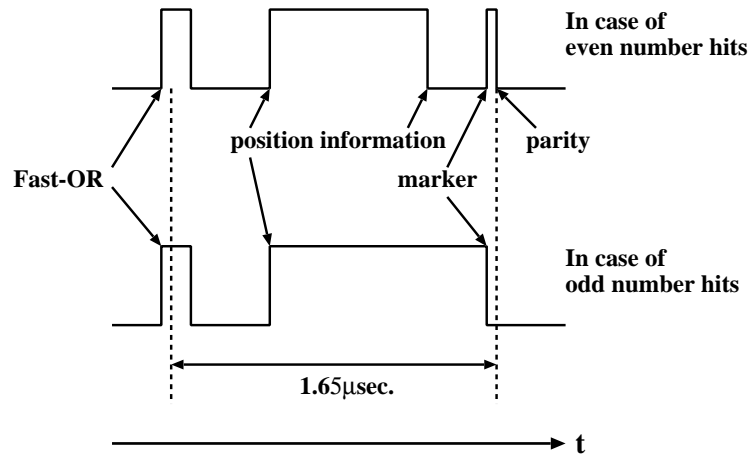


Fig. 132. Schematic diagram of readout board output signals.

converts the hit strip information of each 12-strip inputs to the timing signals of one channel output using a 10 MHz system clock. The output signal also has time information of the earliest input among 12 strips (Fast-OR). Fig. 132 shows a schematic diagram of signals of the readout board output. A Fast-OR signal is sent first, and then the converted position information is sent next. Finally, a marker signal which shows the end of position information and a parity signal which is used for checking the number of hit strips are sent. Thus, one signal train lasts at least 1.65  $\mu\text{s}$  (max. 1.75  $\mu\text{s}$ ). The length depends on the timing of raw signal inputs, because Fast-OR is asynchronous to the system clock. The output signals are sent to the TDC inputs in the electronics hut via 50-m long twisted pair cables. For the triggering purpose, barrel  $z$  and end-cap  $\theta$  readouts are used.

#### 11.4.2. KLM trigger scheme

The KLM trigger system consists of 2 CAMAC ULM2366 modules fabricated by LeCroy and custom-made 12 NIM modules for signal OR, called "OR-module". OR-modules pick up readout board output signals of the trigger layers with high impedance input. Then, OR-module makes an ORed signal for each 4 input channels that correspond to one superlayer. The output signal width of OR-module is made 1.8  $\mu\text{s}$  in order to mask the trailing output signals of the readout

board which hold position information. The output of OR module is sent to CAMAC ULM2366 which produces a trigger signal. In order to reduce accidental trigger rates, the signal length at the input of ULM is shortened to 25–50 ns from 1.8  $\mu\text{s}$ . The length depends on the timing between the input signals and the ULM system clock.

Fig. 133 shows the signal flow of the KLM trigger system. In the case of barrel KLM, 4 superlayers among 15 superlayers were selected as trigger layers, i.e. layers 02, 03, 10, and 11. The layer numbers start from 00. In order to reduce the inefficiency caused by the gap between forward and backward barrel KLMs, forward and backward superlayers, which are located at the same layer number and the same sector number, are logically connected in ULM, and treated as one superlayer. When 2 out of 4 superlayers in a sector have coincidental hits, a trigger signal is made. Trigger signals from all the sectors are ORed, and then sent to GDL. Since a ULM module has a limited number of input channels, signals from barrel KLM are divided into 2 ULMs. Thus, the barrel trigger output from one ULM is connected in series to another ULM. In the 2nd ULM, all barrel trigger signals are ORed.

In the case of end-cap KLM, 2 layers among 14 superlayers were selected as trigger layers, i.e. layers 04 and 05. In order to avoid fake trigger signals caused by beam backgrounds, the outer

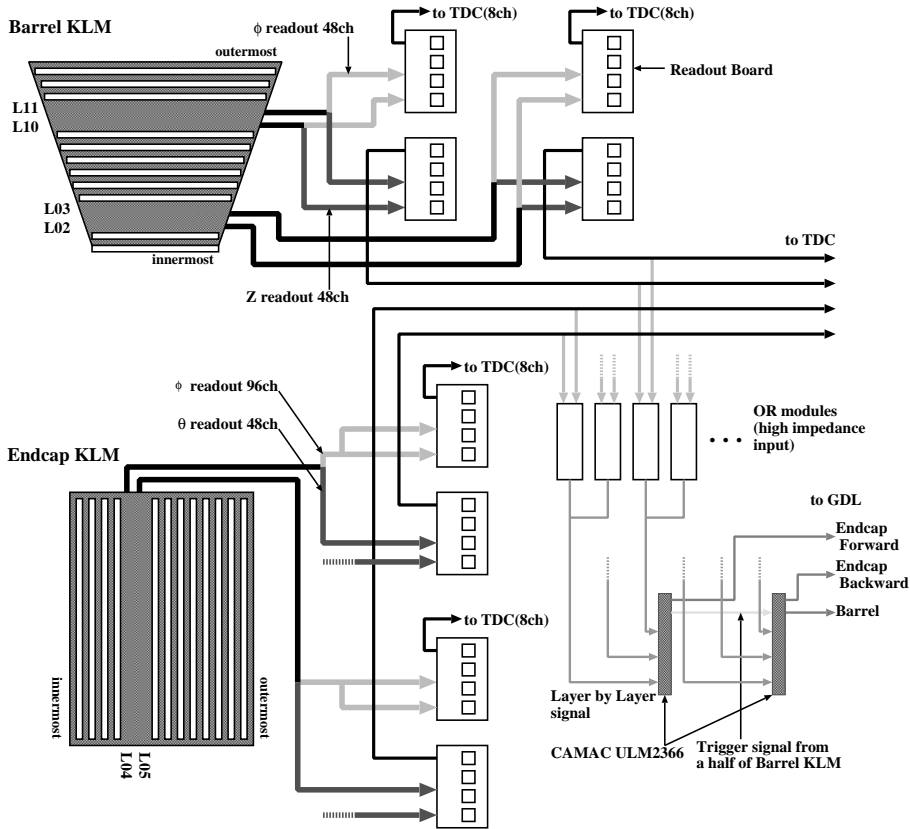


Fig. 133. Schematic diagram of the KLM readout board output signals and the trigger system.

superlayers are not used as trigger layers. When both trigger layers have coincidental hits, a trigger signal is made. Trigger signals from 4 sectors of each part are ORed separately and then sent to GDL.

Thus, the KLM trigger system makes three types of trigger signals; barrel, end-cap forward, and end-cap backward.

### 11.4.3. Trigger efficiency

Since the KLM trigger and hit information are not required in  $\mu$ -pair event selection criteria, the KLM trigger efficiency was studied using  $\mu$ -pair event samples. Fig. 134 shows track by track trigger efficiencies as functions of  $\cos \theta$ ,  $\phi$ , and run number.

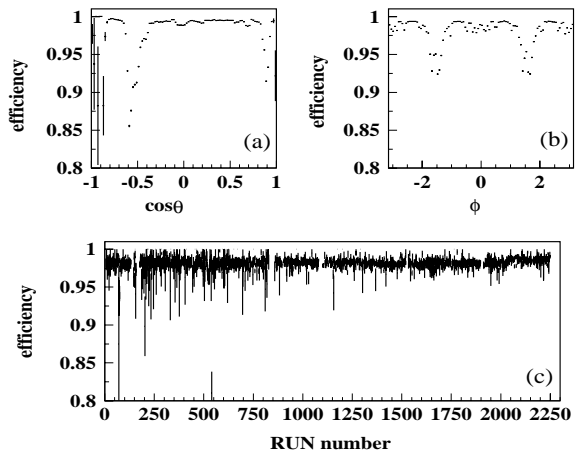


Fig. 134. Trigger efficiency using  $\mu$ -pair events: (a)  $\cos \theta$  dependence, (b)  $\phi$  dependence, and (c) run number dependence.

The two dips at  $\cos\theta = -0.6$  and  $0.9$  in Fig. 134(a) are caused by the KLM geometry. This is due to the chimney hole of the superconducting solenoid around  $\cos\theta = -0.6$ . Muon tracks which go through the hole do not yield trigger signals. When one track goes through the chimney hole, the other track tends to go to the forward end-cap region. The dip at  $\cos\theta = 0.9$  is caused by tracks which go to a sector gap of forward end-cap KLM. The cause for the dips shown in Fig. 134(b) is the same. Since the chimney hole is located around  $\phi = 1.2-1.9$ , the dip at this region is directly caused by tracks which go through this region and the dip around  $\phi = -1.5$  is caused by the other tracks of  $\mu$ -pairs.

Except for this geometrical effect, the trigger efficiency is kept about 98% in average. Fig. 134(c) shows the long-term stability of the KLM trigger efficiency from Jan. 2000 to Jun. 2000. Most of this period, the trigger efficiency has been kept above 97.5% and its fluctuation has been within statistical errors.

### 11.5. EFC trigger system

The EFC trigger provides two types of trigger information according to the energy and location of signals in the BGO crystals.

- *Bhabha trigger*: coplanar forward/backward coincidence of energetic EM showers in EFC
- *Two-photon trigger*: single EM shower together with some CDC tracks or ECL clusters.

The basic EFC trigger unit is a trigger cell. Two neighboring  $\phi$  segments have three trigger cells according to different  $\theta$  angles. In the innermost ring, a trigger cell is formed by two crystals. The other two trigger cells consist of four crystals each. The analog sum of crystal signals from the same trigger cell is fed into a constant fraction discriminator and gives the trigger output. Currently the trigger cell threshold is set at about 1 GeV. These trigger cells are then grouped into four sectors in  $\phi$  in the forward and the backward EFC separately. The trigger logic is made by a logical “OR” of all trigger cells inside each sector.

The logic output of one sector is used to form a back-to-back logic for a Bhabha trigger and also used as the gate signal for the MQT300A chips within the same sector. Another trigger scheme, called EFC-Tag, is formed by a logical “OR” of the four forward EFC trigger sectors. It is combined with central tracking and calorimeter information to provide a tagged two-photon trigger. A schematic diagram of the EFC trigger logic is shown in Fig. 135.

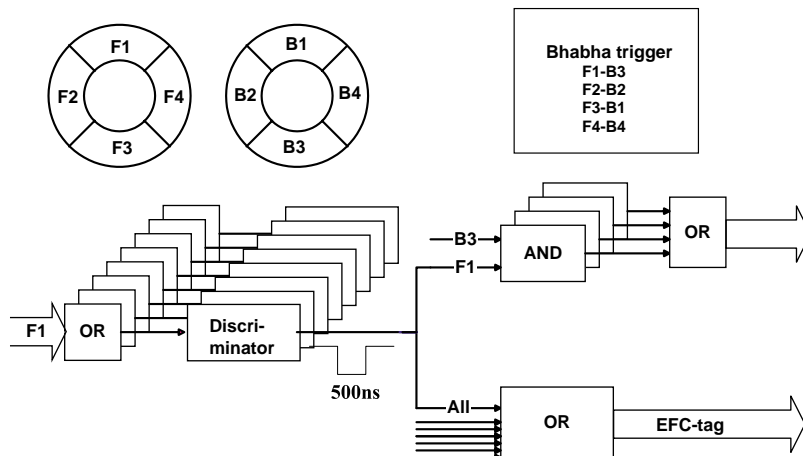


Fig. 135. Schematic diagram of the EFC trigger arrangement.

### 11.6. GDL

The configuration of GDL is shown in Fig. 136. GDL receives up to 48 trigger signals from sub-detectors and makes global correlations among them. It generates up to 48 types of event trigger signals. It is designed to function in a pipelined manner with a 32 MHz clock in order to avoid deadtime losses and it takes 350 ns to generate the final trigger signal. The functionality of GDL is shared by several types of modules as shown in Fig. 136:

- Input Trigger Delay (ITD) which adjusts the timing of input trigger signals to meet the latency of 1.85  $\mu$ s,
- Final Trigger Decision (FTD) which performs the global trigger logic, correlating the information from sub-detector triggers,
- Prescale and Mask (PSNM) which prescales the high rate input triggers for calibration and monitoring purpose and disables the unused triggers from FTD, and
- Timing Decision (TMD) which generates the final trigger signal at 2.2  $\mu$ s latency based on the timing information of the “timing trigger” from TSC and ECL.

The ITD, FTD, PSNM and TMD modules serve as the components of GDL. They are designed as single width 6U VME modules. These modules extensively use Xilinx FPGA and CPLD chips [84] in order to provide sufficient flexibility in the system.

The timing decision logic uses a 64 MHz clock to provide 16 ns ( $\pm 8$  ns) timing accuracy. The trigger signals from GDL are synchronized to the beam crossing time since clock signals are made from the KEKB RF signal. The final trigger from GDL provides the timing for ADC gates and TDC stops. The trigger signals at each step of GDL are sent to scalers to monitor rates and deadtimes. They are also fed into FASTBUS multi-hit TDCs (LeCroy 1877S) to record the timing so that the timing and logic of GDL can be verified. The detailed description of the GDL system can be found in Ref. [83].

### 11.7. Trigger operation for beam run

Table 14 summarizes the sub-triggers fed into GDL. The final triggers are categorized as follows:

- (1) *Multi-track triggers:* These require three or more tracks in CDC  $r-\phi$  and at least one track in CDC  $z$ -trigger. Several types are formed

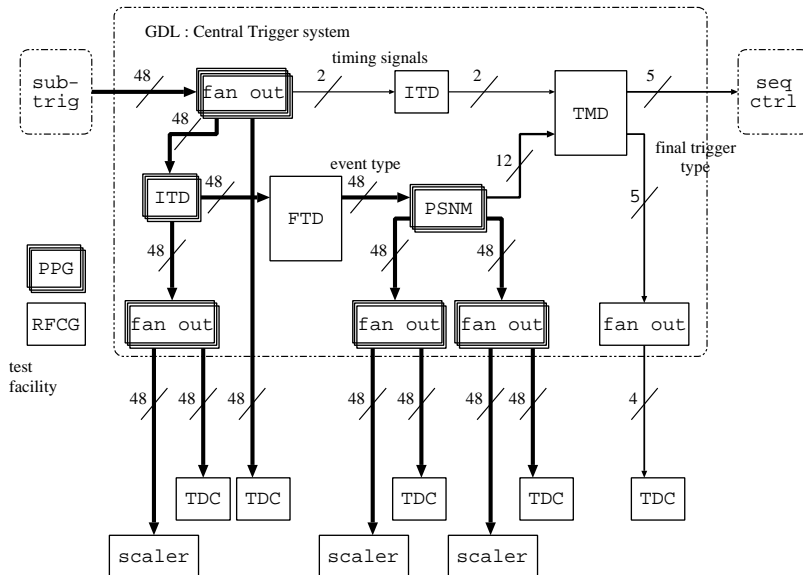


Fig. 136. Schematic design of GDL.

Table 14  
Summary of sub-detector triggers to GDL

Detector		Label	No. of Bits	Comments
CDC	$r\phi$	$N_{\text{CDR-Full}}$	2	CDC full track ( $N = 1, 2, \geq 3$ )
		$N_{\text{CDR-Short}}$	3	CDC short track ( $N = 1, 2, \dots, \geq 7$ )
		CDC:BB	1	CDC back-to-back tracks
		CDC:open	1	$\phi_{\text{open}} > 135^\circ$
TSC	Z	$N_{\text{CDZ}}$	2	CDC Z-track ( $N = 1, 2, \geq 3$ )
		TSC:timing	1	TSC timing trigger ( $N_{\text{TSC}} \geq 2$ )
		$N_{\text{TSC}}$	2	# of TSC hits ( $N = 1, 2, \geq 3$ )
		TSC:multi	1	$N_{\text{TSC}} \geq \text{Min}(= 2)$
ECL		TSC:patt	1	TSC pattern (1–3 back-to-back)
		$E_{\text{Tot}}$	3	$E_{\text{Tot}} > E_1, E_2, E_3(0.5, 1, 3 \text{ GeV})$
		$N_{\text{icl}}$	4	Number of isolated clusters (0–7, $\geq 8$ )
		ECL:BB <sub>pre</sub>	1	ECL Bhabha (prescaled)
		ECL:BB	1	ECL Bhabha (non-prescale)
		ECL:cosmic	1	ECL cosmic
KLM		ECL:timing	1	ECL timing (cluster $\geq 1$ )
		MU	3	Hits in KLM Fwd,Barl,Bwd
EFC		EFC:BB	1	EFC Bhabha
CALIB		EFC:Tag	1	Tag for two-photon
		Random	1	Random trigger
CALIB		Revolution	1	Revolution signal
		Total	32	+14 spare (= 48)

depending on the condition for the number of full tracks, opening angle, TSC/TOF hits, and ECL cluster hits.

- (2) *Total energy triggers*: These are based on the ECL energy sum triggers and vetoed by ECL Bhabha and cosmic triggers.
- (3) *Isolated cluster counting trigger*: We require four or more ECL isolated clusters, which avoid Bhabha events but still require cosmic veto to reduce the cosmic rate.
- (4) *Bhabha triggers*: We prescale these triggers depending on the luminosity to keep the rate less than 10 Hz.
- (5) *Two-track triggers*: These triggers take two or more tracks in CDC  $r\text{-}\phi$  and at least one in CDC  $z$ -triggers. In order to reduce the rate, these require CDC opening angle, TSC/TOF hits, and ECL energy or clusters.
- (6) *Muon triggers*: These require two or more CDC  $r\text{-}\phi$  tracks and KLM trigger. The track trigger conditions are loose.

- (7) *Monitor triggers*: These include a random trigger and prescaled triggers with loose conditions for monitoring purpose.

Triggers 1–3 are intended to catch multi-hadronic events, which provide a redundancy.

In a typical running condition, the average trigger rate is about 200 Hz. According to increase of the beam current and luminosity during several months of runs, we adjusted the trigger condition and prescale values keeping the average trigger rate less or around 200 Hz. The trigger rate is dominated by the beam background. Fig. 137 shows the trigger rate as a function of beam current of each electron and positron beam. The contribution of the electron beam dominates over that of positron. The trigger rate due to the collision of the beams is  $\sim 40 \text{ Hz}/10^{33}/\text{cm}^2/\text{s}$  under the present conditions.

The trigger efficiency is monitored from the data using the redundant triggers. Each of the multi-track, total energy, and isolated cluster counting

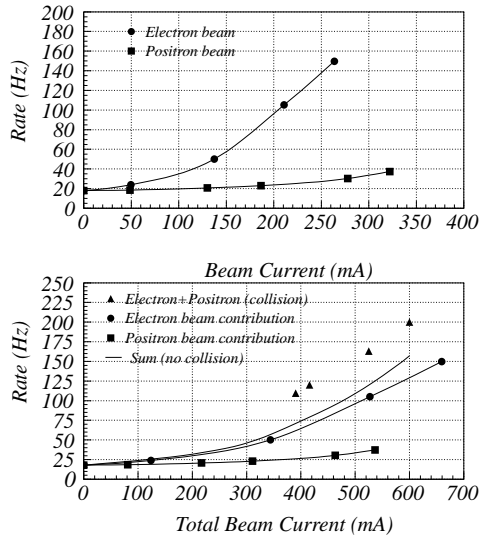


Fig. 137. Trigger rate as a function of beam current for electron or positron single beam runs (top), and total beam current in a collision run (bottom). Contributions of electron and positron single beams are also plotted for a typical beam current ratio of  $I_{e^+}/I_{e^-} = 1.5$ .

triggers provides more than 96% efficiency for multi-hadronic data samples. The combined efficiency is more than 99.5%.

## 12. Data acquisition

In order to satisfy the data acquisition requirements so that it works at 500 Hz with a deadtime fraction of less than 10%, the distributed-parallel system has been devised. The global scheme of the system is shown in Fig. 138. The entire system is segmented into 7 subsystems running in parallel, each handling the data from a sub-detector. Data from each subsystem are combined into a single event record by an event builder, which converts “detector-by-detector” parallel data streams to an “event-by-event” data river. The event builder output is transferred to an online computer farm, where another level of event filtering is done after fast event reconstruction. The data are then sent to a mass storage system located at the computer center via optical fibers.

A typical data size of a hadronic event by  $B\bar{B}$  or  $q\bar{q}$  production is measured to be about 30 kB,

which corresponds to the maximum data transfer rate of 15 MB/s.

### 12.1. Readout

#### 12.1.1. FASTBUS TDC readout systems

We adopted a charge-to-time ( $Q$ -to- $T$ ) technique to read out signals from most of the detectors. Instead of using ADC to digitize the amplitude of a signal, the charge is once stored in a capacitor and discharged at a constant rate. Two pulses, the separation of which is proportional to the signal amplitude, are generated at the start and stop times of the discharge. By digitizing the time interval of the two timing pulses with respect to a common stop timing, we can determine both the timing and the amplitude of the input signal. The hold timing is generated either by a self-gate method or the trigger signal from a timing distributor module, TDM. The mechanism is illustrated in Fig. 139.

For time digitization, we use a multi-hit FASTBUS TDC module, LeCroy LRS1877S. Up to 16 timing pulses are recorded for 96 channels in a single width module with a sparsification capability. The least significant bit is 500 ps. A programmable time window has a 16-bit range, which corresponds to a full scale of 32  $\mu$ s.

Most of the detectors, CDC, ACC, TOF, ECL and EFC, are read out by using the  $Q$ -to- $T$  and TDC technique. The use of the  $Q$ -to- $T$  technique reduces the number of cables for CDC wires into a half. In the case of TOF, the time resolution of 100 ps is achieved by using a time stretcher which expands the pulse width by a factor of 20. In the case of ECL, a 16-bit dynamic range is achieved by using three ranges. A signal is divided and fed into three preamplifiers of different gains, converted to the time pulse and merged with an exclusive-OR logic circuit. For a small signal, all the three ranges give short pulses and the final output has 4 time pulses. By contrast, for a large signal, high and middle gain pulses overflow and the final output has only 2 time pulses from the low gain range. After digitization, the range is identified by the number of time pulses for the pulse.

The KLM strip information is also read out by using the same type of TDC. Strip signals are

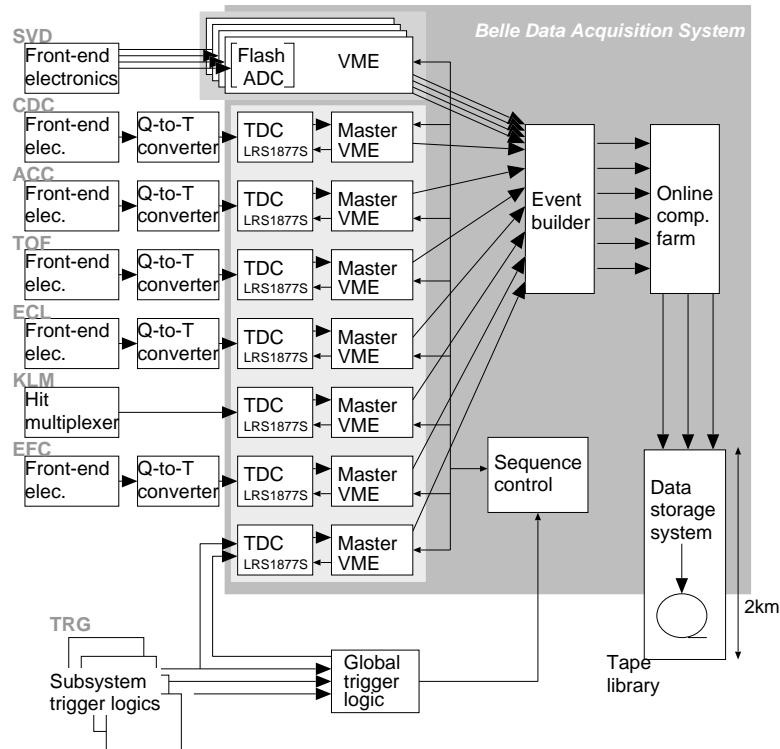


Fig. 138. Belle DAQ system overview.

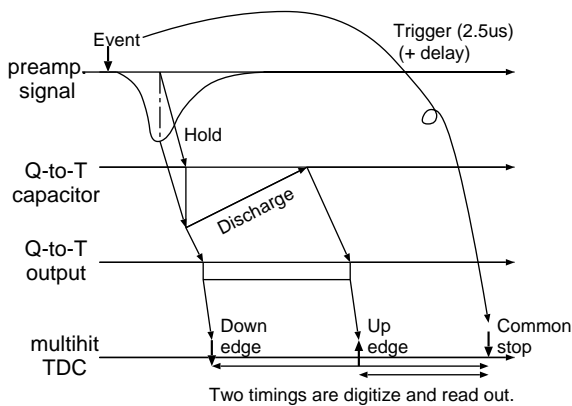


Fig. 139. Concept of the Q-to-T and TDC based digitization.

multimultiplexed into serial lines and recorded by TDC as the time pulses. These pulses are decoded to reconstruct hit strips. Similarly, a large number of trigger signals including those for the intermediate stages are recorded using TDC. A full set of trigger signals gives us complete information for trigger study.

We developed a unified FASTBUS TDC read-out subsystem that is applicable to all the detectors except SVD. A FASTBUS processor interface, FPI, developed by us controls these TDC modules, and FPI is controlled by a readout system controller in a master VME crate. Readout software runs on the VxWorks real-time operating system on a Motorola 68040 CPU module, MVME162. Data are passed to an event builder transmitter in the same VME crate. A schematic view of the system is shown in Fig. 140. The overall transfer rate of the subsystem is measured to be about 3.5 MB/s.

#### 12.1.2. SVD readout system

SVD data are read out from 81,920 strip channels, whose occupancy is typically a few percent depending on the beam condition. The charge information is read out by intelligent flash ADC modules with an embedded DSP, which performs data sparsification [86]. The resulting

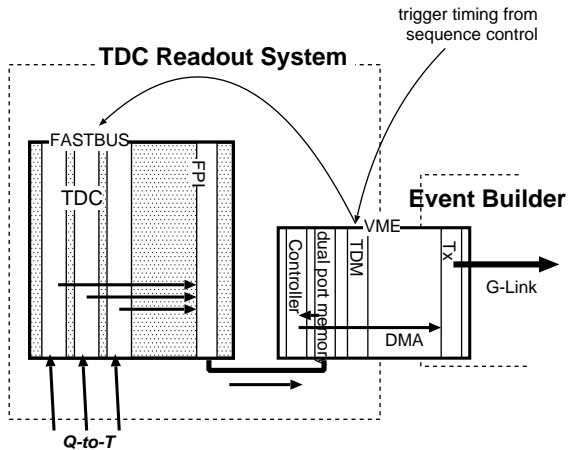


Fig. 140. Schematic view of the FASTBUS TDC readout system.

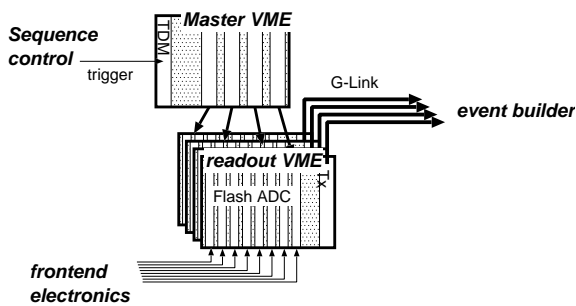


Fig. 141. Schematic view of the SVD readout system with 4 readout VME crates.

data size is 10–20 kB, which is larger than the capacity of a single event builder transmitter. The SVD readout system is divided into four VME crates, in each of which signals are read out in the flash ADC modules and transferred to the event builder in parallel. The SVD readout sequence is synchronized from an external control crate which receives the timing signal from the sequence controller. The schematic diagram of the SVD readout system with 4 readout VME crates is shown in Fig. 141.

The readout software for flash ADC is combined with the event builder transmitter software that runs on a SPARC VME CPU. By doing this, the overhead of extra data copying is minimized.

### 12.1.3. Readout sequence control

A timing signal for a readout sequence is handled by a central sequence controller and TDMs. The sequence controller receives a timing signal from the trigger system and distributes it to TDM located at the VME crate of each detector readout system. The handshake sequence is simply accomplished with the level of a single busy line from TDM to the sequence controller. Upon receiving a trigger signal, TDM generates an interrupt or raise a data ready flag to start a readout sequence. The busy line has to be raised and reset either by an external signal or by setting an internal register to receive the next trigger. The length of the deadtime after resetting the busy line is programmable, in order to compensate the cable delay between the readout crate and the front end electronics.

If no busy lines from the TDM modules are raised, the sequence controller initiates a readout sequence by a timing signal received from the trigger system. The trigger related information, such as trigger rates, deadtimes, and the beam bunch number, is monitored. In addition, the response time of the busy line from each sub-detector TDM is separately monitored, so that the location of a problem can be easily identified. The system is driven by 16/64 MHz clock pulses derived from the accelerator RF, and 16 MHz clock pulses are also distributed to TDM.

### 12.2. Event builder

The event builder constructs a complete event data from detector signals. Data are sent from seven VME crates of the FASTBUS TDC readout systems and four SVD VME crates. The output of the event builder is connected to six VME crates of the online computer farm. We use 1.2 Gbps ECL-level line, G-Link, for the data transfer layer [87]. The event builder is a  $12 \times 6$  barrel shifter consisting of 12 transmitters, 6 receivers and a set of  $4 \times 4$  and  $2 \times 2$  barrel shifter switches. The data path and the control path are shown in Fig. 142.

The barrel shifting sequence is controlled by an external controller through a 50 Mbps serial line, TAXI. The barrel shifter switches the

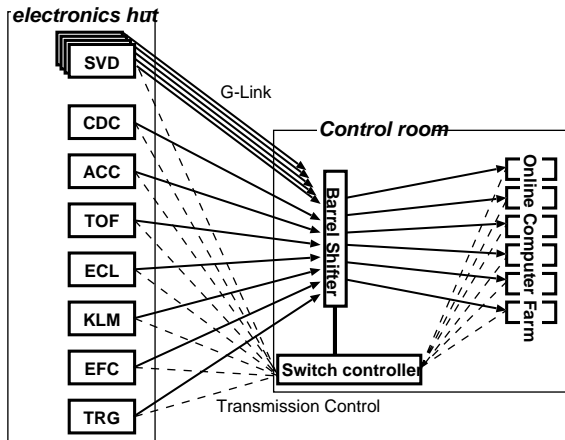


Fig. 142. The data flow and the control flow of the event builder.

configuration event-by-event according to the configuration given by the external controller to form an event.

The readout VME crates are located in the electronics hut near the detector, while the farm crates are in the control room. Thus, a long connection of about 100 m is required. G-Link signals are transferred via optical fibers, and TAXI signals are transferred by unshielded twisted pair cables. The transmitter and receiver modules are built as S-Bus adaptor cards, so that the VME SPARC CPU, FORCE CPU-7V, can be used as the controller. We are using Solaris OS for the control software.

### 12.3. Online computer farm

The role of the online computer farm [88] is to format an event data into an off-line event format and to proceed background reduction (the Level 3 trigger) using a fast tracking program [89]. Fig. 143 shows the architecture of the online farm. The farm consists of six VME crates. Each VME crate contains a Power-PC based control processor, Motorola MVME-2604, and 16 MC88100 event processors in four VME modules, Motorola MVME-188s. The interfaces for the event builder and the mass storage system are also implemented in each crate.

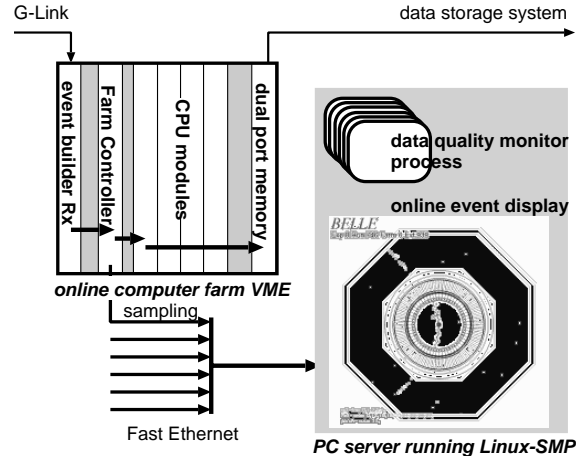


Fig. 143. The online computer farm, that consists of six VME crates of processors. Also shown is the data monitoring system using an external Linux-SMP PC server for data quality monitoring.

In each crate, data from the event builder interface are distributed to 16 event processors through the VME backplane, and the event formatting and background reduction are performed in parallel. The processed data are then sent to the mass storage interface. The throughput of a crate is 2.8 MB/s which corresponds to more than a 15 MB/s transfer rate with all the six crates.

The software for the online farm can be developed on a host workstation which has the off-line software development environment and the executable image developed on the workstation can be directly downloaded to the online farm.

### 12.4. Data monitoring system

A fraction of events are sampled on the online computer farm and sent to a PC server via Fast Ethernet for the real-time monitoring of data quality. The sampling rate is typically up to 20 Hz. On the PC server which is operated with Linux, the sampled data are placed on the shared memory and delivered to a set of monitoring programs under a control of a buffer manager, NOVA. Multiple monitoring programs including event displays run in parallel. The monitoring programs

are developed in the off-line environment and can be plugged into the sampled data stream without affecting the execution of others.

### 12.5. Mass storage system

Our mass storage system consists of two components. One is the data transfer system to send the data from the online computer farm to the tape library at the computer center which is located 2 km away from the experimental hall. The other is the high-speed tape drive. The system is shown in Fig. 144. The data transfer system is based on a set of one-way reflective memory modules connected via optical fibres. The point to point transfer rate is about 8 MB/s. Data from the six online farm crates are first transferred to three intermediate crates and then sent to the computer center via three optical fibers.

The data are received by a SUN workstation using a reflective memory module with the S-Bus interface and then written on a tape. The tape drive, SONY DIR-1000, has a capability to record

data at a 15 MB/s rate. Three drives are connected to the SUN workstation via the SCSI interface. One tape can contain 80 MB, which corresponds to a total capacity of 24 TB in the tape library. While one of three tape drives is used for recording, the second one stands by with a loaded tape, and the third one is reserved as a backup drive. By loading tapes on two drives, the tape change procedure completes in a few second although the loading and unloading procedure usually takes 2 min.

### 12.6. Run control

The control of all the Belle DAQ components is done based on the Ethernet/Fast Ethernet connection. A communication software called NSM, Network Shared Memory, is developed for the run control. NSM has two functionalities. One is the shared memory facility over the network space and the other is the function execution on a remote node by sending a message. Fig. 145 shows the architecture of NSM. The run control and the monitoring of the DAQ system are implemented over the NSM framework.

### 12.7. Performance

Fig. 146 shows the total deadtime of the DAQ system as a function of trigger rate measured in real-beam runs. The typical trigger rate is 200–250 Hz. The deadtime linearly increases as the trigger rate increases and reaches up to 4% at 250 Hz which is consistent with the designed value. The overall error rate of the data acquisition flow is measured to be less than 0.05%.

## 13. Offline computing system

The computing and software system is of great importance to the Belle experiment as very complex data analysis techniques using a large amount of data are required for physics discoveries. A traditional HEP computing model has been adopted by the Belle collaboration. Namely, the Belle collaboration has chosen to use tape library systems with the sequential access method

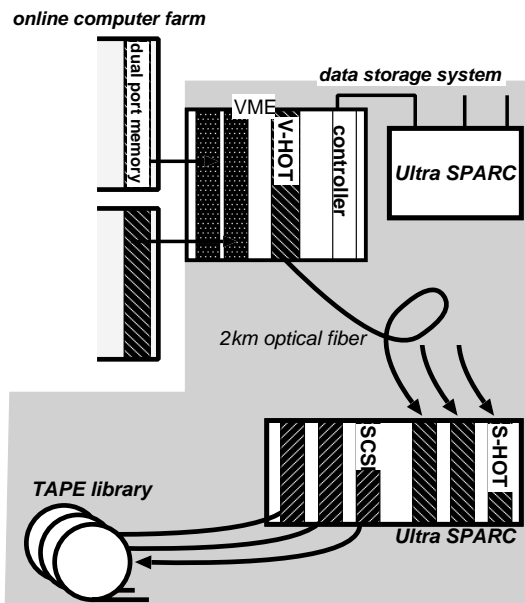


Fig. 144. Data storage system that transfers data from the online computer farm to the tape library system.

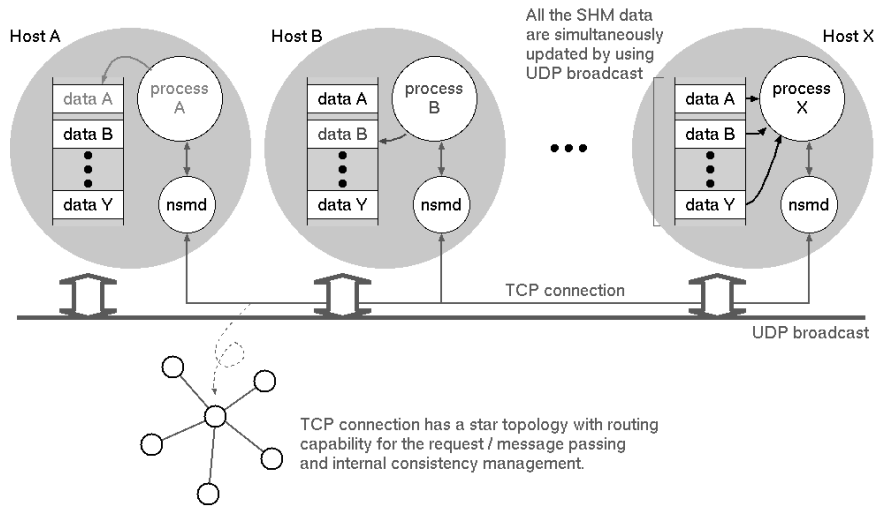


Fig. 145. Architecture of Network Shared Memory (NSM).

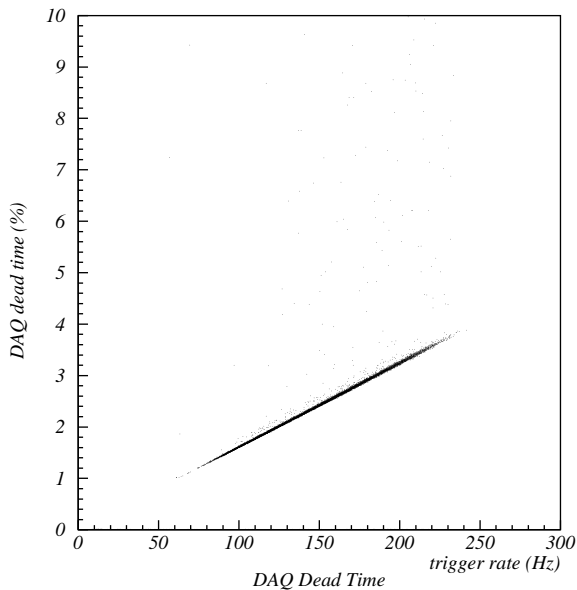


Fig. 146. DAQ deadtime as a function of trigger rate.

for the input and output of experimental data as the mass storage system.

### 13.1. Computing power

The maximum data rate from the Belle detector, discussed in the previous section, is 15 MB/s,

which corresponds to the maximum trigger rate of 500 Hz and the maximum event size of 30 KB. Raw data are accumulated at the rate of about 5 MB/s, corresponding to 400 GB/day or 80 TB/yr. The traditional style data summary tapes, DSTs, are produced from tape to tape by running the reconstruction algorithms on raw data. DSTs contain only physics events and thus the size of DST is reduced to 4 GB per  $\text{pb}^{-1}$ . As we have taken data of 6.8/fb between October 1999 and July 2000, we have produced 28 TB of DST.

In order to satisfy the above offline computing needs, a large computing system has been set up at the computing research center of KEK. The system consists of a computing server system, a RAID disk system and tape library system for mass storage, work group servers, and high-speed network systems. The network systems connect all the subsystems. The main purpose of the offline computing system is to process data taken by the Belle detector and to store them so that users can analyze them. Fig. 147 shows a schematic diagram of the Belle computing system.

The computing server system consists of seven Ultra Enterprise servers. Each server has 28 167-MHz Ultra SPARC CPUs and is rated to be more than 7000 SpecInt92s. Each server has 7 GB of physical memory so that the parallel

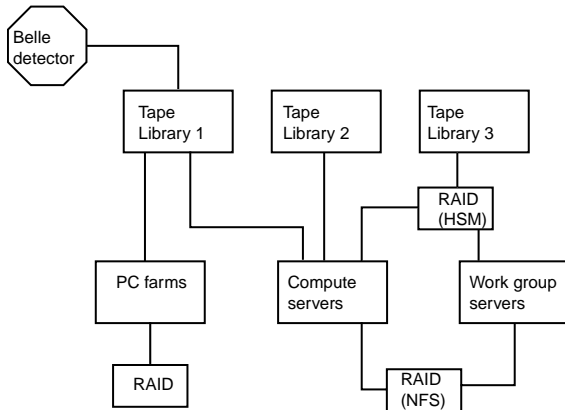


Fig. 147. Block diagram of the Belle computing system.

reconstruction processes can be run without swapping memories.

### 13.2. Tape libraries and servers

The tape library systems consist of (1) SONY PetaSite DMS-8800, (2) SONY PetaSite DMS-8400 and (3) two sets of SONY PetaSite DMS-8400 with PetaServe hierarchical storage system software. Tape library system (1) has a capacity of 25 TB and contains two DIR-1000 tape drives with a writing speed of 32 MB/s and nine DIR-1000M tape drives with a writing speed of 16 MB/s. The two 32-MB/s DIR-1000 and one 16-MB/s DIR-1000M drives are connected to the fast data transfer system and used to write online data. Six 16-MB/s DIR-1000M tape drives are each connected to six of seven computing servers and used for DST production. The remaining two drives are connected to a less powerful compute server (11 CPU) and used for the backup of the system. Tape library system (2) has a capacity of 75 TB and contains 15 DTF tape drives with a data transfer speed of 12 MB/s. Attached on each computing server are two DTF drives. Each set of tape library system (3) can hold 25 TB of data. The PetaServe hierarchical storage system software functions as if all files were on a hard disk.

The RAID system consists of six Gen5 (Strategy S-Series XL) storage servers. Five of the six Gen5

servers have 640 GB each and the 6th one 480GB. Each storage server has up to 8 independent SCSI host connections and therefore the disks are connected to 31 data servers and 11 work group servers.

The data servers and the compute servers are integrated into Fujitsu Parallel Server AP3000 with a proprietary network, called AP-Net by Fujitsu Ltd. The network has a two-dimensional torus topology with the maximum point to point data transfer speed of 200 MB/s.

For each sub-detector group and each core software group, a work group server has been allocated. The number of CPUs varies from 2 to 6 depending on the size of the group. Eight of 12 work group servers have 2 to 6 250-MHz ultra SPARC II CPUs and four sets of 6 167-MHz ultra SPARC CPUs. Each group server has a 40 or 80 GB RAID system described above. Users, who usually log in to these work group servers, develop and debug programs, and analyze data.

In the RAID system the storage capacity of 1.36 TB, which is mounted on the data servers, serves as NFS disks and holds mini-DST data. The capacity of 1.12 TB is also mounted on the data servers and serves as NFS disks with migration using 50 TB capacity of tape library (3).

All servers run Solaris 2.5.1 operating system. The group and computing servers run Distributed Computing Environment/Distributed File System (DCE/DFS) from IBM and LSF (Load Sharing Facility, <http://www.platform.com>) from Platform computing. The KEKB computing system described above was set up in January 1997 and has been running since. The system is on a lease contract that ends in January 2001. A new system will be installed to replace the current system.

### 13.3. PC farms

Two PC farms have been added to incorporate ever growing demands for generic Monte Carlo generation. The first farm, added in 1999, consists of 16 4 CPU DELL Power Edge servers. CPUs are 550 MHz Pentium III Xeon processors. The second farm, which was added 1 yr later, consists of 20 4 CPU DELL Power Edge servers with 550 MHz Pentium III processors and 2.4 TB

RAID systems attached to four 2 CPU servers. All compute nodes are connected via 100 BaseT and two farms are connected using GbE hub. These nodes are connected to two data servers of the KEKB computing system. A little less than one million Monte Carlo events can be generated in 1 day if the entire farms are used. The third PC farm which consists of 40 sets of 2 800-MHz Pentium III processors has been set up for DST production. Two tape servers have been set up to distribute data read from raw and/or DST tapes. The tape servers are connected to PC farm disk servers via GbE (Giga bit Ethernet).

#### 13.4. Offline software

All software except for a few HEP-specific and non-HEP-specific free software packages has been developed by the members of the Belle collaboration. In particular, the mechanisms to handle event structure and input and output formatting and to process events in parallel on a large Symmetric Multiple Processor (SMP) compute server have been developed locally using C and C++, programming languages. GEANT3 has been used in simulations [90].

The event processing framework, called Belle Analysis Framework (BASF) [89], takes users' reconstruction and analysis codes as modules which are linked dynamically at the run time. A module is written as an object of a class of C++. The class, inherited from the module class of BASF which has virtual functions for events, begins and ends run processing and other utility functions such as initialization, termination and histogram definitions. Modules written in Fortran and C can also be linked using wrapper functions.

The data transfer between modules is managed by PANTHER, an event and I/O management package developed by the Belle collaboration. PANTHER describes the logical structure and inter-relationships of the data using an entity relationship model. In order to store data (structure) in the event structure one writes a description file as an ASCII text file. A PANTHER utility converts the description file into C and C++ header files and source code. The user will include the header files in his/her code and the source code

is compiled and linked into the user module to have access to the data structure in the module.

The standard reconstruction modules for sub-detectors and global reconstruction of four momenta, production vertices and likelihoods for being specific species such as electrons, muons, pions, kaons, protons and gammas of charged and neutral particles have been prepared and used to produce physics results as well as detector performance results described in this paper.

#### 13.5. Level 4 offline trigger software

The purpose of Level 4 software filtering is to reject backgrounds just before full event reconstruction in the very beginning of the DST production chain. At the same time, high efficiencies for signal events are also required. The signal events include not only  $B\bar{B}$  events but also other physics related events such as  $\gamma\gamma$  or  $\tau$  events, and events necessary for detector calibration, etc. such as di-muon events.

Most of backgrounds are related to beam activities by both electrons and positrons. Fig. 148 shows  $dr$  (top) and  $dz$  (bottom) distributions obtained by a fast tracker, *fzisan* [91], which has been developed for the use in Level 4. The open histograms are track-by-track basis distributions, and the hatched distributions are for tracks closest to the coordinate origin in each event. It can be clearly seen that many tracks are created at the beam pipe and that a large fraction of tracks are generated far away from the origin in the  $z$  direction caused by beam interactions with residual gases in the beam pipe. Therefore, the basic strategy to reject backgrounds is to select events with tracks originating from the interaction point, IP.

There are low multiplicity (in terms of charged particles) events even in  $B\bar{B}$  decays such as  $B^0 \rightarrow K_s \pi^0$ . In order to save these events, we keep events with large energy deposits in the electromagnetic calorimeter, ECL, redundantly.

The Level 4 algorithm consists of 4 stages of event selections as follows:

- *Selection by Level 1 trigger information.* Because of demands from the sub-detector groups,

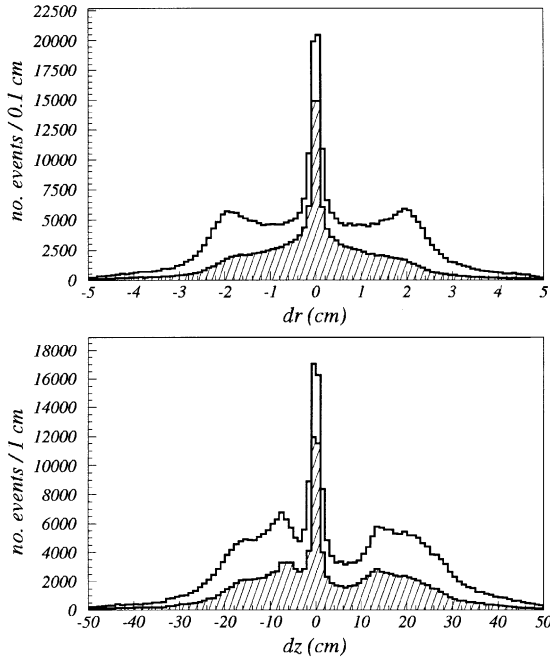


Fig. 148.  $dr$  (top) and  $dz$  (bottom) distributions. The open histograms are for track-by-track basis and the hatched histograms show  $dr$  or  $dz$  distributions closest to the origin in each event.

events with some specific trigger bits are saved without any further processing.

- **Energy measured by ECL.** We require the ECL energy reconstructed by *fzisan* to be greater than 4 GeV. Concurrently a veto logic using Level 1 information is applied, which is formed as a coincidence of ECL and KLM hits, to suppress background events induced by cosmic-rays.
- **Selection of events with a track coming from IP.** By reconstructing charged tracks by *fzisan*, events with at least one “good track” are selected, where a “good track” is defined as a track with  $p_t$  greater than 300 MeV/ $c$ ,  $|dr|$  less than 1.0 cm, and  $|dz|$  less than 4.0 cm. This corresponds to the application of cuts on the hatched distributions in Fig. 148.
- **Level 4 monitoring.** For monitoring of the performance of Level 4, 1% of events which fail our selection criteria are saved and passed to further full reconstruction.

Table 15

Fraction of events which satisfy the requirements of Level 4 in various samples of real data

Event type	Fraction passing Level 4 (%)
All triggered events	26.7
Hadronic events (loose selection)	98.1
Hadronic events (tight selection)	99.8
Muon pair events	98.7
Tau pair events	97.6
Two photon candidates	92.9

In order to reduce CPU usage, events satisfying our requirement in each stage are selected immediately and submitted to the full reconstruction chain without further processing.

Table 15 summarizes the Level 4 efficiency measured for various real data samples.

It can be seen that the data are significantly reduced while keeping high efficiencies for the signals. The efficiency for the high-purity hadronic sample is very close to 100%. The efficiency for two specific decay modes are also tested using MC data. First is a so-called gold-plated mode,  $B \rightarrow J/\psi K_s^0$  where the  $J/\psi$  and  $K_s^0$  decay generically and the decay of the other  $B$  is also generic. Second is  $B \rightarrow K_s \pi^0$  where again the daughter particles and the other  $B$  decay generically. Out of 1000 generated events each, the efficiency of Level 4 is 100% for both decay modes.

For the remaining events, the purity is 76.5% where the purity is defined as the number of events used in either physics analysis or calibration jobs divided by the number of events passing Level 4. This implies that only 6% more events can be suppressed even if we achieve 100% of purity ( $26.7\% \times (1 - 0.765) = 6.3\%$ ). Therefore, the reduction rate by Level 4 is close to the optimal value. The further drastic suppression requires changes in the definition of signals, i.e. tighter cuts in the event classification.

Fig. 149 shows the run dependence of the fraction of events which pass the Level 4 requirements.

There are some steps and bunch structures. Such structures are caused by the changes in the

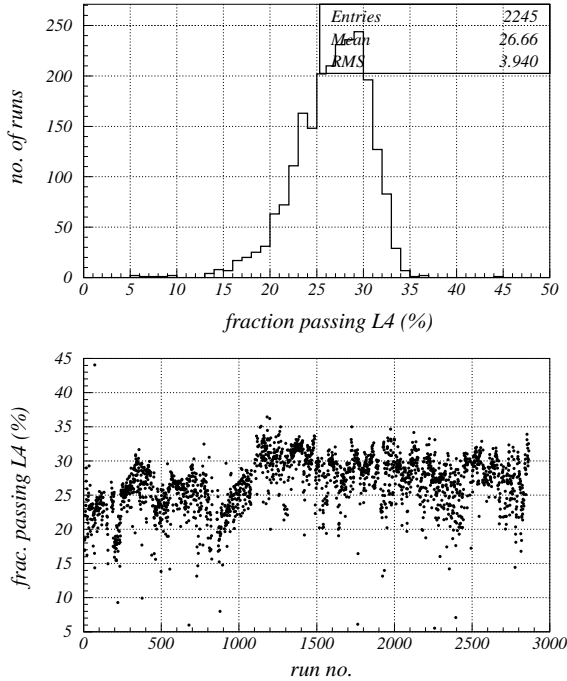


Fig. 149. Fraction of events which pass the Level 4 requirements as a function of run number (the full range is about 6 months). The macro structure is due to changes in the accelerator parameters.

accelerator parameters. Except for the macro structures, the Level 4 performance has been reasonably stable.

### 13.6. DST production and skimming

The events accepted by the Level 4 software filter are reconstructed and the information is stored as DST. In this stage, raw data, the contents of which are direct logs from data acquisition devices, are converted into physics objects of 4-vectors of  $x_\mu$  and  $p_\mu$ .

The most downstream of the reconstruction flow is the event classification and skimming. Here, all events are examined in such a way that certain selection criteria are applied to select events of our interest from a large number of background events. Once events are satisfied with our cuts, they are recorded into not only DST but also specific data files on the disk as skimmed data. In

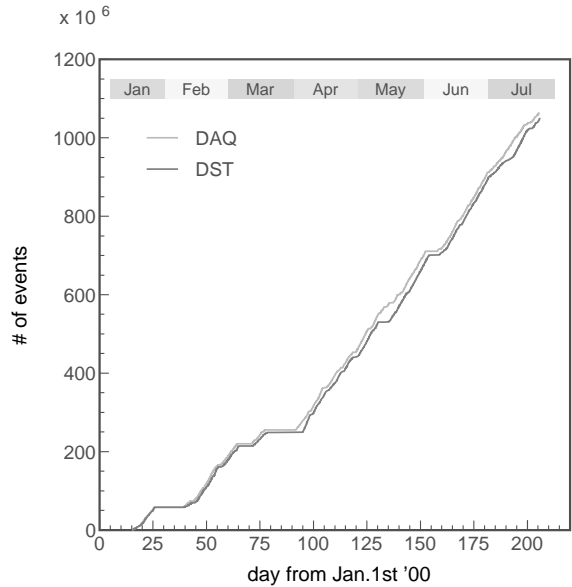


Fig. 150. History of the event processing rate together with the data acquisition rate.

this way, physics events such as hadronic events and Bhabha candidates are stored. Based upon those data, detector calibrations are carried out in detail and the offline luminosity is computed.

After all information is reconstructed, monitoring modules are called to keep our data quality reasonably high. Basic observables like the number of charged tracks reconstructed are booked and those histograms are checked by experts.

A typical processing speed of DST production, including skimming part, is around 40 Hz, depending on beam conditions. In our computing machines, we can process about 80/pb of data a day when three CPU servers out of seven are allocated. Fig. 150 shows a history of our event processing rate together with the data acquisition rate in the recent runs. Our offline processing has been well tracked to the online trigger rate with normally 1 day delay. The data size of DST is about 100 and 60 KB for hadronic and Bhabha events, respectively.

The calibration constants, which are used to correct detector responses, are kept in *postgresql* ([www.postgresql](http://www.postgresql)) database in our system. During the period of an experiment, detector raw

responses can be shifted due to changes in environmental conditions. The energy loss measurements by CDC, for example, suffer from atmospheric pressure changes. After checking skimmed data created by DST production job, the detector constants are improved on the weekly basis to correct for this sort of effects. By getting updated constants, the re-processing has been made for hadronic events.

In physics analyses, one does not need complete information available in DST. Instead, easy access to experimental data is highly demanded because we must play with a large amount of beam data at the B-factory. For this purpose, minimal sets of DST (“mini-DST”), which is compact but sufficient to study physics channels, are created for all runs. The hadronic event size at this level is about 40 KB.

## Acknowledgements

We extend deep thanks to the staffs of KEK and collaborating institutions for their contributions to the present work. We acknowledge support from the Ministry of Education, Science, Sports and Culture of Japan and the Japan Society for the Promotion of Science; the Australian Research Council and the Australian Department of Industry, Science and Resources; the Department of Science and Technology of India; the BK21 program of the Ministry of Education of Korea and the Basic Science program of the Korea Science and Engineering Foundation; the Polish State Committee for Scientific Research under contract No.2P03B 17017; the Ministry of Science and Technology of Russian Federation; the National Science Council and the Ministry of Education of Taiwan; the Japan-Taiwan Cooperative Program of the Interchange Association; and the US. Department of Energy.

## References

- [1] M. Kobayashi, T. Maskawa, *Prog. Theor. Phys.* 49 (1973) 652.
- [2] K. Abe, et al., KEK Report, 90-23, 1991; KEK Report, 92-3, 1993; KEK Report, 93-1, 1993.
- [3] M.T. Cheng, et al., Letter of intent for a study of CP violation in B meson decays, KEK Report, 94-2, 1994.
- [4] Belle Technical Design Report, KEK Report, 95-1, 1995.
- [5] KEKB B-Factory Design Report, KEK Report, 95-7, 1995.
- [6] Belle Progress Report, March 1997.
- [7] K. Ueno, et al., Proceedings of the Calorimetry Conference, 1999.
- [8] M.Z. Wang, et al., Belle Note # 164, 1996.
- [9] K. Ueno, et al., *Nucl. Instr. and Meth. A* 396 (1997) 103.
- [10] S.K. Sahu, et al., *Nucl. Instr. and Meth. A* 388 (1997) 144.
- [11] K.C. Peng, et al., *Nucl. Instr. and Meth. A* 427 (1999) 524.
- [12] K.C. Peng, et al., *Nucl. Instr. and Meth. A* 452 (2000) 252.
- [13] R. Akhmetshin, et al., *Nucl. Instr. and Meth. A* 455 (2000) 324.
- [14] K.C. Peng, et al., *Nucl. Instr. and Meth. A* 384 (1997) 544.
- [15] H.C. Huang, et al., *Nucl. Instr. and Meth. A* 385 (1997) 559.
- [16] Porous Fluorocarbon (Teflon) Sheets from Gore-Tex Inc., Japan.
- [17] M.Z. Wang, et al., *Nucl. Instr. and Meth. A* 455 (2000) 319.
- [18] E. Nygård, et al., *Nucl. Instr. and Meth. A* 301 (1991) 506; O. Toker, et al., *Nucl. Instr. and Meth. A* 340 (1994) 572.
- [19] V. Chabaud, et al., *Nucl. Instr. and Meth. A* 368 (1996) 314.
- [20] Omnetics Connector Corp., Minneapolis, MN.
- [21] M. Tanaka, et al., *Nucl. Instr. and Meth. A* 432 (1999) 422.
- [22] Y. Tsujita, Ph.D. Thesis, University of Tsukuba, March 1999.
- [23] N. Bingefors, M. Burns, FASTBUS version of the Silicon Read Out Camac Controller (SIROCCO), in: M. Budinich et al. (Eds.), Proceedings of the International Conference on the Impact of Digital Electronics and Microprocessors on Particle Physics, Trieste, Italy, 1988, World Scientific, Singapore, p. 116.
- [24] Tmpscan/1100, IOtech, Inc., USA.
- [25] S249PD12, Minco Products, Inc., USA.
- [26] Hamamatsu Photonics K.K., Japan.
- [27] REM OXFORD Ltd., UK and SPA Detector Ltd., Ukrain.
- [28] G. Alimonti, et al., *Nucl. Instr. and Meth. A* 453 (2000) 71.
- [29] R. Abe, et al., Conference Record of the 2000 IEEE Nuclear Science Symposium, IEEE Trans. on Nucl. Sci., submitted for publication.
- [30] S. Uno, *Nucl. Instr. and Meth. A* 379 (1996) 421.
- [31] H. Hirano, et al., *Nucl. Instr. and Meth. A* 455 (2000) 294.
- [32] S. Uno, et al., *Nucl. Instr. and Meth. A* 330 (1993) 55.
- [33] J.A. Kadyd, *Nucl. Instr. and Meth. A* 300 (1991) 436.
- [34] M. Akatsu, et al., *Nucl. Instr. and Meth. A* 454 (2000) 322.
- [35] O. Nitoh, K. Takahashi, T. Shinomura, O. Tsumura, S. Uno, *Jpn. J. Appl. Phys.* 33 (1994) 5929.
- [36] K. Emi, et al., *J. Phys. Soc. Jpn.* 65 (1996) 657; K. Emi, et al., *Nucl. Instr. and Meth. A* 379 (1996) 225.
- [37] Y. Fujita, et al., *Nucl. Instr. and Meth. A* 405 (1998) 105.

- [38] M. Morii, T. Taniguchi, M. Ikeno, KEK Internal Report 87-14, 1987.
- [39] MQT300 Fabrication Package, LeCroy Research System, 1995.
- [40] See TOF section in this report.
- [41] R. Früwirth, Nucl. Instr. and Meth. A 262 (1987) 444; R. Harr, IEEE Trans. Nucl. Sci. 42 (1995) 134.
- [42] T. Iijima, et al., Nucl. Instr. and Meth. A 379 (1996) 457.
- [43] T. Sumiyoshi, et al., A 433 (1999) 385.
- [44] T. Iijima, et al., A 387 (1997) 64.
- [45] I. Adachi, et al., A 355 (1995) 390.
- [46] H. Yokoyama, M. Yokogawa, J. Non-Cryst. Solids 186 (1995) 23.
- [47] T. Sumiyoshi, et al., J. Non-Cryst. Solids 225 (1998) 369.
- [48] S.K. Sahu, et al., Nucl. Instr. and Meth. A 382 (1996) 441.
- [49] Hamamatsu Photonics, 314-5 Shimokanzo, Toyooka, Shizuoka 438-0193, Japan.
- [50] R. Enomoto, et al., Nucl. Instr. and Meth. A 332 (1993) 129.
- [51] M.H.R. Khan, et al., Nucl. Instr. and Meth. A 413 (1998) 201; erratum A 432 (1999) 544.
- [52] R. Suda, et al., Nucl. Instr. and Meth. A 406 (1998) 213.
- [53] T. Iijima, et al., Nucl. Instr. and Meth. A 453 (2000) 321.
- [54] H. Kichimi, et al., Nucl. Instr. and Meth. A 325 (1993) 451.
- [55] H. Kichimi, G. Varner, Belle Note # 138, 1996.
- [56] T. Yamaguchi, Belle Note # 133, 1996.
- [57] H. Kichimi, et al., Belle Note # 223, April 1997.
- [58] H. Kichimi, et al., Nucl. Instr. and Meth. A 453 (2000) 315.
- [59] Y. Ohshima, et al., Nucl. Instr. and Meth. A 380 (1996) 517.
- [60] M. Tanaka, H. Ikeda, K. Tamai, M. Takemoto, H. Hayashii, IEEE Trans. Nucl. Sci. NS-41 (1994) 1208.
- [61] K. Kazui, et al., Nucl. Instr. and Meth. A 394 (1997) 46.
- [62] V.M. Aulchenko, et al., Nucl. Instr. and Meth. A 379 (1996) 491.
- [63] H.S. Ahn, et al., Nucl. Instr. and Meth. A 410 (1998) 179.
- [64] H. Ikeda, et al., Nucl. Instr. and Meth. A 441 (2000) 401.
- [65] E. Bulcher, et al., Nucl. Instr. and Meth. A 249 (1986) 201.
- [66] E. Aker, et al., Nucl. Instr. and Meth. A 321 (1992) 69.
- [67] B.G. Cheon, ICHEP99.
- [68] A. Abashian, et al., Nucl. Instr. and Meth. A 449 (2000) 112.
- [69] R. Cardarelli, et al., Nucl. Instr. and Meth. A 263 (1988) 20.
- [70] Yu.N. Pestov, Nucl. Instr. and Meth. 196 (1982) 45.
- [71] R. Santonico, R. Cardarelli, Nucl. Instr. and Meth. 187 (1981) 377.
- [72] F. Romano, et al., Proceedings of the Vulcano Workshop Conference, Vulcano, Italy, 1990, p. 337.
- [73] E. Gorini, Nucl. Phys. B 23 (1991) 249; L. Antoniazzi, et al., Nucl. Instr. and Meth. A 307 (1991) 312.
- [74] V.V. Parkhomchuck, et al., Nucl. Instr. and Meth. 93 (1971) 269; W.B. Atwood, et al., Nucl. Instr. and Meth. 206 (1983) 99.
- [75] N. Morgan, Second Int. Workshop on Resistive Plate Chambers and Related Detectors, Pavia, Italy, 1995, p. 101.
- [76] A. Yamaguchi, Fourth International Workshop on Resistive Plate Chambers and Related Detectors, Naples, Italy, 1997, p. 281.
- [77] Y. Makita, et al., Adv. Cryog. Eng. 37 (1992) 401; Adv. Cryog. Eng. A 43 (1998) 221;; H. Mukai, et al., in: Proceedings of the 15th International Conference on Magnet Technology (MT-15) (1998) 1044.
- [78] N. Tan, et al., KEK Preprint 2000-97, submitted Nucl. Instr. and Meth. A.
- [79] T. Ogitsu, et al., in: Proceedings of the 6th European Accelerator Conference (EPAC98), 1988. p. 2038.
- [80] Fukoku Co. Ltd. Motor Department, Oura-cho, Oura, Gumma, Japan.
- [81] ZOA99-3202 probe with Model 9953 Gaussmeter made by F.W. Bell, Division of Bell Technologies, 6120 Hanging Moss Rd., Orlando, FL, USA.
- [82] Echo Electronics Co. Ltd., Kashiwa-cho, Shiki, Saitama, Japan.
- [83] Y. Ushiroda, et al., Nucl. Instr. and Meth. A 438 (1999) 460.
- [84] The Programmable Logic Data Book 1998, Xilinx, Inc.
- [85] M. Tomoto, et al., Nucl. Instr. and Meth. A 447 (2000) 416.
- [86] M. Tanaka, et al., Nucl. Instr. and Meth. A., submitted for publication.
- [87] S.Y. Suzuki, et al., Proceedings of the XIth IEEE NPSS Real Time Conference, June 1999.
- [88] R. Itoh, Proceedings of the International Conference on Computing in High Energy Physics, 1992, p. 475.
- [89] T. Higuchi, et al., Proceedings of the International Conference on Computing in High Energy Physics, 1998.
- [90] GEANT Detector Description and Simulation Tool, CERN Program Library Long Writeup W5013, 1994.
- [91] K. Hanagaki, M. Hazumi, H. Kakuno, The Level 4 Software Trigger at Belle, Belle Note # 299.